Ore mineralogy and geochemistry in the M2 orebody, Challenger, SA: Implications for gold distribution and remobilisation

Royce Haese - 1160832

School of Earth and Environmental Sciences, University of Adelaide, South Australia, 5005

Phone: 0408897407

Email: royce.haese@student.adelaide.edu.au

Supervisors

Nigel J. Cook, Cristiana L. Ciobanu

School of Earth and Environmental Sciences, University of Adelaide, South Australia, 5005

Abstract

The Challenger gold deposit, northwest Gawler Craton, South Australia, underwent granulite-facies metamorphism during the Sleafordian orogeny. Since its discovery, debate has focused on the genetic history of the Challenger deposit and whether the mineralisation is metamorphogenic (syn-orogenic) or metamorphosed (pre-metamorphic precursor). Unlike other studies that have targeted the silicate assemblages in the wallrock to understand ore evolution, the present study attempts to unravel part of the genetic history from the ore minerals themselves, specifically from the main ore minerals (löllingite, arsenopyrite and pyrrhotite) and various trace minerals. The study is also the first which has been able to access the entire strike of the M2 orebody, which forms the mainstay of current exploitation. One goal of the work was to establish if distinctions could be made between mineralogy and textures in the M2 orebody and those in distinct high-grade areas of the deposit.

By integrating microscopy, electron probe analysis, determination of trace element distributions in ore minerals by laser-ablation ICP mass spectroscopy (LA-ICP-MS), electron back-scatter diffraction (EBSD) and transmission electron microscopy of pyrrhotite, the study has established that grain-scale remobilisation of lattice-bound gold to form visible gold took place by mineral-fluid interaction via coupled dissolution-reprecipitation reaction. This is in addition to the melt-assisted remobilisation of Au, which is considered to account for the high-grade ore. The study shows that the ore mineral assemblage in M2 ore is broadly similar to that of M1, except that there are some significant differences with respect to the association of gold; Au-Ag-Te associations appear to be more important in M2 than Au-Bi associations described in earlier publications.

The LA-ICP-MS data show that tens of ppm Au are retained in the löllingite lattice, but that coexisting arsenopyrite is a very poor host for invisible Au. The trace element contents of the two minerals in different textural settings can help to constrain the metamorphic development of the ore. Furthermore, the pioneering attempt to use EBSD to study associations of löllingite and arsenopyrite show promise for relating gold remobilisation to deformation. Mineral assemblages and trace element signatures observed in the present study are consistent with a precursor, zoned, epithermal-style deposit.

The mineral inventory of the Challenger deposit has been expanded by the identification of several telluride minerals previously unreported from Challenger (hessite, petzite, hedleyite, volynskite), as well as greenockite, scheelite and gahnite. Two less-common pyrrhotite types (3C and 1C) are also reported. The presence of Ag-rich electrum, sub-microscopic gold at reaction fronts between arsenopyrite and löllingite, 'invisible' gold in löllingite, and the presence of graphite in the M2 ore, all carry implications for mineral processing and gold recovery.

TABLE OF CONTENTS

1. INTRODUCTION

In highly metamorphosed terrains, significant challenges are present at all stages of development, from discovery to recovery. Initially the continuum model (Groves 1993) was applied to 'gold-only' deposits in Archaean domains; this model implies a syn-peak development of gold-rich zones throughout the 20-25km crustal profile. Phillips & Powell (2009) use Challenger as a case study of how this model does not adequately explain Archaean gold deposits, citing observations made by Tomkins & Mavrogenes (2002) that infer a pre-peak origin of gold deposition, with partial melting during granulite-facies metamorphism further remobilising and concentrating the gold. Such a model presents further challenges, however, when attempting to reconstruct ore genesis. The high degree of deformation experienced by these deposits effectively obscures many of the diagnostic features of gold deposits, both mineralogically and structurally, that would otherwise allow interpretation of the method of gold emplacement.

Thus, alternative techniques must be developed and investigated. Whole rock geochemistry can provide insight into alteration undergone in the area pre-peak metamorphism (McFarlane *et al.* 2007) and the studying and interpretation of structural features of the deposit can be used to interpret pre-deformation geometries (McGee *et al.* 2010).

Until now there exists a significant gap in knowledge about this type of deposit, that is, an in-depth understanding of the sulphide and arsenide minerals that are intimately associated with gold emplacement. In this study, sulphide and arsenide minerals are comprehensively investigated using a series of state-of-the-art methods to establish ore mineral distribution, geochemistry and deformation history encoded in the ore minerals from the mine- to the atomic-scale. The refractory character of some of the ore minerals means that they effectively record portions of their complex deformational and metamorphic history.

In their 2002 paper, Tomkins & Mavrogenes gave a description of the Challenger deposit as it was known at that time (pre-production). In that study sampling was restricted to the M1 orebody. The present work takes account of several years gold production and the access which this has provided to a much larger part of the deposit. In particular, the present study is focussed on the M2 orebody which contributes the bulk of present production, and is the first study to attempt to document possible differences in mineralogy and ore texture across the depth of current operations.

2. GEOLOGICAL SETTING

2.1 Regional geology

The Challenger gold deposit is located within the Christie sub-domain of the Mulgathing complex in the northwest Gawler Craton, South Australia (Fig. 1a). The Mulgathing complex is made up of the Christie Gneiss, the Kenella Paragneiss, the Harris Greenstone Belt, the Devils Playground Volcanics and the Glenloth Granite (Daly & Fanning 1993; Daly *et al.* 1998).

The Christie sub-domain includes aluminous metasediments, quartzite, banded iron formation, marble (locally dolomite), and calc-silicate domains (Daly & Fanning 1993; Daly *et al.* 1998). The aluminous metasediments represent the majority of the Christie Gneiss and are coarse-grained, granulite-facies, plagioclase-K-feldspar-quartz-garnet-cordierite-biotite-sillimanite gneisses with localised garnet-bearing leucosomes. Peak metamorphism reflects the granulite-facies regional event achieved during the Sleafordian Orogeny (2437 ± 11Ma, U-Pb dating of zircon; Fanning 1997), with calculated peak pressure-temperature conditions reaching 4.5-5.5kbar and 750-800 ºC (Teasdale 1997).

Swain *et al.* (2005) integrated existing regional data to interpret a convergent margin setting with coeval back-arc or arc-rift deposition of the major metasedimentary and metavolcaniclastic units that make up the late Archaean sequences of the Gawler Craton. Basin development was terminated by crustal thickening and associated granulite-facies metamorphism during the Sleafordian Orogeny. Later granulite-facies metamorphism observed elsewhere within the Gawler Craton during the Kimban Orogeny (1845-1700 Ma; Parker 1993) and the Kararan Orogeny (*ca* 1650 Ma; Teasdale 1997) is only expressed as greenshist-facies retrograde metamorphism in the Christie gneiss (Tomkins *et al.* 2004). Tomkins *et al.* (2004) also hypothesise exhumation of the deposit to be associated with the 1200-1100 Ma Grenvillian Orogeny.

2.2 Deposit/mine geology

The Challenger deposit is hosted within the Christie Gneiss. McFarlane *et al.* (2007) classified the rocks comprising the deposit into four main lithologies: (1) dark-grey granoblastic to locally magmatic garnet-biotite ± orthopyroxene distal gneisses, with sparse pyrrhotite; (2) dark-grey granoblastic garnet-cordierite proximal gneisses locally with elevated As and disseminated pyrrhotite, arsenopyrite, löllingite, chalcopyrite pentlandite, gold and native bismuth; (3) metatexite migmatites containing abundant (30-40%) coarse-grained stromatic leucosomes; and (4) bluish quartz-rich veins, locally intimately associated with migmatite leucosomes. A series of late mafic-ultramafic dykes and sills are also observed. These late lithologies are unaffected by granulite-facies metamorphism but are affected by greenschist-facies retrograde metamorphism (Tomkins & Mavrogenes 2002). More than 500,000 ounces of gold have been produced to date at Challenger. The ore is situated within a series of tightly folded ore-shoots that dip 34º towards 30ºT (Fig. 1b). The ore shoots (9.0 $g.t^{-1}$ average) consist of the M1 shoot, which to date has been the dominant source of the gold produced, the M2 shoot, which is currently being exploited and the M3 shoot, which is beginning to be mined. A series of minor high yield zones have also been identified through exploration drill core sampling. The ore shoots extend down plunge continually for more than 1 km with a slight fault offset interpreted approximately 700 m down plunge.

While it is well understood that gold deposition was pre-peak metamorphism, significant debate exists as to the genesis of the Challenger deposit. McFarlane *et al.* (2007) use whole rock geochemistry to recognise fossil zones of hydrothermal alteration, and physical and geochemical observations to propose an epithermal-style Au deposit that was reworked during collisional orogenesis. Birt & Reid (2007) and McGee *et al.* (2010) favour a mesozonal-orogenic style system due to the absence of elements associated with felsic magmatism such as Cu, Mo and Ag.

3. APPROACH AND METHODOLOGY

To characterize the Challenger ore, underground fieldwork was undertaken on mining levels accessible in February 2010 in order to collect samples and map selected faces. 62 samples were collected *in situ*. From these, 22 one-inch polished blocks were prepared. Each of these was examined by optical and scanning electron microscopy. Selected samples were then analyzed by electron probe microanalyzer (EPMA) to make quantitative determinations of key ore minerals, and by laser-ablation inductively-coupled spectroscopy to determine concentrations of trace elements in those minerals. One selected sample was also examined using Electron Back-Scatter Diffraction (EBSD). Focused Ion Beam (FIB) techniques were used to extract a thin foil from another sample for investigation of pyrrhotite structure using transmission electron microscopy (TEM).

3.1 The sample suite

For this study three main sample sets were used. Initially, teaching samples procured by Adelaide University Geology & Geophysics Department (courtesy of Prof. Andreas Schmidt-Mumm) were studied. These samples were from an area of extraordinarily high-grade ore. These samples are labelled with the prefix “Chal” in following sections. The second set of samples was procured during a third year mineral exploration field trip to Challenger in September 2009. Due to the short amount of site time during that visit, no complex mapping of each sampling location was possible. Regardless, this visit did allow a lot of mine exposure with samples from both the M1 and M2 procured over a fairly wide depth range. These samples are labelled with the prefix “CH”. Finally, during a site visit in February 2010, four levels were mapped in detail with more precise sampling taking place. These were ore zones within the 840, 580, 760 and 800 RL. Each mapping area was selected based on the criteria of having economic ore grade and availability for an extended period of time to allow detailed mapping. Samples from this group are labelled with the prefix “RH”. As a result of having these three sample sets, a strong coverage of the entire mine has been achieved, both over the lateral extent and through each ore zone. Table 1 gives abbreviations used throughout the tables and figures. More detailed description of the sample suite is given below and in Table 2.

3.2 Analytical methodology

3.2.1 OPTICAL MICROSCOPY

A Leitz Laborlux-12-Pol polarizing microscope, operating in reflected light mode and in both air and oil immersion, was used to examine the polished blocks. The microscope was equipped with a digital camera.

3.2.2 SCANNING ELECTRON MICROSCOPY

The Philips XL30 scanning electron microscope (SEM) with energy dispersive X-ray spectrometry (EDAX) and back-scattered electron (BSE) imaging at Adelaide Microscopy was used, operating at 20 eV. Back-scatter imaging coupled with semi-quantitative EDAX facilities allowed rapid identification of trace minerals, resolution of the smallest Au- and Ag-bearing grains (down to 1-2 micron) and identification of the alteration silicates.

3.2.3 ELECTRON MICROPROBE ANALYSIS

The CAMECA SX-51 electron microprobe (EPMA) with wavelength dispersion spectrometers at Adelaide Microscopy Centre, University of Adelaide, Australia was used. This provided quantitative compositional data on pyrrhotite, arsenopyrite, löllingite, accessory sulphides and various minor minerals including native gold/electrum. Operating conditions were an accelerating voltage of 20 kV and beam current of 19.5 nA. The following X-ray lines and standards were used: Au (Au Mα), Bi_2Se_3 (Bi Mα, Se Lα), PbS (Pb Mα), Ag_2Te (Ag Lα, Te Lα), Sb_2S_3 (Sb Lα), CoAsS (Co Kα, As Lα), Ni (Ni Kα), $CuFeS_2$ (Cu Kα), HgS (Hg Mα) and FeS_2 (Fe Kα, S Kα).

3.2.4 LASER-ABLATION INDUCTIVELY-COUPLED MASS SPECTROMETRY

LA-ICPMS analysis of arsenopyrite and löllingite (plus 2 pyrrhotite and one chalcopyrite) was made using the Agilent HP-7500 Quadrupole ICPMS instrument at Adelaide Microscopy. The instrument is equipped with a New Wave UP-213 Nd:YAG laser ablation system equipped with MeoLaser 213 software. Data reduction was performed using Glitter software.

Pre-defined areas of the polished blocks were ablated. These had been inspected by SEM to check for inclusions and other textures that might affect the quality of the trace element data. Analyses were made with spot size diameter of 25 µm and 35 µm in cases where the grains were large enough. The laser system was operated at pulse rates of 5 and 10 Hz, and 75% power level; laser energy was typically 5-6 Jcm^{-2}, giving an ablation rate of approx. 1.5 µm/sec. The following isotopes were monitored: ^{33}S, ^{34}S, ^{51}V, ^{52}Cr, ^{55}Mn, ^{57}Fe, ^{59}Co, ^{60}Ni, ^{65}Cu, ^{66}Zn, ^{69}Ga, ^{75}As, ^{82}Se, ^{95}Mo, ^{107}Ag, ^{111}Cd, ^{115}In, ^{118}Sn, ^{121}Sb, ^{125}Te, ^{184}W, ^{197}Au, ^{202}Hg, ^{205}Tl, ^{208}Pb and ^{209}Bi. Analysis time for each sample was 90 seconds (30 second measurement of background with laser off, and a 60 second analysis with laser-on. Data reduction was undertaken using Fe as the internal standard.

Calibration was performed using the USGS sulphide standard MASS-1. This is a sulphide matrix, trace element-doped precipitated powder fused to a glass disc that has been specially developed for trace element analysis of sulphides. Mass-1 (previously known as PS-1; Wilson *et al.*, 2002) is certified for a broad range of trace elements including all those listed in the tables. Analytical accuracy is expected to be better than 20%.

The raw analytical data for each spot analysis is plotted as a line graph and the integration times for background and sample signal selected. The counts are then corrected for instrument drift (standards were run after each 1½ hours or 15 unknowns) and converted to concentration values using known values of Fe in the analyzed mineral (from EPMA data). Based on the measured concentrations, detection limits were calculated for each element in each spot analysis.

Six spot analyses of löllingite in one sample were also made in the LAICPMS laboratory at CODES, University of Tasmania, for purposes of comparison. The methodology, standardisation and instrumentation followed that outlined in recent publications using this facility (e.g. Cook *et al.* 2009a).

3.2.5 ELECTRON BACKSCATTER DIFFRACTION

Electron Backscatter Diffraction (EBSD) is an SEM-based crystallographic tool that enables measurement of the crystallographic orientation of individual minerals and the calculation of misorientation axes and angles between data points within or between individual grains. Coupled with orientation-contrast (OC) imaging, EBSD allows otherwise hidden microtextures within the sample to be recognised, intra-grain crystallinity to be measured, and deformation domains mapped at the micron-scale. Background information on the EBSD technique applied to sulphide minerals and the petrographic application of misorientation data has been given by Boyle *et al.* (1998) and Prior *et al.* (1999).

For EBSD analysis the samples need to be properly polished to eliminate any scratching on the surface. The sample analysed was polished using a silica gel and polishing facilities at the South Australian Museum. The sample was coated with a thin carbon film of ~4 nm. Crystallographic orientation data were collected on a preselected area of the polished section using the Philips XL30 FEG-SEM at Adelaide Microscopy (accelerating voltage 20 kV) following the methodology for EBSD given in the literature (e.g., Prior *et al.* 1999). Data were processed using the Channel 5 Electron BackScatter Diffraction System software package from HKL Technologies. The angular resolution of the technique is typically $\leq 0.1°$ allowing for a spatial resolution <1 μm. For crystal structure indexing data from the American Mineralogist Crystal Structure Database (http://rruff.geo.arizona.edu/AMS/amcsd. php) was introduced in the system database. The data were processes using Tango and Mambo software modules for manipulating orientation maps and pole figures, respectively. These software packages are available at the Adelaide Microscopy Centre.

3.2.6 DUAL FOCUSED ION BEAM-SCANNING ELECTRON MICROSCOPY AND TRANSMISSION ELECTRON MICROSCOPY

FIB-SEM (Wirth 2009) was used for cross-section imaging and TEM sample preparation using a FEI-Helios nanoLab DualBeam system. One TEM foil was obtained using the procedure: (1) deposition of Pt-strip in the area of interest (to protect the surface) (2) ion beam (Ga^+) milling on the sides of this strip using a rectangular pattern of 25x12x5 μm (3) lifting, transporting and depositing the slice onto a Cu-grid using a W-needle (4) ion beam thinning of the slice to <100 nm. Platinum was also used for welding operations. Standard operating conditions are 30kV for ion milling and 20kV and 5kV for normal and immersion mode imaging, respectively, using the electron beam.

A Philips 200CM TEM equipped with a double-tilt holder and Gatan digital camera was used at 200kV for obtaining electron diffractions and imaging. Measurements on the diffractions were performed using DigitalMicrograph™ 3.11.1. The identity of the two pyrrhotite species was checked by diffraction simulations using WinHREM™ 3.0 software and data from the American Mineralogist Crystal Structure Database (http://rruff.geo.arizona.edu/AMS/amcsd. php).

4. RESULTS

4.1 Face mapping

Sections of four levels were mapped and sampled. Sections were selected on the criteria of having an economically viable ore grade, and, with the exception of the 580m level, be located within the main M2 ore-body isoclinal folding. Sections were mapped at the 840m, 800m, 760m and 580m levels (Fig. 2, Fig. A1-A3). Mapping was conducted at a scale with much higher resolution than ‘regular’ mine mapping in order to precisely locate sample locations.

4.1.1 840M RL. M2

A total of 16m^2 is mapped at the 840m level (Fig. 2). This section is spread around a corner, with two meters facing down-plunge of the main M2 ore-body and five meters perpendicular to the main dip of the ore-body. This area has the highest previously known gold concentration of the mapped sections, with mine assays recording gold levels in excess of 1,000 ppm within the previously mined shoot. Almost 90% of this section is classified as leucosome. Leucosome composition is perthitic K feldspar + quartz + coarse-grained biotite. The quartz concentration within the leucosome is quite low in comparison to the standard leucosome (as defined in Tomkins & Mavrogenes 2002) observed at other levels with concentrations of <30% common, especially within the main leucosome. Quartz abundance within the leucosome internal to melanosome is closer to standard. Melanosome composition is standard, fine-grained, biotite-rich + quartz and feldspar. Pegmatitic veining, perpendicular to the main veining, is also observed in this section, this veining has similar composition to the main leucosomes however is noticeably coarser, this veining is ptygmatically folded. A total of 8 samples from this level were prepared as polished blocks.

4.1.2 800M RL. M2

A total of $24m^2$ is mapped at the 800m level (Fig. A1). The section is facing up-plunge of the main folded M2 ore-body. This section is characterised by the large 'z' type fold across the entire drive face. Two leucosome lithologies are observable. The main massive fold through the middle consists of perthitic K feldspar + quartz + biotite and is fairly coarse grained. Leucosomes of similar composition and grain size are seen either side of this main fold, these leucosomes have a boudinaged appearance. Within the melanosome the smaller leucosomes are more quartz rich and slightly finer grained. The melanosome is standard, fine-grained, biotite-rich + quartz and feldspar. The two leucosome types appear to have similar fold orientations, with the second type displaying some smaller parasitic folding, especially at the noses of the fold. Coarse-grained garnet, up to 3cm in diameter is observed periodically at the leucosome/melanosome boundary. Halos of pyrrhotite are also observed along these boundaries. Four polished blocks were produced from three samples obtained at this level.

4.1.3 760M RL M2-RIGHT CROSS-CUT

A total of $15m^2$ is mapped at the 760m level (Fig. A2). This section is facing down-plunge of the main isoclinal folding of the M2 ore-shoot, the fold hinges are not visible in this mapping section as they are above and below the mine drive. Some parasitic folding is seen in small leucosome veining within the mesosome allowing identification of the fold orientations. The leucosome composition in this section is standard and consists of coarse grained perthitic K feldspar + quartz + biotite with minor garnet, especially towards the margins. A second leucosome type is also observed - the veining displays a similar composition to the main veining but is slightly coarser grained, and displays strong boudins along the main limb orientation. Leucosomes located completely within the melanosome typically display a slightly higher quartz concentration. The melanosome is standard, fine-grained, biotite-rich + quartz and feldspar. Porphyroblastic garnet is commonly observed at the boundary of leucosomes and melanosomes with some crystals up to 5 cm in diameter (Fig. A2c). Ore minerals, e.g., pyrrhotite, are commonly observed as halos at the boundary of leucosome and melanosome (Fig. A2d). This is especially pronounced along the boundary of the boudinaged leucosomes, with sulphide/arsenides trails developing a sinusoidal pattern parallel to the boudin. Five polished blocks were produced from four samples obtained within the mapping area, with a further polished block produced from a sample slightly outside the mapping area (RH19)

4.1.4 580M RL. M2 LIMB

A total of 32 m^2 is mapped at the 580m level (Fig. A3). Unlike the other sections this face is not located within the main, highest grade, tightly folded section of the M2 ore-body. Prior to mapping, this section was sampled and the gold levels were measured on site, despite this face not being within the main ore body gold concentrations of 4 grams per tonne were recorded. This face is located along one of the limbs that appear to connect the main M2 ore-body with the previously exploited M1 ore-body. The main leucosomes composition in this section is standard blue waxy quartz + perthitic K feldspar + coarse grained biotite with some minor garnet. A second sub-horizontal leucosomes is also observed, with a similar lithology to the main leucosome, however, they are slightly depleted in quartz and are slightly coarser-grained (Fig. A3c). The host melanosome is also standard, fine-grained, biotite-rich + quartz and feldspar. Coarse pyrrhotite is visible at the hand specimen scale at the leucosome/melanosome boundary. This section is cut by a number of sub-vertical joint planes which dip fairly steeply, between 60 and 80 degrees towards the south-south-west direction. Aside from these larger joint planes this section is cross-cut by a moderately strong pervasive foliation. The foliation is pervasive and homogeneously distributed throughout the entire section and dips at 80 degrees towards the south-south-east direction. Three polished blocks were produced from this level.

4.2 Mineralogy and petrography

4.2.1 LITHOLOGY AND ORE MINERALS DISTRIBUTION

The discrimination between the lithologies as introduced in the previous section is given by the relative proportions of the main mineral components, i.e., quartz, feldspar (both plagioclase and potassium feldspar), biotite, garnet, and cordierite. Biotite is dominant in the melanosome (dark bands) whereas quartz and feldspar (light bands) are dominant in the leucosome and pegmatite. Garnet is mostly observed in the melanosome but can also be seen as clots or along trails within the leucosome. Cordierite is mostly observed as a minor component of the leucosome. Whereas for the purpose of face mapping the separation between mesosome and leucosome may appear obvious, in hand specimen there is an apparent mixing between the dark and light bands. This can vary from cm- to mm-scale. Regular mixing of these two types of bands at the mm-scale, over several cm, are interpreted here as melanosomes. The lithologies have a foliated to granoblastic fabric depending upon the dominance of the type of banding; the granoblastic texture is also common within the samples categorised as mesosome. The leucosome is coarser grained >3 mm, up to cm-size, while the mesosome and melanosome are characterised by finer 0.5-1 mm-sizes grains. Porphyroblastic garnet, up to several cm in size, has also been observed within leucosomes and at the boundary of leucosome and melanosome (Fig. A3d); coarser grain size (>1cm) is characteristic of the pegmatite.

Ore minerals are observed, as disseminations and small lenses, in greater abundance within melanosome and at the boundary of melanosome and leucosome. In certain cases, ore minerals are also present within/surrounding the garnets in the leucosome. Of the sample suite from the M2 orebody, only two contain ≥5% ore minerals (CH13, CH18); the others have <2% (Fig. A4).

In the present petrological study, several other minerals have been identified as minor and trace components: Fe-Ti oxides (ilmenite and rutile), monazite, zircon, graphite, molybdenite, an intermediate member of the gahnite-hercynite spinel group, apatite and occasional REE-bearing minerals. Some of these, i.e., Fe-Ti oxides, zircon and monazite are ubiquitous throughout the samples, others, such as graphite and molybdenite, are seen throughout the majority of samples. The Zn-bearing spinel has been observed in abundance in one mesosome sample (RH15). Sulphides/arsenides and associated minerals appear as ≤1 mm patches distributed intergranular to the silicates, as well as locked in the more refractory minerals such as garnet (A5a–c).

The samples from the high-grade ore have a similar appearance, but are coarser-grained, include abundant cordierite and contain neither graphite nor molybdenite. In contrast to M2 samples, the sulphides/arsenides and associated minerals are considerably coarser, have a rounded appearance and are also distributed along several sets of trails which crosscut the silicates (Fig. A5d, e). Along the trails the morphology of the sulphide/arsenides and associated minerals vary from bleb-like to patchy. Such trails are also present in M2 samples but in much lesser abundance and differ in their mineralogy (see next section).

One of the common aspects of the **biotite** is the presence of rutile along the cleavages. Fracturing, bending and replacement of biotite by sulphides (pyrrhotite, molybdenite) and graphite are characteristic for the M2 orebody (Fig. A5f, g); native gold may also replace biotite in the high-grade ore (Fig. A5h).

Potassium feldspar, intermediate **plagioclaise** and **albite** are present within the samples. Potassium-feldspar often displays a perthitic texture which in detail shows exolution of albite, either with sigmoidal development or along two orientations (Fig. A6a, b). Coarse symplectitic intergrowths between plagioclase and quartz can also host finer symplectitic domains especially in the vicinity of perthitic potassium feldspar (Fig. A6c).

In the high-grade ore, in the vicinity/along boundaries between biotite and perthitic potassium feldspar, fine symplectites of quartz and biotite are seen. Micron-size, patchy, sulphides/arsenides are present within such symplectites (Fig. A6d).

Porphyroblastic **garnet** has a poikilitic texture with quartz and in this case it can include a variety of sulphides/arsenides, as well as graphite, zircon and monazite (Fig. A5c, A6e). In contrast, small garnet grains lack inclusions and are sometimes surrounded by pyrrhotite (Fig. A6f). Similarly, sulphides can also envelope **quartz** and in-fill fracturing within the latter (Fig. A6g, h). Fracturing and deformation surrounding sulphide inclusions in garnet has also been observed (Fig. A6i, j).

The **Zn-bearing spinel** is associated with **cordierite** along the foliation (Fig. 3a, b). Interestingly, the Zn-bearing spinel hosts ilmenite with domains of **rutile**, as well as filament exsolutions of a W-bearing mineral (Ferberite? $FeWO_4$; Fig. 3c). **Ilmenite** is otherwise rarely present; most commonly it is replaced by rutile. Replacement of ilmenite results in a bladed or symplectitic texture of rutile and gangue minerals (Fig. 3d, e).

Of particular interest in this study, replacement textures of sulphides/arsenides are observed extensively throughout all samples. Commonly, such textures are represented by halos of gangue minerals and patchy sulphides/arsenides (Fig. 3f, g). Although halo characteristics vary between samples and depend upon ore mineral type, a short-bladed biotite is one of the main gangue components. The halos are also observed surrounding sulphides/arsenides enclosed in the poikilitic garnet (Fig. 3h).

4.2.2 ORE MINERALS

The main ore minerals are pyrrhotite, löllingite and arsenopyrite, forming an Fe-As-S association. Minor ore components are chalcopyrite, pentlandite, molybdenite, Cd-rich sphalerite, Zn-rich greenockite, cobaltite, galena, scheelite and ilmenite, as well as tellurides, native gold, electrum and native bismuth; the latter four will be discussed in section 4.2.3. In most cases the three main ore minerals are associated within the same patch/bleb varying in size from hundreds of microns to a few mm. Single or bi-component grains or patches are rarer and are generally smaller (<100 μm) in size. Their relative size and proportions vary from sample to sample. Fracturing of the main ore minerals is common, with some patches showing intense brittle brecciation textures, particularly within löllingite (Fig. 4a). Marginal zones of higher porosity have also been observed in the main ore minerals.

Pyrrhotite ($Fe_{1-x}S$) is by far the most common ore mineral and two varieties are observed on both optical and back-scattered electron images (BSE): a darker dominant phase which is the host for a second, brighter, species occurring as lamellar exsolutions (Fig. 4b). Such exsolutions are not always seen. There is no preferential orientation of lamellae in relation to the grain elongation. However, they form sets of parallel orientation that are at times undulating or interrupted and displaced. The size of lamellae varies from <1 μm to <5 μm. C**halcopyrite** ($CuFeS_2$) is always intimately associated with pyrrhotite as inclusions which can sometimes displace the pyrrhotite lamellae (Fig. 5a). The lamellae can also be displaced by other minerals such as **molybdenite** (MoS_2) (Fig. 5b) or **sphalerite** ($(Zn,Fe)S$). Exsolutions of **pentlandite** ($(Fe,Ni)_9S_8$) are also noted, in particular in single grains of pyrrhotite, and are at time located along the aforementioned lamellar pyrrhotite (Fig. 5c).

Löllingite ($FeAs_2$) is the second most abundant ore mineral and exists both with other minerals in patches and as idiomorphic grains; the latter is especially found locked in the poikilitic garnet (Fig. 6a). It is mostly seen as relict areas in association with arsenopyrite and pyrrhotite (Fig. 6b). Gold and tellurides are seen along the boundary of löllingite an arsenopyrite (see section 4.2.3). Löllingite does not show any zonation patterns. In M2 samples, löllingite rarely contains any inclusions apart from occasional zircon, whereas in the high-grade ore it can carry inclusions of native gold, bismuth and/or maldonite (see section 4.2.3).

Arsenopyrite (FeAsS), although minor relative to löllingite, is more widespread and displays the greater variety of textures including zonation, seen as variation in grey-scale on the BSE images. This zonation reflects variation in Ni and Co content (see section 4.3). Arsenopyrite is most commonly found as zones of variable width (<10 μm to >50 μm) between pyrrhotite and löllingite (Fig. 6c, d); this is to be referred to as Apy1. Apy1 appears to replace löllingite, with textures showing thin arsenopyrite rims to almost complete replacement of the löllingite (Fig. 6e, f). The morphology of the Apy1 zones shows a straight/angular outline towards pyrrhotite but irregular towards löllingite. In some cases this 'irregular' boundary appears structurally controlled along cleavages (Fig. 6g). In others, small, idiomorphic grains of arsenopyrite are seen as a skeletal growth within löllingite (Fig. 6h). Very rarely, within granoblastic mesosome (RH16), fan-like aggregates of arsenopyrite, pyrrhotite and ilmenite are seen; patchy löllingite exists within arsenopyrite (Fig. 7a).

Grains of arsenopyrite with no adjacent löllingite, but still with pyrrhotite are seen in two cases: (i) as idiomorphic and (ii) hypidiomorphic grains; both (i) and (ii) are referred to as Apy2 (Fig. 7b-f). In case (ii) arsenopyrite shows gold and tellurides, is porous and can be corroded by pyrrhotite (Fig. 7c-f). Some of the strongest zonation patterns are seen in Apy2 in case (ii), but no zonation is seen in Apy2 in case (i). It should be noted that the zonation referred to is very patchy relative to the grain boundary.

Molybdenite, observed in an unexpectedly widespread abundance within the M2 samples, is commonly associated with **graphite**, mixed within graphite blades along with pyrrhotite (Fig. A7). Molybdenite also occurs within narrow, kinked fractures crosscutting pyrrhotite (Fig. A8a, b). **Cobaltite** (CoAsS) has been observed in two samples (RH9, CH3) as small idiomorphic grains within pyrrhotite (Fig. A8c, d). Cadmium-rich **sphalerite** and Zn-rich **greenockite** (Fig. 5d-f) are observed in few samples within the mesosome, one of which also contains Zn-bearing spinel (**gahnite**). **Galena** (PbS), is present as small grains (<1 μm) in several samples (Table 1). In some abundance galena is present in the one sample from the M3 oreshoot (RH13). Here, larger secondary Pb-minerals are also observed. Another minor component that stands out within the arsenopyrite-rich sample (13CH) is **scheelite** ($CaWO_4$). This is observed either as mm-sized aggregates in the rock or as blebs a few μm in size within löllingite and/or along the Apy1 replacement boundary (Fig. A8e-i).

Both chalcopyrite and pyrrhotite are remobilised within the replacement halos mentioned in section 4.2.1 and within adjacent arsenopyrite/löllingite (Fig. 4c, d). Chalcopyrite in particular, is more mobile and thus often observed at the pyrrhotite margins; in the latter case, chalcopyrite is also seen together with rutile as spectacular symplectites (Fig. 4e, f).

4.2.3 GOLD ASSOCIATION

Electrum (AuAg, here defined as Au Ag minerals with <90 atomic % Au) has been observed in half of the M2 orebody samples, where it is commonly associated with tellurides (Table 1, Fig. 8). This is in contrast to **native gold** which is present within all of the high-grade ore samples (section 4.3, Table 8). There is also a marked difference between the Au association in the M2 orebody and the high-grade ore. In M2, Au is associated with the Ag-(Au)-tellurides **hessite** (Ag_2Te) and **petzite** (Ag_3AuTe_2), whereas in the high-grade ore Au is associated with **native bismuth** (Bi), **maldonite** (Au_2Bi) and **hedleyite** (Bi_7Te_3) (Fig. 9). Bismuth- and Bi-Ag-tellurides are rarely present, although they are noted in M2, i.e, unnamed **Bi_3Te_2** and **volynskite** ($AgBiTe_2$).

In the M2 samples, Au and the associated tellurides are small in size (normally a few μm but up to 20 μm). They are found: (i) as inclusions along replacement boundaries between Apy1 and löllingite (Fig. 10a, b); (ii) as clustered inclusions in porous Apy1 (Fig. 11a, b); (iii) rarely as patchy grains attached to the margin of the main ore minerals (Fig. 10c); and (iv) within the silicates (Fig. 12).

In case (i), even though the Apy1-löllingite boundary carries most of the Au observed (~80%), this boundary contains Au-Ag-Te mineral inclusions (Fig. 8) in only ~10% of the observed cases. In the pyrrhotite/arsenopyrite-rich samples (CH13a, 18a), such inclusions are quite abundant and larger in size (Fig. 11c-f). Electrum and hessite are observed coating cleavage-controlled inliers of arsenopyrite within the löllingite (Fig. 11g). In these cases, both arsenopyrite and löllingite are typically highly fractured (Fig. 11c, d). Graphite hosting electrum and hessite has also been seen along the Apy1 and löllingite boundaries (Fig. A9).

Case (ii), although not so common, contains the highest individual concentration of Au in that local area. Electrum is seen within the arsenopyrite pores; at times pyrrhotite is also observed in such pores (Fig. 11a, b).

In case (iii), electrum is located on the boundary of the pyrrhotite and the adjacent silicate host. Within the silicate, halos of minute electrum inclusions are observed (Fig. 10c).

In case (iv) electrum is located along trails of blebs, associated with minor arsenopyrite, or attached onto graphite blades (Fig. 12).

In the high-grade ore, Au-Bi-(Te) minerals form in much greater abundance and are also coarser (up to several hundred μm). Three-component associations consisting of native gold, maldonite and bismuth were observed attached to pyrrhotite (Fig. 9, A10a); hedleyite has also been observed as a fourth component within this association. The inclusions along the Apy1 and löllingite boundaries are also commonly characterised by Au-Bi-(Te) associations but native bismuth and maldonite are the dominant components; hedleyite is also commonly observed as a third component. Native gold, when present, is not observed together with the other Au-Bi-(Te) minerals but instead as a single-phase inclusion.

An important part of the Au is located: (i) along trails of blebs with Au-Bi-(Te) minerals (maldonite + native bismuth ± hedleyite) (Fig. A5e); (ii) patchy native gold along trails/ narrow fractures (Fig. A10b); and (iii) native gold inclusions within blebs of sulphides/arsenides and in adjacent halos/splays of fractures (Fig. A10c, d).

4.3 Mineral chemistry (EPMA data)

Seventeen samples were analysed using electron probe microanalysis (EPMA) with the purpose to characterise chemical variation relative to stoichiometry in the main ore minerals and associated phases, as well as in the minerals associated with Au. The samples were selected to optimally cover all the mine levels as well as the high-grade ore.

The dataset comprises 367 analyses of sulphides/arsenides (arsenopyrite, cobaltite, löllingite, pyrrhotite, pentlandite, sphalerite and greenockite) and minerals representing the Au association (native gold, electrum, maldonite and tellurides). The means and selected single analyses are presented in Tables 3-8. The full datasets, carrying the majority of the data (363 analyses) are included in the appendix (Tables A1-3). Calculation of mineral formulae from wt.% values measured by electron probe microanalysis (EPMA) was done using the number of atoms per formula unit (a.p.f.u.), corresponding to the ideal formulae of each mineral analysed. Each sample was characterised by a mean except in cases where the analyses could be grouped into categories that reflect zonation patterns or morphological variation; single point analyses are included separately in cases where they were distinct from the groups selected for the means.

Analytical results for **arsenopyrite** (Table 3) have been separated into groups depending upon the type of arsenopyrite analysed (Apy1 or Apy2). The calculated formula varies from stoichiometric arsenopyrite ($Fe_{1.0}As_{1.0}S_{1.0}$), with Fe varying from 0.758 to 1.012 a.p.f.u, As varying from 0.954 to 1.168 a.p.f.u and S varying from 0.833 to 1.042 a.p.f.u. The only minor elements present and that show any marked variation are Co and Ni. Co varies from 0.000 to 0.196 a.p.f.u and Ni from 0.000 to 0.104 a.p.f.u.). Selenium is present in minor and relatively constant amounts throughout (~0.007 a.p.f.u.). Analysis of results show Apy 2 to generally be slightly enriched in As and Fe, and correspondingly slightly deficient in S in comparison to Apy 1. Apy 2 also displays the highest concentrations of both Co and Ni out of all of the arsenopyrite.

The microanalytical dataset for **löllingite** (Table 4) shows some variation from stoichiometric löllingite ($Fe_{1.0}As_{2.0}$), with Fe levels varying from a minimum of 0.680 to 0.990 a.p.f.u and As levels varying from 1.769 to 1.944 a.p.f.u. Once again Co and Ni are present in minor quantities and their abundance varies between samples. Co contents are from 0.003 to 0.130 a.p.f.u and Ni varies from 0.017 to 0.187 a.p.f.u. The trace amounts of sulphur also vary between 0.048 and 0.230 a.p.f.u. Selenium is present in minor and relatively constant amounts throughout (~ 0.013 a.p.f.u).

Electron probe microanalysis of **pyrrhotite** (Table 5) also shows variation from stoichiometric pyrrhotite ($Fe_{1.0}S_{1.0}$), with Fe contents varying from 0.918 to 0.992 a.p.f.u and S varying from 1.005 to 1.007 a.p.f.u. It is clear that the only compositional variation in pyrrhotite results is expressed by the proportions of Fe and S with no other detected element (Co, Ni, Se) returning results exceeding 0.005 a.p.f.u. Comparison of the metal to sulphide ratios of the lamellae and the host show the lamellae have a Fe:S ratio much closer to 1:1 (i.e., approaching troilite) whereas the host is slightly deficient in metals relative to sulphur. Although the wt.% values are extremely small, some spots do indicate trace amounts of Co and Ni within pyrrhotite, with the largest values returned in host pyrrhotite rather than lamellae.

Analysis of **cobaltite,** CoAsS, shows a marked deviance from stoichiometric cobaltite (Table 6), with mean Co contents of 0.511 and 0.583 a.p.f.u, mean As contents of 0.965 and 0.974 and mean S contents of 1.007 and 1.023 a.p.f.u from each of the two samples (9RH and 3CH respectively). The low Co values returned imply that the cobaltite within these samples are not end-member cobaltite but rather a member of the (Fe,Co,Ni)AsS solid solution series. Mean contents of Fe (i.e., arsenopyrite component) are 0.261 and 0.212 a.p.f.u and mean contents of Ni (gersdorffite component) are 0.255 and 0.206 a.p.f.u in the set of analyses for each sample.

The three analysis of **pentlandite,** $(FeNi)_9S_8$, (Table 6) give the formulae $Fe_{5.256}Ni_{2.474}S_{8.453}$, $Fe_{5.779}Ni_{2.636}S_{8.309}$, $Fe_{4.777}Ni_{3.722}S_{8.199}$, with reasonably high values of Co (0.808, 0.262 and 0.373 a.p.f.u., respectively).

Analyses of **sphalerite** group minerals are shown in (Table 7). Results are split into two analysis of **Cd-rich sphalerite** and two representing **Zn-rich greenockite**. Results were re-calculated as mol.% ZnS, CdS and FeS. Cadmium-rich sphalerite was calculated as 68.6 and 62.0 mol.% ZnS, 13.5 and 15.9 mol.% CdS, and 17.5% and 22.2 mol.% FeS in the two analyses. The two analyses of zinc-rich greenockite were calculated as 41.3 and 40.8 mol.% ZnS, 44.9% and 45.4 mol.% CdS and 13.8 and 13.7 mol.% FeS.

Analysis of **native gold** within the Chal samples (Table 8) returned very high concentrations of Au, ranging from 99.49 to 99.82 wt.%; trace amounts of Ag, Cu and Bi are also present. Analysis of **electrum** within the main sample set (M2) shows a large variation in Au and corresponding Ag concentrations, with Au content varying from 54.24 to 93.34 wt.% and Ag varying from 47.29 to 7.68 wt.%. The two lowest Ag values are both from grains where electrum coexists with hessite (sample CH13a). Trace amounts of Cu and Bi are also present in each analysis. The single analysis of **maldonite** (Table 8) shows that maldonite is very close to ideal composition (Au_2Bi) with the calculated empirical formula being $Au_{2.07}Bi_{0.946}$. **Hessite** also gives results very close to ideal composition (Ag_2Te), with calculated empirical formulae of $Ag_{1.981}Te_{0.999}$ and $Ag_{1.997}Te_{0.997}$.

Figure 13a is a plot of a.p.f.u Ni versus a.p.f.u Co for löllingite, arsenopyrite and cobaltite. A number of clear trends can be identified. Firstly, there is a good positive correlation between the Ni and Co contents of the mineral, with all data plotting reasonably close to the 1:1 ratio line. Secondly, it is clear that löllingite always has a higher concentration of Ni (and thus Ni/Co>1) than arsenopyrite; arsenopyrite is correspondingly more Co rich (Ni/Co generally <1). This shows a favoured partitioning of Ni into löllingite, and of Co into arsenopyrite where the two minerals coexist. Within the dataset for arsenopyrite, a number of sub-populations can be identified. It can be seen that, overall, the Chal samples are deficient in Ni and Co compared to the M2 samples, with all analysed grains plotting in the lower left of the plot close to the minimum detection limit. The remainder of the analyses of Apy1 show slightly higher Ni and Co concentrations; those grains of Apy1, which are not adjacent to löllingite, and which also contain inclusions of electrum, displaying rather higher Ni and Co concentrations. The Apy2 population plot across a fairly broad field on the figure, but the majority of the Apy2 points cluster towards the upper right part of the figure with some of the higher Ni and Co concentrations. Cobaltite obviously displays the highest concentration of Co, but also of Ni. The löllingite data show a more limited range of Ni and Co. All points from the Chal samples cluster in the central part of the diagram.

Figure 13b shows a portion of the ternary FeAsS-CoAsS-NiAsS diagram to demonstrate compositional variation and solid solution between arsenopyrite, gersdorffite and cobaltite. All analysed arsenopyrite from Challenger plots reasonably close to the FeAsS corner of the diagram; CoAsS component never exceeds 20 mol.%. The cobaltite also plots within its typical range, extending to more Ni-rich compositions. None of the analysed grains correspond compositionally to glaucodot, the intermediate member of the arsenopyrite-cobaltite series. The figure brings out the trends noted above, i.e. that Apy1 grains not situated adjacent to löllingite and which contains inclusions of electrum to be richer in Co and that the Apy2 sub-population plot the furthest from stoichiometric arsenopyrite, towards the cobaltian end-member.

Figure 13c shows a portion of the corresponding ternary $FeAs_2$-$CoAs_2$-$NiAs_2$ diagram (end-member minerals are löllingite, safflorite and rammelsbergite). This diagram shows the variable composition of the analysed löllingite. Löllingite composition varies from close to stoichiometric $FeAs_2$, to Ni-enriched compositions, with modest Co also noted. Two outlier points are noted (18aCH.14 and 3CH.5).

Figure 14a shows a plot of atom.% As versus atom.% S(+Se) for arsenopyrite (and cobaltite). The diagram clearly displays a number of discrete sub-populations within the arsenopyrite, mostly related to the variances in morphology and association referred to above. The majority of the Apy1 data points show compositions that are close to stoichiometric (ideal FeAsS is shown as a black star on the diagram), trending towards As-rich and S(+Se)-poor compositions. Apy2 once again shows a fairly broad compositional range, but Apy2 in two samples have the highest values of As within the entire dataset; they are thus very S(+Se) deficient. The most S(+Se)-rich arsenopyrite group are of Apy1 type without adjacent löllingite but with inclusions of electrum. Cobaltite compositions are also shown on the figure; the mineral is extremely S(+Se)-rich and As-deficient.

Figure 14b is a ternary plot of As+Sb, Fe+Co+Ni and S+(Se) in arsenopyrite (and cobaltite). While most results plot fairly close to stiochiometric arsenopyrite, with the Chal sample especially clustered, there is nonetheless some variation. Apy2 is distinctly richer in As(+Sb) and cobaltite is the most S(+Se)-rich. The significance of these compositions will be discussed in section 5 below.

Figure 14c shows an equivalent ternary diagram plotting As+Sb, Fe+Co+Ni and S+(Se) in löllingite. All data points plot fairly close to stoichiometric löllingite with some slight trend towards S(+Se)-enrichment. Point 16RHl5.4 is a notable outlier and contains more S than is typical for löllingite.

On Fig. 15a, total metal content in pyrrhotite (expressed as atom.%) is plotted against atom.% S+Se. This plot shows the substantial variation in Fe:S ratio in Challenger pyrrhotite. The lamellae are notably enriched in metal (i.e., Fe:S closer to 1:1) than 'host' pyrrhotite. Figure 15b also shows atom.% S+Se, but instead of total metal content, just the Fe content is plotted. This effectively shows the substitution of Fe by other metals (Co, Ni). Deviation from the line shows the degree of replacement of Fe by other cations. It can be seen that pyrrhotite which is not directly adjacent to löllingite and/or arsenopyrite contains the highest level of Co+Ni substitution. Pyrrhotite adjacent to Apy2 also contains comparatively high levels of substitution. Pyrrhotite with pentlandite exsolution also appears to have some degree of substitution, although not as high as in the other two cases. The diagram also shows the relative position of the host and lamellae relative to the ideal fields of the main species of pyrrhotite. The host pyrrhotite appears to correspond to Fe_7S_8, with a spread towards $Fe_{10}S_{11}$, whereas the lamellae show a pronounced spread towards troilite (FeS). The overlap between the two datasets (host and lamellae) is also due to the very fine intergrowths between the two in some analysed grains.

4.4 Trace element geochemistry of the main ore minerals (LA-ICPMS data)

Eleven samples were analysed using laser ablation-inductively coupled plasma mass spectrometry (LA-ICPMS) with the purpose of investigating trace-element distribution and variance within arsenopyrite and löllingite. Nine samples were selected from the M2 samples in order to get a good coverage of the orebody; 2 samples were selected from the high-grade Chal samples. Analysed grains were carefully selected from samples that had been previously thoroughly analysed by SEM.

The dataset includes 132 individual analyses: 72 of löllingite, 56 of arsenopyrite, 3 of pyrrhotite and 1 of chalcopyrite. Results are presented as ppm values in Tables 9, 10 and 11 and are arranged within each sample set in order of decreasing Au concentrations. Means and standard deviations are presented following the data for each sample.

The results show that the trace element endowment of the analysed minerals varies slightly from sample to sample, with a few exceptions. **Gold** concentration shows the most variance (Fig. 16), with the highest concentrations determined in both arsenopyrite and löllingite being from the Chal samples. It should be noted, however, that some of the extreme values returned are interpreted as the result of inclusions of Au(-Bi) minerals rather than a measure of solid solution gold. Gold concentrations are consistently higher in löllingite than in arsenopyrite. In löllingite Au ranges vary from 15.54 to 927.1 ppm and, on average has a concentration 62.38 ppm. In arsenopyrite Au ranges from levels below detection limit to 2,128 ppm Au and on average have a concentration of 202 ppm. The higher apparent average in arsenopyrite than löllingite is attributed to the larger number of anomalously high results. The range of gold concentrations in löllingite across mine levels in M2 and high-grade ore is depicted schematically on Fig. 17.

Concentrations of **silver** are consistently low (typically <1 ppm) in both arsenopyrite and löllingite, with two notable exceptions ('a18CH5' in arsenopyrite and '1RH2' in löllingite); both spot analyses intercepted inclusions of hessite and both also display elevated Te values. **Bismuth** shows great variation in both löllingite and arsenopyrite (Fig. 16). The highest measured concentrations are from the Chal samples, differing markedly with the relatively low levels measured in the M2 samples. These high values are interpreted as related to the presence of Bi-bearing inclusions. **Cobalt** and **nickel** values show variations of up an order of magnitude between samples in both löllingite and arsenopyrite, mirroring the EPMA data reported above. **Tin** and **antimony** are present in negligible amounts, although there are two exceptions in arsenopyrite (spots '1Chal1' and '1Chal5') in which 331 and 2,559 ppm Sn were measured respectively. **Tellurium** is generally observed at trace levels in all samples (Fig. 16), with some points ('a18CH5' in particular) displaying anomalously high levels of Te, most likely due to telluride inclusions. **Selenium** is reported at low and fairly constant values throughout all analyses. Other elements (In, Zn, Cu) were consistently close to, or below the minimum detection limit.

Figure 18 shows a selection of time-resolved depth profile to illustrate features in the LA-ICPMS dataset from the high-grade ores, with the analysed grains themselves also shown (Fig. 18a, d). Figure 18b shows a typical depth profile for lollingite. Note the parallel and fairly flat signals for each element, especially Au, throughout the duration of ablation. This implies a homogeneous trace element distribution throughout löllingite, indicating that the elements are likely in solid solution rather than as microscopic or sub-microscopic inclusions. Although many of the LA-ICPMS are flat, there are, nevertheless, exceptions. Figure 18c shows a time-resolved depth profile for one of the high-gold löllingite grains from the high-grade ore. It can be seen that for the first portion of ablation the depth profile is flat, however, after 15 seconds there is an abrupt spike in Au and Bi (and to a lesser extent also Ag and Pb). This is interpreted as representing an inclusion of maldonite, most likely at a boundary between Apy1 and löllingite (the latter suggested by an accompanying drop in the Fe signal. Inclusions are also readily recognised on the depth profiles for arsenopyrite spots. An inclusion containing Au and Bi (maldonite) can be seen on Fig. 18a. Note that on Fig. 18a, there are two sets of laser spot analyses marked; those labelled in red were obtained in

Adelaide, those in blue in Hobart. A reasonable correspondence can be seen between the two, although some concentrations measured in neighbouring spots are different due to the inhomogeneous character of the inclusions. Arsenopyrite1 from the high-grade ore (Fig. 18d) can also host maldonite inclusions as shown in the spectra in Fig. 18e.

Depth profiles for löllingite grains in samples from M2 are shown in Fig. 19. A smooth profile showing moderate Au (and Te) is shown in Fig. 19a. Fig. 19b and c refer to a small, 'isolated' löllingite grain with higher Au content (89 ppm). Figure 19e shows a time-resolved depth profile for löllingite (Fig. 19d) in which there are high initial Ag and Te peaks, which rapidly decreases away after the first 5 seconds of ablation. This is interpreted to represent an inclusion of hessite. Note that the adjacent arsenopyrite (located on Fig. 19d) contains negligible Au (<0.21 ppm). Figure 19f shows an arsenopyrite from the Apy2 generation – two of the three laser spots contain <1 ppm Au, but the third contains modest Au (7.53 ppm). The corresponding time-resolved depth profile (Fig 19f) shows an irregular profile for Au that is suggestive of inclusions**.**

Fig. 20 shows a number of binary plots for elements of relevance. The marked tendency for arsenopyrite to be enriched in Co, and Ni in löllingite is shown in Fig. 20a. Spot analyses of arsenopyrite plot on, or just below the Co:Ni 1:1 line. The pronounced Au enrichment in löllingite is seen in Fig. 20b, on which Au is plotted vs. Bi. There is no correlation between Au and Bi in löllingite but a pronounced correlation for arsenopyrite (r^2=0.68). The range in Bi values is significantly greater for the high-grade samples. The Au vs. Ag, and Ag vs. Se plots (Fig. 20c, d) show no correlation between each respective sets of elements; arsenopyrite is higher in Se than löllingite. The Ag vs. Te plot (Fig. 20e) shows a similar pattern – much of the data for the two minerals shows a cluster rather than a correlation, but there are outliers showing enrichment in both elements. These are plausibly attributable to the presence of hessite inclusions as was documented above. The final plot [Au vs. (Te+Ag)] (Fig. 20f) emphasizes the same trend – the two minerals show separate, wedge-shaped distributions in which Au is generally, but not always, higher where there is enrichment in Ag+Te.

4.5 Relative grain orientation of arsenopyrite and löllingite: Electron Back-Scattered Diffraction

Application of EBSD to minerals that have undergone metamorphism and in particular pyrite is a useful method to address grain, or inter-granular deformation relative to the deformational regime or regional-scale deformation history (e.g., Boyle *et al.* 1998). It also allows for understanding whether the chemical patterns (zonation) as observed on BSE images are concordant with deformation. Furthermore, it allows for understanding epitaxial growth between different minerals across a common boundary.

In M2 the replacement textures between Lo and Apy1 are associated with formation of Au minerals along the replacement boundary. Understanding if the replacement took place during a deformational event, as well as how the two minerals are oriented, one relative to another, across the replacement boundary (Apy1 and löllingite), can provide further insight into the Au remobilisation during metamorphism. Whereas pyrite from metamorphic environment has been extensively studied by EBSD, no study has been undertaken so far on either löllingite or arsenopyrite.

The Apy1-löllingite–pyrrhotite patch selected for EBSD study has a general orientation along the main foliation (F1; Fig. 21a) but is slightly rotated relatively to a second, less pronounced foliation (F2; Fig. 21a). The replacement boundary is parallel to weak zonation in Apy1, i.e., a (Co+Ni)-enriched zone is seen along the replacement contact (Fig. 21b). Along the same contact graphite is also present and this hosts both electrum and hessite (Fig. 21c, d).

The area selected for mapping was oriented along the replacement boundary so that löllingite and Apy1 with the zonation was included (Fig. 21b). In order to be able to index the two minerals, the crystal structures for Co- and Ni- bearing löllingite and arsenopyrite were entered into the software database from Ondrus *et al.* (2001) and Fuess *et al.* (1987), respectively. These crystal structures matched well both minerals with mean angular deviance (MAD) <0.7° used as the cut-off for indexing the analytical points. Once the indexing was calibrated the entire area was mapped with lower resolution (5 µm) to test indexing throughout, and also to identify if there are domains of different orientation. The results were promising, in that, the map showed misorientation points coinciding with the zonation in Apy1. The selected area was finally analysed at 0.5µm steps using electron back-scattered diffraction. A total of 105,114 data points were analysed, with 88,319 being in arsenopyrite, and 16,795 within löllingite.

Initially the selected area was imaged using forescatter imaging (Fig. 22a). Forescatter detection images are dominated by crystallographic-orientation contrast. The forescatter image appears to identify a series of domains within the arsenopyrite grain that are not visible in backscattered imaging. These domains appear as darker zones parallel to the main arsenopyrite grain orientation and do not appear to be related to the fracturing within the arsenopyrite grain. These domains would appear to represent domains of misaligned crystallographic orientation in relation to the main crystal. However, when analysed using EBSD, when the Euler angles are plotted, (Fig 22b) there is no apparent major change in crystallographic orientation within the grain related to the forescatter contrast changes. There are two domains that do appear at a slightly different orientation to the main grain (~1°) (dark pink and outlined in red on Fig. 22b). Throughout the arsenopyrite grain there are a number of points that are displayed in Euler space (blue on Fig. 22b) that overlap with the dark zones in the Apy1. It is possible that these points are somehow related to the forescatter imaging contrast domains; it is, however, difficult to determine a direct relationship. The fact that the 'blue' points scattered on the Euler map are actually not as well indexed as the main part of the grain is also shown by the lack of clear grain boundaries even when choosing a very small misorientation angle, e.g., 1° on Fig. 22c. Even though the maps may have been improved by a better indexing for the unsubstituted Apy1 (introducing a second setting for the arsenopyrite structure), it is unlikely that there is significant difference in the orientation between the two zones in the Apy1. The löllingite appears homogeneous in both the Euler angle plot and the forescatter image.

A series of pole diagrams were plotted to display the variance of crystal alignment within the arsenopyrite (Fig. 23a-d). These diagrams show the alignment of the recorded crystal grains in reference to the individual pole outlined in each diagram. Each diagram uses equal area projection and is projected within the upper hemisphere. Beneath each pole diagram is a pole plot displaying the number of points at each angle within that specific pole diagram. It can be observed that the points recorded as pink (A), in the Euler angle diagram, and the points recorded as blue (B) plot opposite to each other along the <100> pole and the <110> pole. In the case of the <101> pole the points plot together and along the <111> pole they plot perpendicular to each other. In all cases each series of points have the same angle of misalignment away from the pole regardless of which direction that misorientation is, as shown in Figs. 23 e-h. It can be observed that along all orientations plotted, löllingite remains in extremely tightly grouped clusters (Fig. 23 i-k), further supporting observations, seen in Figure 22b, that löllingite has the same crystallographic orientation throughout the grain. The pole diagrams down the <100> and <110> axes show similar plot orientation for both Apy1 and löllingite suggesting parallel alignment between the two grains.

The lack of gradational contrast on the OC map corroborated with the small spread of the points on the Euler angle diagrams indicates that there is little deformation if at all during replacement of löllingite by Apy1.

4.6 Characterisation of pyrrhotite species: Focused Ion Beam and Transmission Electron Microscopy

Pyrrhotite, $Fe_{1-x}S$, where $0<x<0.125$, is an interesting mineral group both in geological and crystallographic terms. The wide compositional range obtained from EPMA data (Fig. 15) and the textural relationships observed between the two pyrrhotite species in the ores at Challenger suggest the presence of different structural types one of which could be troilite, FeS. The second could be one of the $Fe_{1-x}S$ superstructures widely debated in the literature (Posfai & Buseck 1997). Identification of the specific types of pyrrhotite could provides additional constrain on the metamorphic and cooling history at Challenger. Recent comparable studies (Becker *et al.* 2010) have shown the value of correlating composition and crystal structure in pyrrhotite.

The cell parameters of the pyrrhotite structures can be expressed in terms of the hexagonal NiAs sub-cell which has A=3.5 Å, C=5.7 Å (Posfai & Dodony 1990). The structures have hexagonal close packed (hcp) layers of S with Fe atoms occupying octahedral interstices between the S layers. All octahedral positions are occupied in troilite (stoichiometric FeS; hexagonal P-62c, 2C with $a=\sqrt{3}A=5.97$ Å and $c=2C=11.76$ Å; Skala *et al.* 2006), whereas the non-stoichiometric pyrrhotites have vacancies on the Fe positions. The ordered or disordered arrangement of the vacancies along the **c** axis defines the groups of ordered (3C, 4C and 5C) and disordered (nC) pyrrhotites, respectively (Posfai & Buseck 1997). The most common forms in nature are monoclinic 4C pyrrhotite with ideal formula Fe_7S_8 and hexagonal 5C pyrrhotite with ideal formula Fe_9S_{10} (Becker *et al.* 2010). 3C pyrrhotite (Fe_7S_8) is trigonal ($P3_1$; $a=2A=6.9$ Å and $c=17.1$ Å) and has been documented only from synthetic material (Fleet 1971). Whereas 4C pyrrhotite is ferromagnetic, troilite is antiferromagnetic at temperatures below 140 °C and 1 bar, but undergoes an α-magnetic phase transition (1C, 2A pyrrhotite) above 140 °C and a ß-phase transition at 315 °C (Curie temperature) when it transforms in the disordered 1C, 1A pyrrhotite with the sub-cell NiAs structure (e.g., Fleet *et al.* 2006).

Characterisation of the two pyrrhotite species present at Challenger was undertaken by Transmission Electron Microscopy (TEM) study of a foil prepared using Dual Focused Ion Beam and Scanning Electron Microscopy (FIB-SEM; Fig. A11). One of the typical pyrrhotite-Apy2-löllingite assemblages was selected for study (Fig. 24a). A foil was prepared by cutting a slice, 25 x 12 x 5 μm in size, oblique to the lamellar exsolutions in a grain of host pyrrhotite (Fig. 24b). The slice was transported to a Cu-grid, thinned to <100 nm and imaged in high-resolution mode using the immersion lens (Fig. 24c). A lamella, about 2 μm-wide, is present in the thinned foil; the contact between lamella and host is sharp without any sub-μm intergrowths between the two.

The foil was studied by TEM and electron diffractions were taken from both host and lamella at two characteristic orientations using tilting of the specimen in the holder at locations shown in Fig. 24d. The two phases display the same preferred orientation (epitaxial; Fig. 24e). Characteristic selected areas of electron diffractions (SAED) are shown for both lamella and host in Fig. 25a-d; these are assigned to zones {c* x a*} and {0-21}. The two phases have the same spacing defined between main reflections, i.e. 5.7 and 2.8 Å on the (100) zone giving c=5.7 Å and a=2.8/cos30=3.23 Å; these correspond to the 1C, 1A NiAs sub-cell. The difference, however, is that the host shows two satellite reflections between the main reflections along the c axis, indicating a 3C-fold superstructure of a sub-cell. It also shows a second row of reflections at a*/2, typical for pyrrhotite 2A superstructures (Posfai & Buseck 1997). Electron diffractions corresponding to zones {100} and {0-21} were simulated for troilite 2C (Fig. 25e, f) using the atomic positions given by Skala *et al.* (2006). These are nicely comparable with the corresponding SAEDs shown for both lamella and the sub-cell in the host pyrrhotite as outlined by the black circles on Fig. 25 b, d and f. The fact that the host pyrrhotite is a superstructure of the same sub-cell with the lamella is shown in the additional satellite reflections (in red on the SAED shown in Fig. 25d). Based on all the above the types of pyrrhotite host and lamella are confidently identified as 3C pyrrhotite (Fleet 1971) and 1C pyrrhotite (high-temperature modification of troilite).

5 DISCUSSION

The present study has focused on various aspects of the association pyrrhotite + arsenopyrite + löllingite which is common in many gold deposits from metamorphic terrains. Both arsenopyrite and löllingite can host invisible Au (lattice-bound Au and particles <10Å) (Cook & Crysssoulis 1990) and thus, understanding the relationships between crystal-chemistry, trace element variation and textures among these minerals plays a key role in ‘mapping’ the Au distribution and remobilisation during the protracted geological history at Challenger. Compiling the new data brought in by the study of the M2 orebody allows for an improved reconstruction of the mineral system at Challenger.

5.1 Mineral non-stoichometry, textures and replacement processes

Analytical data for Challenger arsenopyrite show a variety of compositions that have implications for understanding ore evolution. The arsenopyrite geothermometer is based upon the non-stoichiometry of As to S ratio in this mineral and has application to distinguishing metamorphic conditions at the time of arsenopyrite generation (e.g., Sharp *et al.* 1985). The two types of arsenopyrite identified (Apy1, Apy2) are clearly discriminated as distinct generations upon plotting representative means from the EPMA dataset on the atomic % As vs temperature (T) diagram, on the Apy = Lo + Po line and the Po + L = Apy line respectively. These are: Apy1, low-T (<300 - 400 C) and Apy2, high-T (600 - ~700 C) (Fig. 26a). Such temperature estimations, even though they are produced ignoring the amount of Co and Ni present (up to 8 wt% in some cases), are reasonable in the context of known metamorphic history at Challenger (Tomkins & Mavrogenes, 2002).

Using the temperature ranges and the mineral association for Apy1 and Apy2, further constraints can be made on the genetic conditions in terms of sulphur fugacity (fS_2). Using the sulfidation curves in the system Fe-As-S (Barton 1969) the plots for Apy1 and Apy2 show much higher sulfidation condition of the system for Apy2 relative to Apy1 (Fig. 26b). Furthermore, Apy2 plots in the melt region of the diagram (Tomkins *et al.* 2006), suggesting that Apy2 can be considered melt derived. In contrast, Apy1 is in the solid part of the diagram.

Tomkins & Mavrogenes (2001) have already discussed textural aspects, such as those presented here for Apy1, with respect to redistribution of Au within arsenopyrite and löllingite, and, used this as a tool for establishing the timing of mineralisation at Challenger. They used solid state experiments to determine; (i) solubility of gold in löllingite coexisting with pyrrhotite, during prograde metamorphism of arsenopyrite, and (ii) retrograde metamorphism of löllingite (containing invisible gold) and pyrrhotite, reacting to form arsenopyrite. Using an experimental procedure that allowed them to simulate high metamorphic conditions (T up to 750 °C and P 2-5 Kbar) Tomkins & Mavrogenes (2001) obtained concentrations of gold in löllingite (i) in the range of 330-543 ppm, and much lower concentrations (2.4-4.7 ppm) in arsenopyrite (ii). These results show that even under the relatively inhibiting temperature conditions for Au incorporation during metamorphism, a substantial amount of Au can, nevertheless, be included in löllingite.

Of interest here, is the discussion concerning stages of destruction of prograde Au-bearing löllingite by reaction with pyrrhotite to form arsenopyrite (scenario ii), progressing until replacement of löllingite is complete. As the arsenopyrite is produced along the boundary between the pyrrhotite and löllingite, Au will, at first, diffuse into the löllingite and away from the reaction zone. Following this, as the reaction progresses, native gold nucleates at the löllingite-arsenopyrite reaction front. Finally, as löllingite is completely consumed, its position is marked by clusters of Au inclusions in a mass of arsenopyrite, the end product of this reaction. This mechanism of Au redistribution should have resulted, at the intermediate stages of replacement, in a zonation within the löllingite, an aspect that could not be documented by their investigation.

Although the final stage is also observed, the intermediate stage of replacement of löllingite by arsenopyrite is the dominant aspect preserved in assemblages from the M2 orebody at Challenger (Fig. 6ab-f). This reaction boundary carries most of the observed Au, as electrum. The natural Challenger löllingite analysed by Tomkins & Mavrogenes (2001) contained residual Au concentrations an order of magnitude lower than the synthetic löllingite (means 17 and 54 ppm in two samples, 4 and 2 spots, respectively). The present, much larger and more representative dataset (72 LA-ICPMS spots on 10 samples) gave broadly similar Au concentrations in löllingite (tens of ppm). This dataset also showed no evidence of variation in Au concentration within individual grains. Moreover, the inclusions consist of electrum ± hessite rather than native gold. There is insufficient Ag and Te in solid solution within löllingite (Fig. 16) to account for the observed Au-Ag-Te association which characterises the reaction boundary. Therefore, input of these elements via interaction with a fluid has to be assumed. This cannot have been via dry, solid state diffusion, as implied by Tomkins & Mavrogenes (2001), but rather by a fluid-mediated mechanism that can extract minor elements from a carrier and lock them within the reaction boundary. Coupled dissolution-reprecipitation reactions (CDRR; Putnis 2009) advance via a transient porosity at the reaction front and provide for sites of precipitation of end-products once coupling can no longer be sustained. Moreover, in the presence of reductants along the boundary zone, such as graphite, CDRR offers an efficient mechanism to concentrate gold (Cook *et al.* 2009b).

Furthermore, EBSD analysis on one such assemblage has shown that arsenopyrite zonation with respect to Co/Ni is unrelated to deformation domains within the grain, and arsenopyrite and löllingite have very similar orientations (Fig. 23), indicating replacement during a period of relaxation. Secondly, CDRR generally operates by pseudomorphism and the replacing mineral mimics the orientation of the precursor, resulting in epitaxial growth of the two phases, such as can be inferred from the EBSD study.

The present study has identified two unusual types of pyrrhotite. The dominant phase, 3C, is reported for the first time in natural environment. The lamellae exsolution of 1C pyrrhotite is a structural modification of troilite, stable above the Curie temperature. Troilite is most commonly found in meteorites with few previous terrestrial occurrences reported (e.g. Merensky Reef, South Africa, Voisey's Bay, Canada; e.g., Becker *et al.* 2010). The origin of such lamella can be associated with chemical gradients remobilising Fe and other minor elements (Ni, Co) within the 3C pyrrhotite under deformation, shown in the bending and undulating of the lamellae themselves

(Fig. 4b). Fulfilment of the Fe vacancies within the pyrrhotite structure along these deformational domains results also in the rejection of other elements from the crystal lattice as seen in the nucleation of Ni (Co) rich minerals, such as pentlandite which has been observed along the lamellae (Fig. 5c).

5.2 Reconstruction of the ore system at Challenger

The study was designed to recognise differences in ore mineral assemblages in the various lithologies, along the strike of the M2 orebody, as well as to compare them with prevailing assemblages in high-grade ore. There are no major differences with respect to the main ore minerals (arsenopyrite, löllingite, pyrrhotite), their textures and associations. There is, however, a marked difference in terms of trace element distribution in arsenopyrite/löllingite and in the mineralogical character of the gold association between M2 and the high-grade ore. The latter has a pronounced Au-Bi±Te signature and features abundant bleb morphologies and trails (Fig. A5d, e). These are very similar to aspects of gold mineralisation reported by Tomkins & Mavrogenes (2002), which were interpreted to result from polymetallic (Bi-As-Au-bearing) melts. However, the melt-derived associations observed in the samples from the high-grade ores feature less As, but a marked Au-Bi±Te character (maldonite + gold + bismuth ± hedleyite; Fig. 9). Moreover, the presence of native gold in the same blebs with maldonite and Bi (Fig. 9a) indicates formation at temperatures above the peritectic in the system Au-Bi at 371 °C. The melt scenario propagated by Tomkins & Mavrogenes in 2002 and in numerous subsequent publications can be endorsed for the high-grade ores, but not in M2. In the latter, there is a pronounced Au-Ag-Te association, expressed both mineralogically (electrum, hessite, petzite; Fig. 8) and in the trace element geochemistry of the main ore minerals.

The gold seen in this study is dominantly tied to arsenopyrite-löllingite assemblages which are the product of retrograde replacement of löllingite + pyrrhotite, as discussed in the previous section. Reversal of the prograde löllingite-forming reaction of Barnicoat *et al.* (1991) can illustrate the key mineral transformation on the retrograde path

$$FeAs_2 + FeS + 0.5S_2 \rightarrow 2FeAsS \qquad (1)$$

Attention is drawn to the fact that this would not be a dry solid state reaction, but rather fluid-mediated, thus allowing for exchange of minor components by CDRR as outlined above.

The present study has also contributed the following new information about Challenger. Firstly, Mo, as molybdenite (Figs. A7, A8a, b), is an abundant minor component throughout the M2 ores, and W, as scheelite and ferberite (?) is also documented (Figs. A8e-i, 3c). Secondly, unusually Zn-Al-rich lithologies were identified, with gahnite-hercynite solid solution abundant; some of the sphalerite encountered as inclusions in pyrrhotite shows rare compositions in the middle range of the system ZnS-CdS. Thirdly, graphite appears to be unexpectedly abundant in M2 ores. Aside from the potential processing implications of the latter, these mineralogical aspects, plus the new information on the gold association, can help to better understand the likely precursor deposit.

Based on whole rock geochemistry and identification of a fossil alteration zone, McFarlane *et al.* (2007) argued that Challenger is a metamorphosed deposit with an Archean precursor which is comparable to modern epithermal-style settings, such as a back-arc basin proximal to an active volcanic arc. The evidence presented here reinforces the hypothesis of an epithermal precursor, in that the geochemical signature (complete with base metals, granitophile elements and characteristic minor elements, such as Te) is that of an epithermal system (Fig. 27a). Moreover, the discrepancy in mineralogy between the present observations on M2 and earlier work on M1 (Tomkins & Mavrogenes 2002) suggests that a primary zonation, like the hydrothermal alteration halo, was not completely obliterated by the granulite-facies metamorphism (Fig. 27b). Such a scenario is contradictory to the shear-hosted (i.e., orogenic) deposit model put forward by Birt & Reid (2007) and McGee *et al.* (2010). One argument made by Birt & Reid (2007) against an epithermal precursor was the lack of Cu, Mo or Ag; a point that the present study has invalidated.

Granulite-facies metamorphism implies substantial or total modification to mineralogy and ore textures (Fig. 27c). Assuming that the precursor deposit was a relatively sulphide-poor gold ore, it is reasonable that the main sulphides were arsenopyrite and pyrite. Prograde metamorphism would have likely transformed arsenopyrite into löllingite and pyrrhotite, according to reaction (2).

$$2FeAsS + FeS_2 \rightarrow FeAs_2 + 2FeS + S_2 \qquad (2)$$

This reaction partially explains observed assemblages and would releases sulphur. It is assumed that gold in the precursor epithermal arsenopyrite was transferred during this reaction into the löllingite lattice. During the retrograde path, reaction (1) produces the dominant Apy1 generation of arsenopyrite. Apy2, which is compositionally distinct (high-As) and occurs only with pyrrhotite, should have been formed from a different initial assemblage at high temperature. It is hypothesised that a reaction involving realgar, like reaction (3), could explain Apy2 formation.

Reaction (3) also releases S, and would account for the As-rich composition of this arsenopyrite generation.

$$2FeS_2 + AsS \rightarrow FeS + FeAsS + 3/2S_2 \qquad (3)$$

Isolated löllingite grains can be similarly accounted for by a reaction involving realgar and pyrite (reaction 4)

$$FeS_2 + 2AsS \rightarrow FeAs_2 + 2S_2 \qquad (4)$$

The composition and crystal structure modifications in pyrrhotite are also compatible with formation during the retrograde event, prior to cooling below the Curie point (315 °C).

The high-grade ore could have resulted from the formation of an immiscible polymetallic melt within the silicate melt towards the peak of metamorphism, as proposed by Tomkins & Mavrogenes (2002). This consisted of Bi-As-dominant chalcophile elements and may have concentrated Au, accounting for the high-grade intersections in M1.

The metamorphic history was concluded during the latest Kimban orogenic event (Daly 1998) at which time a further, local remobilization of gold may have occurred (e.g., patchy trails and haloes). Extensive transport of gold would, however, have been impeded by being locked within refractory minerals such as garnet, quartz and feldspar which neither reacted nor recrystallized at the greenschist facies conditions. Some observed features, such as formation of haloes of gangue silicates surrounding sulphides (Fig. f-h), late remobilisation of chalcopyrite and development of rutile-chalcopyrite symplecites (Fig. 4e, f). Other features, such as gahnite forming at the expense of sphalerite (Fig. 3a) and a second set of albite exsolutions in perthitic feldspar (Fig. A6b) would best be attributed to the Sleafordian granulite-facies event.

6. CONCLUSIONS

- Although the Fe-As-S ore mineral assemblage in M2 ore is broadly similar to that of M1, there are some marked differences with respect to the Au association. Au-Ag-Te associations appear to be more important than Au-Bi associations in M2.
- Trace element contents of arsenopyrite and löllingite help to constrain the metamorphic development of the ore.
- Mineral assemblages observed are consistent with an epithermal-style precursor. A series of tellurides (hessite, petzite, hedleyite, volynskite) are described for the first time from Challenger. Other minerals not previously described are greenockite, scheelite and gahnite. Two less-common pyrrhotite structures (3C and 1C) were identified.
- In addition to melt-assisted remobilisation of Au, which accounts for the high-grade ore, grain-scale remobilisation of lattice-bound gold to form visible gold took place by mineral-fluid interaction via coupled dissolution-reprecipitation reaction.

- The pioneering EBSD study of löllingite-arsenopyrite associations, if applied systematically, is a good premise for relating gold remobilisation to deformation.
- The presence of Ag-rich electrum, sub-microscopic gold at reaction fronts between arsenopyrite and löllingite, 'invisible' gold in löllingite, and the presence of graphite, may all carry implications for processing and recovery.

ACKNOWLEDGEMENTS

Thanks go to Dominion Gold Operations for their financial and logistic support of this project, to Andy Giles and Paul Androvic for their advice and support, to Luke and Nick for assistance with underground work. I also wish to extend my appreciation to Adelaide Microscopy for assistance with the analytical work and friendly discussion of results, especially to Angus Netting (EPMA), Benjamin Wade (EBSD, LA-ICP-MS) and Leonard Green (FIB and EBSD). The South Australian Museum (SAM) is acknowledged for access to microscope facilities. Fang Xia and Gujie Qian are thanked for their enthusiastic help with sample preparation prior to FIB work. Lastly, I thank my Co-supervisors Cristiana Ciobanu and Nigel Cook for their support, advice and useful discussion throughout the course of the project, and also for Cristiana's assistance with the TEM work.

REFERENCES

BARNICOAT, A. C., FARE, R. J., GROVES, D. I. & MCNAUGHTON, N. J**.** 1991. Synmetamorphic lode-gold deposits in high-grade Archean settings. *Geology* **19**, 921-924.

BARTON, P. B. 1969. Thermochemical study of the system Fe-As-S. *Geochimica et Cosmochimica Acta* **33**, 841-857.

BECKER, M., DE VILLIERS, J. & BRADSHAW, D. 2010. The Mineralogy and Crystallography of Pyrrhotite from Selected Nickel and PGE Ore Deposits. *Economic Geology* **105**, 1025–1037

BIRT, T.& REID, A. J. 2007. Archaean gold mineralisation in the Gawler craton, South Australia. *MESA Journal*, Department of Primary Industries and Resources South Australia, Adelaide **46**, 29-33.

BOYLE, A. P., PRIOR, D. J., BANHAM, M. H. & TIMMS, N. E., 1998. Plastic deformation of metamorphic pyrite: new evidence from electron-backscatter diffraction and forescatter orientation-contrast imaging. *Mineralium Deposita* **34,** 71-81.

COOK, N. J. & CHRYSSOULIS, S. L. 1990. Concentrations of "invisible gold" in the common sulphides. *Canadian Mineralogist* **28**, 1-16.

COOK, N. J., CIOBANU, C. L., PRING, A., SKINNER, W., DANYUSHEVSKY, L., SHIMIZU, M., SAINI-EIDUKAT, B. & MELCHER, F. (2009a): Trace and minor elements in sphalerite: a LA-ICP-MS study. *Geochimica et Cosmochimica Acta* **73**, 4761-4791.

COOK, N. J., CIOBANU, C. L. & MAO, J. W. 2009b. Textural control on gold distribution in As-free pyrite from the Dongping, Huangtuliang and Hougou gold deposits, North China Craton, (Hebei Province, China). *Chemical Geology* **264**, 101-121.

DALY, S. J. & FANNING, C. M. 1993. Archaean. In: *The geology of South Australia; Volume 1 The Precambrian (*J.F. Drexel, W.V. Preiss & A.J. Parker, eds,). Bulletin 54, Geological Survey of South Australia, Adelaide, p. 32-49.

DALY, S. J., FANNING, C. M. & FAIRCLOUGH, M. C. 1998. Tectonic evolution and exploration potential of the Gawler Craton, South Australia. *Journal of Australian Geology and Geophysics* **17**, 145-168.

FANNING, C. M. 1997. *Geochronological synthesis of South Australia, Part II: The Gawler Craton*. Research School of Earth Sciences, Australian National University PRISE Report (unpublished)

FLEET, M. E. 1971. The Crystal Structure of a Pyrrhotite (Fe_7S_8), *Acta Crystalographica B* **27**, 1864-1867.

FLEET, M. E., 2006. Phase equilibria at high temperatures. *Reviews in Mineralogy and Geochemistry* **61**, 365–419.

FUESS, H, KRATZ, T., TOPEL-SCHADT, J. & MIEHE, G. 1987. Crystal structure refinement and electron microscopy of arsenopyrite. *Zeitschrift fur Kristallographie* **179**, 335-346.

GROVES, D. I. 1993. The crustal continuum model for late-Archaean lodegold deposits of the Yilgarn Block, Western Australia. *Mineralium Deposita* **28**, 366–374.

MCFARLANE, C. R. M. 2006. Paleoproterozoic evolution of the Challenger Au deposit, South Australia, from monazite geochronology. *Journal of Metamorphic Geology* **24**, 75-87.

MCFARLANE, C. R. M., MAVROGENES, J. A, & TOMKINS, A. G. 2007. Distinguishing hydrothermal alteration at Challenger, South Australia: a metamorphosed Au deposit. *Chemical Geology* **243**, 64-89.

MCGEE, B., GILES, D., KELSEY, D. E. & COLLINS, A. S. 2010. Protolith heterogeneity as a factor controlling the feedback between deformation, metamorphism and melting in a granulite-hosted gold deposit. *Journal of the Geological Society, London* **167**, 1089–1104.

ONDROUS, P., VAVRIN, I., SKALA, R. & VESELOVSKY, F. 2010. Low-temperature Ni-rich löllingite from Haje, Pibram, Czech Republic. *Neues Jahrbuch fur Mineralogie, Monatshefte* **2001**, 169-185.

PARKER, A. J. 2003. Geophysical characteristics of shear zone-hosted Proterozoic gold, Nuckulla Hill, South Australia. *In:* Geophysical Signatures of South Australian Mineral Deposits (M.C. Dentith, Ed.), *ASEG Special Publication* **12**, p. 67-76.

PHILLIPS, G. N. & POWELL, R. 2009. Formation of gold deposits: Review and evaluation of the continuum model. *Earth-Science Reviews* **94**, 1–21.

POSFAI, M. & BUSECK, P. R. 1997. Modular structures in sulfides: sphalerite/wurtzite-, pyrite/marcasite-, and pyrrhotite-type minerals. *EMU Notes in Mineralogy* **1**, 193–235.

POSFAI, M. & DODONY, I. 1990. Pyrrhotite superstructures. Part I: Fundamental structures of the *NC* (N = 2, 3, 4 and 5) type. *European Journal of Mineralogy* **2**, 525–528.

PRIOR, D. J., BOYLE, A. P., BRENKER, F., CHEADLE, M. C., DAY, A., LOPEZ, G., POTTS, G. J., REDDY, S. M., SPIESS, R., TRIMBY, P. W., WHEELER, J. & ZETTERSTRÖM, L. 1999. The application of electron backscatter diffraction and orientation contrast imaging in the SEM to textural problems in rocks. *American Mineralogist* **84**, 1741–1759

PUTNIS, A. 2009. Mineral replacement reactions. *Reviews in Mineralogy & Geochemistry* **70**, 87-124.

SHARP, Z. D., ESSENE, E. J. & KELLY, W. C. 1985. A re-examination of the arsenopyrite geothermometer: pressure considerations and applications to natural assemblages. *Canadian Mineralogist* **23**, 517–534.

SKALA, R., CISAROVA, I. & DRABEK, M. 2006. Inversion twinning in troilite. *American Mineralogist* 91, 917–921.

SWAIN, G., WOODHOUSE, A., HAND, M., BAROVICH, K., SCHWARZ, M. & FANNING, C. M. 2005. Provenance and tectonic development of the late Archaean Gawler Craton, Australia; U-Pb zircon, geochemical and Sm-Nd isotopic implications. *Precambrian Research* **141**, 106–136.

TEASDALE, J. 1997. *Methods for understanding poorly exposed terranes: The interpretive geology and tectonothermal evolution of the Western Gawler Craton*. Unpublished Ph.D. thesis, University of Adelaide,

TOMKINS, A. G. & MAVROGENES, J. A. 2001. Redistribution of gold within arsenopyrite and löllingite during pro- and retrograde metamorphism. Application to timing of mineralization. Economic Geology 96, 525–534.

TOMKINS, A.G, & MAVROGENES, J. A. 2002. Mobilization of Gold as a polymetallic Melt during Pelite Anatexis at the Challenger Deposit, South Australia: A metamorphosed Archean Gold Deposit. *Economic Geology* **97**, 1249-1271.

TOMKINS, A. G., DUNLAP, W. J., & MAVROGENES, J. A. 2004. Geochronological constraints on the polymetamorphic evolution of the granulite- hosted Challenger gold deposit: implications for assembly of the northwest Gawler Craton. *Australian Journal of Earth Sciences* **51**, 1-14.

TOMKINS, A. G., FROST, B. R. & PATTISON, D. R. M. 2006. Arsenopyrite melting during metamorphism of sulfide ore deposits. *Canadian Mineralogist* **44**, 1045–1062.

WILSON, S. A., RIDLEY, W. I. & KOENIG, A. E. 2002. Development of sulfide calibration standards for the laser ablation inductively-coupled plasma mass spectrometry technique. *Journal of Analytical Atomic Spectrometry* **17**, 406-409.

WIRTH, R. 2009. Focused Ion Beam (FIB) combined with SEM and TEM: Advanced analytical tools for studies of chemical composition, microstructure and crystal structure in geomaterials on a nanometre scale. *Chemical Geology* **261**, 217 229.

Figure captions

Figure 1. (a) Schematic geological map of the Gawler Craton, South Australia, showing the location of the Challenger Mine. Adapted from Geoscience Australia (2010), Gawler Mineral Promotion webpage, viewed 16 September 2010.

(http://www.ga.gov.au/minerals/research/regional/gawler/gawler.jsp)

(b) Schematic 3D section of the Challenger Mine from surface to -150 m RL, showing the distribution of the M1, M2 and M3 oreshoots and the location of sampled mining levels.

Figure 2. (a) Photograph of mapping area, level 840m. (b) Digitised image of the same photograph showing lithologies. (c and d) Close-up photographs showing details of the lithologies on the wall. (e) Hand-specimen RH7 (melanosome).

Figure 3. Back-scattered electron images showing aspects of gangue mineralogy. (a) Gahnite and cordierite intergrowths (RH15) (b) Ilmenite associated with gahnite and cordierite (RH15). (c) Detail of Fig. 3b showing rutile exsolved in ilmenite. Ilmenite contains exsolutions of a W-bearing mineral (ferberite?). (d) Rutile-ilmenite replacement texture within biotite (RH15). (e) Rutile replacing ilmenite at a pyrrhotite grain boundary, pyrrhotite and quartz are also observed within the bladed rutile texture (CH18a). (f) Reaction halo at pyrrhotite-feldspar boundary, halo reaction zone is characterised by rutile and quartz intergrowth (RH17). (g) Reaction halo at pyrrhotite-feldspar boundary (CH18a). (h) Reaction halo surrounding pyrrhotite enclosed within garnet (CH3). (For abbreviations refer to Table 1).

Figure 4. Reflected-light microscope photomicrographs illustrating (a) 'Brecciated' texture of sulphide minerals, especially arsenopyrite (18CH). (b) Typical löllingite-arsenopyrite-pyrrhotite ore mineral assemblage with pyrrhotite displaying bright lamella exsolutions (examples outlined in green) (CH13a). (c) Pyrrhotite and chalcopyrite remobilised within adjacent arsenopyrite (CH8a). (d) Pyrrhotite and chalcopyrite remobilised within grain-adjacent halos. Grain boundary between adjacent löllingite and arsenopyrite is outlined in red (CH8a). (e) Chalcopyrite remobilised within rutile adjacent pyrrhotite (CH8a). (f) Chalcopyrite forming symplectitic intergrowths with rutile adjacent pyrrhotite in oil immersion (CH8a). (For abbreviations refer to Table 1).

Figure 5. Back-scattered electron images showing (a) Lamella exsolution in pyrrhotite displaced by chalcopyrite grains (RH16). (b) Lamella exsolution in pyrrhotite displaced by molybdenite (RH17). (c) Lamella exsolution in pyrrhotite being replaced by pentlandite along the main lamella orientation (RH9). (d) Cadmium-rich sphalerite and Zn-rich greenockite within pyrrhotite and chalcopyrite. Electrum is also observed at the boundary of pyrrhotite and in the adjacent quartz (RH15). (e) Detail of Zn-rich greenockite and Cd-rich sphalerite within chalcopyrite (RH15). (f) Detail of Zn-rich greenockite within pyrrhotite and pyrrhotite lamella (RH15). (For abbreviations refer to Table 1).

Figure 6. Back-scattered electron images showing (a) Löllingite grain locked within garnet (RH16) (b) Typical pyrrhotite-löllingite-arsenopyrite ore mineral association (RH11). (c) Fairly extensive replacement of löllingite by arsenopyrite with electrum exsolution at the reaction boundary (RH16). (d) Typical pyrrhotite-löllingite-arsenopyrite ore mineral association (Chal10) (e) Limited replacement of

löllingite by arsenopyrite with some electron seen along the reaction boundary (RH2) (f) Fairly extensive replacement of löllingite by arsenopyrite from RH1. (g) Irregular, potentially structurally controlled arsenopyrite within pyrrhotite with very minor löllingite present (Chal2). (h) Skeletal growth of idiomorphic arsenopyrite within löllingite (CH8a). (For abbreviations refer to Table 1).

Figure 7. Back-scattered electron images showing (a) Fan-like aggregate of pyrrhotite, arsenopyrite, löllingite and ilmenite surrounding a zircon grain. From RH16 (b) Idiomorphic grain of Apy2 within pyrrhotite (RH16). (c) idiomorphic grain of arsenopyrite with associated pyrrhotite within silicate minerals (RH14). (d) Idiomorphic grain of Apy2 with associated pyrrhotite with electrum in pores (RH14). (e) Hypidiomorphic grain of Apy2 with associated pyrrhotite with electrum in the pores (RH14). (f) Hypdiomorphic grain of Apy2 with associated pyrrhotite with well developed zonation patterns in the arsenopyrite (RH14). (For abbreviations refer to Table 1).

Figure 8. Back-scattered electron images showing (a) Electrum and hessite intergrowth at the arsenopyrite-löllingite grain boundary (1RH). (b) Hessite at the arsenopyrite-löllingite grain boundary (16RH). (c) Electrum at the arsenopyrite-löllingite grain boundary (17RH). (d) Unnamed mineral (Bi3Te2) at the löllingite-arsenopyrite grain boundary (1RH). (e) Volynskite and hessite intergrowth at the arsenopyrite-löllingite grain boundary (17RH). (f) Petzite and hessite intergrowth at the arsenopyrite-löllingite grain boundary (17RH). (g) Hessite at the arsenopyrite-löllingite grain boundary (RH19). (h) Electrum and hessite intergrowth at the arsenopyrite-löllingite grain boundary (CH18a). (i) Electrum and hessite intergrowth at the arsenopyrite-löllingite grain boundary from (CH18a). (j) Electrum at the arsenopyrite-löllingite grain boundary from (CH18a). (k) Hessite at the arsenopyrite-löllingite grain boundary (CH13a). (l) Petzite and hessite intergrowth at the arsenopyrite-löllingite grain boundary (CH13a). (For abbreviations refer to Table 1).

Figure 9. Back-scattered electron images showing representative gold associations in high-grade ore (Chal1 and Chal10). (a) Three-component maldonite-bismuth-gold patch. (b and c) Typical bi-component patches of maldonite + bismuth along replacement boundary between löllingite and Asp1. (d-f) Three-component maldonite-bismuth-hedleyite assemblage. (For abbreviations refer to Table 1).

Figure 10. Reflected-light microscope photomicrographs illustrating (a) Electrum at the arsenopyrite-löllingite boundary (green dotted line) (RH20). (b) Electrum at the arsenopyrite- löllingite boundary (green dotted line) with detail inset (RH9). (c) Electrum at the boundary of pyrrhotite and the adjacent silicate, and within associated halo as minute inclusions (RH15). (For abbreviations refer to Table 1).

Figure 11. Back-scattered electron images showing gold associations in Apy1. (a) Zonation within arsenopyrite caused by variance in Co and Ni concentrations, and included electrum (CH18c). (b) Electrum and hessite within pores at the löllingite arsenopyrite boundary (RH17) (c) Electrum and hessite within pores at the löllingite -arsenopyrite boundary (CH13a). (d) Electrum and hessite at the löllingite -arsenopyrite boundary (CH13a). (e) Electrum and hessite at the löllingite -arsenopyrite boundary (CH18a). (f) Electrum and hessite at the löllingite-arsenopyrite boundary (CH18a). (g) Detail of electrum and hessite, showing grains with both electrum and hessite present, at the löllingite-arsenopyrite boundary (CH18a). (For abbreviations refer to Table 1).

Figure 12. Reflected-light microscope photomicrographs in oil immersion illustrating. (a) Graphite blade with small native gold grain attached (CH13a). (b) Bleb-like trails of gold with minor arsenopyrite (CH13a). (For abbreviations refer to Table 1).

Figure 13. (a) Ni vs. Co binary plot showing variation in composition of arsenopyrite (+ cobaltite) and löllingite as determined by electron probe microanalysis (expressed in atoms per formula unit; a.p.f.u). Dashed line shows 1:1 correlation between the two elements. Note that arsenopyrite plots below this line, i.e., Co-enriched relative to Ni) and löllingite plots above the line (Ni-enriched relative to Co. (b) Ternary plots in FeAsS – CoAsS - NiAsS and FeAs2 - CoAs2 - NiAs2 space, showing the composition of analysed arsenopyrite and löllingite and trends among the dataset with respect to textural type of arsenopyrite. (For abbreviations refer to Table 1).

Figure 14. (a) Binary plot of atom.% As vs. atom.% S(+Se) showing non-stoichiometry among the analysed arsenopyrite (+ cobaltite) population as determined by electron probe microanalysis, and how this variation in composition correlates with textural type. (b) Ternary plot of Fe+Co+Ni – As+Sb – S+Se (atom.%) illustrating compositional variation in arsenopyrite (+ cobaltite) is expressed in terms of the three components of the mineral formula. Note that main figure represents only a small, central portion of the entire ternary. (c) Similar ternary plot (atom.% Fe+Co+Ni – As+Sb – S+Se) illustrating limited compositional variation in löllingite. Note also here that the main figure represents only the As-apex of the entire ternary. Abbreviations: Apy = arsenopyrite, Cob = cobaltite, Gers = gersdorffite, Lin = linnaite, Lo = löllingite, Py = pyrite, Ram = rammelsbergite, Saf = safflorite.

Figure 15. (a) Binary plot of atom.% M (metals; Fe+Co+Ni) vs. atom.% S (+Se) for Challenger pyrrhotite as determined by electron probe microanalysis. Note that compositions range from close to FeS to ~Fe7S8. (b) Similar binary plot for pyrrhotite, but only for Fe rather than Fe+Co+Ni. Note that the most non-stoichiometric compositions (Fe10S11, Fe9S10, Fe7S8) plot below the line due to the presence of Co and Ni.

Figure 16. (a) Histograms (logarithmic axis on horizontal axis) showing the distribution of Au, Bi and Te concentrations in arsenopyrite and löllingite from high-grade ores and from the M2 orebody, as measured by LA-ICPMS. Note the significant differences between the respective sub-populations (see also text for further explanation).

Figure 17. Schematic diagram depicting the range of variation in Au concentration within löllingite in samples from each of the sampled mine levels, and from high-grade ore. Individual LA-ICPMS spot analyses are shown, arranged in order of decreasing Au within each sub-population.

Figure 18. (a) Reflected light 'map' of laser spot analyses in löllingite from high-grade ore. Numbers in brackets are Au concentrations (in ppm) from individual spots. Note that most laser spots are in pairs: the ones labelled in red were analysed in Adelaide; those in blue were made at the LA-ICPMS facility in Hobart. (b) Time-resolved LA-ICPMS depth profile for spot 'H1 Chal' (located on a) showing flat profile for Au suggestive of Au in solid solution (108 ppm). (c) Time-resolved LA-ICPMS depth profile for spot '1Chal 13' (also located on a) showing noisy profile for Au and Bi correlated with an inclusion of maldonite. (d) Reflected light 'map' of laser spot analyses in arsenopyrite from high-grade ore. (e) Time-

resolved LA-ICPMS depth profile for spot ‘1Chal 1’ (located on d) showing noisy profile indicative of maldonite inclusions.

Figure 19. (a) Time-resolved LA-ICPMS depth profile of löllingite from the M2 orebody (spot ‘13aCH5) showing flat spectra for Au and Te suggesting that both elements are present in solid solution (28 and 90 ppm, respectively). (b) Reflected light ‘map’ of laser spot analysis in löllingite from M2. Number next to spot is the Au concentrations (in ppm). (c) Time-resolved LA-ICPMS depth profile for spot ‘1RH6’ (located on b) showing reasonably flat spectrum for Au suggestive of Au in solid solution (89 ppm). (d) Reflected light ‘map’ of laser spot analysis in löllingite and coexisting arsenopyrite (Apy1) from M2. Numbers next to spots are the Au concentrations (in ppm). (e) Time-resolved LA-ICPMS depth profile for spot ‘1RH2’ (located on d) showing noisy spectra for Ag and Te explained by an inclusion of hessite. (f) Reflected light ‘map’ of laser spot analyses in Apy-2 arsenopyrite from M2. (g) Time-resolved LA-ICPMS depth profile for spot ‘17RH6’ (located on f) showing 7.5 ppm Au, probably as inclusions.

Figure 20. Binary element plots illustrating trends in the trace element data obtained by LA-ICPMS for arsenopyrite and löllingite. (a) Co vs. Ni plot showing the marked tendency for arsenopyrite to be enriched in arsenopyrite, and Ni in löllingite. Spot analyses of arsenopyrite plot on, or just below the Co:Ni 1:1 line. (b) Au vs. Bi illustrating Au enrichment in löllingite relative to arsenopyrite and that the range of Bi concentrations is significantly greater for löllingite than for arsenopyrite. (c) Au vs. Ag shows the far greater range of Ag concentrations in löllingite and also the lack of correlation between the two precious metals. (d) Ag vs. Se, showing no discernable correlation between the two elements, although many of those spots with high Ag also have higher Se. (e) Ag vs. Te, showing that much of the data for the two minerals plot as a cluster rather than a linear correlation; outliers show enrichment in both elements. (f) [Au vs. (Te+Ag)], emphasizing the separate, wedge-shaped distributions for the two minerals in which Au is generally, but not always, higher where there is enrichment in Ag+Te.

Figure 21. Secondary electron (SE) images showing details of the löllingite Apy1 patch analysed by EBSD (specimen tilted at 70°). (a) orientation of the patch relative to the main and secondary foliations (F1 and F2). (b) close-up of the entire patch showing the replacement boundary between löllingite and Apy1 and the fact that this is parallel to the zonation in Apy1. (c and d) Details of the enclosed graphite showing its position across the replacement boundary and electrum-hessite inclusions. (For abbreviations refer to Table 1).

Figure 22. Selection of EBSD maps assembled using Tango software. (a) Orientation contrast-forescatter map showing löllingite and Apy1 and domains in the latter. The löllingite-arsenopyrite boundary is marked in green and the arsenopyrite zones of differing crystallographic orientation are marked in red in both (a) and (b). (b) EBSD map showing Euler angle results for the mapping area. Löllingite is green and arsenopyrite is pink. Blue points indicate potential misorientation domains (see text for further explanation). (c) Map of grain boundaries using minimum misorientation angle of <1°.

Figure 23. Pole figures plotted on axes as indicated for arsenopyrite and löllingite obtained using Mambo software. (a-c) Misorientation angles for arsenopyrite plotted against each pole as outlined. Construction lines and angles are included for interpreting deviation from the pole. (d–f) Pole plots for each respective

pole diagram measuring deviance from the pole. (g and h) Misorientation angles for löllingite plotted against each pole as outlined. Construction lines and angles are included for interpreting deviation from the pole.

Figure 24. (a) Secondary electron (SE) image showing the location of the pyrrhotite grain used for TEM study on a foil prepared using FIB cut2. (b) Close-up of the pyrrhotite grain showing the position of the FIB cut relative to the lamella. Specimen is tilted at 52° during milling of the hole prior to slice extraction. (c) High-resolution SE image obtained in immersion mode showing the pyrrhotite lamella (arrowed) within the host. Note the sharp contact between the two phases. (d) Low-resolution TEM image of the FIB-prepared foil showing the location of the selected areas of electron diffractions (SAED) in (e) (rectangle) and in Figure 25 a-d. (e) SAED at the junction between pyrrhotite host and lamella showing the parallel orientation along the c* axis between the two phases.

Figure 25. (a-d) SAEDs representative for lamella (a, b) and host pyrrhotite (c, d), where the electron beam is parallel to the c* axis (a, c) or to zone {0-21} (b, d). The SAEDs along the c* axis show that the host pyrrhotite is a 3C-, 2A-fold superstructure of the phase in the lamellae; the latter represents the 1C, 1A NiAs subcell (high-T troilite). The position of superstructure reflections along c* are marked by arrows in (c). E, f) electron diffractions simulated for troilite (crystal structure parameters from Skala et al. 2006) for zones {100} and (0-21} in e and f, respectively. The concordance between the troilite and the lamella as well as the subcell in the host pyrrhotite is shown in the motif outlined by dark circles on the {0-21} zone for all phases; the superstructure reflections on this zone are shown in red for host pyrrhotite (d).

Figure 26. (a) Plot of atom.% As in arsenopyrite vs. temperature (after Sharp et al. 1985) showing stability fields for arsenopyrite-bearing assemblages at a range of geological temperatures. The composition of selected individual arsenopyrite grains are shown on the line representing their assemblage. (b) Corresponding diagram showing log fS2 vs. temperature (after Barton 1969) showing the range of log fS2 and temperature conditions considered realistic for crystallization of Apy1 and Apy2. Dashed line on (b) represents the boundary between solid arsenopyrite and liquid.

Figure 27. (a) Schematic diagram representing the hypothesized (pre-metamorphic) epithermal formation model for the Challenger deposit. (b) Schematic figure illustrating the 3 orebodies within the proximal gneiss deformed during granulite-facies metamorphic overprinting of the Challenger orebody during the Sleafordian Orogeny. (c) Schematic time vs. temperature diagram showing development of key ore mineral reactions discussed in this thesis during prograde- and retrograde segments of granulite-facies metamorphism.

FIGURES

Figure 1

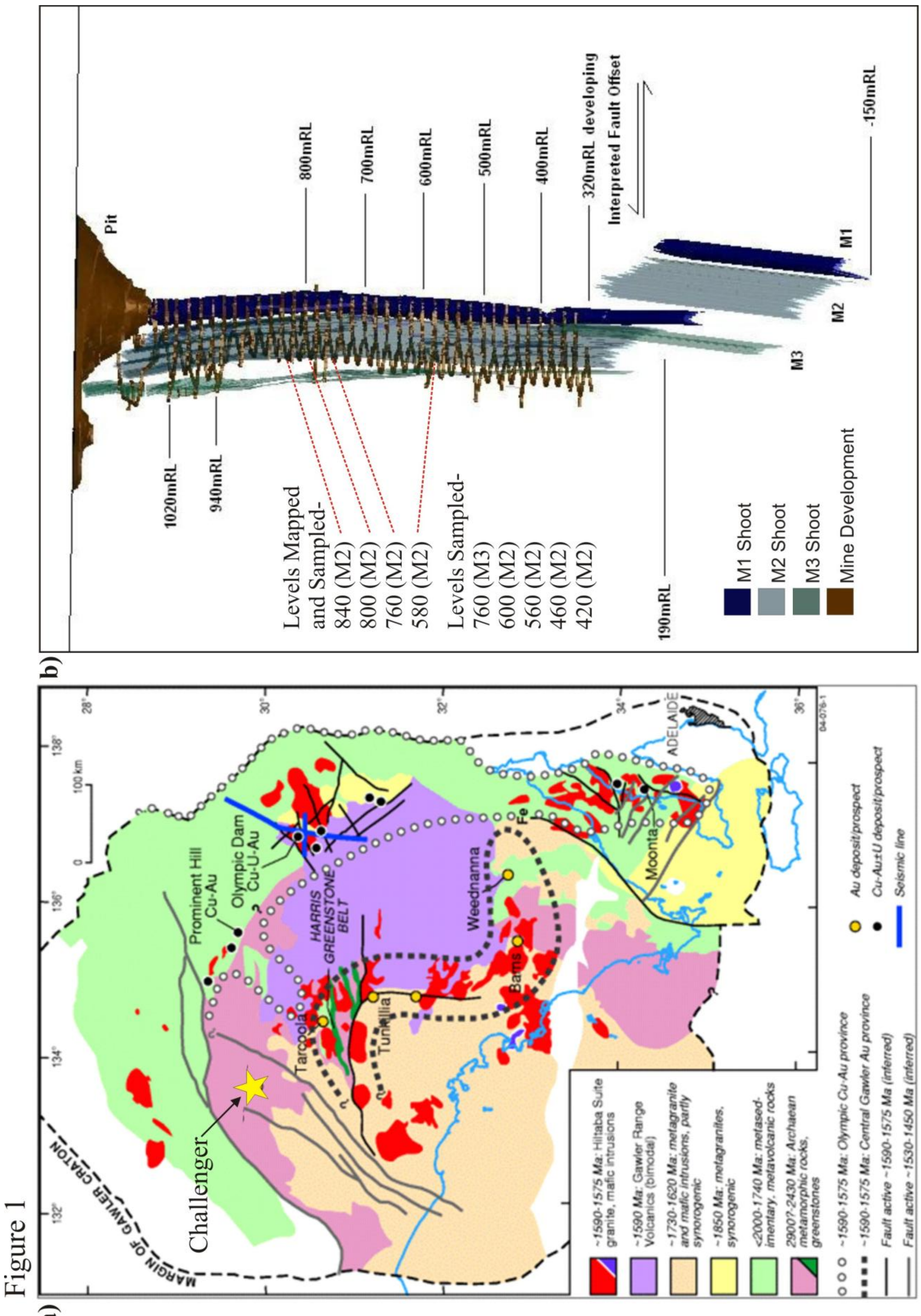

Figure 2; 840m M2

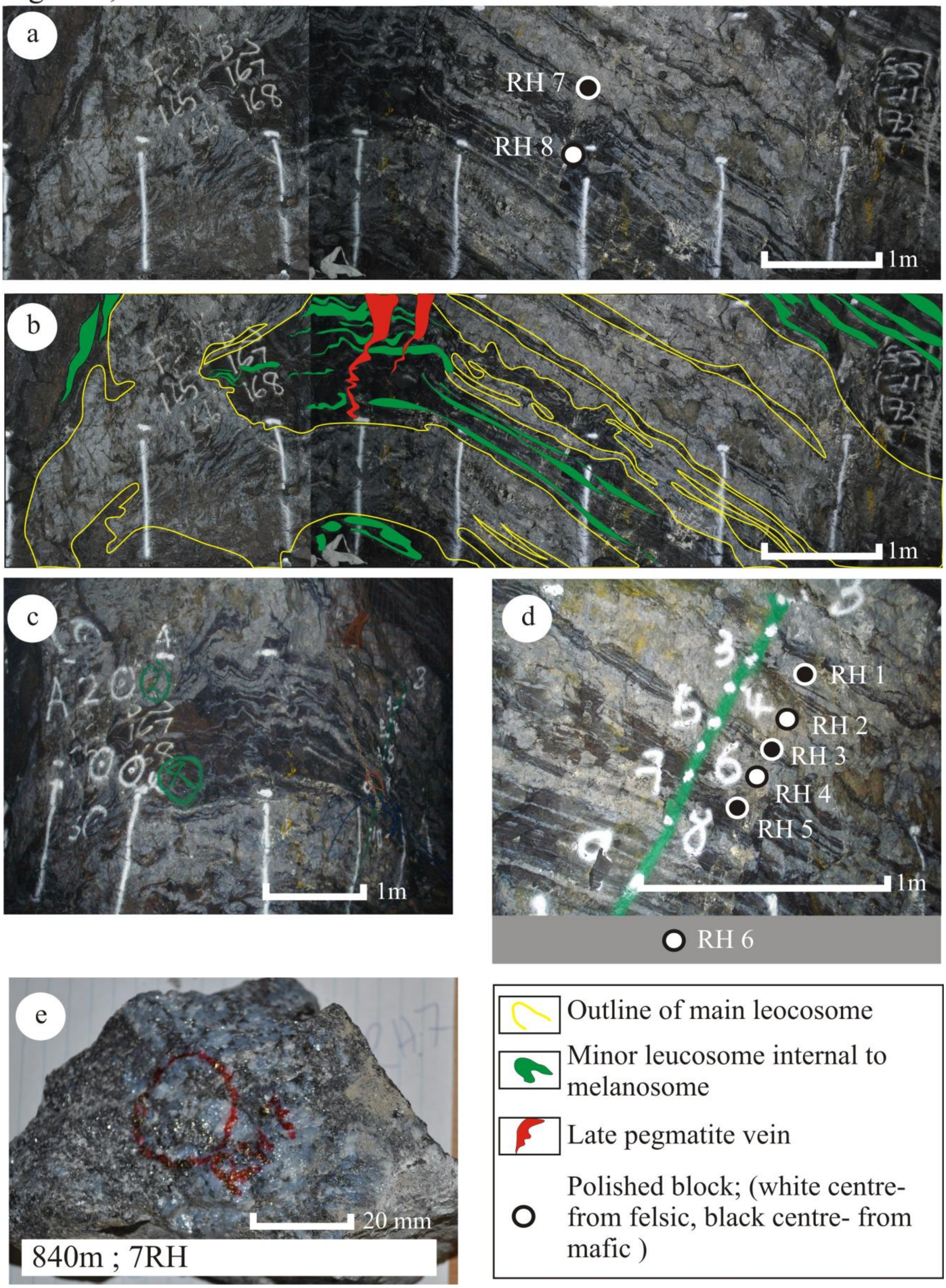

Figure 3

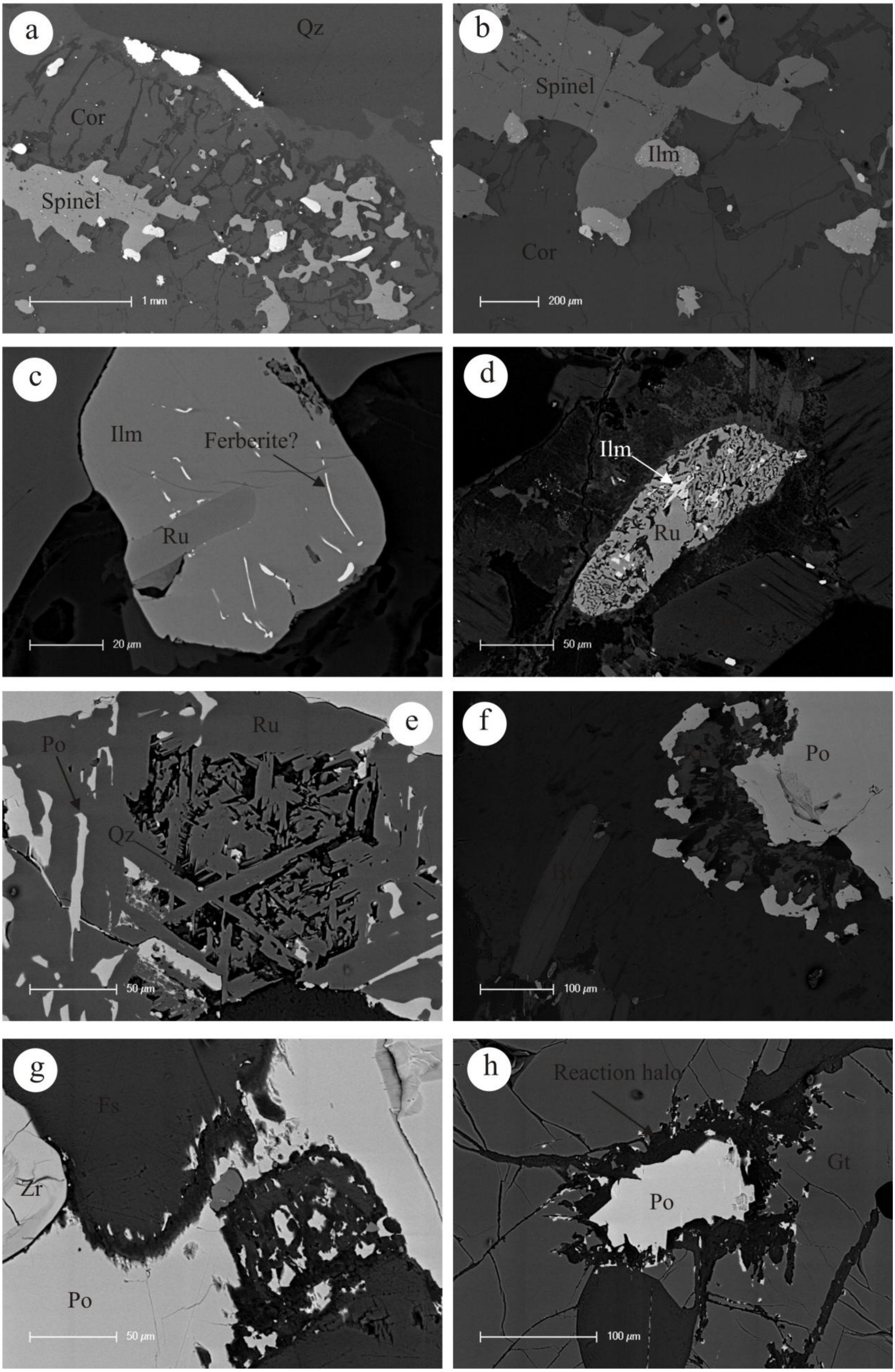
a
Qz
Cor
Spinel
1 mm
b
Spinel
Ilm
Cor
200 μm
c
Ilm
Ferberite?
Ru
20 μm
d
Ilm
Ru
50 μm
e
Ru
Po
Qz
50 μm
f
Po
100 μm
g
Fs
Zr
Po
50 μm
h
Reaction halo
Gt
Po
100 μm

Figure 4

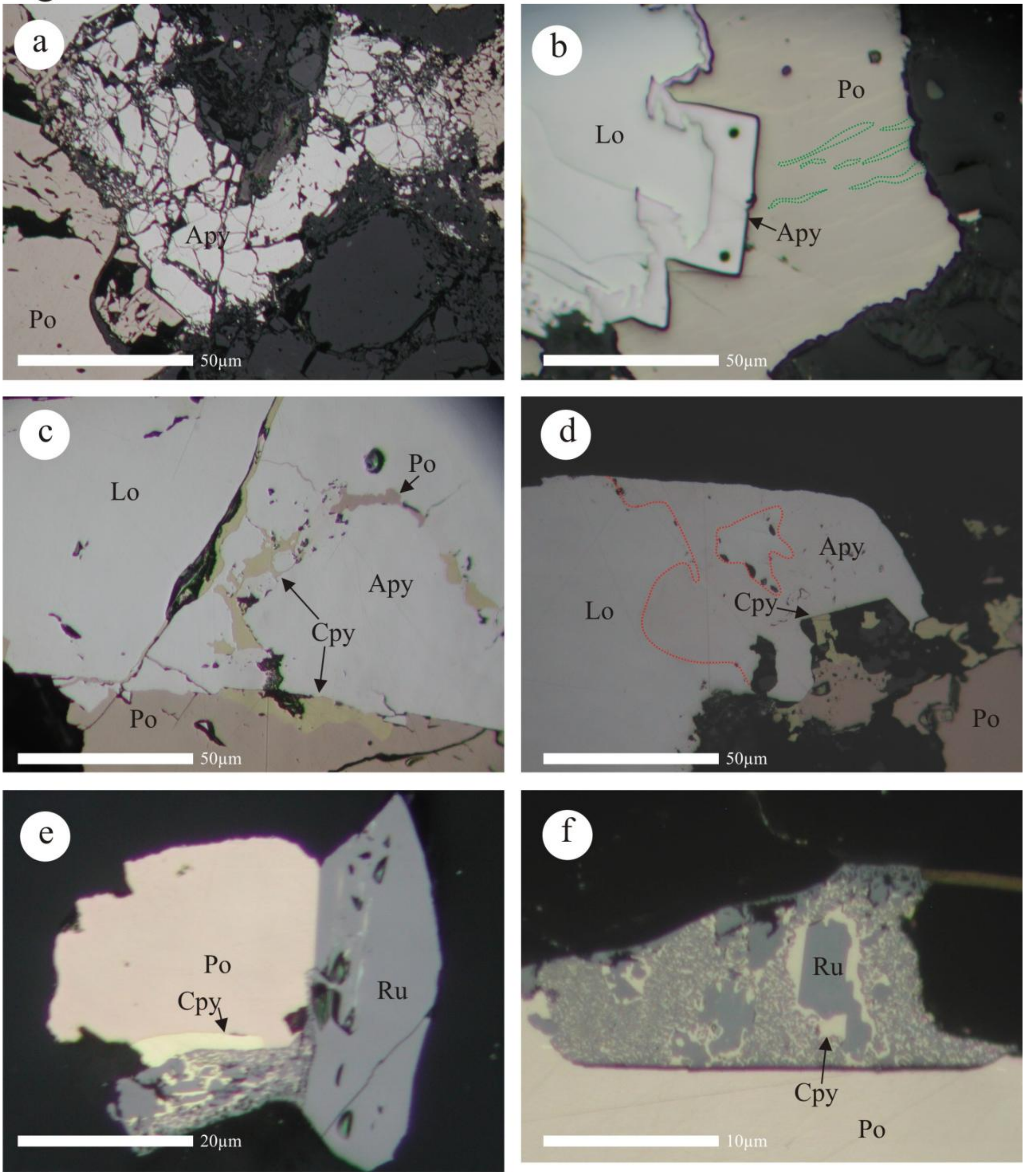

a
Apy
Po
50µm
b
Lo
Po
Apy
50µm
c
Lo
Po
Apy
Cpy
Po
50µm
d
Apy
Lo
Cpy
Po
50µm
e
Po
Cpy
Ru
20µm
f
Ru
Cpy
Po
10µm

Figure 5

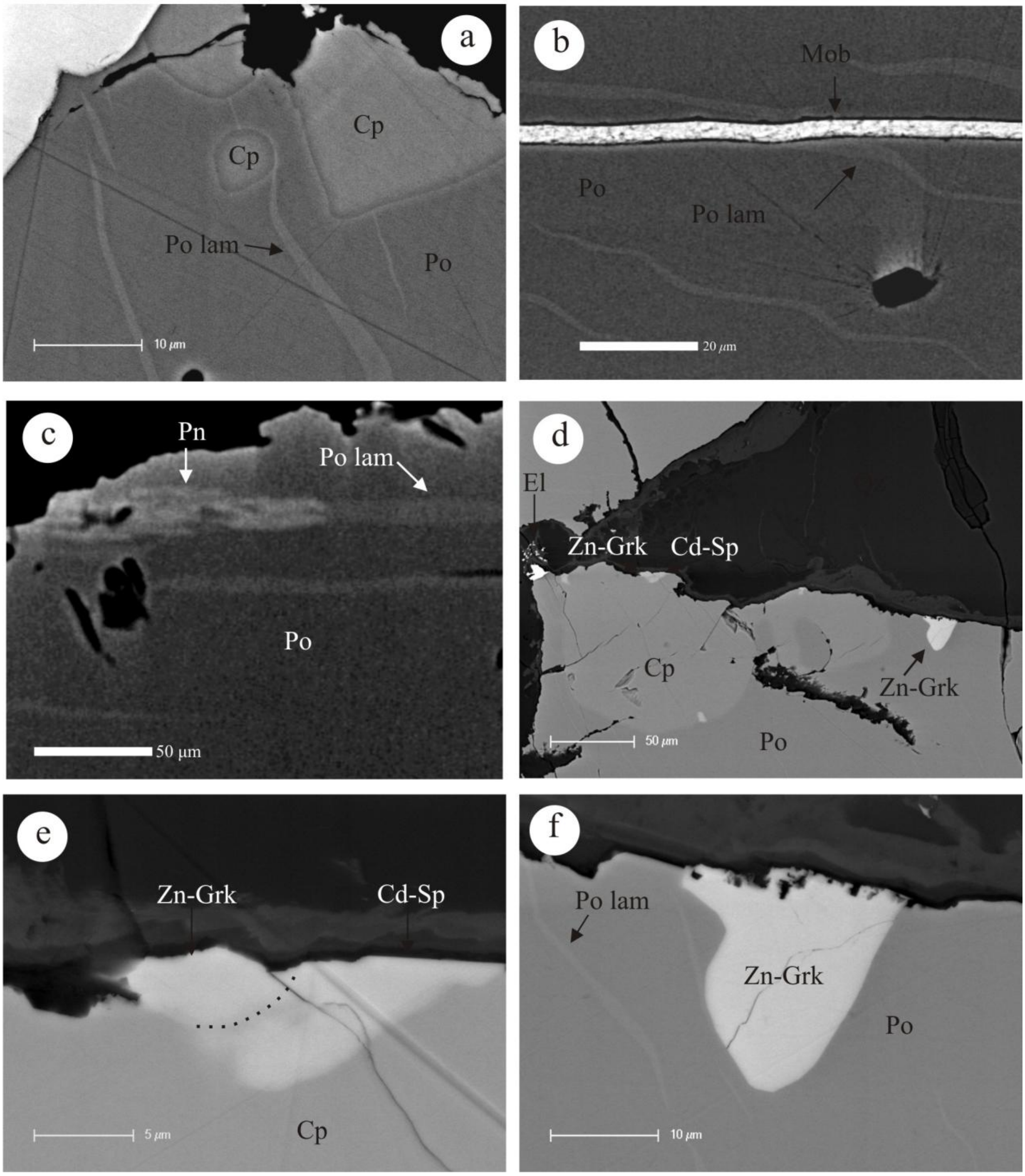
a
Cp
Cp
Po lam
Po
10 μm
b
Mob
Po
Po lam
20 μm
c
Pn
Po lam
Po
50 μm
d
El
Zn-Grk
Cd-Sp
Cp
Zn-Grk
50 μm
Po
e
Zn-Grk
Cd-Sp
5 μm
Cp
f
Po lam
Zn-Grk
Po
10 μm

Figure 6

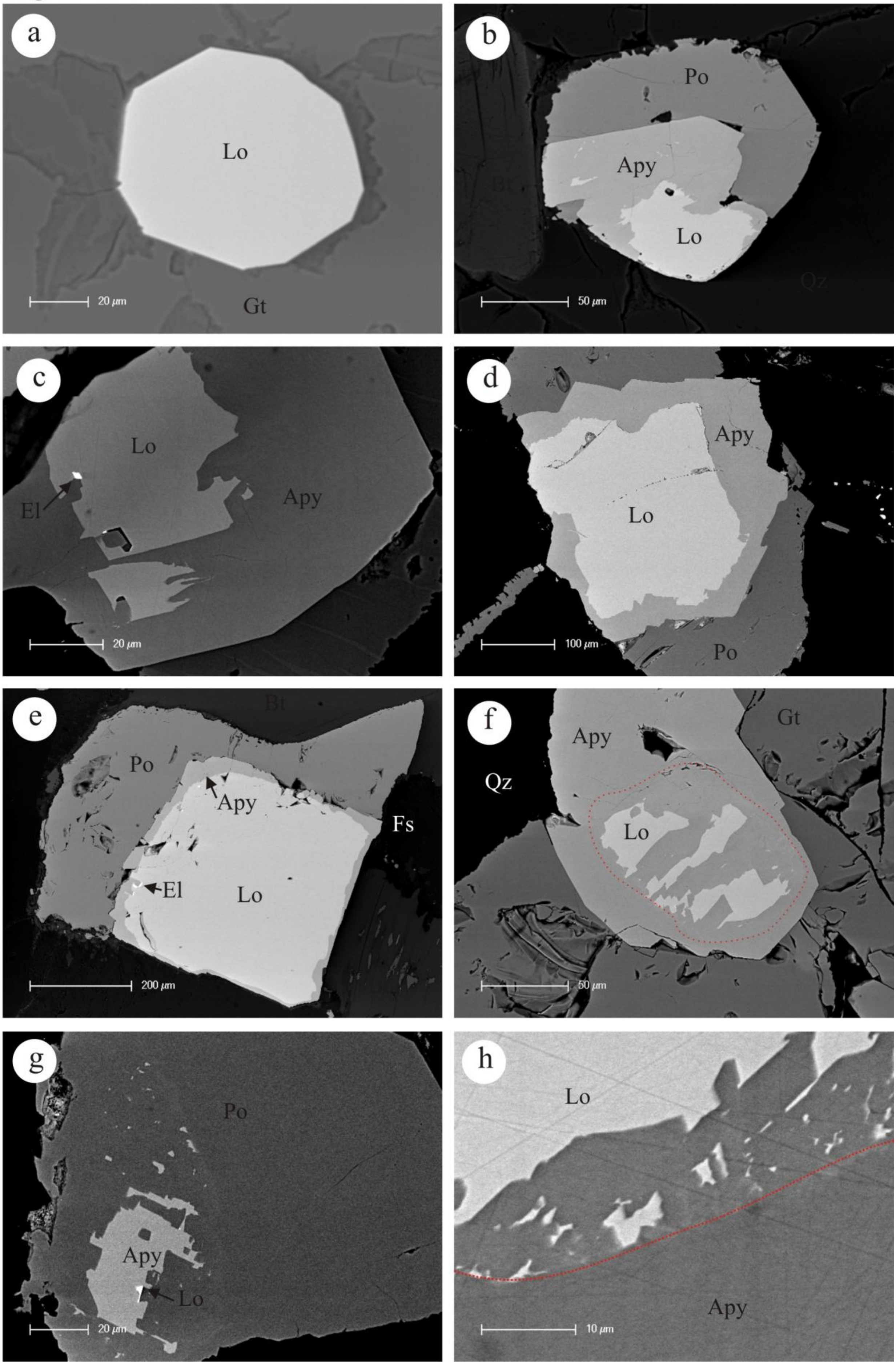
a
Lo
20 μm
Gt
b
Po
Apy
Lo
50 μm
c
Lo
El
Apy
20 μm
d
Apy
Lo
100 μm
Po
e
Po
Apy
El
Lo
Fs
200 μm
f
Apy
Gt
Qz
Lo
50 μm
g
Po
Apy
Lo
20 μm
h
Lo
Apy
10 μm

Figure 7

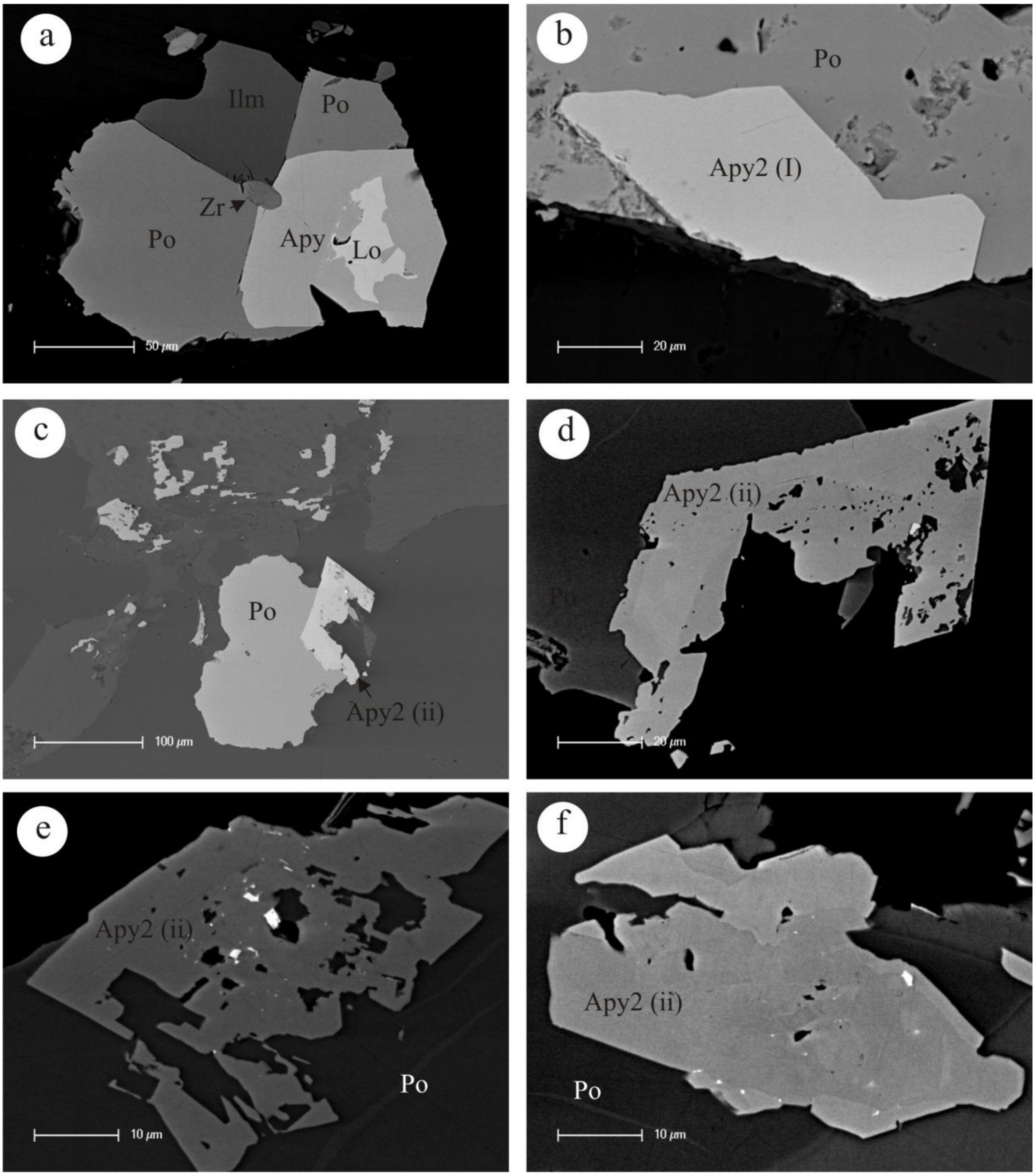
a
Ilm
Po
Zr
Po
Apy
Lo
50 μm
b
Po
Apy2 (I)
20 μm
c
Po
Apy2 (ii)
100 μm
d
Apy2 (ii)
Po
20 μm
e
Apy2 (ii)
Po
10 μm
f
Apy2 (ii)
Po
10 μm

Figure 8

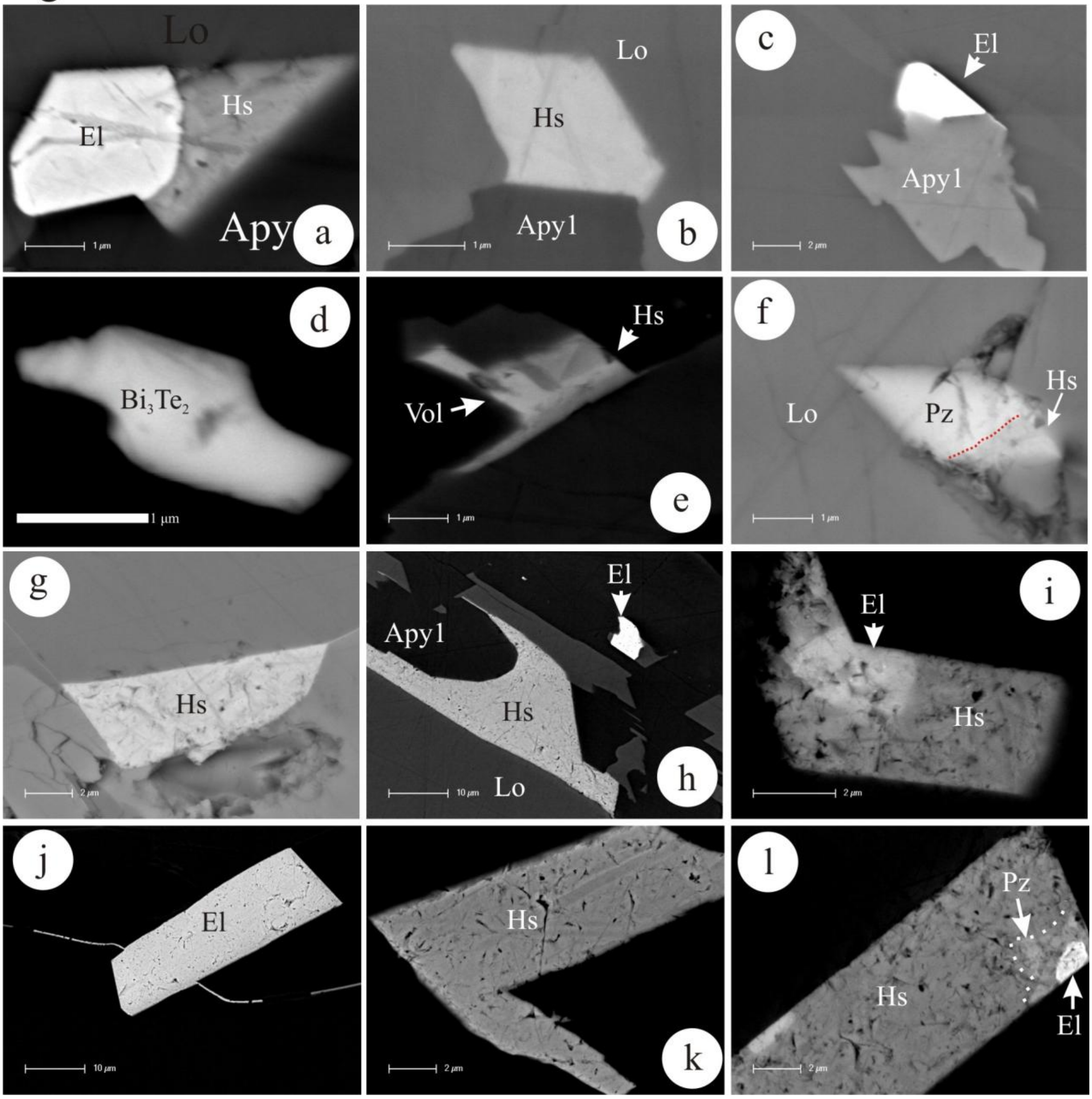
Lo
Hs
El
Apy
a
1 μm
Lo
Hs
Apy1
b
1 μm
c
El
Apy1
2 μm
d
Bi_3Te_2
1 μm
Hs
Vol
e
1 μm
f
Lo
Pz
Hs
1 μm
g
Hs
2 μm
El
Apy1
Hs
Lo
h
10 μm
El
i
Hs
2 μm
j
El
10 μm
Hs
k
2 μm
l
Pz
Hs
El
2 μm

Figure 9

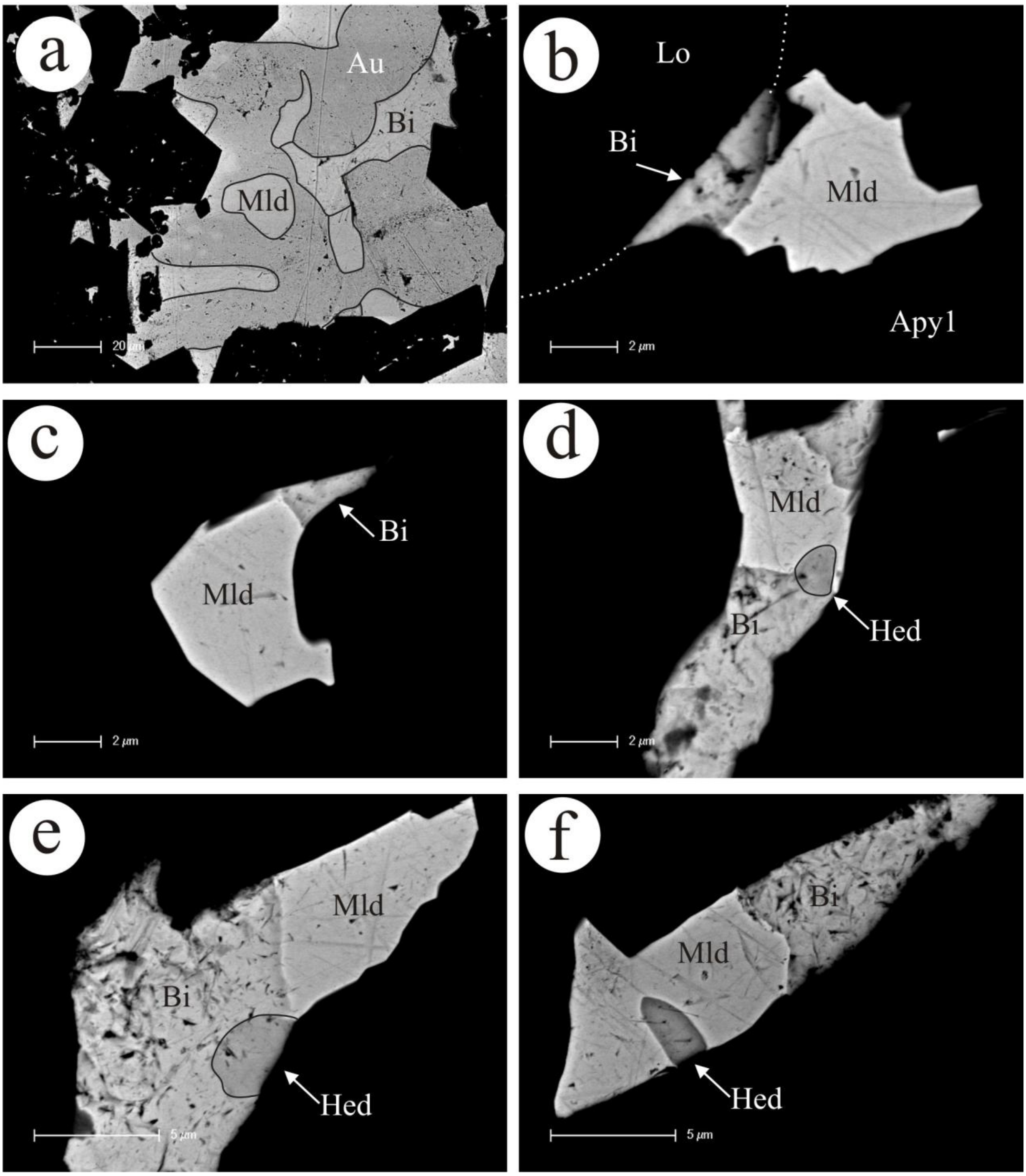

a
Au
Bi
Mld
20 μm
b
Lo
Bi
Mld
Apy1
2 μm
c
Bi
Mld
2 μm
d
Mld
Bi
Hed
2 μm
e
Mld
Bi
Hed
5 μm
f
Bi
Mld
Hed
5 μm

Figure 10

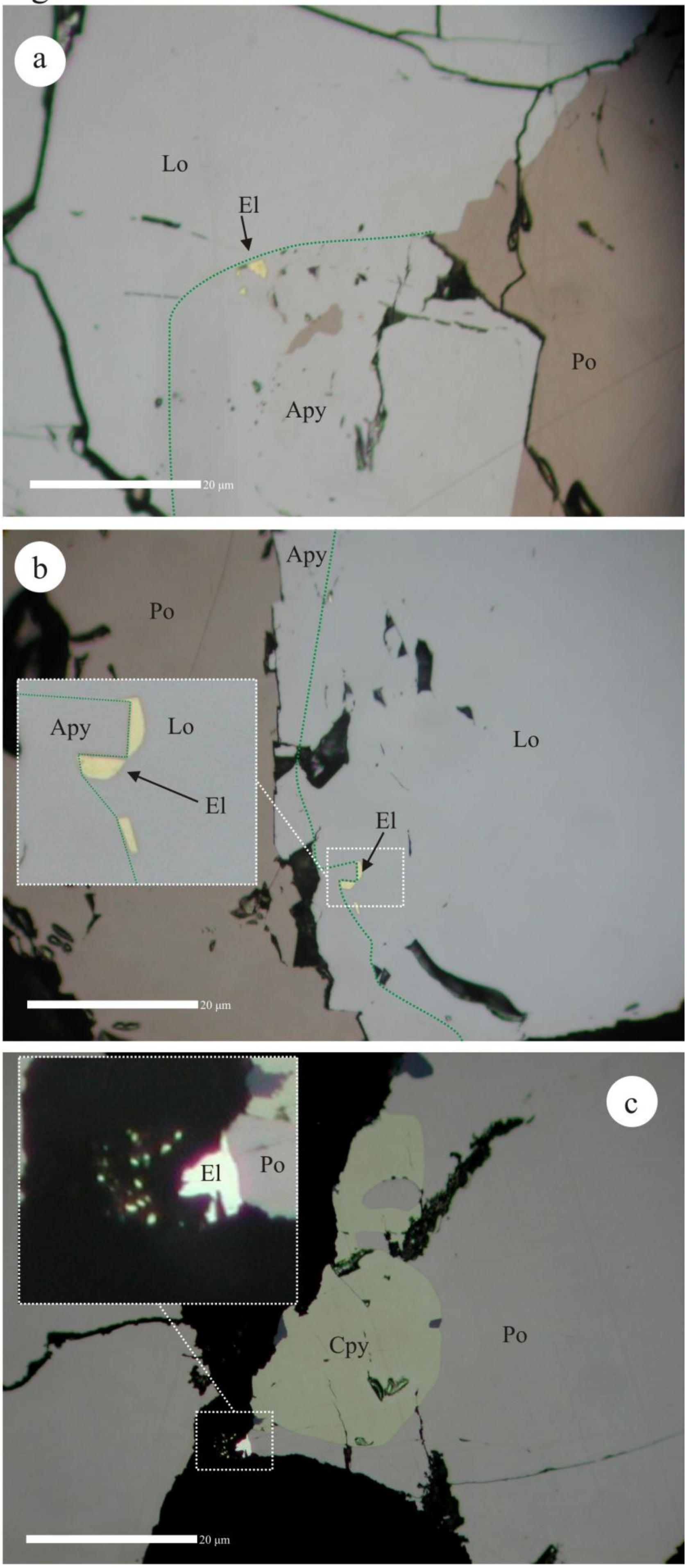

Figure 11

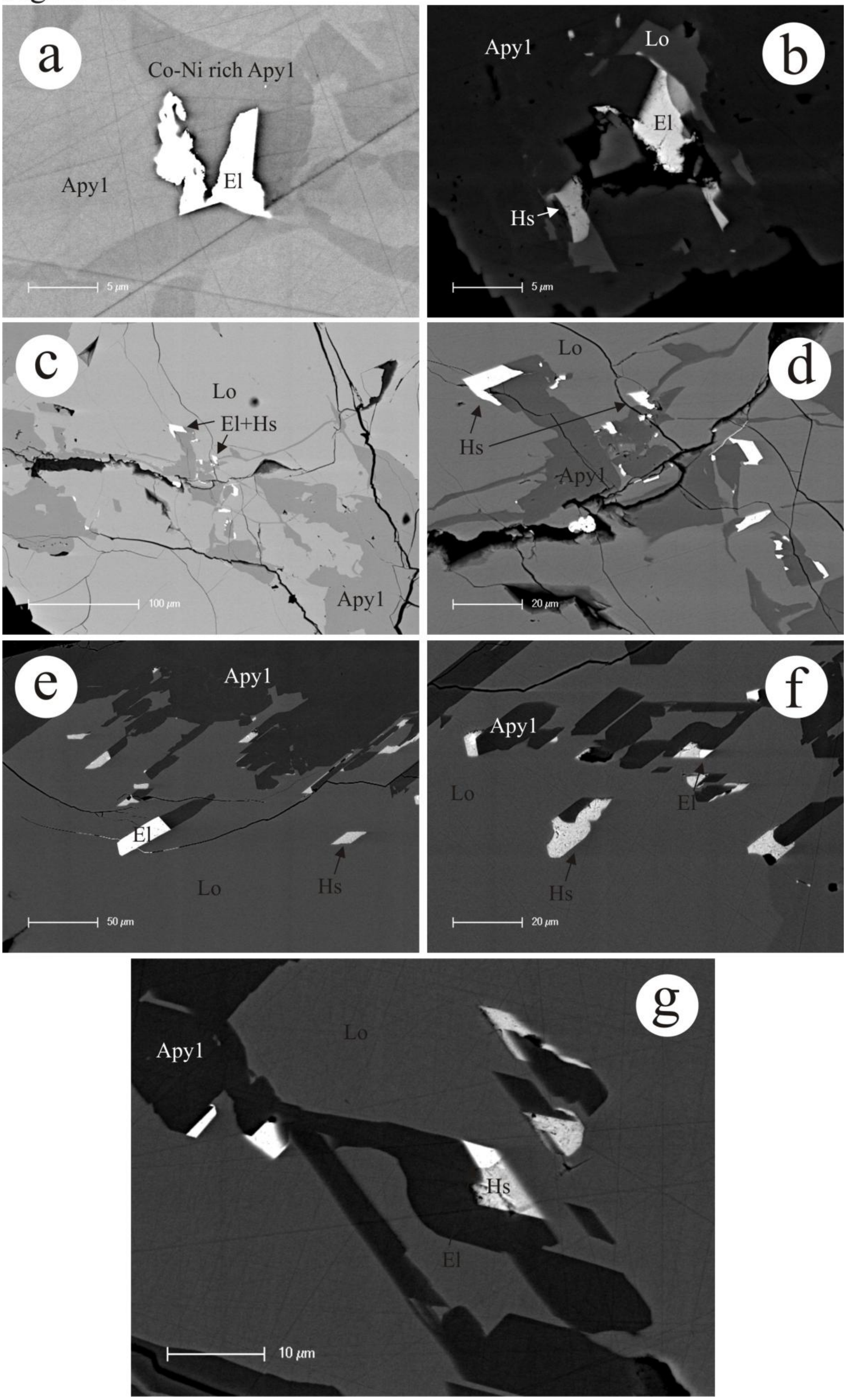
a
Co-Ni rich Apy1
Apy1
El
5 μm
b
Apy1
Lo
El
Hs
5 μm
c
Lo
El+Hs
Apy1
100 μm
d
Lo
Hs
Apy1
20 μm
e
Apy1
El
Lo
Hs
50 μm
f
Apy1
Lo
El
Hs
20 μm
g
Lo
Apy1
Hs
El
10 μm

Figure 12

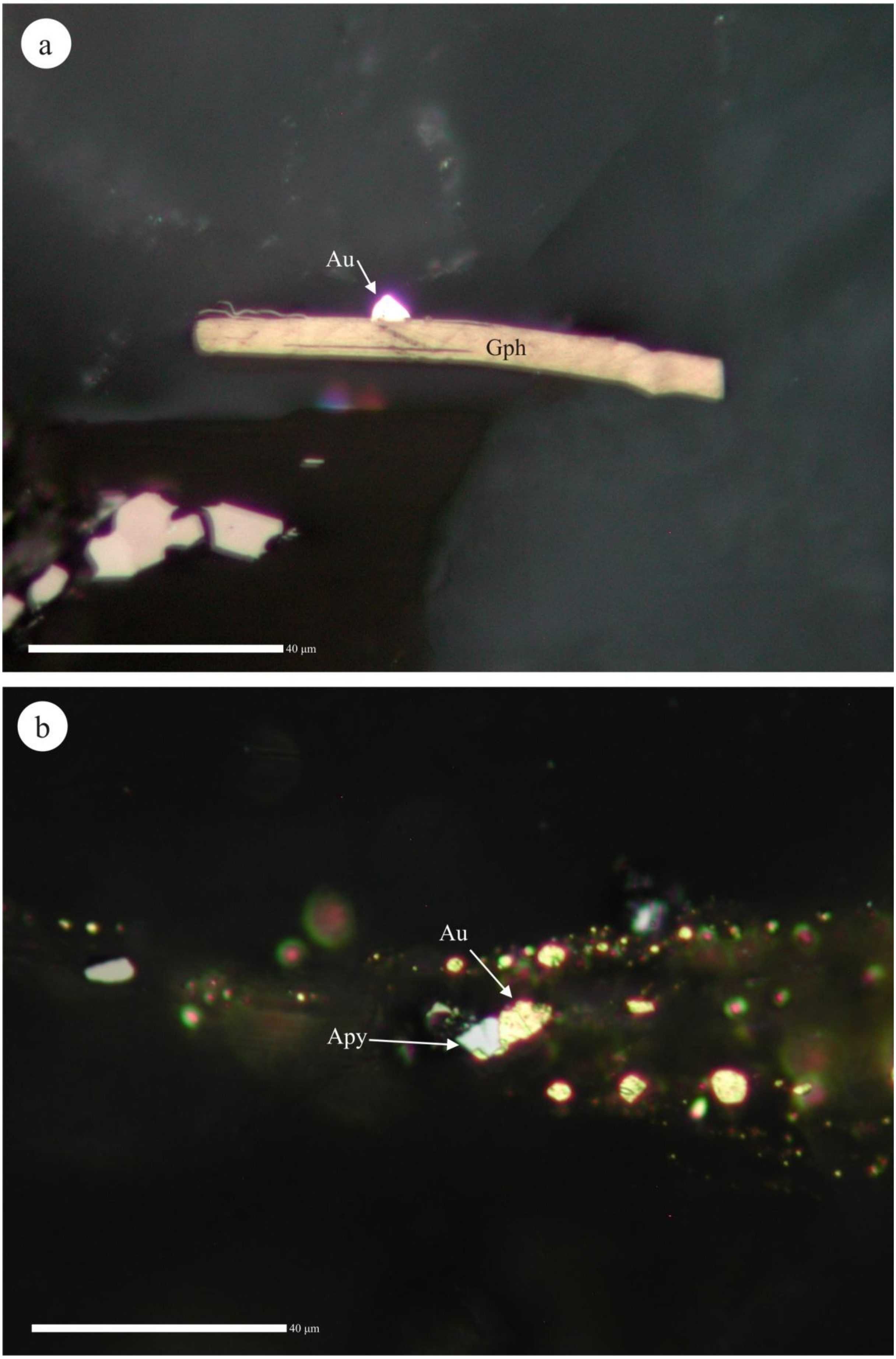

Figure 13

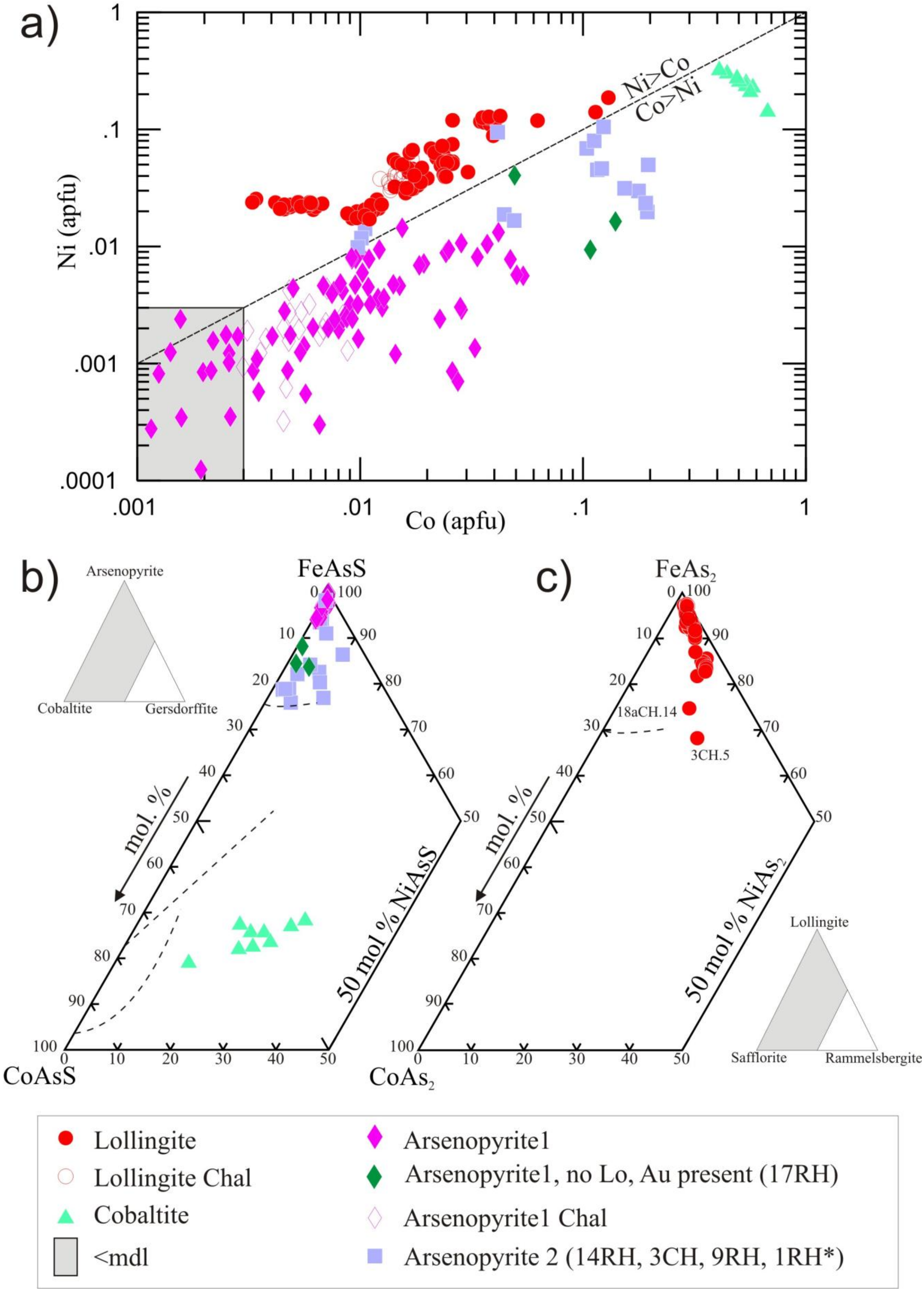
a)
Ni (apfu)
Co (apfu)
Ni>Co
Co>Ni
1
.1
.01
.001
.0001
.001
.01
.1
1
b)
Arsenopyrite
Cobaltite
Gersdorffite
FeAsS
CoAsS
mol. %
50 mol % NiAsS
c)
FeAs2
CoAs2
18aCH.14
3CH.5
mol. %
50 mol % NiAs2
Lollingite
Safflorite
Rammelsbergite
Lollingite
Lollingite Chal
Cobaltite
<mdl
Arsenopyrite1
Arsenopyrite1, no Lo, Au present (17RH)
Arsenopyrite1 Chal
Arsenopyrite 2 (14RH, 3CH, 9RH, 1RH*)

Figure 14

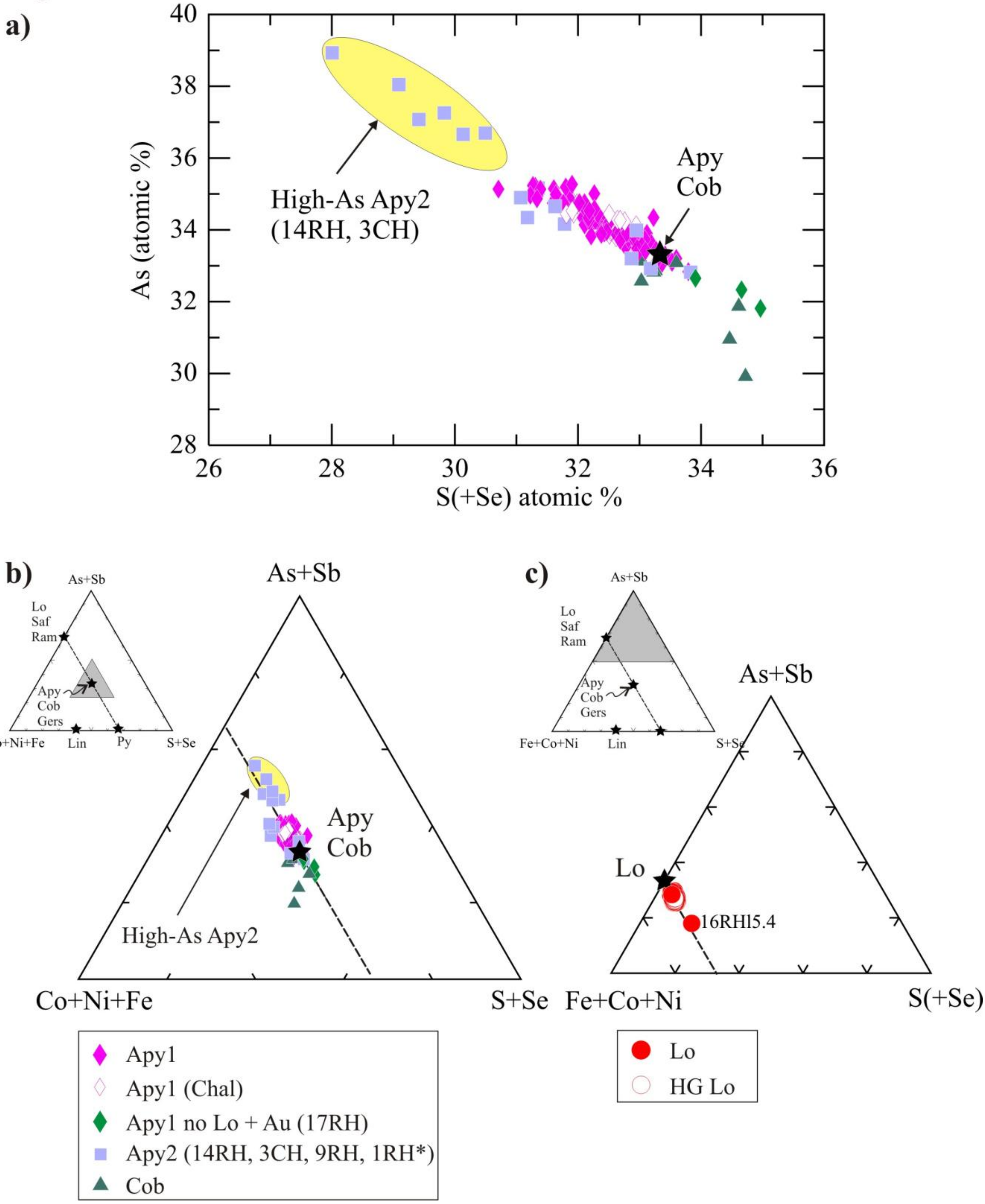
a)
High-As Apy2
(14RH, 3CH)
Apy
Cob
As (atomic %)
S(+Se) atomic %
40
38
36
34
32
30
28
26
28
30
32
34
36
b)
As+Sb
Lo
Saf
Ram
Apy
Cob
Gers
Co+Ni+Fe
Lin
Py
S+Se
As+Sb
Apy
Cob
High-As Apy2
Co+Ni+Fe
S+Se
Apy1
Apy1 (Chal)
Apy1 no Lo + Au (17RH)
Apy2 (14RH, 3CH, 9RH, 1RH*)
Cob
c)
As+Sb
Lo
Saf
Ram
Apy
Cob
Gers
Fe+Co+Ni
Lin
S+Se
As+Sb
Lo
16RHl5.4
Fe+Co+Ni
S(+Se)
Lo
HG Lo

Figure 15

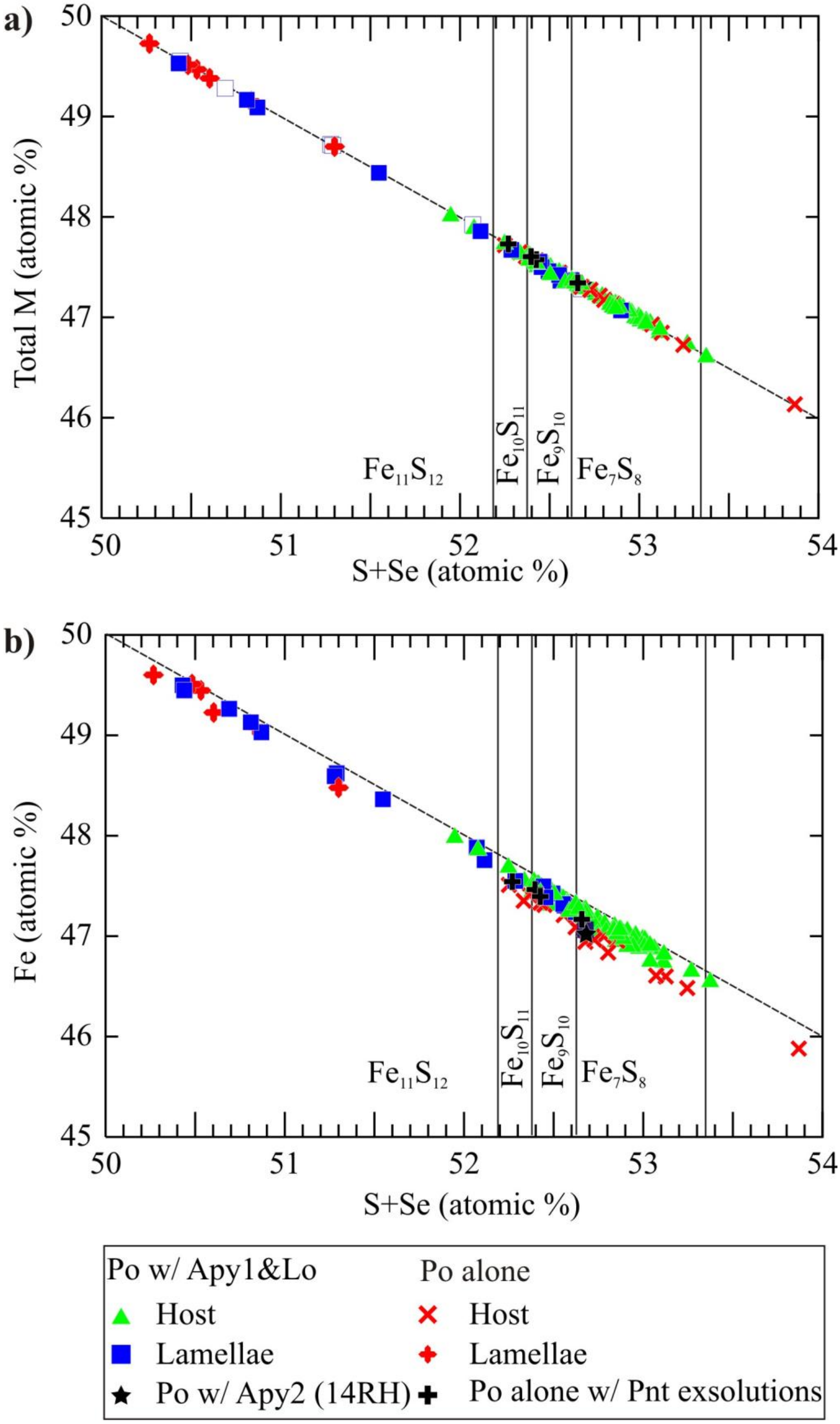

a)
Total M (atomic %)
S+Se (atomic %)
$Fe_{11}S_{12}$
$Fe_{10}S_{11}$
Fe_9S_{10}
Fe_7S_8
b)
Fe (atomic %)
S+Se (atomic %)
$Fe_{11}S_{12}$
$Fe_{10}S_{11}$
Fe_9S_{10}
Fe_7S_8
Po w/ Apy1&Lo
Host
Lamellae
Po w/ Apy2 (14RH)
Po alone
Host
Lamellae
Po alone w/ Pnt exsolutions

Figure 16

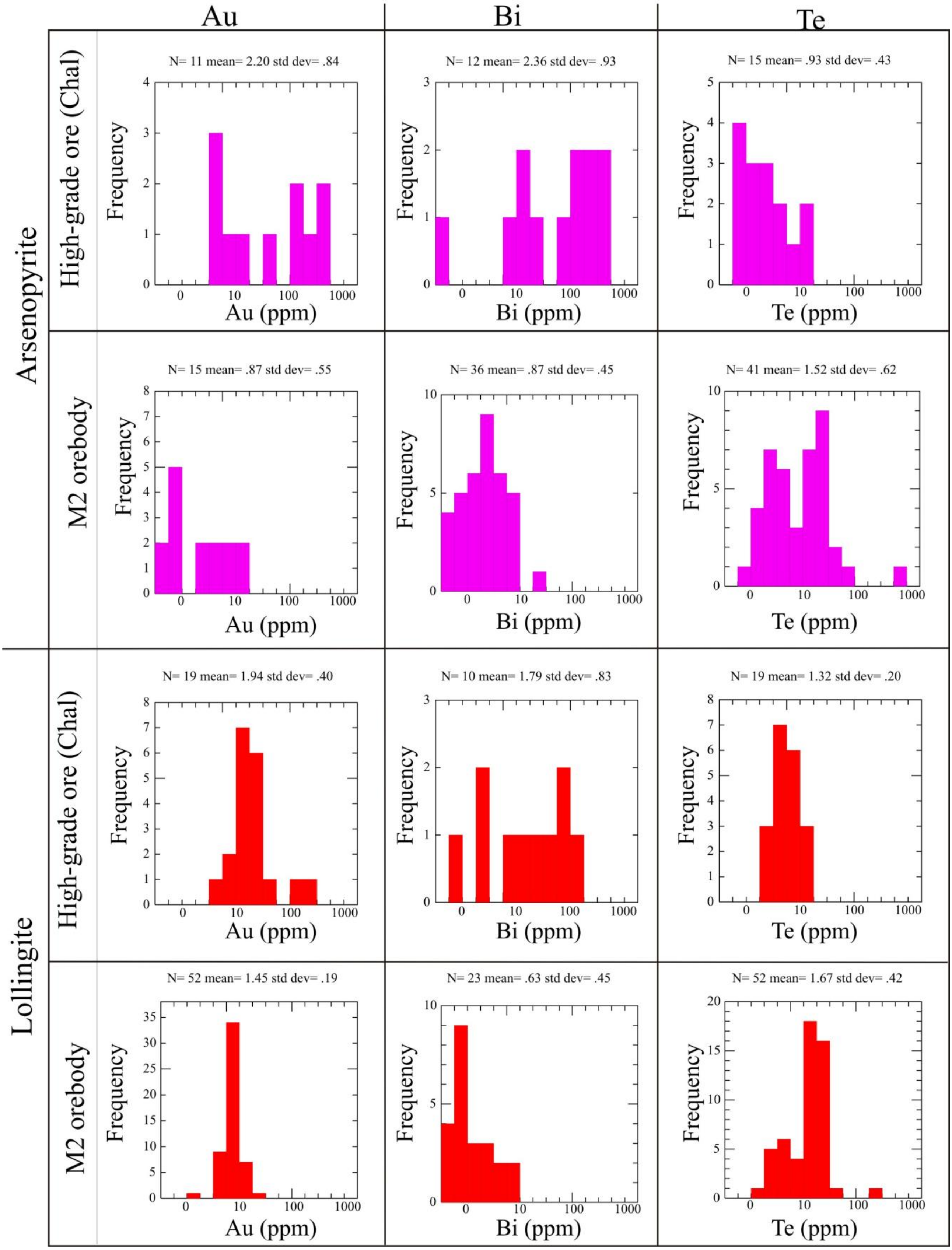

Au
Bi
Te
Arsenopyrite
Lollingite
High-grade ore (Chal)
M2 orebody
N= 11 mean= 2.20 std dev= .84
N= 12 mean= 2.36 std dev= .93
N= 15 mean= .93 std dev= .43
N= 15 mean= .87 std dev= .55
N= 36 mean= .87 std dev= .45
N= 41 mean= 1.52 std dev= .62
N= 19 mean= 1.94 std dev= .40
N= 10 mean= 1.79 std dev= .83
N= 19 mean= 1.32 std dev= .20
N= 52 mean= 1.45 std dev= .19
N= 23 mean= .63 std dev= .45
N= 52 mean= 1.67 std dev= .42
Frequency
Au (ppm)
Bi (ppm)
Te (ppm)

Figure 17

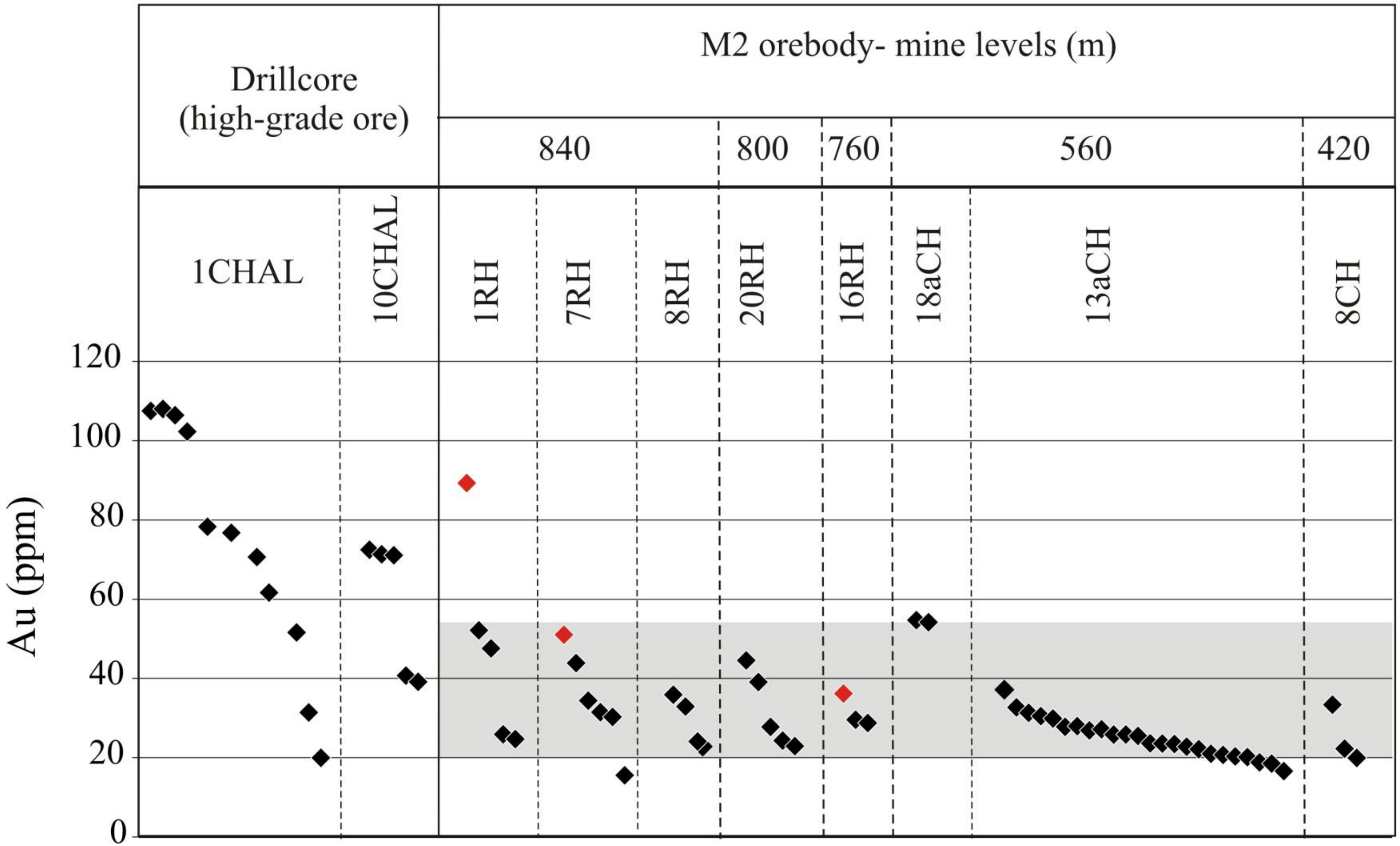

Drillcore (high-grade ore)
M2 orebody- mine levels (m)
840
800
760
560
420
1CHAL
10CHAL
1RH
7RH
8RH
20RH
16RH
18aCH
13aCH
8CH
Au (ppm)
120
100
80
60
40
20
0

Figure 18

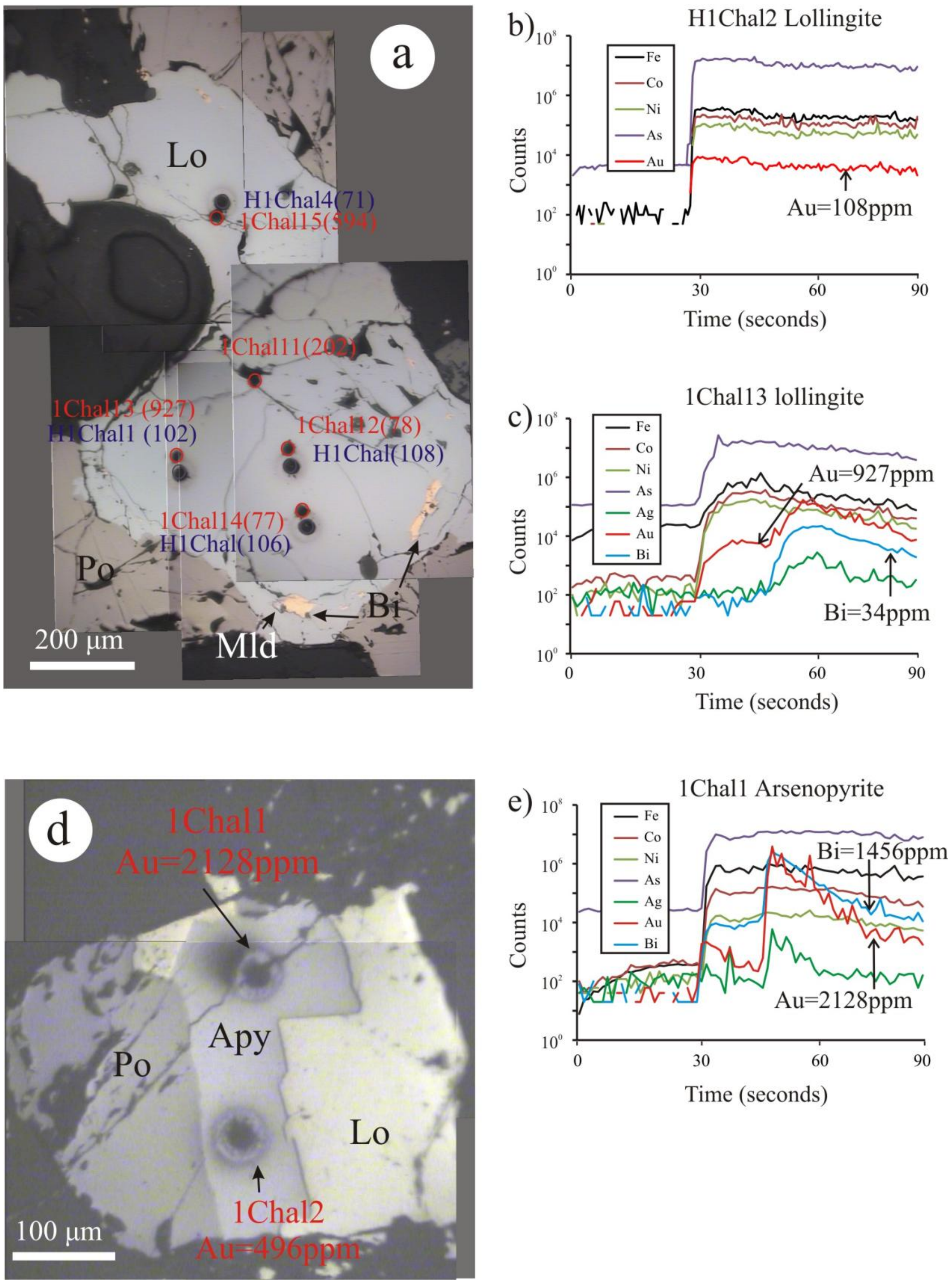
a
Lo
H1Chal4(71)
1Chal15(594)
1Chal11(202)
1Chal13 (927)
H1Chal1 (102)
1Chal12(78)
H1Chal(108)
1Chal14(77)
H1Chal(106)
Po
Bi
Mld
200 μm
b)
H1Chal2 Lollingite
Fe
Co
Ni
As
Au
Au=108ppm
Counts
Time (seconds)
c)
1Chal13 lollingite
Fe
Co
Ni
As
Ag
Au
Bi
Au=927ppm
Bi=34ppm
Counts
Time (seconds)
d
1Chal1
Au=2128ppm
Apy
Po
Lo
1Chal2
Au=496ppm
100 μm
e)
1Chal1 Arsenopyrite
Fe
Co
Ni
As
Ag
Au
Bi
Bi=1456ppm
Au=2128ppm
Counts
Time (seconds)

Figure 19

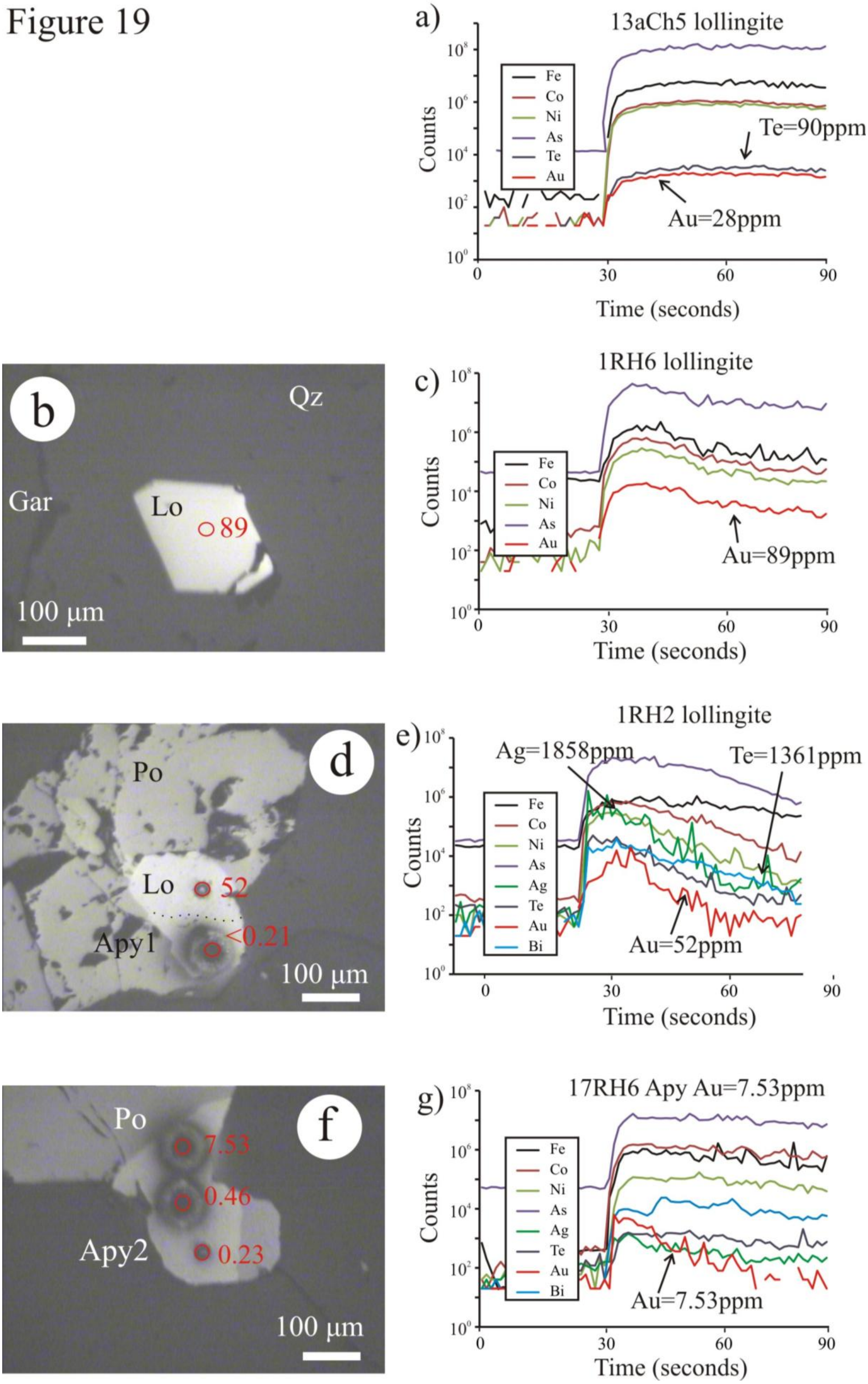

a)
13aCh5 lollingite
Counts
Time (seconds)
Fe
Co
Ni
As
Te
Au
Te=90ppm
Au=28ppm
b
Qz
Gar
Lo
89
100 µm
c)
1RH6 lollingite
Counts
Time (seconds)
Fe
Co
Ni
As
Au
Au=89ppm
d
Po
Lo
52
Apy1
<0.21
100 µm
e)
1RH2 lollingite
Ag=1858ppm
Te=1361ppm
Counts
Time (seconds)
Fe
Co
Ni
As
Ag
Te
Au
Bi
Au=52ppm
f
Po
7.53
0.46
Apy2
0.23
100 µm
g)
17RH6 Apy Au=7.53ppm
Counts
Time (seconds)
Fe
Co
Ni
As
Ag
Te
Au
Bi
Au=7.53ppm

Figure 20

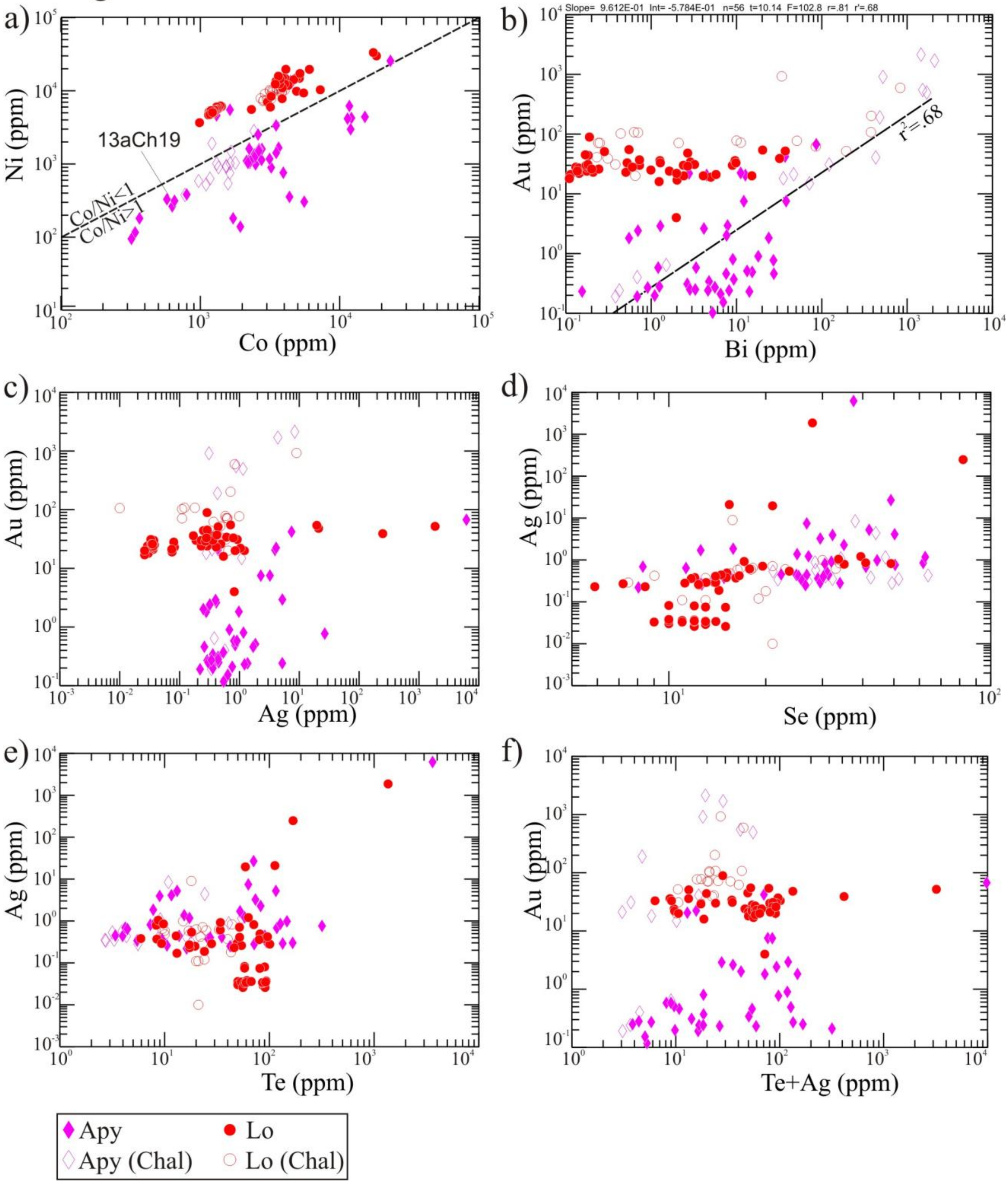

a)
Ni (ppm)
Co (ppm)
13aCh19
Co/Ni<1
Co/Ni>1
b)
Slope= 9.612E-01 Int= -5.784E-01 n=56 t=10.14 F=102.8 r=.81 r²=.68
Au (ppm)
Bi (ppm)
r²=.68
c)
Au (ppm)
Ag (ppm)
d)
Ag (ppm)
Se (ppm)
e)
Ag (ppm)
Te (ppm)
f)
Au (ppm)
Te+Ag (ppm)
Apy
Lo
Apy (Chal)
Lo (Chal)

Figure 21

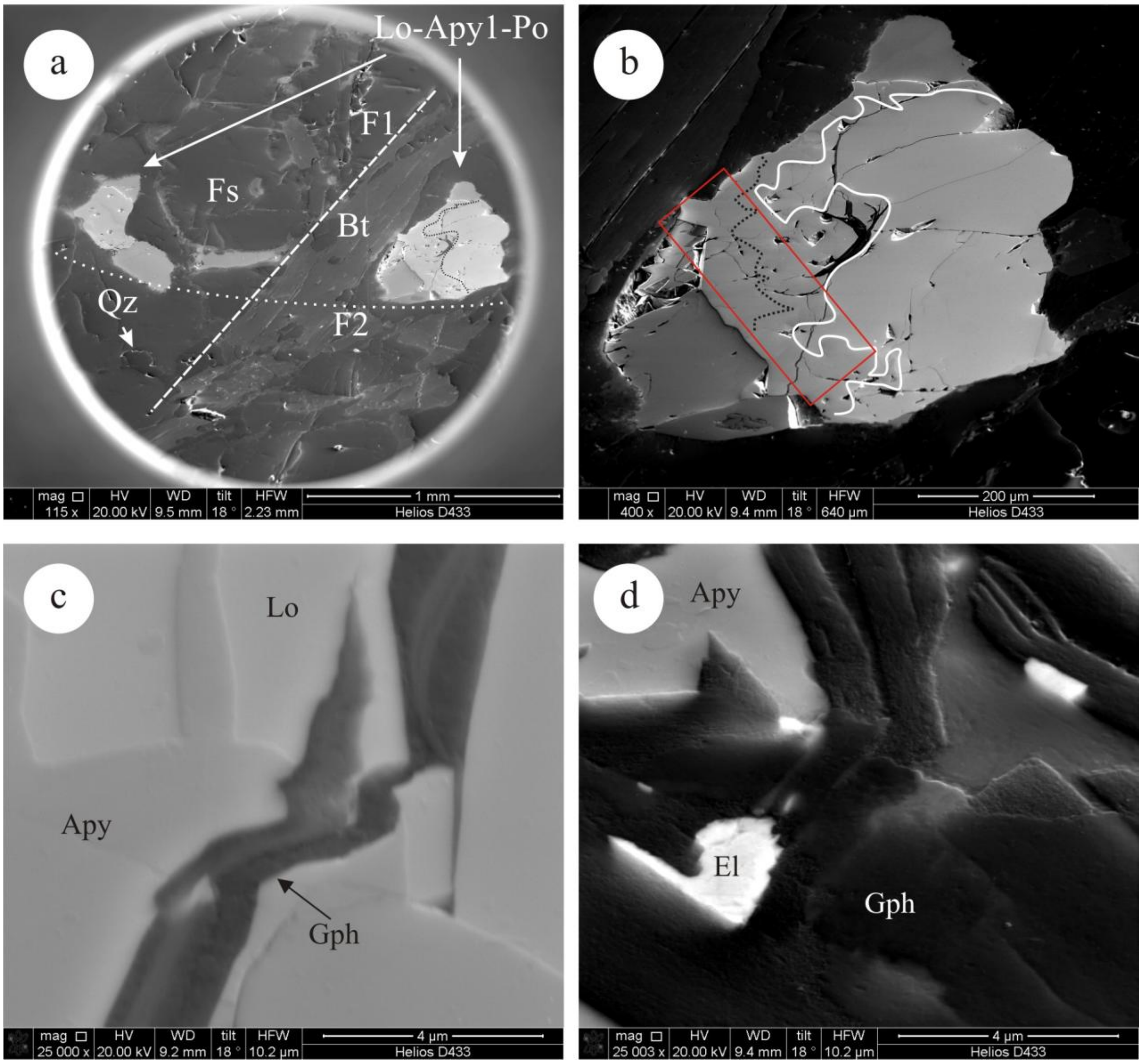
a
Lo-Apy1-Po
F1
Fs
Bt
Qz
F2
mag □ 115 x
HV 20.00 kV
WD 9.5 mm
tilt 18 °
HFW 2.23 mm
1 mm
Helios D433
b
mag □ 400 x
HV 20.00 kV
WD 9.4 mm
tilt 18 °
HFW 640 µm
200 µm
Helios D433
c
Lo
Apy
Gph
mag □ 25 000 x
HV 20.00 kV
WD 9.2 mm
tilt 18 °
HFW 10.2 µm
4 µm
Helios D433
d
Apy
El
Gph
mag □ 25 003 x
HV 20.00 kV
WD 9.4 mm
tilt 18 °
HFW 10.2 µm
4 µm
Helios D433

Figure 22

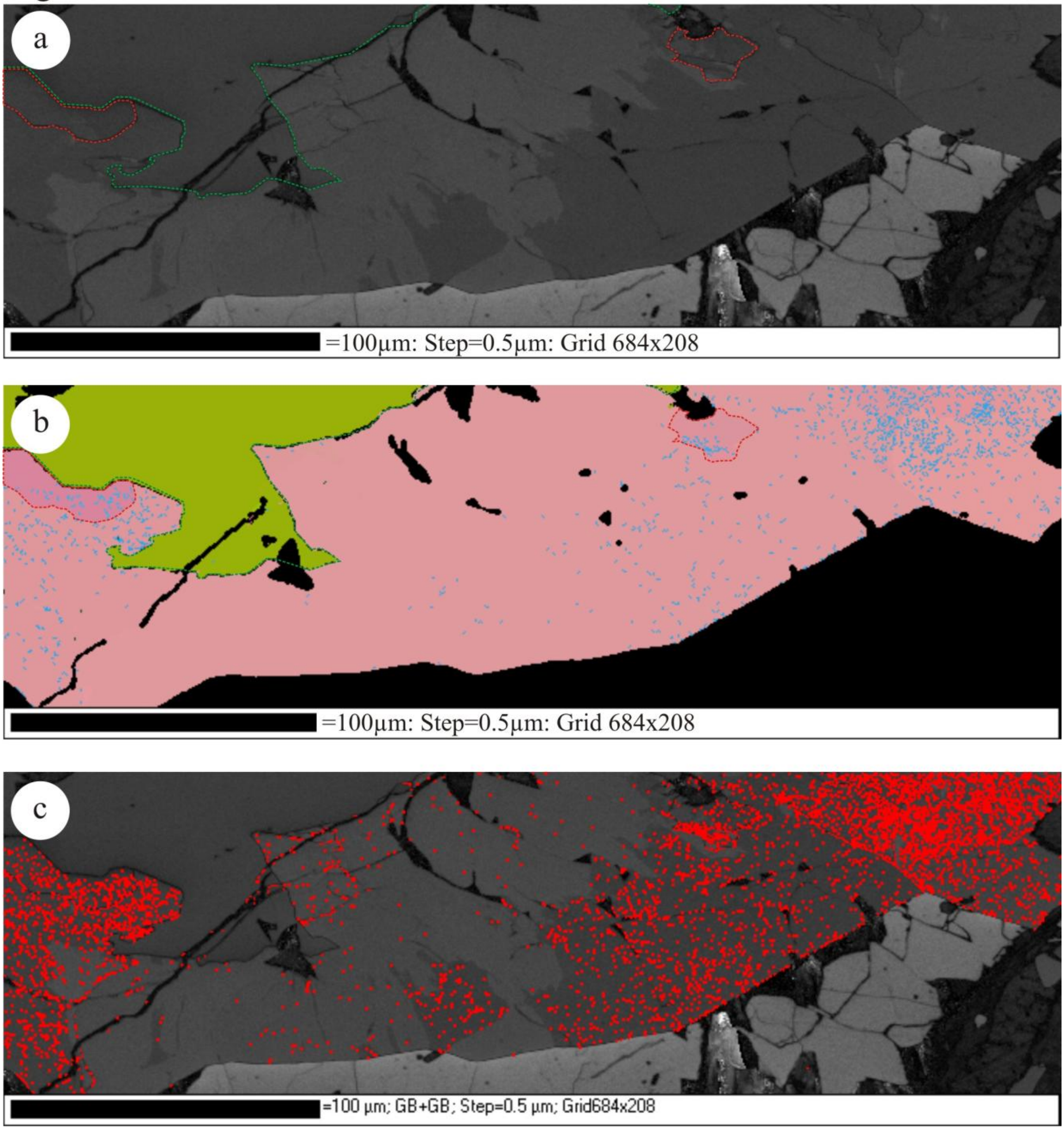
a
=100µm: Step=0.5µm: Grid 684x208
b
=100µm: Step=0.5µm: Grid 684x208
c
=100 µm; GB+GB; Step=0.5 µm; Grid684x208

Figure 23

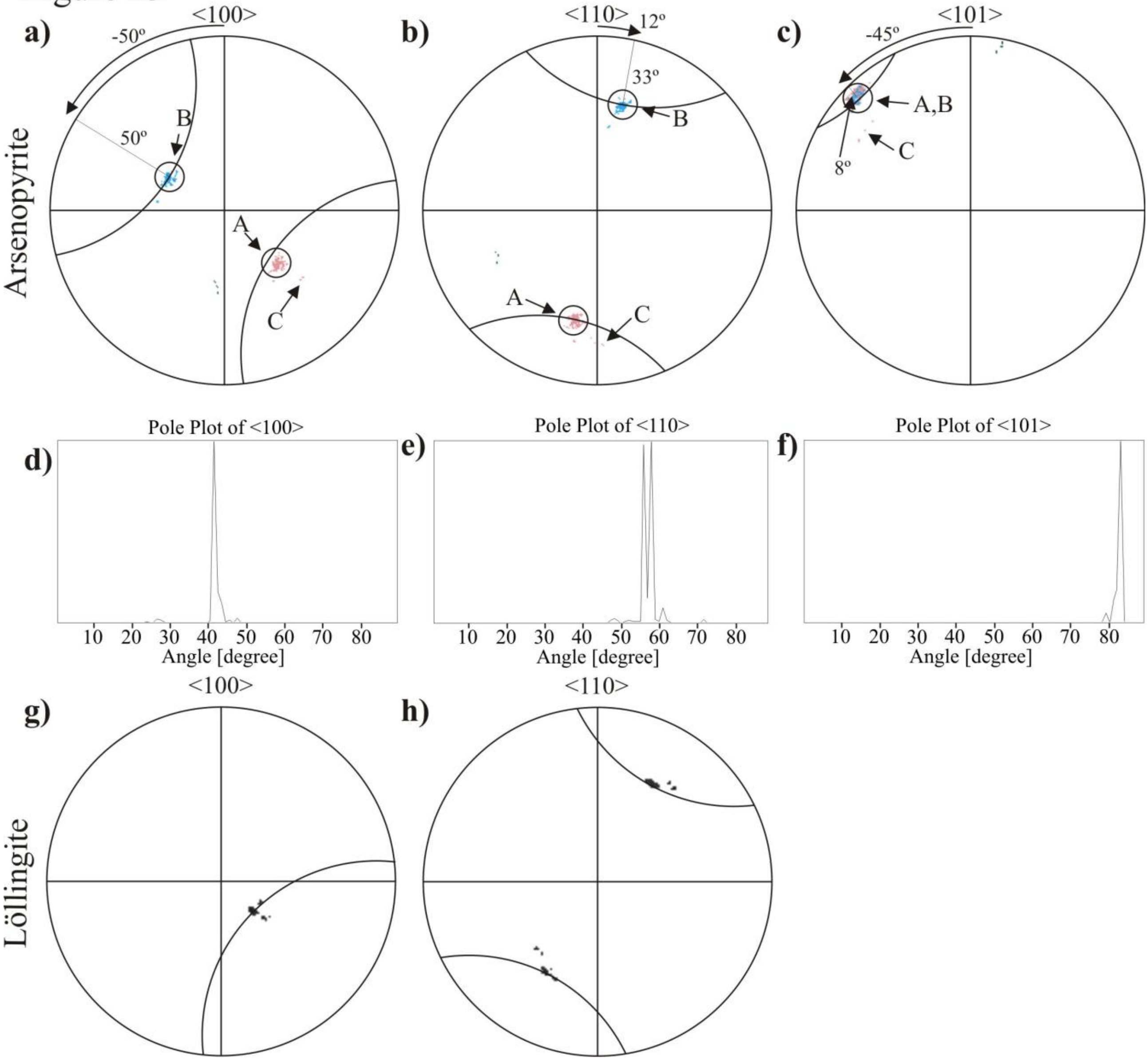

a)
b)
c)
Arsenopyrite
<100>
-50º
50º
B
A
C
<110>
12º
33º
B
A
C
<101>
-45º
A,B
C
8º
d)
Pole Plot of <100>
10 20 30 40 50 60 70 80
Angle [degree]
e)
Pole Plot of <110>
10 20 30 40 50 60 70 80
Angle [degree]
f)
Pole Plot of <101>
10 20 30 40 50 60 70 80
Angle [degree]
g)
<100>
h)
<110>
Löllingite

Figure 24

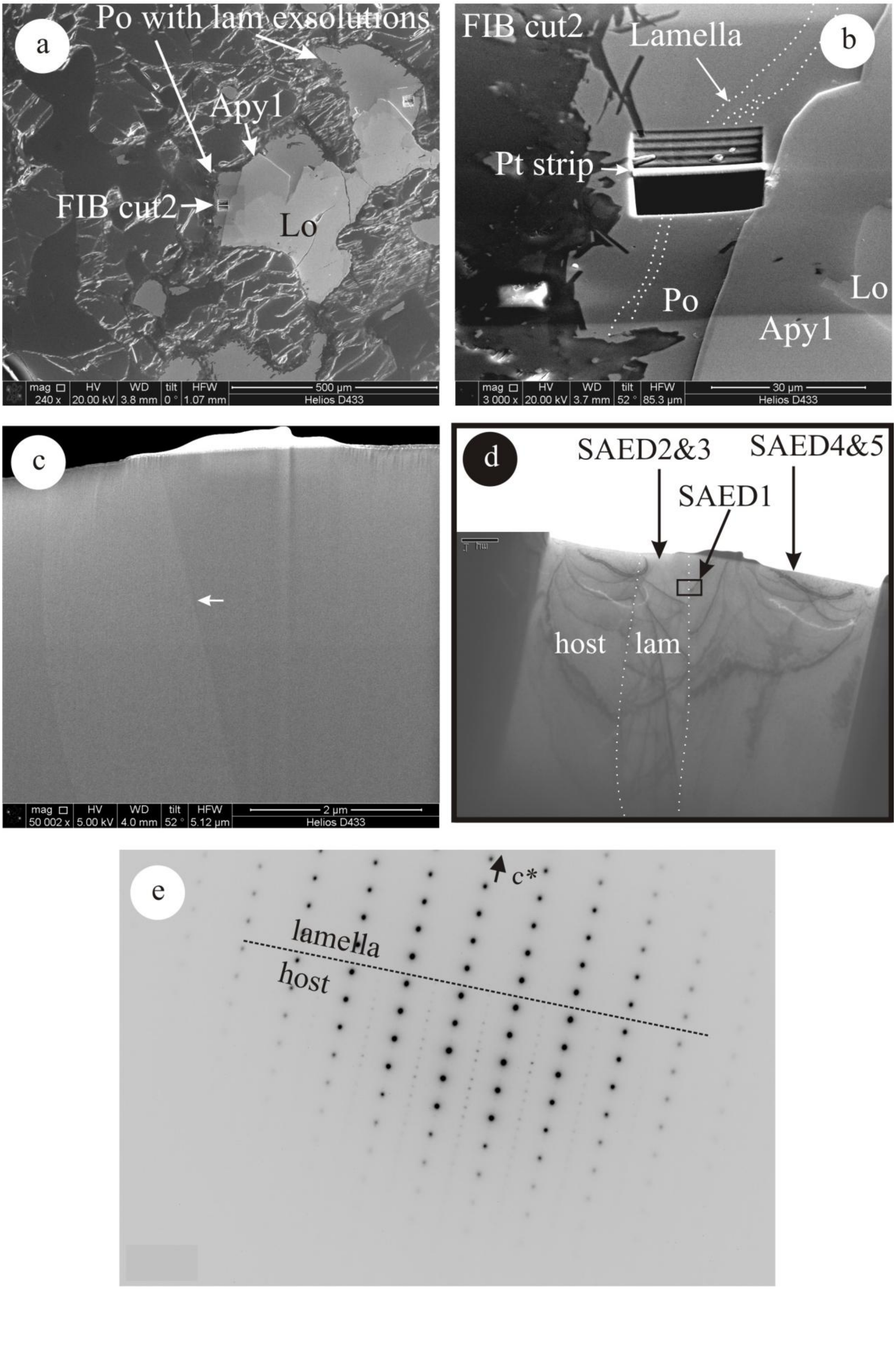

a
Po with lam exsolutions
Apy1
FIB cut2
Lo
mag □ 240 x
HV 20.00 kV
WD 3.8 mm
tilt 0 °
HFW 1.07 mm
500 µm
Helios D433
b
FIB cut2
Lamella
Pt strip
Po
Lo
Apy1
mag □ 3 000 x
HV 20.00 kV
WD 3.7 mm
tilt 52 °
HFW 85.3 µm
30 µm
Helios D433
c
mag □ 50 002 x
HV 5.00 kV
WD 4.0 mm
tilt 52 °
HFW 5.12 µm
2 µm
Helios D433
d
SAED2&3
SAED4&5
SAED1
host
lam
e
c*
lamella
host

Figure 25

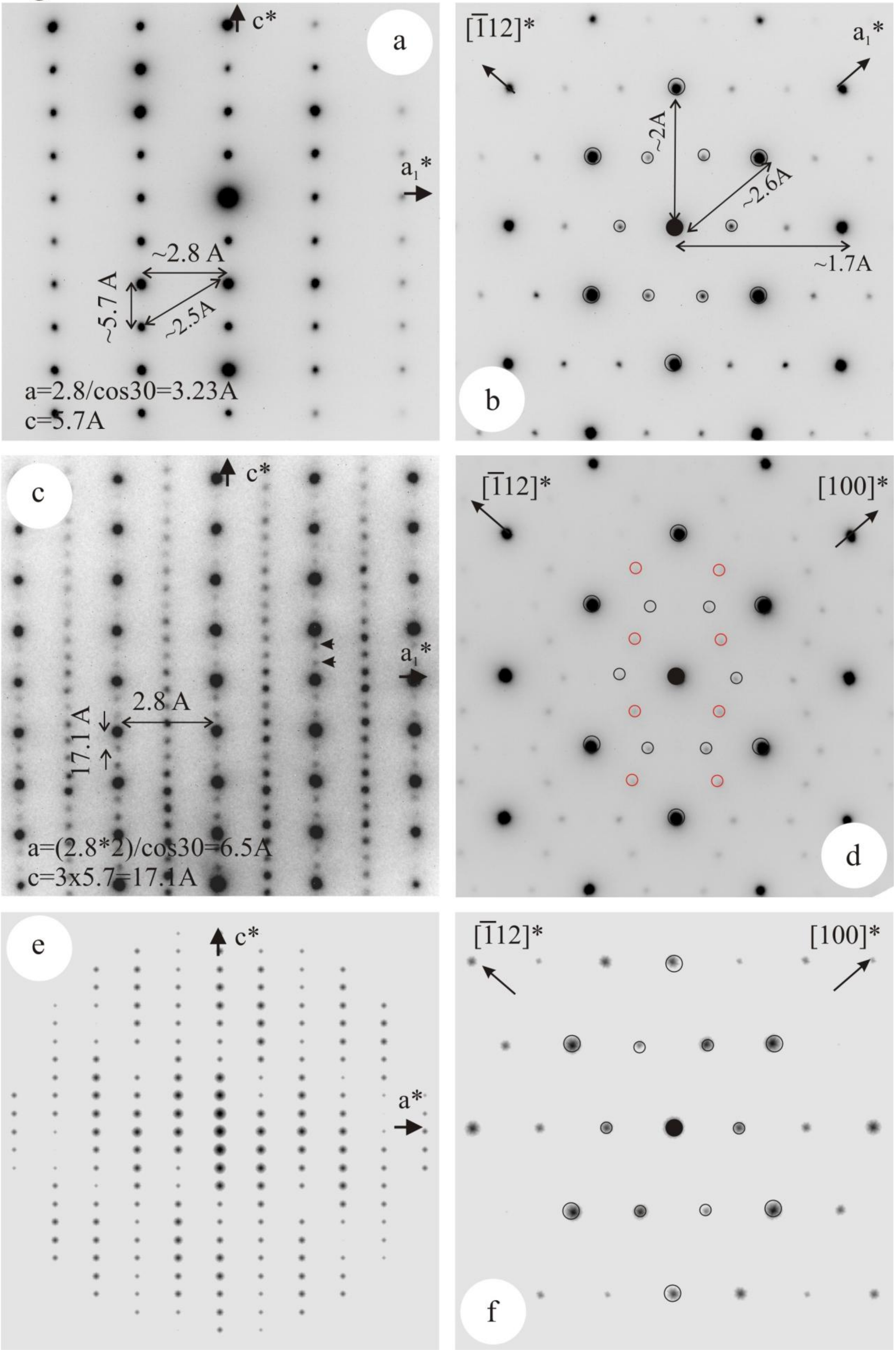
a
c*
a$_1$*
~2.8 A
~5.7 A
~2.5A
a=2.8/cos30=3.23A
c=5.7A
b
[$\bar{1}$12]*
a$_1$*
~2A
~2.6A
~1.7A
c
c*
a$_1$*
2.8 A
17.1 A
a=(2.8*2)/cos30=6.5A
c=3x5.7=17.1A
d
[$\bar{1}$12]*
[100]*
e
c*
a*
f
[$\bar{1}$12]*
[100]*

Figure 26

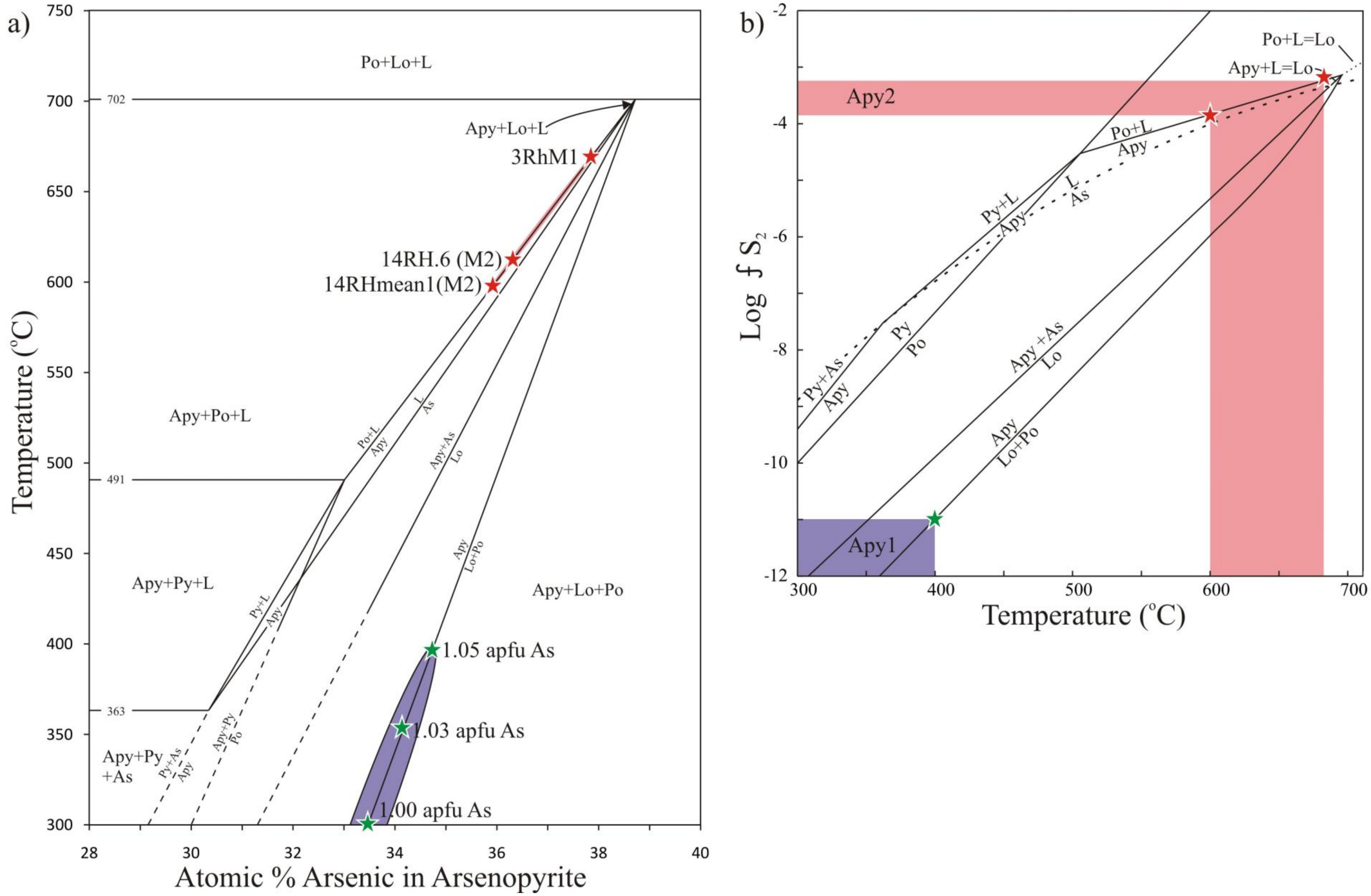

a)
Po+Lo+L
Apy+Lo+L
3RhM1
14RH.6 (M2)
14RHmean1(M2)
Apy+Po+L
Apy+Py+L
Apy+Lo+Po
Apy+Py
+As
1.05 apfu As
1.03 apfu As
1.00 apfu As
702
491
363
Temperature (°C)
Atomic % Arsenic in Arsenopyrite
b)
Po+L=Lo
Apy+L=Lo
Apy2
Apy1
Log ƒ S2
Temperature (°C)

Figure 27

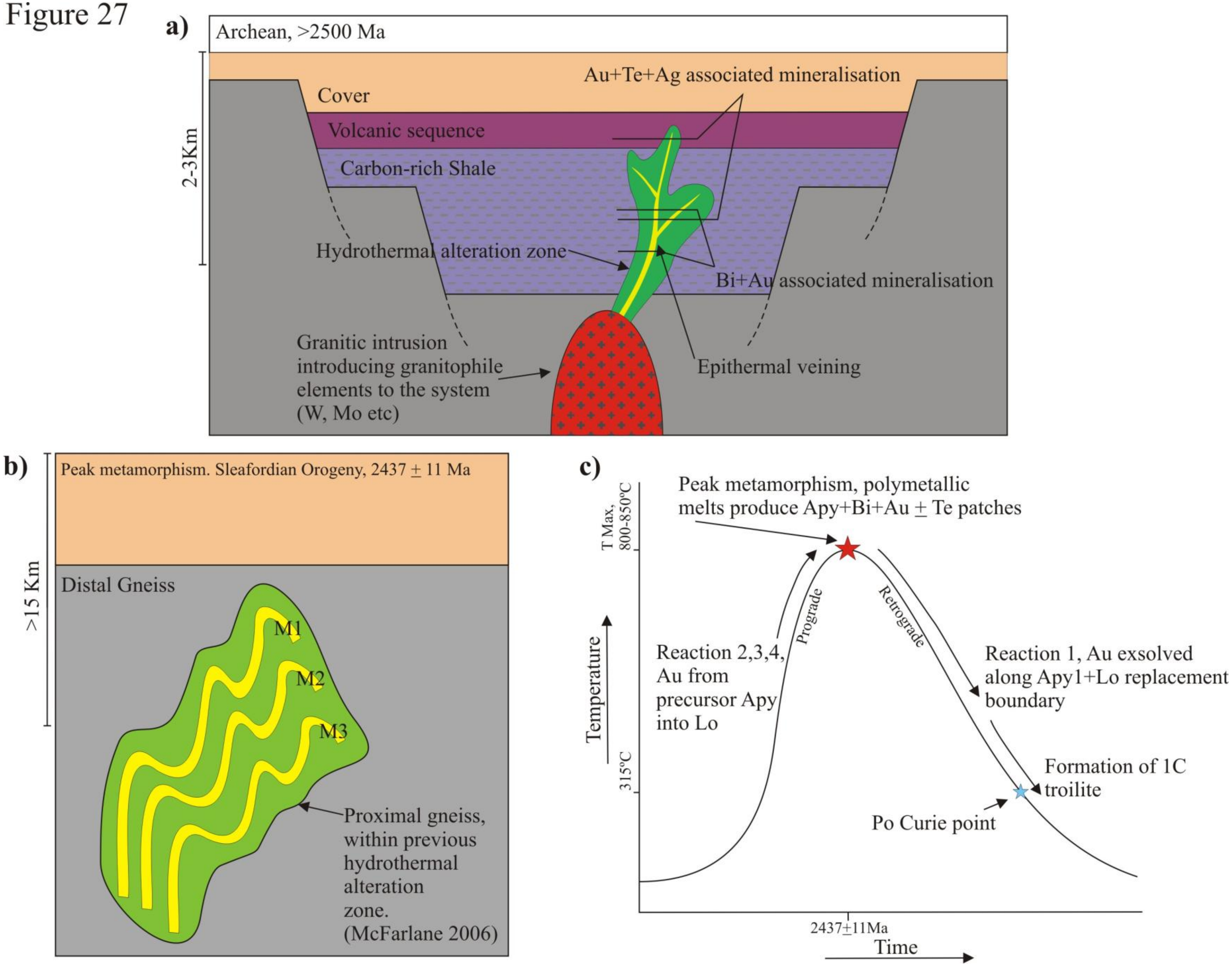
a)
Archean, >2500 Ma
2-3Km
Au+Te+Ag associated mineralisation
Cover
Volcanic sequence
Carbon-rich Shale
Hydrothermal alteration zone
Bi+Au associated mineralisation
Granitic intrusion introducing granitophile elements to the system (W, Mo etc)
Epithermal veining
b)
Peak metamorphism. Sleafordian Orogeny, 2437 ± 11 Ma
>15 Km
Distal Gneiss
M1
M2
M3
Proximal gneiss, within previous hydrothermal alteration zone. (McFarlane 2006)
c)
Peak metamorphism, polymetallic melts produce Apy+Bi+Au ± Te patches
T Max, 800-850°C
315°C
Temperature
Prograde
Retrograde
Reaction 2,3,4, Au from precursor Apy into Lo
Reaction 1, Au exsolved along Apy1+Lo replacement boundary
Formation of 1C troilite
Po Curie point
2437±11Ma
Time

Table 1. Key to abbreviations used

Rocks

Le	Leucosome
Me	Melanosome
Ms	Mesosome (fine-banded Me & Le)

Gangue minerals

Ap	Apatite
Bt	Biotite
Cor	Cordierite
Fs	Feldspar
Gah	Gahnite
Gar	Garnet
Gph	Graphite
Mon	Monazite
Qz	Quartz
Rut	Rutile
Zr	Zircon

Opaque minerals

Apy	Arsenopyrite
Au	Native gold
Bi	Native Bismuth
Cob	Cobaltite
Cpy	Chalcopyrite
El	Electrum
Gn	Galena
Grk	Greenockite
Hed	Hedleyite
Hs	Hessite
Ilm	Ilmenite
Lo	Löllingite
Mld	Maldonite
Moly	Molybdenite
Pn	Pentlandite
Po	Pyrrhotite
Pz	Petzite
Sch	Scheelite
Sp	Sphalarite
Vol	Volynskite

Table 2. Sample description

Sample ID/ location	Lithology	Gangue Minerals	Ore minerals	Minor/trace ore minerals	Au association	Study methods		
						SEM	EPMA	LA-ICPMS
840m, M2								
Rh1	Melanosome	Bt>Fs>Qz,	Po, Apy, Lo	Gph	**El, Hs, Bi3Te2**	X	X	X
Rh2	Leucosome	Qz>Fs>Bt	Po, Lo, >>Apy	Gph	**El**	X	X	
Rh3	Melanosome	Bt>Fs>Qz	Po, Apy, Lo	Cp, Gph				
Rh4	Leucosome	Qz>Fs	Po	Sp		X		
Rh5	Melanosome	Bt>Qz>Fs	Po, Apy	Cp, Gph				
Rh6	Leucosome	Fs>Qz>Bt	Po, Apy	Cp, Gph				
*Rh7	Melanosome	Fs>Qz>Bt	Po, Apy, Lo	Gph, Cp	**El, Hs**	X	X	X
Rh8	Leucosome	Qz>Fs>Bt>Gar	Po, Apy, Lo	Gph, Gn	**El**	X	X	X
800m right, M2								
Rh20	boundary Me/Le	Bt>Fs>Qz	Po, Apy, Lo	Gph	**El**	X	X	X
Rh21	boundary Me/Le	Bt>Fs>Qz	Po, Apy	Gph, Cp				
Rh22	boundary Me/Le	Qtz>Fs>Bt	Po, Apy, Lo	Cp				
Rh23	Coarse Gar, Me/Le	Fs>Gar>Qz>Bt	Po	Gph, Cp				
760m right cut, M2								
Rh14	Msesosome	Bt>Qz>Fs>>Gt	Po, Apy	Grk, Mob, Gph	**Hs, El**	X	X	
Rh15	Msesosome	Fs>Qz>Bt, Gah, Cor	Po, Apy, Lo	Cp, Sp-Grk, Ferb?	**El**	X	X	
Rh16	Melanosome	Qts>Fs>Bt>Gar, Ap	Po, Apy, Lo		**Hs, El**	X	X	X
Rh17	boundary Me/Le	Fs>Qz>Gar,Bt,	Po, Apy, Lo	Gn, Mob	**Hs, El, Pz, Vol**	X	X	X
Rh18	Le within Me	Bt>Fs>Qz>Gar	Po, Apy, Lo	Cp, Gph				
Rh19	Late pegmatite in Le	Qz>Fs>Bt	Po, Apy, Lo	Mob, >>Gph	**El, Hs**	X		
760 rise, oreshoot M3								
Rh13	Le, x-cutting fol	Qtz>Fs>>Bt>>Ap	Po, Apy	Gn, Sp		X		
600m, M2								
Ch1a	Po-rich Le, Gar	Qtz>Fs>Bt	Po			X		
Ch1b	at boundary Me	Qtz>Fs>Bt	Po>> Lo			X	X	
580m access (between M1 and M2)								
Rh9	boundary Me/Le	Qz>Fs>Bt	Po, Apy, Lo	Cob, Pn, Gph		X	X	
Rh10	boundary Me/Le	Qz>Fz>Bt>>Gar	Po, Apy, Lo	Gn		X		
Rh11	Late pegmatite in Ms	Qz>Fs>Bt>Gar	Po, Apy, Lo			X		
560m, M2								
**Ch13a	Apy-rich Le	Fs>Qz>Bt	Po, Apy, Lo	Cp, Sch	**Hs, El**	X	X	X
Ch13b		Qz>Fs>Bt	Po, Apy, Lo	Mob	**Hs, El**	X		
Ch13c		Qz>Fs>Bt>Gar	Po, Lo, Apy	Sch		X		
Ch18a	Po-rich, Me/Le	Qz>Fs>Bt	Po, Apy, Lo	Mob	**Hs, El**	X	X	X
Ch18b	x-cutting fol	Qz>Fs>Bt	Po, Apy, Lo			X		
Ch18c		Qz>Fs>Bt	Po, Apy	Cp	**Hs, El**	X		
420m, M1								
Ch3	Gar, boundary Me/Le	Qz>Fs>Bt, Gar	Po, Apy, Lo	Pn, Mob, Gph, Cp, Cob	**El**	X	X	
420m M2								
Ch8a	Po specks boundary Me/Le , x-cutting fol	Qz>Fs>Bt	Po, Lo>Apy	Cp	**El**	X	X	X
Drillcore high-grade ore								
Chal1		Qz>Fs>Bt	Po, Lo, Apy	Cp	**Au, Mld, Bi, Hed**	X	X	X
Chal2		Qz>Fs>Bt>>Cor	Po, Apy, Lo	Cp	**Au, Mld, Bi**	X		
Chal10		Qz>Fs>Bt	Po, Apy, Lo	Cp	**Au, Mld, Bi, Hed**	X	X	X

x-cutting fol: crosscutting foliation

Zr, Mon, Ilm, Ru present in all samples

* sample used for EBSD; ** sample used for FIB-TEM

Table 3. Summary of electron microprobe data for arsenopyrite

	840m (M2)							800m (M2)		760m (M2)				
	Apy 1													
	1RH		2RH	7RH	7RH.9	7RH	8RHp3	20RH	20RHl3.3	16RH		17RH	17RH.4	17RH
	mean1	mean2	mean	mean1		mean2		mean		mean1	mean2	mean1		mean2
	n=5	n=8	n=6	n=4		n=5		n=5		n=9	n=10	n=4		n=2
Cu	0.01	0.02	<mdl	<mdl	0.02	0.01	0.02	0.01	0.02	0.05	0.02	0.01	0.01	<mdl
Mn	0.01	0.01	0.01	0.01	0.00	0.02	0.01	0.03	0.02	0.01	0.01	0.01	<mdl	0.01
Fe	33.80	33.37	34.01	33.15	33.52	33.76	33.00	33.10	33.34	33.48	33.06	31.98	31.28	28.94
Co	0.21	0.33	0.12	0.41	0.30	0.24	0.55	0.41	0.27	0.61	0.59	1.49	1.80	4.40
Ni	0.03	0.29	0.03	0.17	0.09	0.06	0.52	0.24	0.08	0.05	0.21	0.33	1.46	0.45
Sb	0.02	0.02	0.01	0.02	<mdl	0.01	0.01	0.01	<mdl	0.02	0.02	0.02	<mdl	0.02
As	46.05	47.01	46.19	47.15	46.70	46.84	46.77	47.36	46.82	46.13	47.01	47.04	44.18	44.01
S	19.40	18.39	19.08	18.48	18.80	18.72	18.73	18.03	18.22	19.15	18.69	18.60	20.63	19.73
Se	0.37	0.34	0.33	0.34	0.48	0.35	0.32	0.35	0.36	0.33	0.37	0.39	0.36	0.38
Total	**99.92**	**99.76**	**99.77**	**99.74**	**99.91**	**100.01**	**99.93**	**99.54**	**99.13**	**99.83**	**99.97**	**99.87**	**99.72**	**97.94**
Formulae, calculated to 3 a.p.f.u														
Cu	0.000	0.000	-	-	0.000	0.000	0.001	0.000	0.001	0.001	0.001	0.000	0.000	-
Mn	0.000	0.000	0.000	0.000	0.000	0.000	0.000	0.001	0.001	0.000	0.000	0.000	-	0.000
Fe	0.990	0.988	1.000	0.982	0.988	0.994	0.973	0.986	0.994	0.983	0.975	0.945	0.907	0.859
Co	0.006	0.009	0.003	0.012	0.008	0.007	0.015	0.012	0.008	0.017	0.017	0.042	0.049	0.124
Ni	0.001	0.008	0.001	0.005	0.002	0.002	0.014	0.007	0.002	0.002	0.006	0.009	0.040	0.013
Sum metals	**0.997**	**1.006**	**1.004**	**0.998**	**0.999**	**1.004**	**1.004**	**1.006**	**1.005**	**1.003**	**0.998**	**0.997**	**0.997**	**0.997**
As	1.005	1.038	1.012	1.041	1.026	1.028	1.028	1.052	1.041	1.010	1.034	1.037	0.954	0.974
Sb	0.000	0.000	0.000	0.000	-	0.000	0.000	0.000	-	0.000	0.000	0.000	-	0.000
Sum (As+Sb)	**1.006**	**1.038**	**1.012**	**1.041**	**1.026**	**1.029**	**1.028**	**1.052**	**1.041**	**1.010**	**1.034**	**1.037**	**0.954**	**0.975**
S	0.990	0.949	0.977	0.953	0.965	0.960	0.962	0.935	0.946	0.980	0.960	0.958	1.042	1.021
Se	0.008	0.007	0.007	0.007	0.010	0.007	0.007	0.007	0.008	0.007	0.008	0.008	0.007	0.008
Sum (S+Se)	**0.997**	**0.956**	**0.984**	**0.961**	**0.975**	**0.968**	**0.969**	**0.943**	**0.954**	**0.986**	**0.968**	**0.966**	**1.049**	**1.029**

	600m (M2)	560m (M2)		420m (M1)	420m (M2)		Drillcore			840m (M2)	760m (M2)			560m (M2)	420m (M1)
	Apy 1									Apy2					
	1bCH3	13aCH	18aCH	3CH.4	8aCH		1Chal	10Chal		1RH	14RH		14RH.6	9RH	3CH
		mean	mean		mean1	mean2	mean	mean1	mean2	mean	mean1	mean2		mean	mean
		n=14	n=3		n=2	n=4	n=10	n=8	n=3	n=3	n=2	n=2		n=3	n=3
Cu	0.01	0.03	0.01	0.02	0.02	0.02	0.01	0.03	0.03	0.01	0.02	0.01	<mdl	0.02	0.01
Mn	0.01	0.01	0.00	0.01	0.01	0.01	0.01	0.01	0.01	0.01	0.02	0.01	<mdl	0.01	0.01
Fe	29.13	34.24	32.56	27.47	33.68	33.44	33.74	33.91	33.65	33.59	26.11	31.91	28.60	28.09	25.77
Co	4.37	0.07	1.51	6.90	0.21	0.34	0.18	0.18	0.21	0.27	6.54	1.69	1.45	5.57	3.90
Ni	1.62	0.04	0.20	0.85	0.06	0.23	0.06	0.05	0.14	0.16	0.87	0.64	3.30	1.50	2.90
Sb	0.08	0.01	0.03	<mdl	0.02	<mdl	0.01	0.02	0.02	0.02	<mdl	<mdl	0.01	<mdl	<mdl
As	48.02	46.57	46.90	45.39	46.05	47.36	46.72	46.87	46.98	46.53	49.49	46.07	49.04	46.72	49.98
S	17.82	19.24	18.83	19.42	19.22	18.24	18.92	18.93	18.75	18.90	17.06	19.59	17.10	18.44	16.14
Se	0.39	0.32	0.33	0.39	0.28	0.34	0.34	0.32	0.36	0.35	0.34	0.30	0.37	0.33	0.36
Total	**101.44**	**100.51**	**100.36**	**100.44**	**99.54**	**99.99**	**99.99**	**100.32**	**100.16**	**99.84**	**100.43**	**100.22**	**99.86**	**100.67**	**99.07**
Formulae, calculated to 3 a.p.f.u															
Cu	0.000	0.001	0.000	0.000	0.001	0.000	0.000	0.001	0.001	0.00	0.000	0.000	-	0.001	0.000
Mn	0.000	0.000	0.000	0.000	0.000	0.000	0.000	0.000	0.000	0.00	0.001	0.000	-	0.000	0.000
Fe	0.857	0.999	0.956	0.802	0.991	0.990	0.992	0.994	0.990	0.99	0.783	0.931	0.860	0.826	0.790
Co	0.122	0.002	0.042	0.191	0.006	0.010	0.005	0.005	0.006	0.01	0.186	0.047	0.041	0.155	0.113
Ni	0.045	0.001	0.005	0.024	0.002	0.007	0.002	0.001	0.004	0.00	0.025	0.018	0.094	0.042	0.084
Sum metals	**1.025**	**1.003**	**1.004**	**1.017**	**0.999**	**1.007**	**1.000**	**1.002**	**1.001**	**1.002**	**0.995**	**0.996**	**0.996**	**1.024**	**0.988**
As	1.005	1.013	1.027	0.988	1.010	1.045	1.024	1.025	1.030	1.02	1.107	1.002	1.100	1.024	1.142
Sb	0.000	0.000	0.000	-	0.000	-	0.000	0.000	0.000	0.00	-	-	0.000	-	-
Sum (As+Sb)	**1.006**	**1.013**	**1.027**	**0.988**	**1.010**	**1.045**	**1.024**	**1.025**	**1.031**	**1.022**	**1.107**	**1.002**	**1.100**	**1.024**	**1.142**
S	0.990	0.978	0.963	0.987	0.985	0.941	0.969	0.967	0.961	0.97	0.892	0.996	0.896	0.944	0.862
Se	0.008	0.007	0.007	0.008	0.006	0.007	0.007	0.007	0.008	0.01	0.007	0.006	0.008	0.007	0.008
Sum (S+Se)	**0.997**	**0.984**	**0.970**	**0.995**	**0.991**	**0.948**	**0.976**	**0.973**	**0.968**	0.98	**0.899**	**1.002**	**0.904**	**0.951**	**0.869**

Apy: arsenopyrite, Po: pyrrhotite. Apy1 - formed by replacement of Lo, Apy2 - Idiomorph grains in Po

Table 4. Summary of electron microprobe data for löllingite

	840m (M2)					800m (M2)	760m (M2)			560m (M2)		420m (M1)	420m (M2)
	1RH	1rh19	**2RH**	**7RH**	**8RH**	**20RH**	14RH2	**16RH**		**13aCH**	18ach14	3ch5	**8aCH**
	mean		mean	mean	mean	mean		mean1	mean2	mean			mean
	n=6		n=14	n=5	n=6	n=5		n=13	n=10	n=23			n=5
Cu	0.03	0.01	0.01	0.01	0.01	0.01	0.01	0.01	0.01	0.01	0.02	<mdl	0.01
Mn	<mdl	0.02	0.01	<mdl	0.01	<mdl	0.03	0.01	0.01	0.01	<mdl	0.03	0.00
Fe	26.07	23.83	26.97	25.35	26.26	26.12	22.37	25.61	23.22	27.19	20.64	18.56	25.60
Co	0.46	0.76	0.31	0.71	0.50	0.50	1.81	0.70	1.11	0.15	3.30	3.75	0.52
Ni	1.24	3.46	0.57	1.46	0.92	1.32	3.44	1.53	3.44	0.66	4.05	5.36	1.69
Sb	0.02	0.04	0.01	0.02	0.02	<mdl	<mdl	0.02	0.02	0.01	<mdl	<mdl	0.02
As	70.00	69.92	70.05	70.15	70.16	69.91	71.46	70.44	70.05	70.58	70.15	71.13	70.48
S	1.45	1.34	1.50	1.35	1.28	1.49	0.87	1.18	1.56	1.29	1.15	0.75	1.12
Se	0.50	0.38	0.50	0.46	0.55	0.48	0.49	0.52	0.53	0.53	0.61	0.49	0.49
Total	**99.78**	**99.75**	**99.93**	**99.51**	**99.70**	**99.84**	**100.48**	**100.02**	**99.96**	**100.43**	**99.92**	**100.08**	**99.95**
Formulae, calculated to 3 a.p.f.u													
Cu	0.001	0.000	0.000	0.000	0.000	0.000	0.000	0.000	0.000	0.000	0.000	-	0.000
Mn	-	0.001	0.000	-	0.000	-	0.001	0.000	0.000	0.000	-	0.001	0.000
Fe	0.945	0.865	0.975	0.923	0.954	0.945	0.813	0.929	0.840	0.980	0.752	0.680	0.930
Co	0.016	0.026	0.011	0.024	0.017	0.017	0.062	0.024	0.038	0.005	0.114	0.130	0.018
Ni	0.043	0.120	0.020	0.051	0.032	0.045	0.119	0.053	0.119	0.023	0.141	0.187	0.058
Total Metals	**1.004**	**1.012**	**1.005**	**0.999**	**1.004**	**1.008**	**0.996**	**1.007**	**0.998**	**1.009**	**1.007**	**0.998**	**1.007**
As	**1.891**	**1.893**	**1.887**	**1.904**	**1.900**	**1.886**	**1.936**	**1.905**	**1.890**	**1.897**	**1.905**	**1.941**	**1.909**
Sb	0.000	0.001	0.000	0.000	0.000	-	-	0.000	0.000	0.000	-	-	0.000
S	0.092	0.085	0.095	0.085	0.081	0.094	0.055	0.074	0.098	0.081	0.073	0.048	0.071
Se	0.013	0.010	0.013	0.012	0.014	0.012	0.013	0.013	0.014	0.013	0.016	0.013	0.013
S(+Se)	0.104	0.095	0.108	0.097	0.095	0.106	0.068	0.087	0.112	0.095	0.089	0.061	0.083

	Drillcore	
	1CHAL	**10CHAL**
	mean	mean
	n=5	n=9
Cu	0.02	0.02
Mn	0.02	0.01
Fe	26.10	26.28
Co	0.44	0.42
Ni	1.15	1.10
Sb	<mdl	0.01
As	70.38	70.78
S	1.41	1.37
Se	0.46	0.46
Total	**99.96**	**100.45**
Formulae, calculated to 3 a.p.f.u		
Cu	0.001	0.000
Mn	0.001	0.000
Fe	0.945	0.947
Co	0.015	0.014
Ni	0.039	0.038
Total Metals	**1.000**	**1.000**
As	**1.899**	**1.902**
Sb	-	0.000
S	0.089	0.086
Se	0.012	0.012
S(+Se)	0.101	0.098

Table 5. Summary of electron microprobe data for pyrrhotite

	840m (M2)				800m (M2)	760m (M2)				600m (M2)	580m (M2)	560m (M2)	
	Host pyrrhotite (Fe1-xS)												
	1RH	**2RH**	**7RH**	**8RH**	**20RH**	14RHp7	**15RH**	**16RH**	**17RH**	1bCH2	**9RH**	**13aCH**	18aCH10
	mean	mean	mean	mean	mean		mean	mean	mean		mean	mean	
	n=2	n=11	n=2	n=7	n=9		n=5	n=13	n=9		n=11	n=13	
Cu	0.03	0.01	0.04	0.03	0.02	<mdl	<mdl	0.02	0.01	0.06	0.02	0.05	0.02
Mn	0.02	<mdl	<mdl	0.01	0.01	0.01	<mdl	<mdl	0.01	0.01	0.01	<mdl	<mdl
Fe	59.70	60.16	59.81	59.93	59.85	60.35	60.97	60.66	60.39	60.32	59.85	61.14	60.44
Co	<mdl	<mdl	0.01	0.01	<mdl	<mdl	0.01	<mdl	<mdl	<mdl	<mdl	<mdl	<mdl
Ni	0.02	0.02	0.03	0.02	0.03	0.31	0.15	0.07	0.17	0.24	0.27	0.02	0.13
As	0.03	0.02	<mdl	<mdl	0.04	0.05	0.02	0.03	0.02	0.04	0.01	0.03	0.02
Sb	0.01	0.07	0.10	0.07	0.09	0.08	0.08	0.07	0.09	0.03	0.05	0.05	0.08
S	39.01	38.96	38.70	38.70	38.47	38.82	38.74	38.67	38.80	38.74	38.46	38.71	38.82
Se	0.00	0.02	<mdl	0.01	0.01	<mdl	0.02	0.03	0.03	0.04	0.02	0.01	<mdl
Total	**98.82**	**99.26**	**98.69**	**98.78**	**98.51**	**99.61**	**99.99**	**99.54**	**99.52**	**99.49**	**98.67**	**100.02**	**99.50**
Formulae, calculated to 2 a.p.f.u													
Cu	0.000	0.000	0.001	0.000	0.000	-	-	0.000	0.000	0.001	0.000	0.001	0.000
Mn	0.000	-	-	0.000	0.000	0.000	-	-	0.000	0.000	0.000	-	-
Fe	0.935	0.939	0.939	0.940	0.942	0.940	0.948	0.946	0.942	0.941	0.941	0.950	0.943
Co	-	0.000	0.000	0.000	-	-	0.000	-	-	-	-	-	-
Ni	0.000	0.000	0.000	0.000	0.001	0.005	0.002	0.001	0.003	0.004	0.004	0.000	0.002
As	0.000	0.001	0.001	0.001	0.001	0.001	0.001	0.001	0.001	0.000	0.001	0.001	0.001
Sb	0.000	0.000	-	-	0.000	0.000	0.000	0.000	0.000	0.000	0.000	0.000	0.000
Sum metals	**0.936**	**0.941**	**0.941**	**0.942**	**0.945**	**0.946**	**0.951**	**0.949**	**0.946**	**0.946**	**0.946**	**0.952**	**0.946**
S	1.064	1.059	1.059	1.058	1.055	1.054	1.049	1.051	1.054	1.053	1.054	1.048	1.054
Se	0.000	0.000	0.000	0.000	0.000	0.000	0.000	0.000	0.000	0.000	0.000	0.000	0.000
S(+Se)	**1.064**	**1.059**	**1.059**	**1.058**	**1.055**	**1.054**	**1.049**	**1.051**	**1.054**	**1.054**	**1.054**	**1.048**	**1.054**
M/S	**0.880**	**0.888**	**0.889**	**0.891**	**0.895**	**0.898**	**0.907**	**0.902**	**0.897**	**0.898**	**0.898**	**0.908**	**0.897**

	420m (M1)	420m (M2)	Drillcore		760m (M2)			600m (M2)	580m (M2)	560m (M2)	420m (M2)	Drillcore	
	Host pyrrhotite (Fe1-xS)				Lamellar pyrrhotite (FeS)								
	3CH	**8aCH**	**1CHAL**	**10CHAL**	15RHp1	**16RH**	17RHp5	1bCH1	**9RH**	**13aCH**	8aCH12	1CHAL	**10CHAL**
	mean	mean	mean	mean		mean			mean	mean		p08	mean
	n=5	n=2	n=3	n=8		n=2			n=6	n=11			n=2
Cu	0.02	0.06	0.02	0.06	0.04	0.01	0.01	0.04	0.01	0.05	0.02	<mdl	0.05
Mn	<mdl	0.02	0.02	<mdl	<mdl	<mdl	<mdl	0.01	0.01	0.01	0.01	<mdl	<mdl
Fe	59.66	59.82	59.71	60.40	61.11	61.13	62.10	62.63	62.35	61.18	62.23	61.58	62.48
Co	0.01	<mdl	<mdl	<mdl	<mdl	<mdl	<mdl	<mdl	0.01	<mdl	<mdl	0.01	<mdl
Ni	0.34	0.05	0.02	0.02	0.15	<mdl	<mdl	<mdl	0.06	0.03	0.06	0.01	0.02
As	0.01	0.03	0.03	0.01	0.04	0.06	0.06	<mdl	0.03	0.02	<mdl	<mdl	<mdl
Sb	0.09	0.09	0.05	0.05	0.11	0.11	0.00	0.02	0.06	0.07	0.09	0.12	0.05
S	38.73	38.45	38.62	38.59	38.90	37.59	36.89	36.99	36.84	38.47	36.44	37.29	37.16
Se	0.03	<mdl	0.02	0.02	<mdl	<mdl	<mdl	<mdl	0.01	0.02	<mdl	0.02	<mdl
Total	**98.89**	**98.51**	**98.48**	**99.15**	**100.35**	**98.89**	**99.07**	**99.69**	**99.37**	**99.85**	**98.84**	**99.04**	**99.77**
Formulae, calculated to 2 a.p.f.u													
Cu	0.000	0.001	0.000	0.001	0.001	0.000	0.000	0.001	0.000	0.001	0.000	-	0.001
Mn	-	0.000	0.000	-	-	-	-	0.000	0.000	0.000	0.000	-	-
Fe	0.935	0.942	0.940	0.946	0.946	0.965	0.983	0.985	0.984	0.953	0.989	0.972	0.982
Co	0.000	-	-	-	-	-	-	-	0.000	-	-	0.000	-
Ni	0.005	0.001	0.000	0.000	0.002	-	-	-	0.001	0.000	0.001	0.000	0.000
As	0.001	0.001	0.001	0.001	0.001	0.001	0.000	-	0.001	0.001	-	-	-
Sb	0.000	0.000	0.000	0.000	0.000	0.000	0.000	0.000	0.000	0.000	0.000	0.000	0.000
Sum metals	**0.942**	**0.945**	**0.941**	**0.948**	**0.951**	**0.966**	**0.983**	**0.986**	**0.987**	**0.956**	**0.991**	**0.974**	**0.983**
S	1.058	1.055	1.059	1.052	1.049	1.033	1.017	1.014	1.013	1.044	1.009	1.026	1.017
Se	0.000	-	0.000	0.000	-	-	-	-	0.000	0.000	-	0.000	-
S(+Se)	**1.058**	**1.055**	**1.059**	**1.052**	**1.049**	**1.034**	**1.017**	**1.014**	**1.013**	**1.044**	**1.009**	**1.026**	**1.017**
M/S	**0.890**	**0.896**	**0.889**	**0.900**	**0.906**	**0.935**	**0.967**	**0.973**	**0.974**	**0.915**	**0.983**	**0.950**	**0.967**

Table 6. Electron probe microanalyses of pentlandite and cobaltite

	Cobaltite		Pentlandite		
	580m (M2)	420m (M1)	420m (M1)	560m (M2)	
Label	**9RH**	**3CH**	3CH2	9RHp5	9RHp6
	mean	mean			
	n=7	n=2			
Cu	0.01	0.04	0.04	0.01	0.01
Mn	<mdl	<mdl	0.03	0.03	<mdl
Fe	8.98	7.20	38.78	42.54	34.92
Co	18.55	20.90	6.29	2.03	2.87
Ni	9.21	7.36	19.18	20.39	28.59
Sb	<mdl	<mdl	0.02	0.03	0.02
As	44.49	44.39	<mdl	0.04	0.03
S	19.75	19.83	35.79	35.11	34.07
Se	0.31	0.30	0.03	0.04	0.04
Total	**101.31**	**100.01**	**100.16**	**100.22**	**100.56**
Formulae	calculated to 3 a.p.f.u.		calculated to 17 a.p.f.u.		
Cu	0.000	0.001	0.005	0.001	0.001
Mn	-	-	0.004	0.003	-
Fe	**0.261**	**0.212**	5.256	5.779	4.777
Co	**0.511**	**0.583**	0.808	0.262	0.373
Ni	**0.255**	**0.206**	2.474	2.636	3.722
As	**0.965**	**0.974**	-	0.004	0.003
Sb	-	-	0.001	0.002	0.001
Total M	**1.028**	**1.003**	**8.547**	**8.677**	**8.871**
S	1.001	1.017	8.450	8.309	8.119
Se	0.006	0.006	0.003	0.003	0.004
S(+Te+Se)	**1.007**	**1.023**	**8.453**	**8.313**	**8.124**

Table 7. Electron probe microanalyses of ZnS-CdS minerals

	15RH4	15RH8	15RH6	15RH7
	Cd-rich Sphalerite		Zn-rich greenockite	
Ag	0.02	<mdl	<mdl	<mdl
Cu	0.56	3.52	0.01	0.06
Pb	0.07	0.11	<mdl	0.06
Fe	9.42	11.54	6.61	6.58
Mn	0.07	<mdl	0.05	0.05
Zn	42.15	37.71	23.20	22.88
Bi	0.11	0.13	0.18	0.04
Sb	0.01	0.02	0.02	0.07
Cd	14.25	16.60	43.43	43.78
Se	0.08	0.03	<mdl	0.03
S	30.30	30.66	26.58	26.79
Total	**97.04**	**100.32**	**100.08**	**100.34**
Formulae	calculated to 2 a.p.f.u.			
Ag	0.000	-	-	-
Cu	0.009	0.057	0.000	0.001
Pb	0.000	0.001	-	0.000
Fe	**0.178**	**0.212**	**0.140**	**0.139**
Mn	0.001	-	0.001	0.001
Zn	**0.680**	**0.593**	**0.420**	**0.413**
Cd	**0.134**	**0.152**	**0.457**	**0.459**
Total M	**1.002**	1.015	1.018	1.014
Sb	0.000	0.000	0.000	0.001
Bi	0.001	0.001	0.001	0.000
Total Me	0.001	0.001	0.001	0.001
Se	0.001	0.000	-	0.000
S	**0.996**	**0.984**	**0.981**	**0.985**
Total S,Se,Te	**0.997**	**0.984**	**0.981**	**0.986**
% ZnS	**68.6**	**62.0**	**41.3**	**40.8**
% CdS	**13.5**	**15.9**	**44.9**	**45.4**
% FeS	**17.9**	**22.2**	**13.8**	**13.7**
Total	**100.0**	**100.0**	**100.0**	**100.0**

Table 8. Electron probe microanalyses of native gold, electrum, maldonite and hessite

Label	**1CHAL01**	**1CHAL4**	**1CHAL6**	**0CHAL01**	**8RH01**	**15RH1**	**15RH2**	**18aCH4**	**13aCH10**	**13aCH11**
	Native gold				Electrum					
Au	99.71	99.49	99.82	99.48	80.38	54.24	56.82	77.24	93.34	89.49
Ag	0.94	0.85	0.04	1.10	20.68	47.79	43.43	24.76	7.68	7.02
Cu	0.28	0.29	<mdl	0.23	0.02	0.31	0.27	0.04	0.23	0.24
Fe	<mdl	0.01	<mdl	<mdl	<mdl	0.21	<mdl	<mdl	<mdl	<mdl
Bi	0.39	0.21	0.54	<mdl	0.40	0.10	0.30	0.28	0.12	0.64
Te	<mdl	<mdl	<mdl	<mdl	<mdl	0.05	0.07	<mdl	0.03	0.10
Total	**101.31**	**100.85**	**100.40**	**100.80**	**101.46**	**102.69**	**100.90**	**102.32**	**101.40**	**97.50**
Formulae	calculated to 1 a.p.f.u.									
Au	**0.971**	**0.974**	**0.994**	**0.974**	**0.678**	**0.380**	**0.414**	**0.629**	**0.862**	**0.862**
Ag	**0.017**	**0.015**	**0.001**	**0.020**	**0.318**	**0.611**	**0.577**	**0.368**	**0.130**	**0.124**
Cu	0.008	0.009	-	0.007	0.000	0.007	0.006	0.001	0.007	0.007
Hg	-	0.000	-	-	-	0.001	-	-	-	-
Bi	0.004	0.002	0.005	-	0.003	0.001	0.002	0.002	0.001	0.006
Te	-	-	-	-	-	0.001	0.001	-	0.000	0.001

Label	**1CHAL5**	**18aCH1**	**18aCH2**
	Maldonite	Hessite	
Au	66.96	0.14	0.01
Ag	0.11	61.63	61.90
Cu	<mdl	0.24	0.08
Fe	<mdl	0.11	<mdl
Bi	32.85	0.12	0.05
Te	0.01	36.76	36.56
Total	**99.92**	**98.99**	**98.59**
Formulae	calculated to 3 a.p.f.u.		
Au	**2.047**	0.002	0.000
Ag	0.006	**1.981**	**1.997**
Cu	-	0.013	0.004
Hg	-	0.002	-
Bi	**0.946**	0.002	0.001
Te	0.000	**0.999**	**0.997**

Table 9. LA-ICPMS trace element data for arsenopyrite

Element	**Fe	Co	Ni	Cu	Zn	Se	Ag	In	Sn	Sb	Te	Au	Pb	Bi
Drillcore														
*1CHAL1	334866	1311	1012	13	78	38	8.4	1.7	331	7.1	11	**2128**	3.6	1456
*1CHAL3	333311	1627	754	24	<11	44	4.4	0.25	2.2	10	24	**1697**	3.9	2101
*1CHAL2	334866	1173	630	26	55	47	1.2	0.27	0.69	8.6	54	**496**	6.1	1701
*1CHAL10	333311	972	586	7.5	8.3	21	<0.53	0.2	0.67	4.9	<3.1	**31**	0.37	122
*1CHAL5	333311	1537	912	13	91	34	1.1	5.7	2556	11	9.1	**15**	18	72
1CHAL4	333311	1664	1477	11	<4.2	42	<0.38	0.32	0.64	2.9	8.6	**0.64**	<0.09	1.5
1CHAL7	333311	1640	1015	<7.4	<5.5	29	<0.57	0.32	1.2	2.8	<3.9	**<0.4**	<0.11	0.69
1CHAL														
mean n=8	**333755**	**1418**	**912**	**16**	**58**	**36**	**3.8**	**1.3**	**413**	**6.8**	**21**	**728**	**6.4**	**779**
*10CHAL2	335000	1785	1037	<8.4	20	27	0.31	0.26	0.33	2.5	18	**910**	2.4	521
*10CHAL1	335000	776	377	15	37	28	0.88	0.20	0.47	4.4	41	**548**	0.65	1521
*10CHAL4	335000	1350	901	<8.6	<9.6	64	<0.43	<0.09	<0.44	3.4	<4.3	**190**	0.90	479
*10CHAL8	335000	2428	2819	11	<9.2	31	<0.41	0.28	1.42	5.2	16	**41**	3.2	429
*10CHAL7	335000	1214	1908	<6.4	<12	32	<0.35	0.20	<0.36	0.7	2.7	**21**	<0.09	47
*10CHAL5	335000	1102	525	8.4	<6.6	49	<0.28	0.24	<0.31	2.0	5.6	**18**	<0.07	35
10CHAL3	335000	1537	940	<6.9	<9.4	52	<0.35	0.29	0.52	3.7	3.3	**<0.24**	<0.09	0.42
10CHAL6	335000	1581	541	<5.6	<6.5	22	<0.34	0.24	<0.35	1.5	<2.7	**<0.19**	0.11	0.38
10CHAL														
mean n=8	**335000**	**1427**	**1145**	**11**	**37**	**40**	**0.88**	**0.24**	**0.80**	**3.0**	**14**	**164**	**1.2**	**359**
840m M2														
1RH7	334244	2492	989	17	<5.4	42	5.2	0.27	7.1	<0.21	116	**2.9**	0.93	7.9
1RH10	334244	3503	3359	<7.4	104	44	0.98	0.35	4.6	<0.25	147	**1.8**	1.8	24
1RH3	334244	2599	2521	23	31	41	0.68	0.29	7.2	<0.29	118	**0.90**	1.4	18
1RH4	334244	2272	1040	17	28	62	0.85	0.27	8.2	<0.35	127	**0.49**	3.2	15
1RH1	334244	2453	1356	80	48	50	0.76	0.22	5.2	<0.23	318	**<0.21**	0.83	6.5
1RH														
mean n=5	**334244**	**2664**	**1853**	**34**	**53**	**48**	**1.7**	**0.28**	**6.5**	**-**	**165**	**1.5**	**1.6**	**14**
7RH4	331912	3648	1666	<5.6	<6.4	29	<0.36	0.33	<0.40	0.56	50	**0.34**	0.52	4.8
7RH10	331912	3505	1416	<5.5	<5.3	31	0.44	0.27	0.71	<0.26	14	**<0.31**	0.40	2.7
7RH3	331912	2753	1135	<6.5	276	<14	<0.37	0.25	0.52	0.33	26	**<0.23**	0.13	0.16
7RH8	331912	2459	1240	15	7.2	14	<0.36	0.25	0.71	0.34	9.5	**<0.19**	5.0	1.1
7RH														
mean n=4	**331912**	**3091**	**1364**	**15**	**141**	**25**	**0.44**	**0.28**	**0.65**	**0.41**	**25**	**0.34**	**1.5**	**2.2**
8RH1	335000	2769	1599	<9.9	35	31	<0.54	0.26	0.63	<0.36	18	**<0.37**	1.5	9.3
8RH6	335000	2290	1090	<9.4	7.6	<15	<0.44	0.18	0.78	0.32	<3.9	**<0.28**	0.36	1.2
8RH5	335000	2250	1136	<7.0	<5.8	22	0.45	0.28	0.38	<0.23	3.4	**<0.25**	0.87	2.9
8RH														
mean n=3	**335000**	**2436**	**1275**	**-**	**21**	**27**	**0.5**	**0.24**	**0.60**	**0.32**	**11**	**-**	**0.9**	**4.5**
800m M2														
20RH9	328803	1938	139	<4.52	44	13	<0.26	0.16	<0.28	0.164	11	**0.46**	0.62	7.6
20RH1	328803	2649	1600	172	<6.8	30	<0.29	0.274	<0.36	0.52	134	**<0.27**	3.0	0.91
20RH2	328803	2244	1612	<6.4	<7.18	14	<0.30	0.194	0.43	0.42	167	**<0.25**	4.7	3.3
20RH6	328803	1720	181	15	<4.49	<8.05	<0.22	0.242	0.4	0.28	16	**<0.19**	<0.07	0.69
20RH														
mean n=4	**328803**	**2137.7**	**883.03**	**94**	**44**	**19**	**-**	**0.22**	**0.42**	**0.35**	**82**	**0.46**	**2.8**	**3.1**
760m M2														
16RH8	335000	2633	1585	<9.2	351	16	1.9	0.23	1.09	<0.24	7.8	**0.51**	8.1	13
16RH5	334244	5565	305	34	<6.5	12	<0.34	0.27	<0.32	<0.22	5.5	**0.27**	<0.08	5.6
16RH4	335000	3145	1174	84	138	25	1.4	0.25	<0.41	<0.30	15	**0.24**	2.0	8.2
16RH3	335000	4369	355	26	29	11	0.64	0.27	<0.26	0.21	4.4	**0.15**	1.7	7.0
16RH1	335000	3224	893	8.3	6.6	8.3	0.69	0.22	0.15	0.08	4.2	**0.10**	1.8	5.3
16RH														
mean n=5	**334849**	**3787**	**862**	**38**	**131**	**15**	**1.1**	**0.25**	**0.62**	**0.14**	**7.5**	**0.26**	**3.4**	**7.9**
*17RH6	320019	11738	6183	6.9	6.8	30	3.2	0.25	<0.37	<0.20	74	**7.5**	4.5	38
17RH5	320019	12136	4241	8.0	<3.6	<12	1.7	0.26	<0.37	0.436	53	**0.46**	2.9	27
17RH7	320019	11396	4161	<5.7	<3.9	27	1.2	0.22	<0.37	0.29	58	**<0.23**	2.2	14
17RH														
mean n=3	**320019**	**11757**	**4861.7**	**7.4**	**6.8**	**28**	**2.1**	**0.24**	**-**	**0.36**	**61**	**4.0**	**3.2**	**27**

Table 9. LA-ICPMS trace element data for arsenopyrite (continued)

Element	**Fe	Co	Ni	Cu	Zn	Se	Ag	In	Sn	Sb	Te	Au	Pb	Bi
560m M2														
*13aCH12	345000	1634	5495	<5.4	<5.4	27	0.44	0.67	<0.92	2.0	90	**22**	<1.4	2.8
*13aCH11	345000	1309	4613	137	<3.8	25	<0.44	0.60	<1.0	1.7	91	**21**	<1.7	4.5
13ach24	345000	321	95	3.8	<4.8	30	<0.40	0.23	<0.72	0.53	27	**<2.8**	7.4	1.3
13aCH14	345000	341	116	<3.4	<2.7	25	<0.41	<0.18	<0.90	<0.60	35	**<2.6**	4.6	4.2
13aCH16	345000	653	314	<3.3	<3.9	26	<0.32	0.30	0.71	1.1	93	**<2.4**	3.5	<0.70
13aCH17	345000	366	180	<2.8	9.01	27	<0.25	0.18	<0.75	0.75	42	**<2.0**	12	7.7
13aCH13	345000	576	329	3.4	<3.0	34	<0.28	0.39	<0.67	0.96	72	**<1.8**	<1.0	<0.55
13ach21	345000	799	383	<21	<21	<73	<2.28	<0.86	<4.8	2.8	83	**<14**	9.0	12
13aCH														
mean n=8	**345000**	**750**	**1441**	**48**	**9.0**	**28**	**0.44**	**0.40**	**0.71**	**1.4**	**67**	**21**	**7.4**	**5.4**
*a18CH5	324916	11989	2980	44	18	37	6207	0.22	3.8	13	3621	**67**	8.2	86
*a18CH4	324916	23123	25646	99	<9.4	<26	7.4	0.46	2.7	1.7	63	**42**	15	37
a18CH2	324916	15182	4390	<9.1	<13	49	27	0.30	1.6	1.1	71	**0.77**	0.58	27
a18CH6	324916	3941	760	<6.4	<6.1	<14	5.2	0.13	1.4	<0.28	13	**<0.24**	6.5	4.6
a18CH														
mean n=4	**324916**	**13559**	**8443.9**	**71**	**18**	**43**	**1561**	**0.28**	**2.4**	**5.3**	**942**	**37**	**7.5**	**39**
420m M2														
*8CH3	320019	4430	13531	47	<9.0	<50	4.1	0.48	1.0	<0.80	<11	**22**	1.1	11
8CH1	320019	2631	1514	<9.7	34	<62	<1.2	0.25	<1.0	<0.79	17	**<0.80**	1.5	9.1
8CH5	320019	2148	1102	<7.2	<6.0	<30	<0.81	0.29	<0.81	<0.53	<7.0	**<0.58**	0.99	3.4
8CH6	320019	2196	1037	<8.7	6.6	<31	<0.91	0.18	<0.75	<0.53	<8.0	**<0.58**	0.29	1.2
8CH														
mean n=4	**320019**	**2851.5**	**4296.2**	**47**	**20**	**-**	**4.1**	**0.30**	**1.0**	**-**	**17**	**22**	**0.96**	**6.2**

* inclusions Au and/or Au-minerals (e.g., maldonite)
** values used for Fe from EPMA data

Table 10. LA-ICPMS trace element data for löllingite (ppm)

Element	**Fe	Co	Ni	Cu	Zn	Se	Ag	In	Sn	Sb	Te	Au	Pb	Bi
Drillcore														
H1CHAL 5	260000	3706	9742	4.3	64	20	0.18	1.3	31	4.2	43	**108**	11	377
H1CHAL 2	260000	3831	9533	0.20	0.20	19	0.12	1.5	0.40	0.61	24	**108**	0.16	0.63
H1CHAL 3	260000	3871	9870	0.12	0.81	21	0.01	1.3	0.03	0.71	21	**106**	0.00	0.70
H1CHAL 1	260000	4021	10146	0.20	0.40	13	0.01	1.4	0.02	0.41	21	**102**	0.01	0.44
H1CHAL 4	260000	3804	10568	3.3	5.3	11	0.01	1.5	0.94	0.73	20	**71**	0.54	2.1
H1CHAL 6	260000	3760	11125	1.6	24	13	0.37	3.4	534	5.2	40	**62**	3.5	85
H1CHAL														
mean n=6	**260000**	**3832**	**10164**	**1.6**	**16**	**16**	**0.12**	**1.7**	**94**	**2.0**	**28**	**93**	**2.5**	**78**
Drillcore														
*1CHAL13	262187	2710	7868	<8.8	8.45	<15	9.0	0.32	<0.52	1.2	18	**927**	3.9	34
*1CHAL15	262187	2912	9116	16	88	34	0.83	1.4	215	54	44	**594**	14	831
*1CHAL11	262187	3161	9884	13	67	21	<0.71	2.1	235	5.8	23	**202**	11	380
1CHAL12	262187	3217	8557	<9.7	<4.9	<16	<0.58	0.44	1	1.2	17	**78**	1.9	10
1CHAL14	262187	2824	7233	<7.6	<6.06	30	0.99	0.47	1.2	1.0	15	**77**	5.3	51
1CHAL6	261201	3011	7545	<7.8	<6.1	<15	<0.48	0.37	<0.64	1.7	10	**52**	<0.12	193
1CHAL8	262187	3273	9944	32	<12	18	<0.59	0.34	1.4	0.6	10	**31**	<0.14	0.38
1CHAL9	262187	3542	10467	<19	<15	<18	<0.65	0.45	0.83	0.8	9.5	**20**	<0.17	0.65
1CHAL														
mean n=8	**262064**	**3081**	**8827**	**20**	**54**	**25**	**3.6**	**0.7**	**76**	**8.2**	**18**	**248**	**7.1**	**187**
Drillcore														
10CHAL11	265000.16	3151	10251	<9.3	<9.3	23	<0.60	0.48	1.5	0.45	25	**72**	0.50	11
10CHAL9	265000.16	3316	9635	<9.6	<11	33	0.62	0.48	<0.56	0.80	33	**71**	<0.15	0.24
10CHAL10	265000.16	3534	10881	<10	<10	<16	<0.63	0.48	<0.56	0.69	20	**71**	<0.15	0.25
10CHAL12	265000.16	3214	7731	5.3	53	<7.4	<0.29	0.38	0.53	<0.21	23	**41**	0.10	0.23
10CHAL13	265000.16	2846	7436	<5.1	<5	<9.0	<0.42	0.42	0.43	0.35	22	**39**	<0.09	0.31
10CHAL														
mean n=5	**265000.16**	**3212.1**	**9186.6**	**5.3**	**53**	**28**	**0.62**	**0.45**	**0.83**	**0.57**	**24**	**59**	**0.30**	**2.5**
840m M2														
1RH6	258067.28	2326	5566	<4.0	<2.25	14	0.29	0.37	1.1	0.19	28	**89**	0.13	0.19
1RH2	258067.25	3864	7810	5.5	17	28	1858	0.20	4.7	0.18	1361	**52**	8.7	37
1RH5	258067.27	4064	14721	<9.6	6.9	<15	21	0.54	6.7	<0.30	113	**48**	0.49	2.7
1RH8	258067.3	3031	7017	<8.68	<6.7	<15	<0.49	0.38	6.1	<0.28	81	**26**	<0.14	0.16
1RH9	258067.28	3226	8390	<7.24	15	15	<0.38	0.42	5.8	0.25	89	**25**	<0.09	0.99
1RH														
mean n=5	**258067.276**	**3302.1**	**8700.6**	**5.5**	**13**	**19**	**626**	**0.38**	**4.9**	**0.20**	**334**	**48**	**3.1**	**8.3**
840m M2														
7RH7	258067.23	7254	10310	<6.8	6.8	<14	<0.44	0.42	0.58	0.48	13	**51**	<0.11	0.28
7RH2	258067.2	4902	9870	11	<7.3	<12	<0.25	0.34	0.38	0.49	19	**44**	<0.09	0.18
7RH5	258067.23	5133	14818	<7.8	26	<17	0.6	0.52	0.62	0.69	34	**34**	0.744	2.9
7RH6	258067.23	4888	14962	<8.1	<5.9	17	0.9	0.40	0.56	0.38	34	**31**	1.06	3.2
7RH1	258067.2	3181	5989	<3.4	<5.0	<14	0.2	0.80	<0.38	0.61	24	**30**	10.68	9.0
7RH9	258067.22	4672	14185	<5.7	<4.7	24	0.5	0.32	<0.45	0.39	18	**16**	1.34	1.2
7RH														
mean n=6	**258067.218**	**5004.6**	**11689**	**11**	**16**	**20**	**0.56**	**0.47**	**0.54**	**0.51**	**24**	**34**	**3.5**	**2.8**
840m M2														
8RH4	265000.13	3887	15030	14	<5.8	<16	<0.37	0.36	0.69	<0.26	8.4	**36**	0.45	1.3
8RH7	265000.09	4107	19657	<7.2	10	<12	<0.38	0.29	<0.32	0.24	5.9	**33**	<0.08	0.52
8RH2	225109.31	3487	13410	9.9	5.3	<13	<0.29	0.27	0.52	0.34	9.4	**24**	0.11	1.6
8RH3	265000	4527	12928	54	<9.0	32	3.9	0.49	1.2	<0.36	9.0	**21**	1.2	13
8RH														
mean n=4	**255027.383**	**4001.8**	**15256**	**26**	**7.8**	**32**	**3.9**	**0.36**	**0.79**	**0.29**	**8.2**	**28**	**0.59**	**4.04**

800m M2														
20RH7	260399.22	3833	11880	<4.9	<3.6	13	<0.29	0.37	0.31	<0.21	49	**45**	<0.10	0.17
20RH8	260399.25	4271	11856	<4.4	<3.4	82	248	0.29	0.50	0.36	168	**39**	5694.2	32
20RH3	260399.23	4035	12387	<6.8	<11	12	<0.26	0.36	<0.29	0.42	54	**28**	<0.08	0.13
20RH4	260399.25	3875	10962	<3.9	5.1	<8.4	<0.23	0.30	<0.27	0.31	46	**24**	<0.08	0.18
20RH5	260399.23	3697	12410	<7.2	<5.4	<13	<0.41	0.45	<0.50	0.38	52	**23**	<0.12	0.15
20RH														
mean n=5	**260399.236**	**3942.1**	**11899**	**-**	**5.1**	**36**	**248**	**0.35**	**0.41**	**0.37**	**74**	**32**	**5694.2**	**6.5**

Element	**Fe	**Co**	**Ni**	**Cu**	**Zn**	**Se**	**Ag**	**In**	**Sn**	**Sb**	**Te**	**Au**	**Pb**	**Bi**
760m M2														
16RH2	250000.36	5507	9329	8.2	2.7	0.82	0.17	0.30	2.1	0.11	13	**36**	2.2	9.6
16RH7	250000.34	6065	19614	<7.3	<4.1	<5.8	<0.23	0.31	<0.24	<0.17	17	**30**	0.22	2.4
16RH6	250000.34	5185	17259	51	13	<7.2	<0.27	0.36	0.28	<0.18	17	**29**	0.87	2.7
16RH														
mean n=3	**250000.347**	**5585.7**	**15401**	**29**	**7.6**	**0.82**	**0.17**	**0.32**	**1.21**	**0.11**	**16**	**31**	**1.1**	**4.9**
560m M2														
13ach23	275000.19	1155	5184	4.3	3.9	<16	<0.42	0.90	<0.91	1.6	96	**37**	<1.3	<0.73
13ach22	275000.19	1253	4888	7.4	5.7	<11	<0.28	0.52	<0.77	1.5	101	**33**	1.4	9.9
13aCH7	271747.94	1227	5219	<0.27	0.4	11	<0.03	0.48	0.26	1.5	86	**31**	<0.14	0.18
13aCH15	275000.19	1297	5439	<3.3	<4.78	<11	<0.36	0.53	<0.92	1.6	80	**30**	<1.04	<0.73
13aCH6	272999.41	1256	5471	<0.30	<0.34	12	0.04	0.52	0.36	1.6	93	**30**	<0.12	0.17
13aCh3	268172.31	1205	5067	<0.27	<0.28	13	<0.03	0.46	0.32	1.5	92	**28**	<0.13	0.18
13aCH5	272999.41	1181	5246	8.5	3.0	12	0.08	0.48	0.37	1.3	90	**28**	5.0	0.60
13aCh1	268172.31	1239	5034	0.56	<0.69	13	<0.03	0.51	0.23	1.6	90	**27**	<0.12	0.14
13aCH7	271747.91	1353	5893	<0.31	0.43	9.0	<0.03	0.46	0.25	1.5	58	**27**	<0.11	0.16
13aCH8	271747.94	1193	5378	<0.27	<0.40	14	<0.03	0.45	0.42	1.5	86	**26**	<0.11	0.24
13aCH10	275000.25	1222	5053	<0.25	<0.28	12	0.04	0.50	0.18	1.5	92	**26**	<0.10	0.20
13aCH6	272999.38	1392	6227	<0.33	<0.37	10	0.04	0.50	0.34	1.5	61	**25**	<0.09	0.15
13aCh2	268172.31	1146	4672	<0.19	<0.31	13	<0.02	0.48	0.27	1.4	87	**24**	<0.10	0.14
13aCH10	275000.19	1326	5571	<0.28	<0.30	11	0.04	0.48	0.17	1.4	67	**24**	<0.08	0.18
13aCH5	272999.38	1315	6020	9.6	3.2	10	0.08	0.45	0.35	1.3	58	**23**	3.8	0.51
13aCH8	271747.91	1308	6024	<0.30	<0.43	12	<0.03	0.43	0.40	1.5	60	**23**	<0.09	0.21
13aCh3	268172.28	1364	5958	<0.31	<0.30	10	<0.03	0.42	0.30	1.4	54	**22**	<0.09	0.14
13aCH9	275000.25	1172	4762	1.4	<0.29	15	0.07	0.44	0.34	1.4	81	**21**	0.99	5.8
13aCh1	268172.28	1417	6018	0.66	<0.74	10	<0.03	0.47	0.21	1.5	50	**21**	<0.08	0.11
13ach20	275000.22	987	3665	<9.0	18	<39	<1.21	0.58	<2.6	1.5	63	**20**	<4.4	15
13aCH4	268172.31	1268	5294	<0.20	<0.33	15	<0.02	0.44	0.21	1.4	91	**20**	1.2	2.4
13aCH9	275000.19	1279	5292	1.5	<0.31	13	0.08	0.42	0.33	1.4	58	**19**	0.81	5.0
13aCh2	268172.31	1304	5538	<0.22	<0.33	10	<0.03	0.44	0.24	1.3	50	**18**	<0.07	0.11
13aCH4	268172.28	1420	6124	<0.23	<0.35	12	<0.02	0.41	0.19	1.3	56	**17**	0.9	2.0
13aCH19	275000.19	629	264	7.6	<9.77	49	<0.82	<0.31	1.64	<1.06	71	**<4.2**	2.8	2.0
13aCH														
mean n=27	**271974.781**	**1236.3**	**5172**	**5**	**5.0**	**14**	**0.1**	**0.49**	**0.35**	**1.5**	**75**	**25**	**2**	**2.0**
560m M2														
a18CH1	251848.83	18354	29990	<22	<31	<19	<0.71	0.49	2.3	0.58	52	**55**	<0.17	0.5
a18CH3	251848.83	17430	33317	<9.3	19	<21	20	0.48	2.9	1.1	59	**54**	167	20
a18CH														
mean n=2	**251848.83**	**17892**	**31654**	**-**	**19**	**-**	**20**	**0.48**	**2.6**	**0.84**	**55**	**54**	**167**	**10**
420m M2														
8CH4	256512.66	3722	14425	11	<5.5	<35	<0.79	0.36	<0.76	<0.54	8.3	**33**	0.56	1.3
8CH7	256512.67	3631	15861	<9.2	<5.8	<33	<1.0	0.31	<0.88	<0.67	<8.6	**22**	0.29	2.0
8CH2	256512.64	3451	12320	<7.2	55	<40	<0.85	0.31	<0.71	<0.49	9.8	**20**	<0.24	4.1
8CH														
mean n=3	**256512.657**	**3601.6**	**14202**	**11**	**55**	**-**	**-**	**0.33**	**-**	**-**	**9.0**	**25**	**0.43**	**2.4**

* inclusions Au and/or Au-minerals (e.g., maldonite)

** values used for Fe from EPMA data

Table 11. LA-ICPMS trace element data for pyrrhotite and chalcopyrite

Element	**Fe	**Co**	**Ni**	**Cu**	**Zn**	**Se**	**Ag**	**In**	**Sn**	**Sb**	**Te**	**Au**	**Pb**	**Bi**
760m M2: Pyrrhotite														
17RH1Po	**600001**	127	1163	<26	<15	<29	<0.79	<0.14	<0.79	<0.49	<5.8	<0.46	<0.20	<0.10
17RH2Po	**600001**	129	1280	<16	25	37	1.3	<0.15	<0.99	0.59	<6.3	<0.58	0.28	0.17
17RH3Po	**600001**	127	1128	<12	<14	45	1.1	<0.10	<0.79	<0.44	9.8	<0.44	1.1	<0.09
17RH mean n=3	**600001**	**128**	**1190**	**-**	**25**	**41**	**1.2**	**-**	**-**	**0.6**	**10**	**-**	**0.68**	**0.17**
760m M2: Chalcopyrite														
17RH4Cp	**260399**	8.3	52	237820	400	38	**1.9**	**8.0**	1.7	<0.64	17	<0.69	6.6	1.4

APPENDIX

Figure A1. Mapping area of the 800m M2 ore-shoot. **(a)** Photograph showing mapping area and sample locations. **(b)** Digitised mapping showing main lithologies at the mine scale.

Figure A2. Mapping area of the 750 M2 ore-shoot. **(a)** Photograph showing mapping area and sample locations. **(b)** Digitised mapping showing main lithologies at the mine scale. **(c)** Photograph showing sulphide halos parallel to pegmatitic boudinage. **(d)** Photograph showing porphyroblastic coarse-grained garnet at the leucosome-mesosome boundary.

Figure A3. Mapping area of the 580 M2 limb. **(a)** Photograph showing mapping area and sample locations. **(b)** Digitised mapping showing main lithologies and joint planes at the mine scale. **(c)** Photograph showing two leucosomes with a secondary sub-horizontal set cross-cutting the main vertical leucosomes. **(d)** Photograph showing coarse grained porphyroblastic garnet within the leucosomes and into the melanosome.

Figure A4. Hand specimen photographs showing sulphide associations at the millimetre scale. **(a)** Extremely pyhrrhotite rich sample (CH18). **(b)** Arsenopyrite rich sample (CH13). **(c)** Very fine ptygmatically folded leucosomes within mesosome host (RH14 & 15). **(d)** Sulphide exsolution along the boundary of fine leucosomes (RH7).

Figure A5. Back-scattered electron images showing sulphide relationships within silicates. **(a)** Ore mineral patches observed at silicate grain boundaries (RH16). **(b)** Close-up image showing ore minerals within silicate host (CH13a). **(c)** Pyrrhotite and löllingite observed as single grains within porphyroblastic poikilytic garnet (RH16). **(d)** Intergrowths of Au and pyrrhotite with extensive alteration halos and trails extending from the main patch (Chal1). **(e)** Gold and arsenopyrite rich trails of blebs within quartz and feldspar (Chal10). **(f)** Biotite with quartz and graphite along the cleavage plane observed bending around central fracture (RH10) **(g)** Pyrrhotite-lollingite-arsenopyrite grain with intense reaction zone at pyrrhotite-silicate grain boundary, pyrrhotite is observed intergrown within biotite cleavages (RH20). **(h)** Gold filling biotite cleavages.

Figure A6. Back-scattered electron images showing gangue mineral associations. **(a and b)** Potassium rich feldspar showing albite exsolutions. **(a)** shows two sizes of exsolutions, outlined in green (Chal10). **(b)** shows two phases of albite exolution along different preferential orientations (RH13). **(c)** Quartz and plagioclaise symplectitc intergrowth adjacent perthitic K-feldspar (CH8a). **(d)** Biotite and quartz symplectitc intergrowth with pyrrhotite within the reaction zone (Chal2). **(e)** Ore minerals locked within poikilytic garnet (RH11). **(f)** Pyrrhotite surrounding fractured garnet within quartz (RH17). **(g)** Pyrrhotite, arsenopyrite and lollingite enclosing garnet within quartz (RH7). **(h)** Pyrrhotite surrounding garnet. Pyrrhotite can be seen in-filling fractures within the garnet (CH1). **(I and j)** Pyrrhotite grains within garnet with reaction halos surrounding. Fracturing in garnet is indicative of intense deformation (CH13).

Figure A7. Reflected-light microscope photomicrographs displaying molybdenite relationships with pyrrhotite. **(a)** Molybdenite grain perpendicular to graphite within pyrrhotite. Tellurium and chalcopyrite are observed along the margin of the molybdenite. **(b)** Molybdenite along graphite blades with pyrrhotite observed parallel.

Figure A8. Back-scattered electron images showing minor component associations. **(a and b)** Molybdenite displaying a 'kinked' pattern within pyrrhotite (CH18a). **(c and d)** idiomorphic Apy2 grain within pyrrhotite showing cobaltite exsolution (RH9). **(e)** mm scale scheelite grains associated with pyrrhotite (CH13a). **(f - I)** Scheelite observed as small rounded grains within lollingite (CH13a), **(I)** is at the boundary of arsenopyrite and lollingite however graphite lies between the scheelite grain and the arsenopyrite.

Figure A9. Reflected-light microscope photomicrographs displaying graphite along the arsenopyrite-lollingite boundary with gold in the graphite (RH7). **(a)** Pyrrhotite-lollingite-arsenopyrite grain with graphite along the Apy1-Lo boundary. **(b)** detail showing electrum within the graphite blade itself.

Figure A10. Back-scattered electron images showing Au-Bi associations. **(a)** Pyrrhotite grain with large Au-Bi mineral grains observed at the boundary (Chal10). **(b)** Au rich inclusion trails along annealed fractures cross-cutting silicate feldspar (Chal1). **(c)** Pyrrhotite and chalcopyrite patch with a large grain of Au-Bi minerals attatched, along the boundary of the Au-Bi minerals with fledspar there is a large reaction halo also with inclusions of Au-Bi minerals (Chal10). **(d)** Splays of Au-Bi minerals are observed at the boundary of a pyrrhotite and chalcopyrite patch with feldspar (Chal1)

Figure A11. Secondary electron images FIB procedure to obtain a TEM foil **(a)** Deposition of a platinum strip to protect the surface before milling. Specimen tilted at 52º **(b)** Milling a hole on both sides of the slice to be lifted. Nb. Yellow rectangle represents the milling area with arrow indicating direction of milling. Specimen tilted at 52º. **(c)** Cleaning the surface that has been milled on both sides of the slice in the area shown by the yellow rectangle. Specimen tilted at 52º. **(d)** Slice attatched to a tungsten needle by welding it with platinum. Figure also shows cutting the slice out of the pit before lifting, using a pattern as shown by the yellow rectangle. Specimen tilted at 0º. **(e)** attachment of slice onto a copper grid after lifting and transporting it with the tungsten needle, the slice is welded using platinum as shown by the pattern shown by the green rectangle. Specimen tilted at 52º. **(f)** TEM foil obtained after thinning the slice to below 100nm

Figure A1; 800m M2

a)

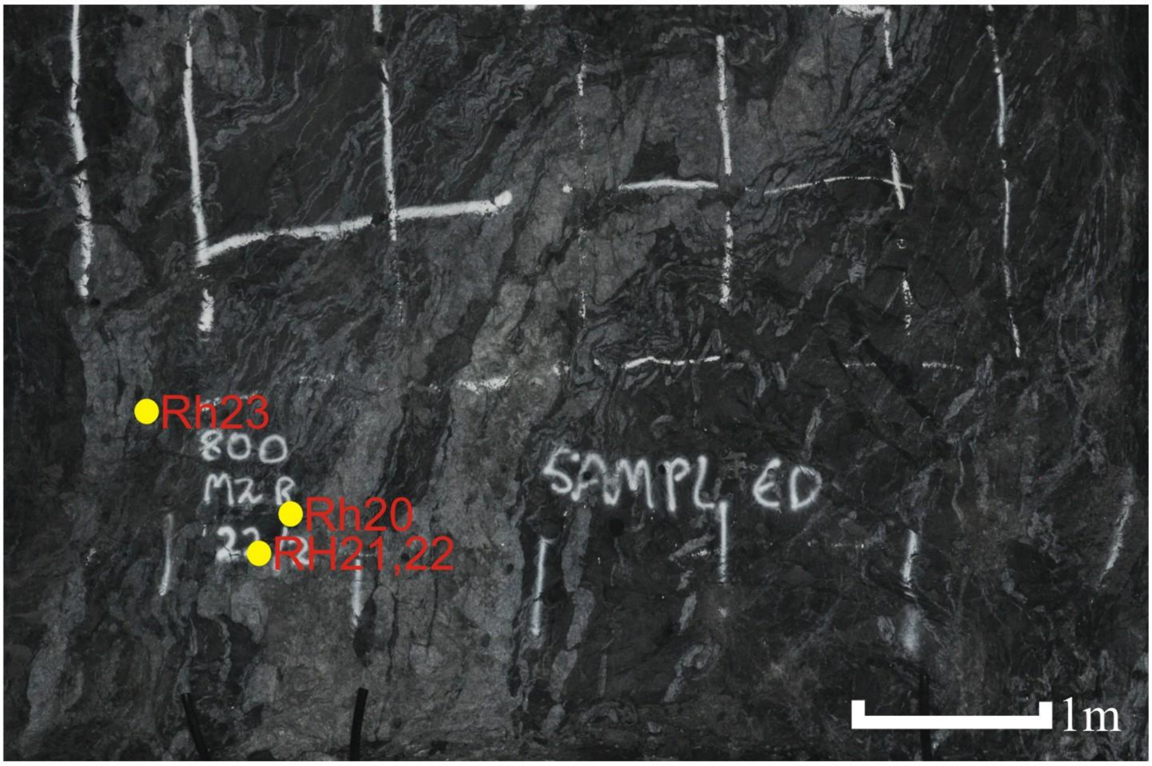

b)

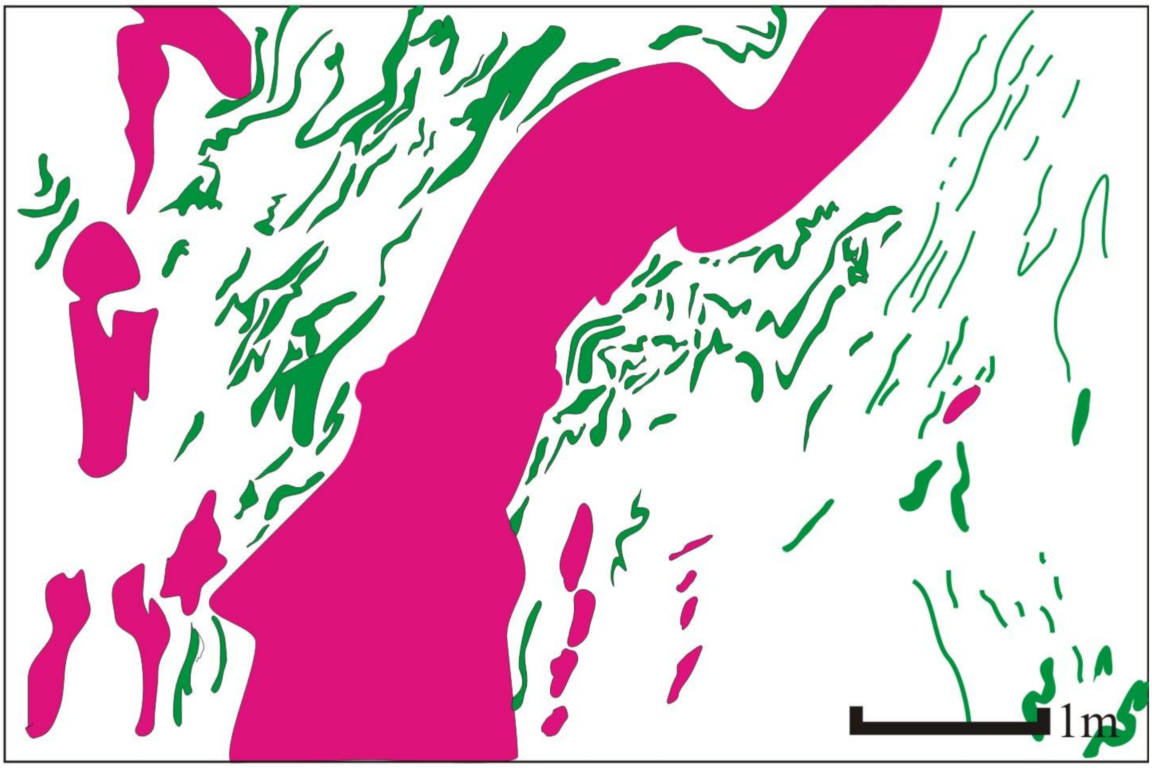

Legend
Sample Location- Rh20
Main Leucosome-
Pegmatitic veining-

Figure A2; 760m M2

a)

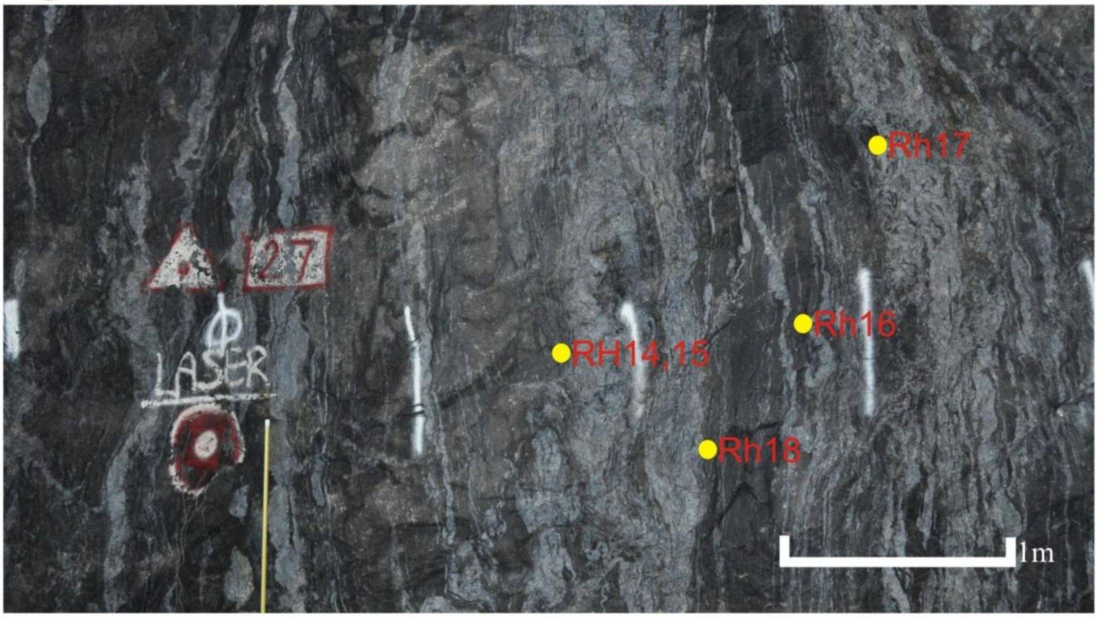

Rh19

b)

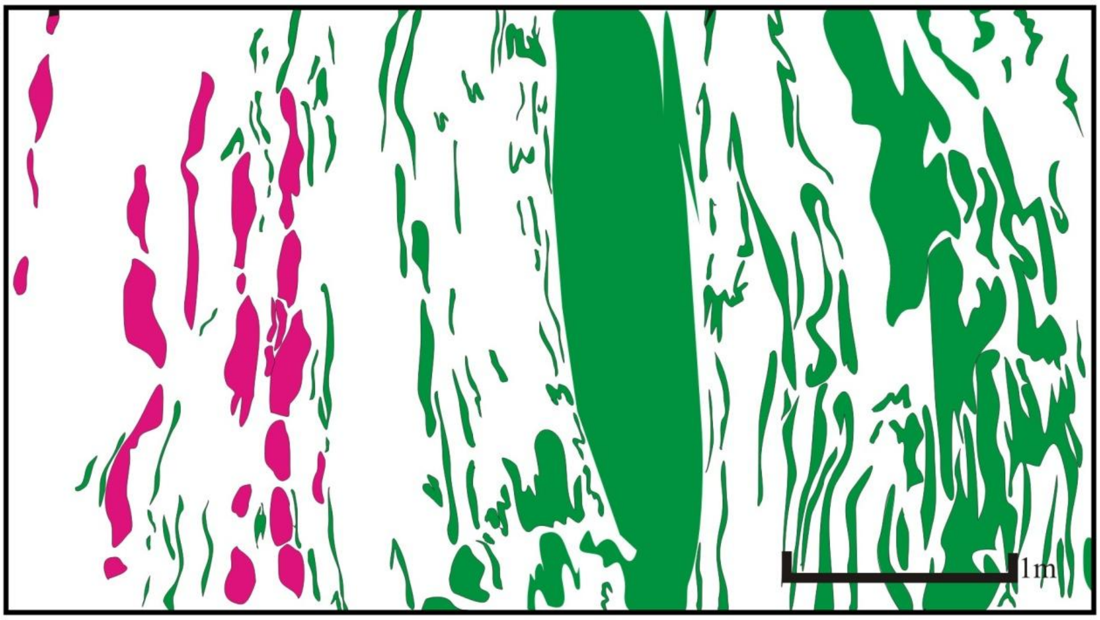

Legend
Sample Location- RH9
Main Leucosome-
Pegmatitic veining-

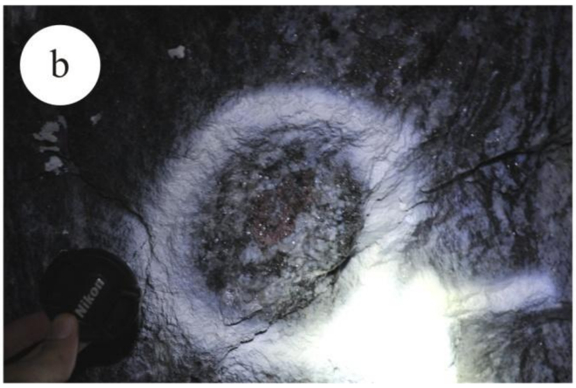

Figure A3; 580m M2

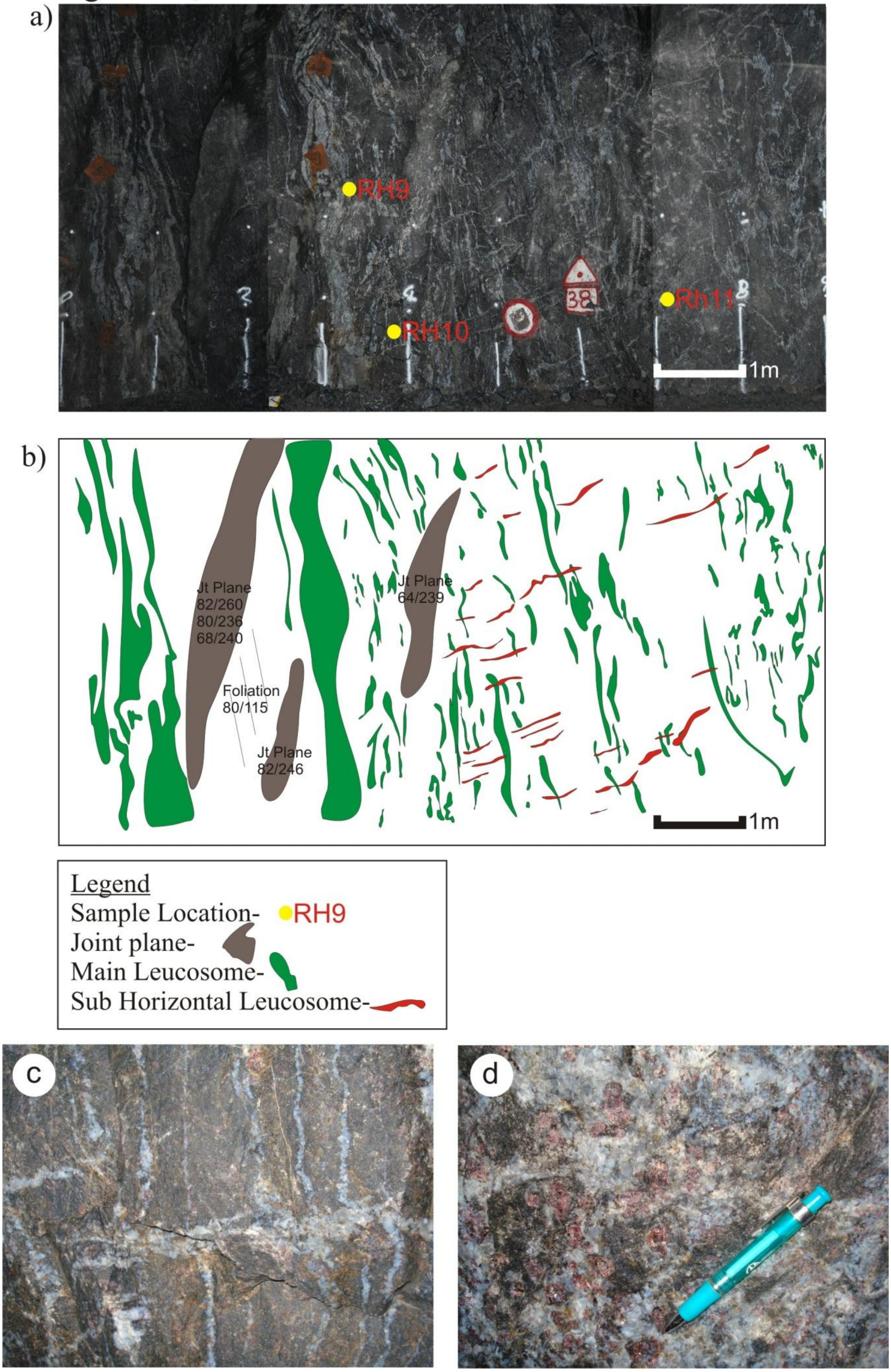

Figure A4

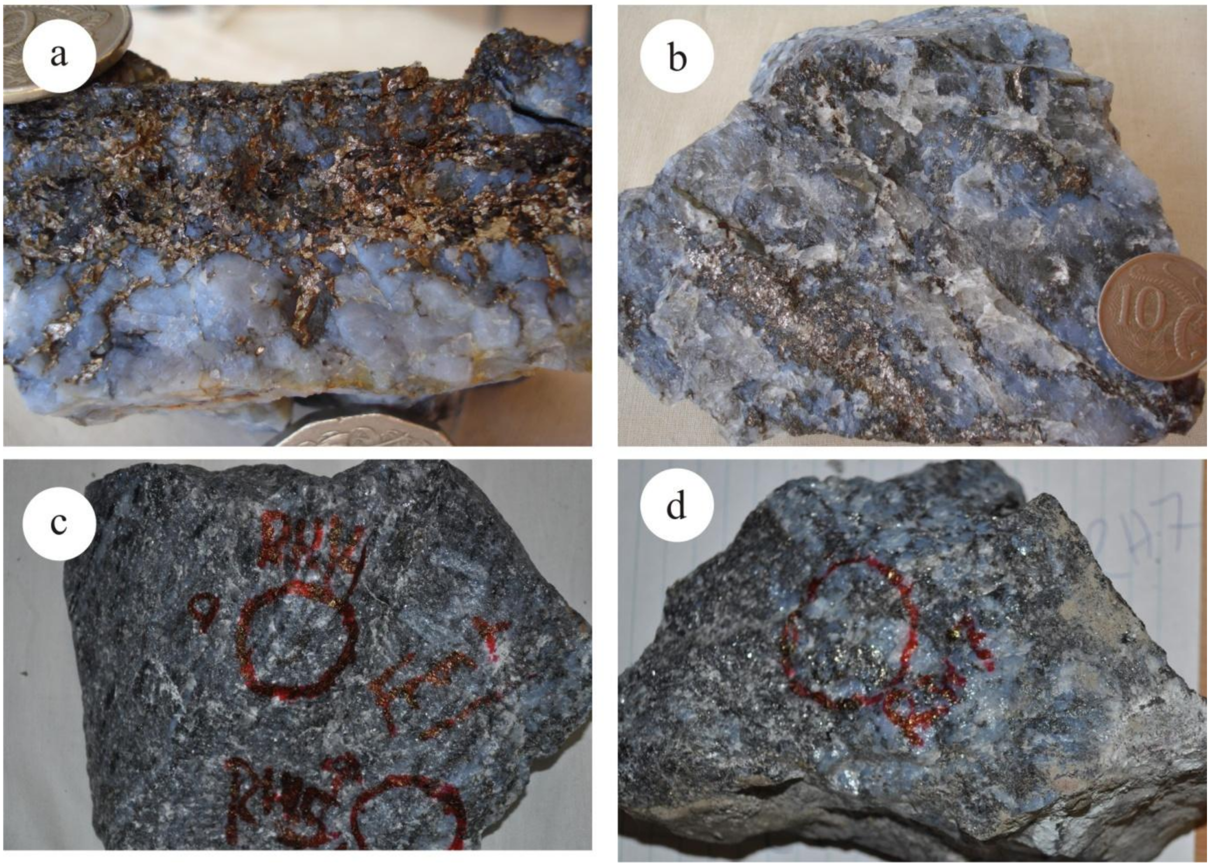

Figure A5

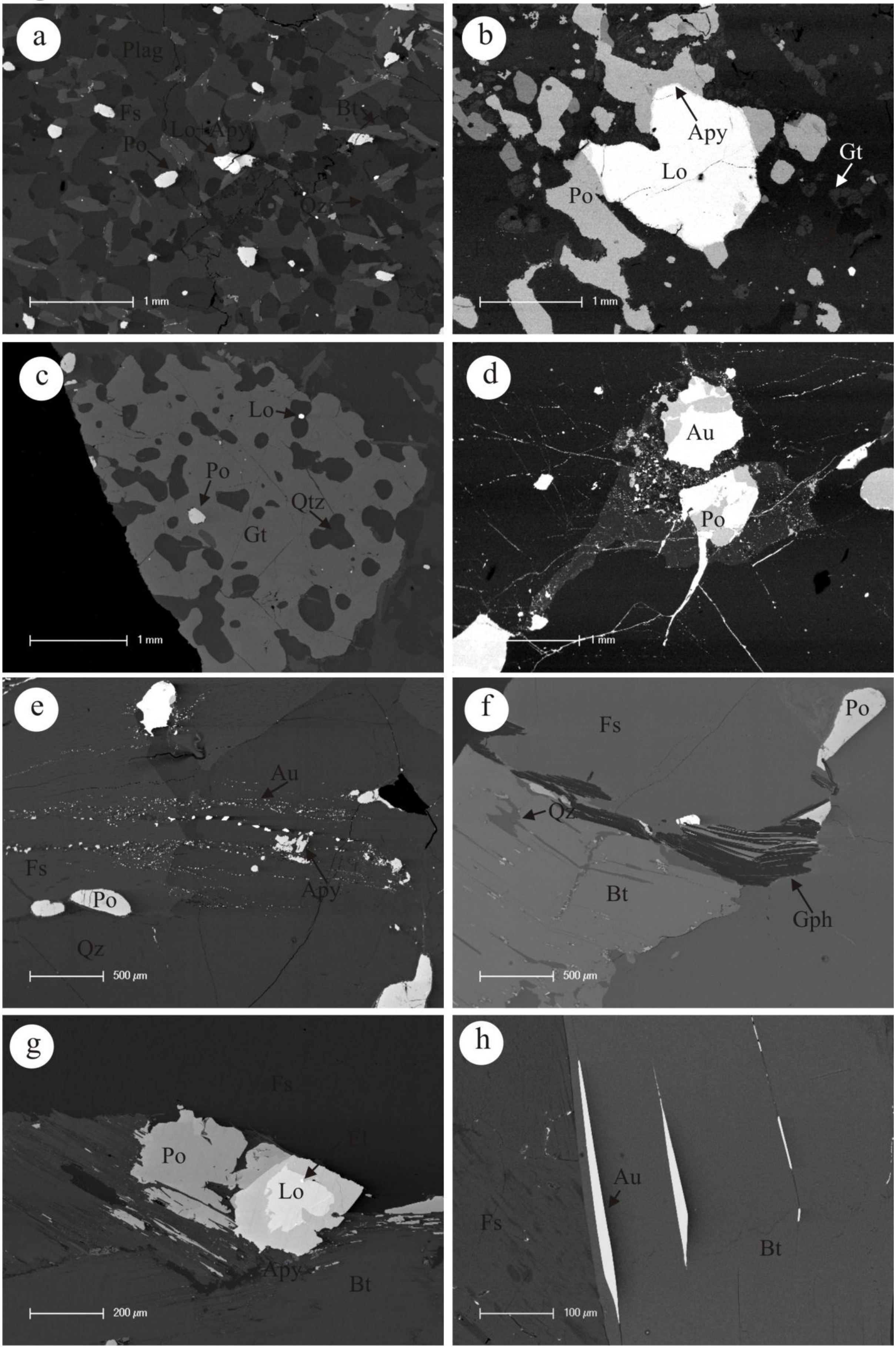
a
Plag
Fs
Lo+Apy
Bt
Po
Qz
1 mm
b
Apy
Gt
Lo
Po
1 mm
c
Lo
Po
Qtz
Gt
1 mm
d
Au
Po
1 mm
e
Au
Fs
Po
Apy
Qz
500 μm
f
Fs
Po
Qz
Bt
Gph
500 μm
g
Fs
Po
Lo
Apy
Bt
200 μm
h
Au
Fs
Bt
100 μm

Figure A6

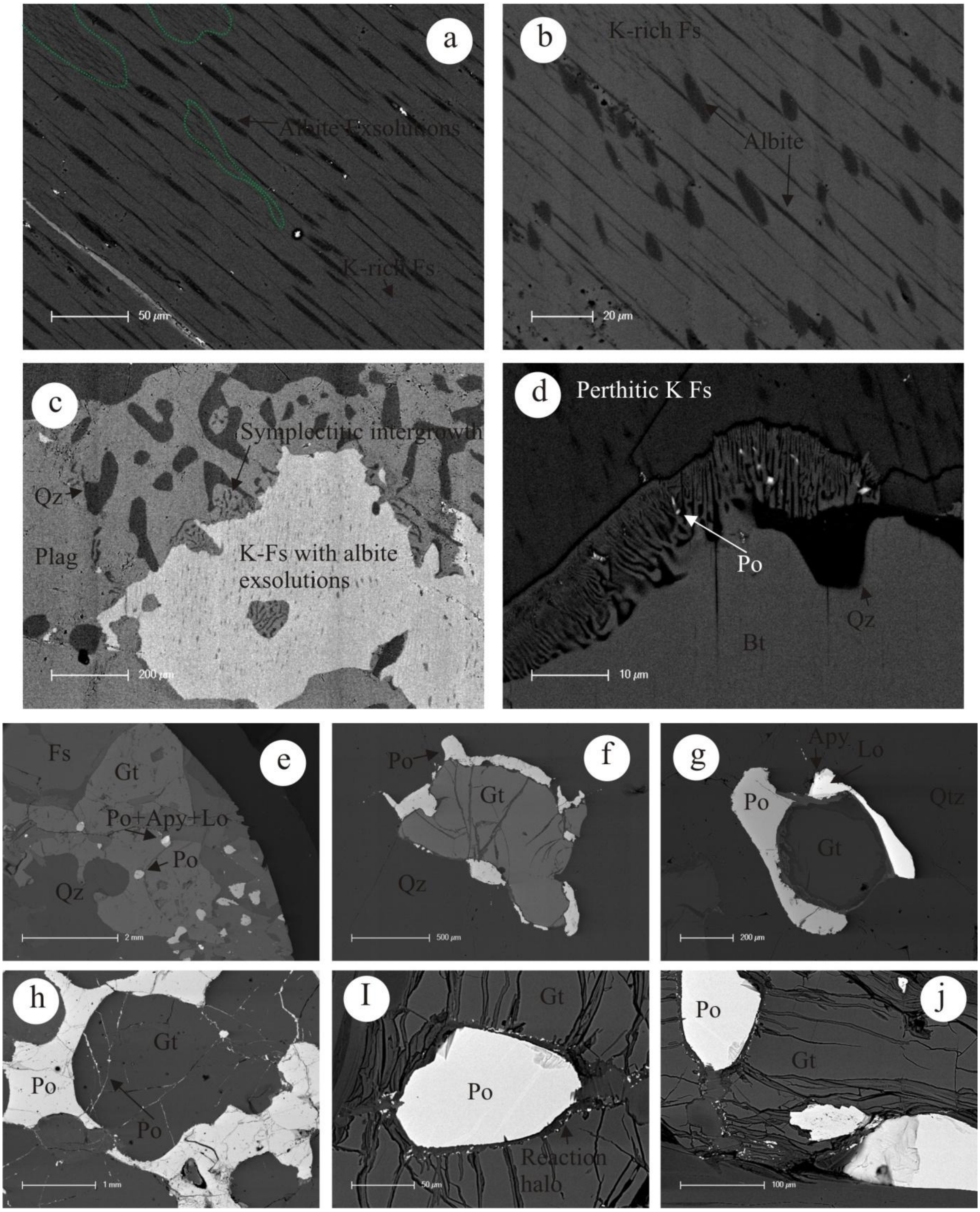
a
Albite Exsolutions
K-rich Fs
50 μm
b
K-rich Fs
Albite
20 μm
c
Symplectitic intergrowth
Qz
Plag
K-Fs with albite exsolutions
200 μm
d
Perthitic K Fs
Po
Qz
Bt
10 μm
e
Fs
Gt
Po+Apy+Lo
Po
Qz
2 mm
f
Po
Gt
Qz
500 μm
g
Apy
Lo
Po
Qtz
Gt
200 μm
h
Gt
Po
Po
1 mm
I
Gt
Po
Reaction halo
50 μm
j
Po
Gt
100 μm

Figure A7

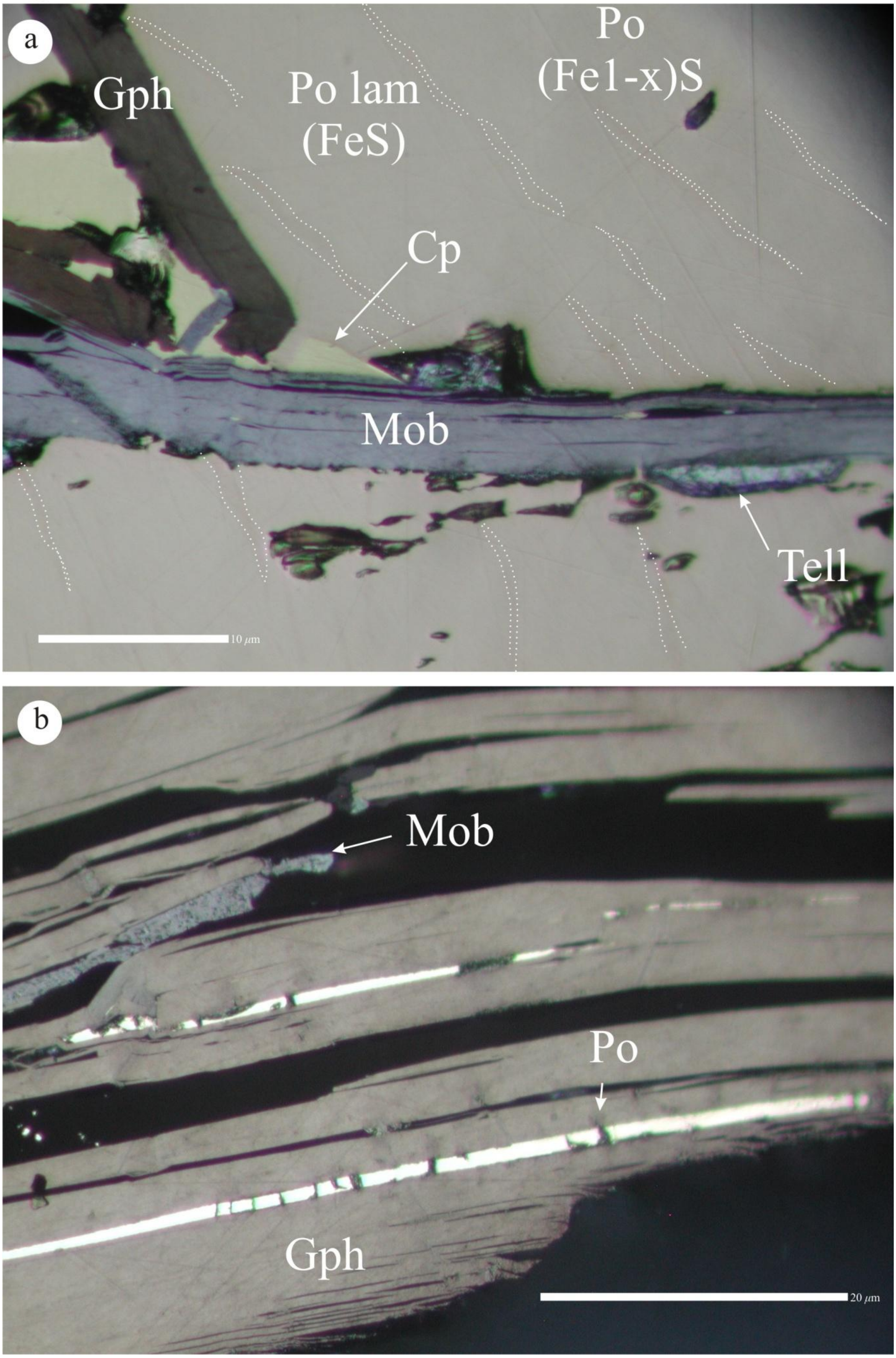

Figure A8

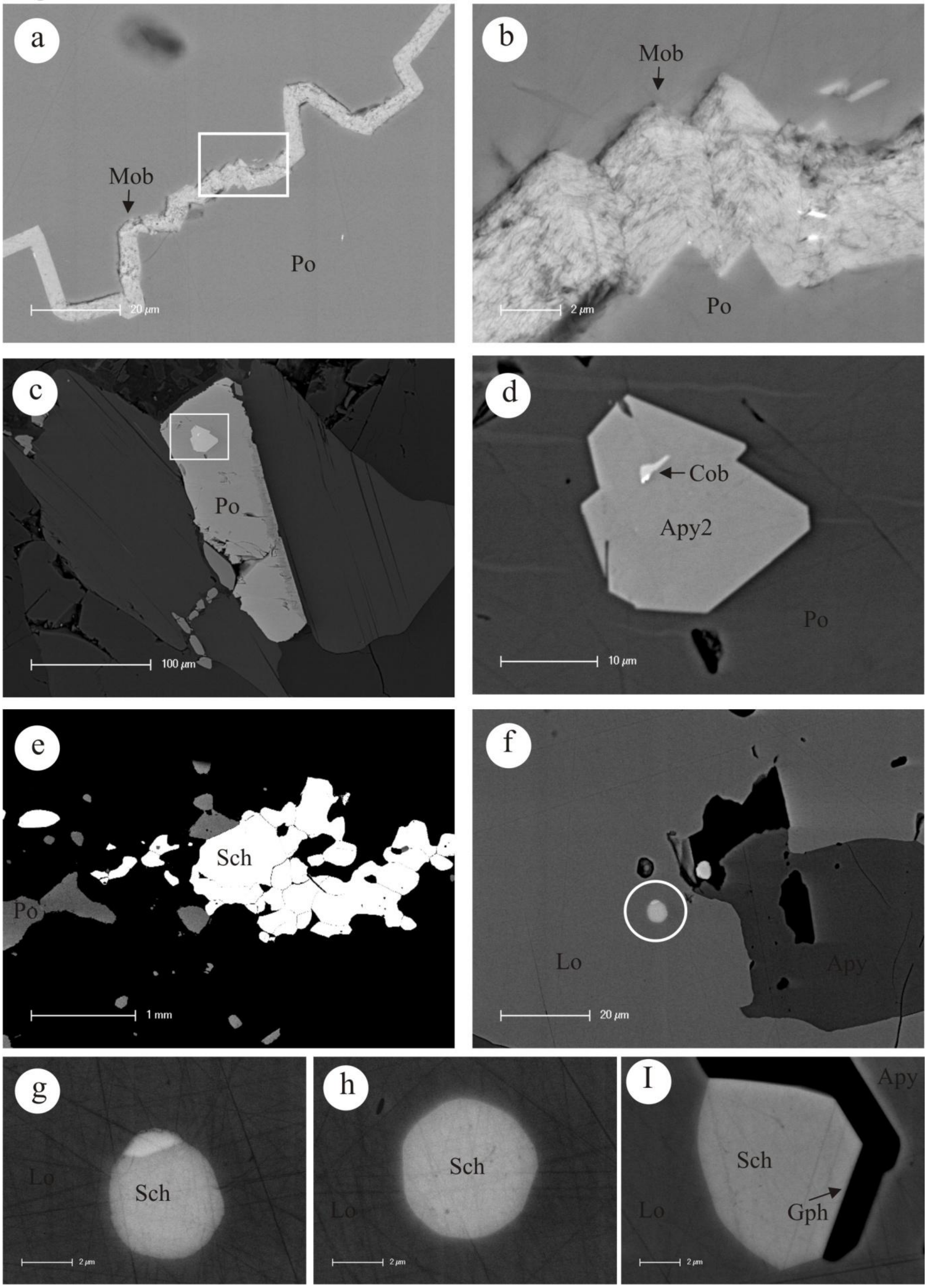

a
Mob
Po
20 µm
b
Mob
Po
2 µm
c
Po
100 µm
d
Cob
Apy2
Po
10 µm
e
Sch
Po
1 mm
f
Lo
Apy
20 µm
g
Lo
Sch
2 µm
h
Sch
Lo
2 µm
I
Apy
Sch
Lo
Gph
2 µm

Figure A9

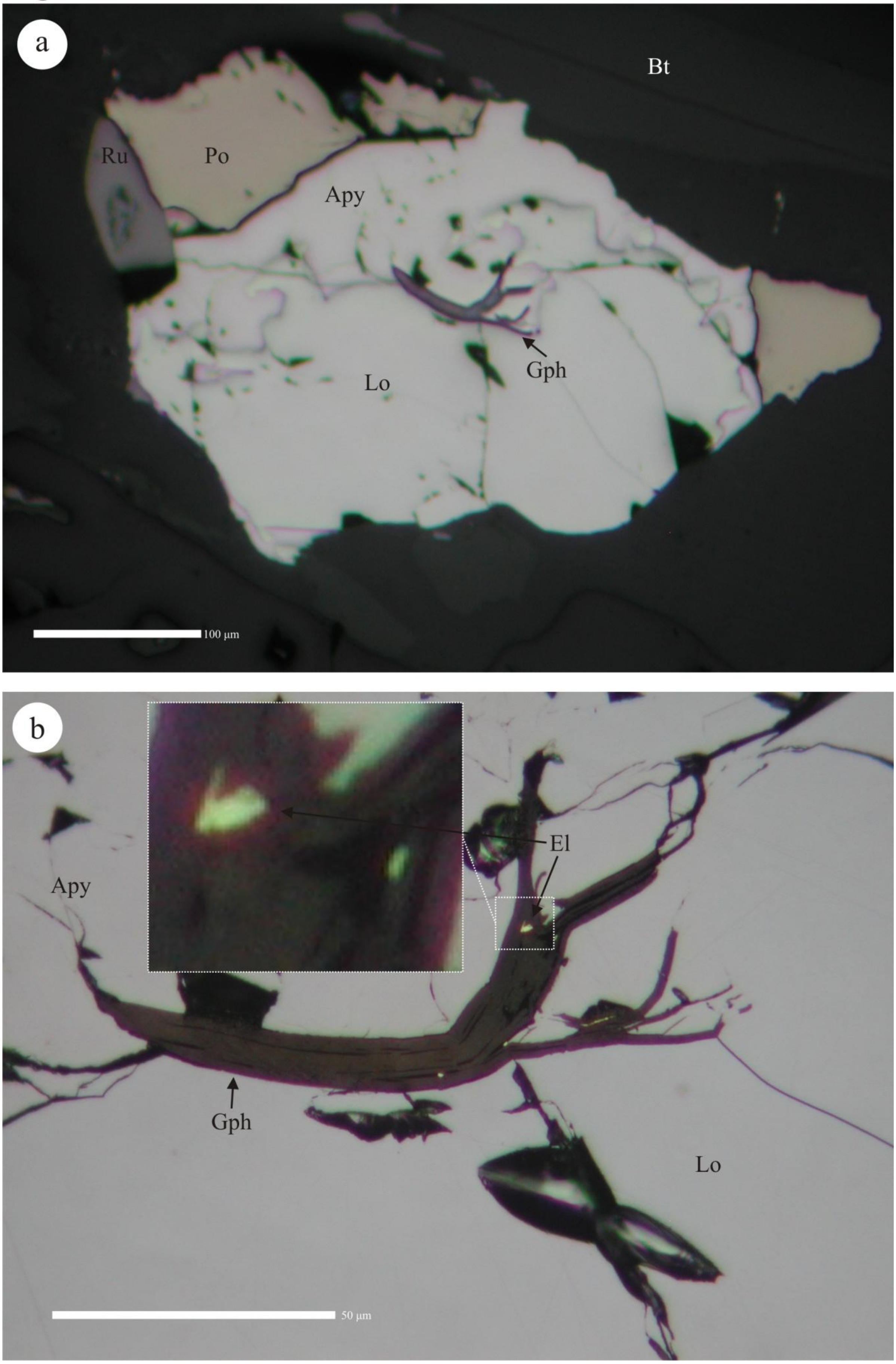

Figure A10

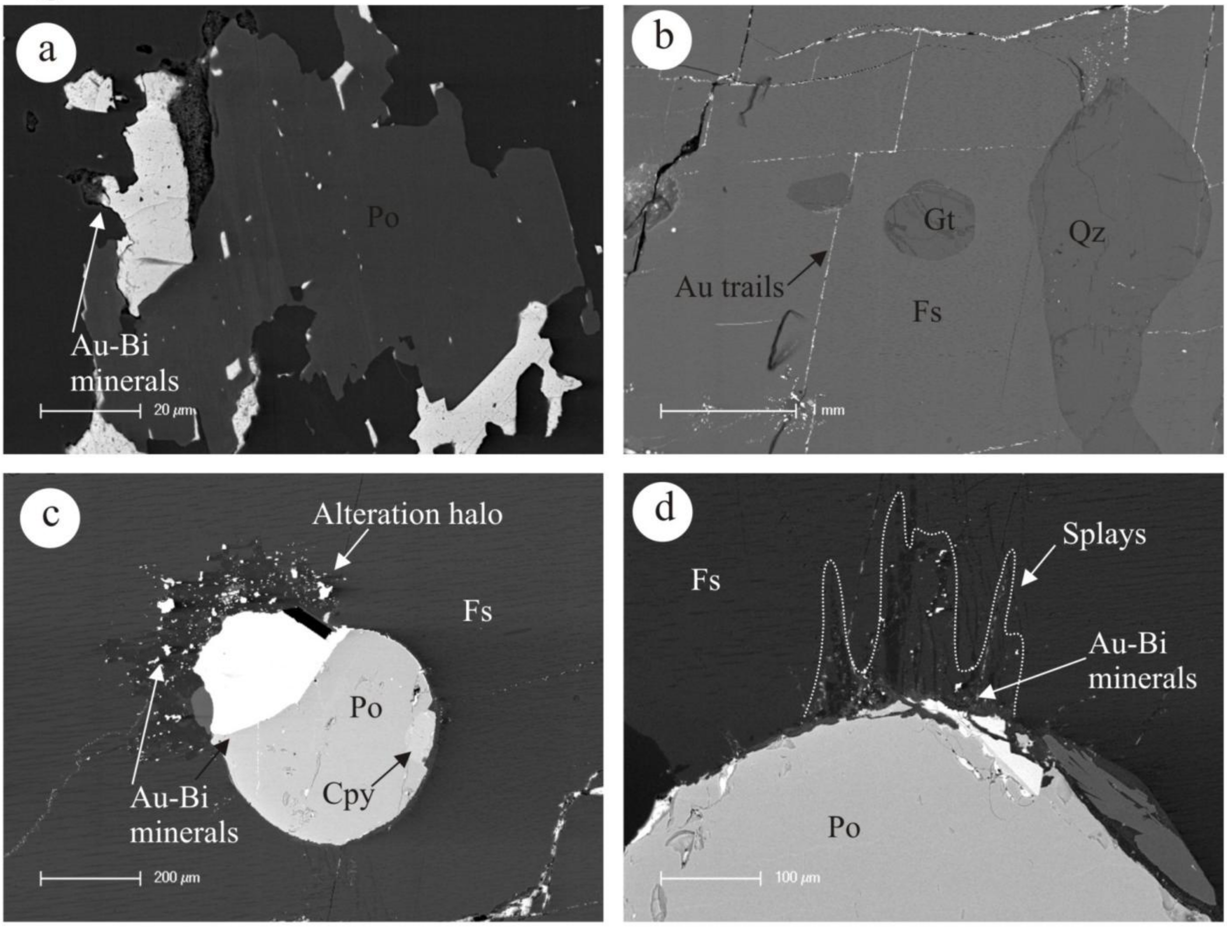
a
Po
Au-Bi
minerals
20 μm
b
Gt
Qz
Au trails
Fs
1 mm
c
Alteration halo
Fs
Po
Cpy
Au-Bi
minerals
200 μm
d
Splays
Fs
Au-Bi
minerals
Po
100 μm

Figure A11

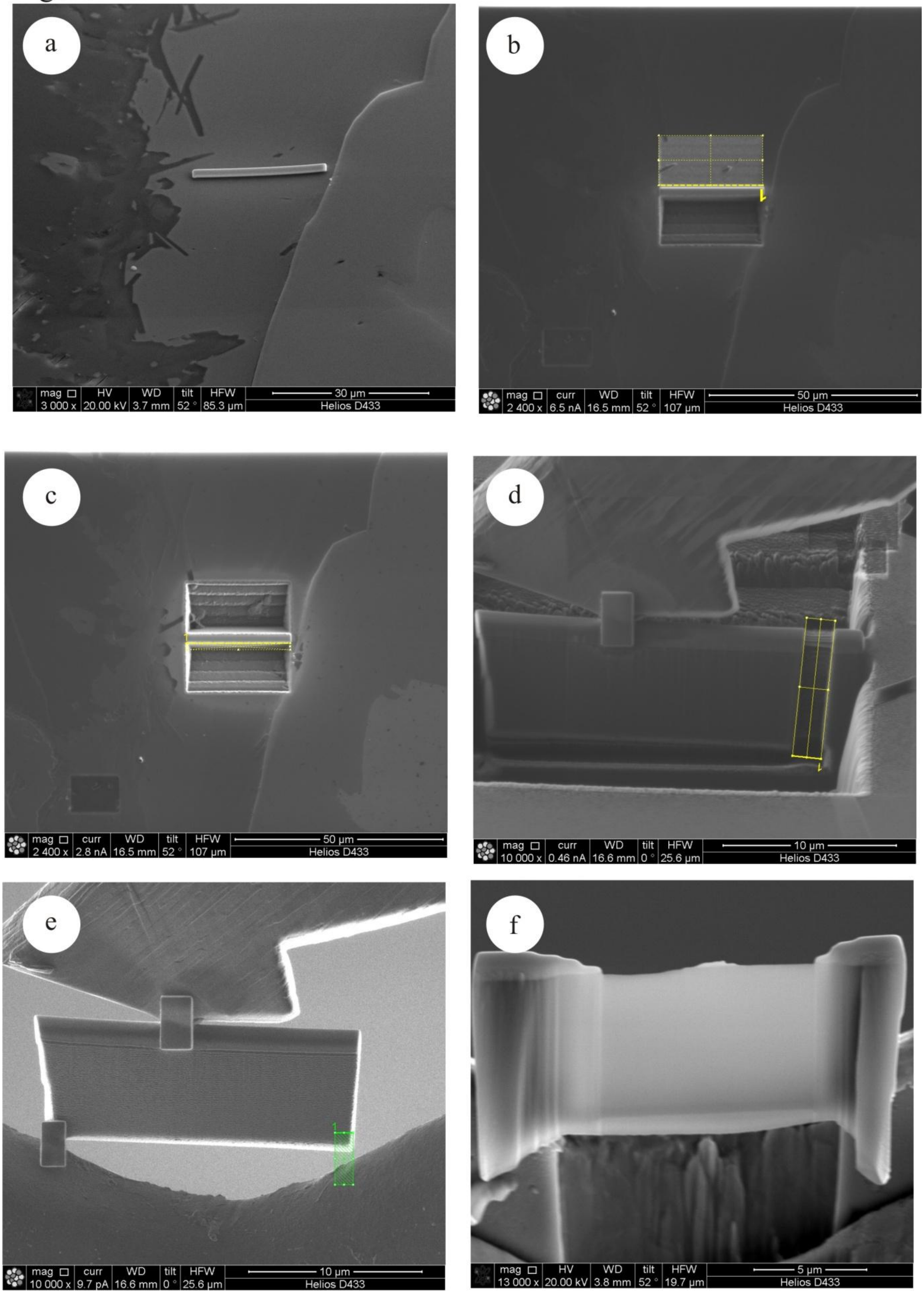
a
mag □ 3 000 x
HV 20.00 kV
WD 3.7 mm
tilt 52 °
HFW 85.3 µm
30 µm
Helios D433
b
mag □ 2 400 x
curr 6.5 nA
WD 16.5 mm
tilt 52 °
HFW 107 µm
50 µm
Helios D433
c
mag □ 2 400 x
curr 2.8 nA
WD 16.5 mm
tilt 52 °
HFW 107 µm
50 µm
Helios D433
d
mag □ 10 000 x
curr 0.46 nA
WD 16.6 mm
tilt 0 °
HFW 25.6 µm
10 µm
Helios D433
e
mag □ 10 000 x
curr 9.7 pA
WD 16.6 mm
tilt 0 °
HFW 25.6 µm
10 µm
Helios D433
f
mag □ 13 000 x
HV 20.00 kV
WD 3.8 mm
tilt 52 °
HFW 19.7 µm
5 µm
Helios D433

Table A1. Complete electron probe microanalysis data for arsenopyrite

840m M2

	Apy at relacement boundaries with Lo												**Idiomorph Apy (no Lo; at Po)**				**Apy at relacement boundaries with Lo**						
	1RH																**2RH**						
	1rh4	1rh7	1rh11	1rh16	1rh24	**mean1**	1rh10	1rh15	1rh20	1rh21	1rh23	**mean2**	1rh6	1rh8	1rh9	**mean3**	2rhp04	2rhp06	2rhp07	2rhp10	2rhp12	2rhp13	**mean**
						n=5						**n=5**				**n=3**							**n=6**
Cu	<mdl	0.02	0.02	<mdl	<mdl	**0.01**	0.01	0.01	<mdl	<mdl	<mdl	**0.01**	0.06	0.02	0.04	**0.04**	<mdl	<mdl	0.01	<mdl	<mdl	<mdl	**0.00**
Mn	0.05	<mdl	<mdl	0.03	0.00	**0.01**	0.02	<mdl	0.01	<mdl	<mdl	**0.01**	<mdl	0.01	<mdl	**0.01**	0.00	0.01	0.03	<mdl	<mdl	<mdl	**0.01**
Fe	33.95	33.92	33.71	33.34	34.09	**33.80**	33.57	33.13	33.08	33.43	33.25	**33.29**	34.22	33.28	33.01	**33.51**	34.56	33.91	33.97	34.18	33.53	33.90	**34.01**
Co	0.20	0.29	0.24	0.17	0.17	**0.21**	0.32	0.30	0.32	0.18	0.44	**0.31**	0.36	0.37	0.36	**0.36**	0.06	0.16	0.12	0.09	0.16	0.13	**0.12**
Ni	0.05	0.07	0.01	0.03	<mdl	**0.03**	0.11	0.15	0.28	0.16	0.33	**0.21**	0.32	0.50	0.43	**0.42**	0.01	0.10	0.03	0.01	0.00	0.02	**0.03**
Sb	0.05	0.06	<mdl	<mdl	0.01	**0.02**	<mdl	<mdl	0.04	<mdl	<mdl	**0.04**	0.07	0.03	<mdl	**0.05**	<mdl	<mdl	0.04	<mdl	<mdl	<mdl	**0.01**
As	45.92	45.60	46.20	46.27	46.29	**46.05**	46.64	46.89	47.16	46.46	47.32	**46.89**	46.94	47.05	47.60	**47.20**	45.77	46.90	46.01	45.75	45.97	46.72	**46.19**
S	19.78	19.60	19.07	19.16	19.40	**19.40**	18.51	18.55	18.20	18.66	18.38	**18.46**	18.59	18.23	18.00	**18.27**	19.63	18.75	19.26	19.01	19.09	18.77	**19.08**
Se	0.30	0.40	0.37	0.46	0.35	**0.37**	0.34	0.23	0.32	0.38	0.33	**0.32**	0.28	0.38	0.41	**0.36**	0.32	0.38	0.33	0.32	0.35	0.27	**0.33**
Total	100.29	99.96	99.62	99.45	100.31	**99.92**	99.53	99.25	99.42	99.27	100.05	**99.50**	100.85	99.88	99.85	**100.19**	100.35	100.22	99.79	99.37	99.11	99.81	**99.77**

Formulae, calculated to 3 a.p.f.u

	1rh4	1rh7	1rh11	1rh16	1rh24	**mean1**	1rh10	1rh15	1rh20	1rh21	1rh23	**mean2**	1rh6	1rh8	1rh9	**mean3**	2rhp04	2rhp06	2rhp07	2rhp10	2rhp12	2rhp13	**mean**
Cu	-	0.000	0.000	-	-	**0.000**	0.000	0.000	-	-	-	**0.00**	0.002	0.000	0.001	**0.00**	-	-	0.000	-	-	-	**0.000**
Mn	0.001	-	-	0.001	0.000	**0.000**	0.001	-	0.000	-	-	**0.00**	-	0.000	-	**0.00**	0.000	0.000	0.001	-	-	-	**0.000**
Fe	0.987	0.991	0.993	0.983	0.995	**0.990**	0.995	0.984	0.985	0.991	0.983	**0.99**	1.001	0.986	0.981	**0.99**	1.005	0.997	0.997	1.008	0.992	0.999	**1.000**
Co	0.006	0.008	0.007	0.005	0.005	**0.006**	0.009	0.008	0.009	0.005	0.012	**0.01**	0.010	0.010	0.010	**0.01**	0.002	0.005	0.003	0.003	0.005	0.004	**0.003**
Ni	0.001	0.002	0.000	0.001	-	**0.001**	0.003	0.004	0.008	0.004	0.009	**0.01**	0.009	0.014	0.012	**0.01**	0.000	0.003	0.001	0.000	0.000	0.001	**0.001**
Sb	0.001	0.001	-	-	0.000	**0.000**	-	-	0.001	-	-	**0.00**	0.001	0.000	-	**0.00**	-	-	0.000	-	-	-	**0.000**
As	0.995	0.993	1.014	1.017	1.007	**1.005**	1.030	1.038	1.047	1.027	1.043	**1.04**	1.024	1.039	1.055	**1.04**	0.992	1.028	1.006	1.006	1.013	1.027	**1.012**
S	1.002	0.997	0.978	0.984	0.986	**0.990**	0.955	0.960	0.944	0.964	0.946	**0.95**	0.948	0.941	0.932	**0.94**	0.994	0.960	0.984	0.977	0.983	0.964	**0.977**
Se	0.006	0.008	0.008	0.010	0.007	**0.008**	0.007	0.005	0.007	0.008	0.007	**0.01**	0.006	0.008	0.009	**0.01**	0.007	0.008	0.007	0.007	0.007	0.006	**0.007**
S(+Se)	1.008	1.005	0.986	0.994	0.993	**0.997**	0.962	0.965	0.951	0.972	0.953	**0.96**	0.953	0.949	0.941	**0.95**	1.001	0.968	0.991	0.983	0.991	0.970	**0.984**

Table A1. Complete electron probe microanalysis data for arsenopyrite (continued)

														800m M2								760m M2 Idiomorph Apy (no Lo; a
	7RH												8RH	20RH								14RH
	7rh02	7rh04	7rh05	7rh10	**mean1 n=4**	7rh09	8rhp1	8rhp2	8rhl5_1	8rhl5_2	8rhl5_3	**mean n=5**	8rhp3	20rhp2	0rhpl03_	0rhpl03_	0rhpl03_	0rhpl05_	0rhpl05_	**mean n=5**	0rhpl03_	14RH1	14RHp1	**mean1 n=2**
Cu	0.01	<mdl	<mdl	<mdl	**0.00**	0.02	<mdl	0.07	<mdl	<mdl	<mdl	**0.01**	0.02	0.04	0.04	0.01	<mdl	<mdl	<mdl	**0.01**	0.02	0.02	0.02	**0.02**
Mn	0.01	0.01	0.03	<mdl	**0.01**	0.00	0.02	<mdl	0.03	0.03	0.01	**0.02**	0.01	<mdl	0.03	0.04	0.02	0.02	0.02	**0.03**	0.02	0.01	0.03	**0.02**
Fe	33.22	33.13	33.33	32.92	**33.15**	33.52	34.06	33.99	33.63	33.71	33.43	**33.76**	33.00	32.58	33.22	32.88	33.01	33.18	33.20	**33.10**	33.34	26.40	25.82	**26.11**
Co	0.39	0.45	0.43	0.39	**0.41**	0.30	0.12	0.15	0.26	0.35	0.30	**0.24**	0.55	1.02	0.27	0.26	0.29	0.55	0.69	**0.41**	0.27	6.85	6.23	**6.54**
Ni	0.16	0.11	0.13	0.28	**0.17**	0.09	0.04	0.06	0.07	0.06	0.09	**0.06**	0.52	0.10	0.15	0.14	0.17	0.51	0.25	**0.24**	0.08	0.69	1.04	**0.87**
Sb	0.04	<mdl	<mdl	0.03	**0.02**	<mdl	<mdl	<mdl	<mdl	0.03	<mdl	**0.01**	0.01	<mdl	<mdl	<mdl	<mdl	<mdl	0.04	**0.01**	<mdl	<mdl	<mdl	**<mdl**
As	47.38	47.16	46.84	47.21	**47.15**	46.70	46.46	46.20	46.45	47.55	47.52	**46.84**	46.77	46.12	47.51	47.25	47.22	47.59	47.20	**47.36**	46.82	49.83	49.14	**49.49**
S	18.42	18.55	18.65	18.32	**18.48**	18.80	18.99	19.26	18.57	18.76	18.01	**18.72**	18.73	19.05	17.91	18.03	17.81	18.13	18.25	**18.03**	18.22	16.79	17.33	**17.06**
Se	0.30	0.37	0.35	0.33	**0.34**	0.48	0.36	0.38	0.33	0.34	0.35	**0.35**	0.32	0.33	0.41	0.38	0.31	0.34	0.32	**0.35**	0.36	0.32	0.35	**0.34**
Total	99.94	99.77	99.76	99.47	**99.74**	99.91	100.05	100.12	99.34	100.84	99.71	**100.01**	99.93	99.23	99.54	99.00	98.83	100.33	99.98	**99.54**	99.13	100.91	99.96	**100.43**
Formulae, calculated to 3 a.p.f.u																								
Cu	0.000	-	-	-	**0.000**	0.000	-	0.002	-	-	-	**0.000**	0.001	0.001	0.001	0.000	-	-	-	**0.000**	0.001	0.000	0.000	**0.000**
Mn	0.000	0.000	0.001	-	**0.000**	0.000	0.000	-	0.001	0.001	0.000	**0.000**	0.000	0.000	0.001	0.001	0.001	0.001	0.000	**0.001**	0.001	0.000	0.001	**0.001**
Fe	0.983	0.980	0.985	0.979	**0.982**	0.988	1.000	0.995	0.997	0.986	0.994	**0.994**	0.973	0.963	0.991	0.984	0.991	0.981	0.983	**0.986**	0.994	0.791	0.776	**0.783**
Co	0.011	0.013	0.012	0.011	**0.012**	0.008	0.003	0.004	0.007	0.010	0.009	**0.007**	0.015	0.029	0.008	0.007	0.008	0.015	0.019	**0.012**	0.008	0.194	0.177	**0.186**
Ni	0.004	0.003	0.004	0.008	**0.005**	0.002	0.001	0.002	0.002	0.002	0.003	**0.002**	0.014	0.003	0.004	0.004	0.005	0.014	0.007	**0.007**	0.002	0.020	0.030	**0.025**
Sb	0.001	-	-	0.000	**0.000**	-	-	-	-	0.000	-	**0.000**	0.000	-	-	-	-	-	0.001	**0.000**	-	-	-	**-**
As	1.045	1.040	1.032	1.046	**1.041**	1.026	1.017	1.008	1.027	1.037	1.054	**1.028**	1.028	1.016	1.056	1.054	1.057	1.048	1.042	**1.052**	1.041	1.112	1.101	**1.107**
S	0.949	0.956	0.960	0.949	**0.953**	0.965	0.971	0.982	0.959	0.956	0.933	**0.960**	0.962	0.981	0.931	0.940	0.932	0.933	0.941	**0.935**	0.946	0.876	0.907	**0.892**
Se	0.006	0.008	0.007	0.007	**0.007**	0.010	0.007	0.008	0.007	0.007	0.007	**0.007**	0.007	0.007	0.009	0.008	0.007	0.007	0.007	**0.007**	0.008	0.007	0.007	**0.007**
S(+Se)	0.956	0.964	0.967	0.956	**0.961**	0.975	0.979	0.990	0.966	0.963	0.940	**0.968**	0.969	0.988	0.939	0.948	0.938	0.940	0.948	**0.943**	0.954	0.882	0.915	**0.899**

Table A1. Complete electron probe microanalysis data for arsenopyrite (continued)

					Apy1																				
at Po)																									
	14RH				**16RH**																				
	14RHp3	14RHp4	**mean2**	**14RHp6**	6RHl1_	6RHl1_	6RHl1_	16RHp5	6RHl8_	6RHl10_	6RHl10_	6RHl10_	6RHl10_	**mean1**	6RHl1_	16RHp3	16RHp4	6RHl7_	6RHl7_	6RHl7_	6RHl7_	6RHl8_	6RHl8_	6RHl8_	**mean2**
			n=2											**n=9**											**n=10**
Cu	<mdl	0.01	**0.01**	<mdl	0.02	0.04	0.05	0.05	<mdl	<mdl	<mdl	<mdl	0.25	**0.05**	<mdl	<mdl	0.02	0.03	<mdl	0.00	0.05	<mdl	0.08	0.07	**0.02**
Mn	0.02	<mdl	**0.01**	<mdl	<mdl	0.01	0.01	0.03	0.03	<mdl	0.01	<mdl	0.02	**0.01**	<mdl	0.02	0.01	0.02	<mdl	0.01	<mdl	<mdl	0.02	<mdl	**0.01**
Fe	31.59	32.24	**31.91**	28.60	33.75	34.15	33.88	33.83	33.43	32.92	33.05	33.36	32.94	**33.48**	34.37	33.15	34.10	31.71	32.20	32.63	32.03	33.36	33.51	33.55	**33.06**
Co	1.59	1.79	**1.69**	1.45	0.31	0.20	0.18	0.33	0.52	0.93	0.99	0.82	1.18	**0.61**	0.25	0.54	0.35	1.01	0.86	0.66	0.89	0.51	0.46	0.40	**0.59**
Ni	0.67	0.60	**0.64**	3.30	0.09	0.02	0.06	0.09	0.04	0.03	0.03	0.09	0.05	**0.05**	0.17	0.16	0.11	0.38	0.31	0.24	0.33	0.17	0.13	0.11	**0.21**
Sb	<mdl	<mdl	**0.00**	0.01	0.01	<mdl	<mdl	<mdl	0.08	<mdl	0.03	<mdl	0.02	**0.02**	<mdl	<mdl	<mdl	<mdl	<mdl	<mdl	0.10	<mdl	<mdl	0.05	**0.02**
As	46.56	45.58	**46.07**	49.04	46.96	46.47	46.27	46.37	45.56	45.97	46.25	46.06	45.30	**46.13**	46.48	47.51	46.92	47.46	47.65	47.10	47.84	46.35	46.28	46.47	**47.01**
S	19.19	19.99	**19.59**	17.10	19.01	18.79	19.11	18.85	19.45	19.28	19.20	19.22	19.39	**19.15**	18.80	18.24	18.76	18.60	18.27	18.43	18.38	18.96	19.21	19.22	**18.69**
Se	0.31	0.29	**0.30**	0.37	0.25	0.48	0.36	0.31	0.33	0.36	0.29	0.39	0.25	**0.33**	0.34	0.44	0.30	0.29	0.39	0.48	0.41	0.36	0.32	0.38	**0.37**
Total	99.94	100.50	**100.22**	99.86	100.39	100.15	99.93	99.85	99.44	99.49	99.85	99.94	99.40	**99.83**	100.40	100.06	100.58	99.49	99.68	99.54	100.03	99.71	100.01	100.25	**99.97**
Formulae, calculated to 3 a.p.f.u																									
Cu	-	0.000	**0.000**	-	0.001	0.001	0.001	0.001	-	-	-	-	0.006	**0.001**	-	-	0.001	0.001	-	0.000	0.001	-	0.002	0.002	**0.001**
Mn	0.001	-	**0.000**	-	-	0.000	0.000	0.001	0.001	-	0.000	-	0.001	**0.000**	-	0.001	0.000	0.000	-	0.000	-	-	0.000	-	**0.000**
Fe	0.928	0.934	**0.931**	0.860	0.988	1.003	0.995	0.996	0.982	0.969	0.970	0.978	0.968	**0.983**	1.007	0.981	0.999	0.941	0.957	0.969	0.949	0.983	0.982	0.982	**0.975**
Co	0.044	0.049	**0.047**	0.041	0.009	0.006	0.005	0.009	0.014	0.026	0.028	0.023	0.033	**0.017**	0.007	0.015	0.010	0.028	0.024	0.018	0.025	0.014	0.013	0.011	**0.017**
Ni	0.019	0.017	**0.018**	0.094	0.002	0.001	0.002	0.002	0.001	0.001	0.001	0.002	0.001	**0.002**	0.005	0.005	0.003	0.011	0.009	0.007	0.009	0.005	0.004	0.003	**0.006**
Sb	-	-	**0.000**	0.000	0.000	-	-	-	0.001	-	0.000	-	0.000	**0.000**	-	-	-	-	-	-	0.001	-	-	0.001	**0.000**
As	1.020	0.985	**1.002**	1.100	1.025	1.018	1.012	1.017	0.998	1.008	1.012	1.007	0.992	**1.010**	1.015	1.048	1.024	1.050	1.056	1.043	1.057	1.018	1.011	1.014	**1.034**
S	0.982	1.009	**0.996**	0.896	0.970	0.962	0.977	0.966	0.996	0.988	0.982	0.982	0.993	**0.980**	0.960	0.941	0.957	0.962	0.946	0.953	0.948	0.973	0.981	0.980	**0.960**
Se	0.006	0.006	**0.006**	0.008	0.005	0.010	0.008	0.006	0.007	0.007	0.006	0.008	0.005	**0.007**	0.007	0.009	0.006	0.006	0.008	0.010	0.009	0.007	0.007	0.008	**0.008**
S(+Se)	0.989	1.015	**1.002**	0.904	0.975	0.971	0.985	0.973	1.003	0.996	0.988	0.990	0.998	**0.986**	0.966	0.950	0.963	0.968	0.954	0.963	0.957	0.981	0.988	0.988	**0.968**

Table A1. Complete electron probe microanalysis data for arsenopyrite (continued)

										600m M1	560m M2											
											cobaltite in Po								Idiomorph Apy (no Lo; at Po)			
	17RH									1bch3	9RH											
	17RHl2_1	17RHl2_2	17RHl2_3	17RHl2_4	**mean1**	17RHp4	17RHp1	17RHp2	**mean2**	1bch3	9rh01	9rhl01_1	9rhl01_2	9rhl01_3	9rhp3	9rhp4	9rhp7	**mean1**	9rhl04_1	9rhl04_2	9rhl04_3	**mean2**
					n=4				**n=2**									**n=7**				**n=3**
Cu	0.01	0.01	0.02	0.02	**0.01**	0.01	<mdl	<mdl	**0.00**	0.01	<mdl	0.04	<mdl	<mdl	0.02	<mdl	<mdl	**0.01**	0.02	<mdl	0.06	**0.02**
Mn	<mdl	<mdl	0.02	0.02	**0.01**	<mdl	0.02	<mdl	**0.01**	0.01	<mdl	<mdl	0.04	<mdl	<mdl	0.03	<mdl	**0.01**	0.01	0.02	<mdl	**0.01**
Fe	31.96	32.43	31.74	31.79	**31.98**	31.28	28.12	29.76	**28.94**	29.13	9.31	7.77	9.68	7.84	9.26	10.13	8.91	**8.98**	29.27	28.92	26.08	**28.09**
Co	1.32	1.20	1.93	1.49	**1.49**	1.80	4.91	3.89	**4.40**	4.37	15.93	20.98	14.61	19.56	19.82	20.84	18.15	**18.55**	4.19	5.53	6.98	**5.57**
Ni	0.37	0.29	0.20	0.47	**0.33**	1.46	0.57	0.34	**0.45**	1.62	10.68	8.21	11.35	8.95	8.53	7.64	9.14	**9.21**	1.62	1.12	1.76	**1.50**
Sb	0.02	0.02	<mdl	0.01	**0.02**	<mdl	<mdl	0.04	**0.02**	0.08	<mdl	<mdl	0.01	0.02	<mdl	<mdl	<mdl	**0.00**	<mdl	<mdl	<mdl	**<mdl**
As	47.11	46.97	46.96	47.14	**47.04**	44.18	43.68	44.33	**44.01**	48.02	45.07	45.07	45.12	45.38	43.42	42.19	45.14	**44.49**	45.69	47.10	47.36	**46.72**
S	18.43	18.62	18.68	18.68	**18.60**	20.63	19.23	20.22	**19.73**	17.82	19.35	19.43	19.11	19.49	20.58	20.85	19.45	**19.75**	19.22	18.17	17.91	**18.44**
Se	0.36	0.38	0.44	0.35	**0.39**	0.36	0.44	0.32	**0.38**	0.39	0.27	0.33	0.37	0.40	0.27	0.26	0.26	**0.31**	0.33	0.31	0.34	**0.33**
Total	99.59	99.93	99.99	99.98	**99.87**	99.72	96.98	98.89	**97.94**	101.44	100.62	101.82	100.28	101.64	101.89	101.95	101.05	**101.32**	100.36	101.17	100.49	**100.67**
Formulae, calculated to 3 a.p.f.u																						
Cu	0.000	0.000	0.000	0.000	**0.000**	0.000	-	-	**0.000**	0.000	-	0.001	-	-	0.001	-	-	**0.000**	0.000	-	0.001	**0.001**
Mn	-	-	0.001	0.001	**0.000**	-	0.001	-	**0.000**	0.000	-	-	0.001	-	-	0.001	-	**0.000**	0.000	0.001	-	**0.000**
Fe	0.949	0.958	0.937	0.939	**0.945**	0.907	0.846	0.873	**0.859**	0.857	0.274	0.226	0.286	0.228	0.266	0.289	0.261	**0.261**	0.856	0.849	0.773	**0.826**
Co	0.037	0.034	0.054	0.042	**0.042**	0.049	0.140	0.108	**0.124**	0.122	0.444	0.578	0.409	0.540	0.539	0.563	0.503	**0.511**	0.116	0.154	0.196	**0.155**
Ni	0.010	0.008	0.006	0.013	**0.009**	0.040	0.016	0.009	**0.013**	0.045	0.299	0.227	0.319	0.248	0.233	0.207	0.254	**0.255**	0.045	0.031	0.050	**0.042**
Sb	0.000	0.000	-	0.000	**0.000**	-	-	0.001	**0.000**	0.001	-	0.000	0.000	0.000	-	-	-	**0.000**	-	-	-	**-**
As	1.042	1.034	1.033	1.037	**1.037**	0.954	0.980	0.969	**0.974**	1.053	0.988	0.977	0.994	0.986	0.929	0.897	0.985	**0.965**	0.996	1.030	1.047	**1.024**
S	0.953	0.958	0.960	0.961	**0.958**	1.042	1.008	1.033	**1.021**	0.913	0.991	0.984	0.983	0.989	1.028	1.036	0.992	**1.001**	0.979	0.929	0.925	**0.944**
Se	0.008	0.008	0.009	0.007	**0.008**	0.007	0.009	0.007	**0.008**	0.008	0.006	0.007	0.008	0.008	0.006	0.005	0.005	**0.006**	0.007	0.006	0.007	**0.007**
S(+Se)	0.961	0.966	0.970	0.968	**0.966**	1.049	1.017	1.040	**1.029**	0.921	0.996	0.991	0.991	0.998	1.034	1.042	0.997	**1.007**	0.986	0.935	0.932	**0.951**

Table A1. Complete electron probe microanalysis data for arsenopyrite (continued)

	560m M2 Apy at relacement boundaries with Lo																			420 M1 Cobaltite in Po		
	13aCH															18aCH				3CH		
	13ach4	13ach8	13ach8	13achpt6	13achpt1	13achpt1	13achpt1	13achpt1	13achpt1	13achpt1	13achpt2	13achl8_	13achl8_	13achl8_	**mean n=14**	18ach8	18ach9	18ach11	**mean n=3**	3ch3	3ch4	**mean n=2**
Cu	0.02	0.05	0.06	0.03	<mdl	<mdl	0.03	0.05	<mdl	<mdl	0.03	0.07	<mdl	0.03	**0.03**	<mdl	<mdl	0.03	**0.01**	0.08	<mdl	**0.04**
Mn	0.01	0.03	<mdl	0.02	<mdl	<mdl	0.02	<mdl	<mdl	0.02	0.01	0.01	0.01	<mdl	**0.01**	<mdl	<mdl	<mdl	**0.00**	0.01	0.01	**0.01**
Fe	34.14	32.30	34.37	34.49	33.90	34.60	34.60	34.63	34.07	34.84	34.46	34.38	34.57	34.07	**34.24**	32.12	32.22	33.35	**32.56**	7.92	6.48	**7.20**
Co	0.04	0.09	0.08	0.06	0.05	0.02	0.05	0.07	0.10	0.02	0.07	0.09	0.09	0.08	**0.07**	1.69	1.81	1.02	**1.51**	17.56	24.23	**20.90**
Ni	0.01	0.04	0.06	0.09	0.04	0.00	0.03	0.00	0.06	0.01	0.03	0.04	0.06	0.03	**0.04**	0.28	0.20	0.11	**0.20**	9.66	5.05	**7.36**
Sb	0.02	<mdl	<mdl	<mdl	0.02	0.01	<mdl	0.03	<mdl	0.03	0.04	<mdl	<mdl	<mdl	**0.01**	0.06	<mdl	0.03	**0.03**	<mdl	<mdl	**<mdl**
As	46.39	46.18	47.31	46.70	46.35	46.64	46.47	46.49	47.08	46.14	45.99	46.62	46.74	46.85	**46.57**	47.80	47.46	45.44	**46.90**	45.08	43.69	**44.39**
S	18.89	18.99	18.89	18.97	19.38	19.50	19.48	19.57	18.76	19.36	19.84	19.18	19.27	19.26	**19.24**	18.16	18.44	19.89	**18.83**	19.51	20.15	**19.83**
Se	0.26	0.31	0.30	0.32	0.20	0.39	0.24	0.36	0.27	0.45	0.28	0.38	0.31	0.34	**0.32**	0.33	0.33	0.33	**0.33**	0.21	0.39	**0.30**
Total	99.77	97.99	101.07	100.68	99.96	101.16	100.91	101.20	100.35	100.87	100.74	100.77	101.06	100.67	**100.51**	100.43	100.46	100.20	**100.36**	100.03	100.01	**100.02**
Formulae, calculated to 3 a.p.f.u																						
Cu	0.000	0.001	0.002	0.001	-	-	0.001	0.001	-	0.000	0.001	0.002	-	0.001	**0.001**	-	-	0.001	**0.000**	0.002	-	**0.001**
Mn	0.000	0.001	-	0.001	-	-	0.000	-	-	0.001	0.000	0.000	0.000	-	**0.000**	-	-	-	**0.000**	0.000	0.000	**0.000**
Fe	1.005	0.967	1.002	1.007	0.993	1.002	1.003	1.001	1.000	1.012	0.997	1.001	1.003	0.993	**0.999**	0.949	0.949	0.969	**0.956**	0.234	0.190	**0.212**
Co	0.001	0.003	0.002	0.002	0.001	0.001	0.001	0.002	0.003	0.001	0.002	0.003	0.003	0.002	**0.002**	0.047	0.050	0.028	**0.042**	0.492	0.674	**0.583**
Ni	0.000	0.001	0.002	0.002	0.001	0.000	0.001	0.000	0.002	0.000	0.001	0.001	0.002	0.001	**0.001**	0.008	0.006	0.003	**0.005**	0.272	0.141	**0.206**
Sb	0.000	-	-	-	0.000	0.000	-	0.000	-	0.000	0.001	-	-	-	**0.000**	0.001	-	0.000	**0.000**	-	-	**-**
As	1.018	1.030	1.028	1.016	1.012	1.006	1.005	1.002	1.030	0.998	0.992	1.012	1.011	1.018	**1.013**	1.053	1.042	0.985	**1.027**	0.993	0.956	**0.974**
S	0.969	0.990	0.959	0.965	0.988	0.983	0.984	0.986	0.959	0.979	1.000	0.973	0.974	0.978	**0.978**	0.935	0.946	1.007	**0.963**	1.004	1.030	**1.017**
Se	0.005	0.007	0.006	0.007	0.004	0.008	0.005	0.007	0.006	0.009	0.006	0.008	0.006	0.007	**0.007**	0.007	0.007	0.007	**0.007**	0.004	0.008	**0.006**
S(+Se)	0.974	0.997	0.965	0.971	0.993	0.991	0.989	0.993	0.965	0.988	1.006	0.981	0.981	0.985	**0.984**	0.942	0.953	1.014	**0.970**	1.008	1.038	**1.023**

Table A1. Complete electron probe microanalysis data for arsenopyrite (continued)

	420m M2													Drillcore										
	Apy at relacement boundaries with Lo					**Apy at relacement boundaries with Lo**																		
	3CH					**8ach5**								**1CHAL**										
	3ch6	3chpt9	3chpt10	**mean n=3**	3chpt4 Apy	8ach5	8ach9	**mean1 n=2**	8ach1	8ach3	8ach8	8ach13	**mean2 n=4**	1chal3	1chalp01	1chalp02	1chalp03	1chalp07	1chalp09	1chalp11	1chalp12	1chalp14	1chalp15	**mean n=10**
Cu	0.03	<mdl	<mdl	**0.01**	0.02	0.02	0.02	**0.02**	<mdl	0.06	0.02	<mdl	**0.02**	<mdl	0.04	0.01	0.03	<mdl	<mdl	0.03	0.01	<mdl	<mdl	**0.01**
Mn	<mdl	0.02	<mdl	**0.01**	0.01	0.02	<mdl	**0.01**	0.03	0.02	<mdl	<mdl	**0.01**	0.02	0.02	0.01	<mdl	<mdl	<mdl	<mdl	0.01	0.01	0.01	**0.01**
Fe	24.80	26.04	26.47	**25.77**	27.47	33.63	33.72	**33.68**	33.83	33.69	33.15	33.09	**33.44**	34.11	34.17	33.44	33.22	33.62	33.49	34.22	33.67	33.92	33.53	**33.74**
Co	4.27	3.90	3.54	**3.90**	6.90	0.19	0.22	**0.21**	0.34	0.33	0.37	0.34	**0.34**	0.32	0.19	0.11	0.25	0.24	0.17	0.16	0.20	0.01	0.17	**0.18**
Ni	3.58	2.79	2.33	**2.90**	0.85	0.04	0.07	**0.06**	0.28	0.28	0.21	0.17	**0.23**	0.05	0.07	0.07	0.08	0.06	0.10	0.01	0.10	0.08	0.02	**0.06**
Sb	<mdl	<mdl	<mdl	**<mdl**	<mdl	0.04	<mdl	**0.02**	<mdl	<mdl	<mdl	<mdl	**<mdl**	<mdl	0.01	0.02	<mdl	<mdl	<mdl	<mdl	<mdl	<mdl	0.04	**0.01**
As	50.12	49.21	50.62	**49.98**	45.39	46.27	45.83	**46.05**	47.79	47.52	46.92	47.20	**47.36**	45.98	47.19	46.73	46.91	47.22	46.85	46.51	46.55	46.34	46.88	**46.72**
S	16.25	16.70	15.46	**16.14**	19.42	19.06	19.38	**19.22**	18.09	18.16	18.57	18.14	**18.24**	19.28	18.51	19.17	18.80	18.69	18.46	18.99	19.06	19.21	19.04	**18.92**
Se	0.36	0.40	0.31	**0.36**	0.39	0.23	0.33	**0.28**	0.43	0.29	0.35	0.31	**0.34**	0.38	0.36	0.35	0.36	0.29	0.35	0.27	0.29	0.32	0.41	**0.34**
Total	99.41	99.06	98.74	**99.07**	100.44	99.51	99.57	**99.54**	100.78	100.33	99.58	99.25	**99.99**	100.13	100.56	99.91	99.66	100.12	99.41	100.21	99.89	99.89	100.10	**99.99**
Formulae, calculated to 3 a.p.f.u																								
Cu	0.001	-	-	**0.000**	0.000	0.000	0.001	**0.001**	-	0.001	0.000	-	**0.000**	-	0.001	0.000	0.001	-	-	0.001	0.000	-	-	**0.000**
Mn	-	0.001	0.000	**0.000**	0.000	0.000	-	**0.000**	0.001	0.001	-	-	**0.000**	0.001	0.001	0.000	-	-	-	-	0.000	0.000	0.000	**0.000**
Fe	0.758	0.793	0.819	**0.790**	0.802	0.991	0.990	**0.991**	0.996	0.995	0.982	0.987	**0.990**	0.997	1.004	0.982	0.981	0.990	0.994	1.003	0.989	0.995	0.985	**0.992**
Co	0.124	0.113	0.104	**0.113**	0.191	0.005	0.006	**0.006**	0.010	0.009	0.010	0.010	**0.010**	0.009	0.005	0.003	0.007	0.007	0.005	0.005	0.005	0.000	0.005	**0.005**
Ni	0.104	0.081	0.069	**0.084**	0.024	0.001	0.002	**0.002**	0.008	0.008	0.006	0.005	**0.007**	0.001	0.002	0.002	0.002	0.002	0.003	0.000	0.003	0.002	0.001	**0.002**
Sb	-	-	-	**-**	-	0.001	-	**0.000**	-	-	-	-	**-**	-	0.000	0.000	-	-	-	-	-	-	0.001	**0.000**
As	1.141	1.118	1.168	**1.142**	0.988	1.017	1.003	**1.010**	1.049	1.046	1.036	1.050	**1.045**	1.002	1.033	1.023	1.033	1.037	1.036	1.016	1.020	1.013	1.026	**1.024**
S	0.865	0.886	0.833	**0.862**	0.987	0.979	0.991	**0.985**	0.928	0.934	0.958	0.943	**0.941**	0.982	0.947	0.981	0.968	0.959	0.955	0.970	0.976	0.982	0.974	**0.969**
Se	0.008	0.009	0.007	**0.008**	0.008	0.005	0.007	**0.006**	0.009	0.006	0.007	0.007	**0.007**	0.008	0.007	0.007	0.008	0.006	0.007	0.006	0.006	0.007	0.008	**0.007**
S(+Se)	0.873	0.895	0.840	**0.869**	0.995	0.984	0.998	**0.991**	0.937	0.940	0.966	0.949	**0.948**	0.990	0.954	0.988	0.975	0.965	0.962	0.975	0.982	0.988	0.983	**0.976**

Table A1. Complete electron probe microanalysis data for arsenopyrite (continued)

	10CHAL												
	10chalp01	10chalp02	10chalp03	10chalp06	10chall2_	10chall2_	10chalp11	10chalp12	**mean1 n=8**	10chalp07	10chall2_	10chall2_	**mean2 n=3**
Cu	0.03	<mdl	<mdl	0.03	0.09	0.03	0.02	0.04	**0.03**	<mdl	0.06	0.03	**0.03**
Mn	0.01	<mdl	<mdl	<mdl	<mdl	0.03	<mdl	0.02	**0.01**	0.03	<mdl	<mdl	**0.01**
Fe	33.99	33.57	34.30	33.99	33.55	34.39	33.22	34.26	**33.91**	33.46	33.53	33.96	**33.65**
Co	0.16	0.20	0.13	0.17	0.30	0.11	0.24	0.14	**0.18**	0.17	0.21	0.26	**0.21**
Ni	0.07	<mdl	0.04	0.06	0.09	0.03	0.07	0.06	**0.05**	0.15	0.11	0.16	**0.14**
Sb	0.05	<mdl	<mdl	<mdl	0.07	0.03	<mdl	0.04	**0.02**	<mdl	<mdl	0.06	**0.02**
As	47.08	46.92	46.54	46.96	47.57	46.38	46.64	46.88	**46.87**	46.10	47.43	47.41	**46.98**
S	18.52	18.98	19.12	18.91	18.60	19.30	18.92	19.08	**18.93**	19.13	18.52	18.59	**18.75**
Se	0.38	0.36	0.24	0.35	0.27	0.26	0.29	0.38	**0.32**	0.25	0.42	0.42	**0.36**
Total	100.28	100.02	100.39	100.46	100.53	100.55	99.41	100.88	**100.32**	99.31	100.29	100.87	**100.16**
Formulae, calculated to 3 a.p.f.u													
Cu	0.001	-	-	0.001	0.002	0.001	0.001	0.001	**0.001**	-	0.001	0.001	**0.001**
Mn	0.000	-	-	-	-	0.001	-	0.000	**0.000**	0.001	-	-	**0.000**
Fe	1.001	0.987	1.003	0.996	0.986	1.002	0.982	0.998	**0.994**	0.987	0.988	0.995	**0.990**
Co	0.005	0.006	0.004	0.005	0.008	0.003	0.007	0.004	**0.005**	0.005	0.006	0.007	**0.006**
Ni	0.002	-	0.001	0.002	0.003	0.001	0.002	0.002	**0.001**	0.004	0.003	0.004	**0.004**
Sb	0.001	-	-	-	0.001	0.000	-	0.001	**0.000**	-	-	0.001	**0.000**
As	1.033	1.028	1.014	1.025	1.042	1.007	1.028	1.018	**1.025**	1.014	1.042	1.035	**1.030**
S	0.950	0.972	0.974	0.965	0.952	0.979	0.974	0.968	**0.967**	0.983	0.951	0.949	**0.961**
Se	0.008	0.007	0.005	0.007	0.006	0.005	0.006	0.008	**0.007**	0.005	0.009	0.009	**0.008**
S(+Se)	0.958	0.979	0.979	0.972	0.958	0.985	0.981	0.976	**0.973**	0.989	0.960	0.957	**0.968**

Table A2. Complete electron probe microanalysis data for lollingite

840m M2

	1RH								2RH														
	1rh2	**1rh3**	**1rh13**	**1rh16**	**1rh17**	**1rh22**	**mean n=6**	1rh19	**2rhl01_1**	**2rhl01_2**	**2rhl01_3**	**2rhl01_4**	**2rhl02_1**	**2rhl02_2**	**2rhl02_3**	**2rhl02_4**	**2rhp08**	**2rhp09**	**2rhl04_1**	**2rhl04_2**	**2rhl04_3**	**2rhl04_4**	**mean n=14**
Cu	0.05	0.03	<mdl	0.03	0.02	0.04	**0.03**	0.01	0.02	<mdl	<mdl	<mdl	<mdl	<mdl	<mdl	<mdl	0.01	<mdl	0.03	0.02	<mdl	0.01	**0.01**
Mn	<mdl	<mdl	<mdl	0.01	<mdl	0.01	**0.00**	0.02	0.02	<mdl	<mdl	<mdl	0.01	0.00	0.04	<mdl	<mdl	0.01	0.01	<mdl	<mdl	0.01	**0.01**
Fe	26.49	26.62	26.44	25.81	25.57	25.51	**26.07**	23.83	26.63	26.75	26.75	26.77	27.25	27.18	26.95	27.10	26.95	26.72	27.18	27.10	27.26	27.00	**26.97**
Co	0.45	0.42	0.34	0.41	0.43	0.68	**0.46**	0.76	0.30	0.31	0.35	0.27	0.34	0.32	0.28	0.31	0.33	0.36	0.26	0.28	0.31	0.32	**0.31**
Ni	0.91	0.94	0.72	1.60	1.50	1.78	**1.24**	3.46	0.59	0.51	0.61	0.51	0.59	0.57	0.58	0.60	0.66	0.66	0.56	0.51	0.54	0.50	**0.57**
Sb	<mdl	<mdl	0.10	<mdl	<mdl	0.05	**0.02**	0.04	0.03	<mdl	0.02	<mdl	0.02	0.05	<mdl	<mdl	<mdl	<mdl	<mdl	0.04	<mdl	<mdl	**0.01**
As	70.14	69.94	70.12	69.91	69.90	70.01	**70.00**	69.92	70.12	69.73	70.08	69.95	70.19	70.32	70.07	69.81	70.10	70.26	69.80	69.97	70.27	70.06	**70.05**
S	1.45	1.53	1.08	1.60	1.51	1.54	**1.45**	1.34	1.52	1.55	1.52	1.59	1.45	1.43	1.47	1.50	1.57	1.52	1.46	1.47	1.46	1.54	**1.50**
Se	0.53	0.56	0.52	0.43	0.46	0.49	**0.50**	0.38	0.47	0.63	0.29	0.63	0.53	0.25	0.52	0.44	0.65	0.54	0.40	0.65	0.49	0.54	**0.50**
Total	**100.03**	**100.03**	**99.33**	**99.80**	**99.37**	**100.10**	**99.78**	99.75	**99.71**	**99.47**	**99.62**	**99.71**	**100.39**	**100.12**	**99.90**	**99.76**	**100.27**	**100.08**	**99.68**	**100.04**	**100.33**	**99.98**	**99.93**
Formulae, calculated to 3 a.p.f.u																							
Cu	0.001	0.001	-	0.001	0.000	0.001	**0.001**	0.000	0.001	-	-	-	-	-	-	-	0.000	-	0.001	0.001	-	0.000	**0.000**
Mn	-	-	-	0.000	-	0.000	**0.000**	0.001	0.001	-	-	-	0.000	0.000	0.001	-	-	0.000	0.000	-	-	0.000	**0.000**
Fe	0.957	0.961	0.967	0.933	0.930	0.921	**0.945**	0.865	0.965	0.971	0.970	0.969	0.980	0.981	0.975	0.980	0.970	0.965	0.984	0.979	0.982	0.975	**0.975**
Co	0.016	0.014	0.012	0.014	0.015	0.023	**0.016**	0.026	0.010	0.011	0.012	0.009	0.011	0.011	0.010	0.011	0.011	0.012	0.009	0.010	0.011	0.011	**0.011**
Ni	0.031	0.032	0.025	0.055	0.052	0.061	**0.043**	0.120	0.020	0.018	0.021	0.017	0.020	0.020	0.020	0.021	0.023	0.023	0.019	0.017	0.018	0.017	**0.020**
Total M	**1.006**	**1.008**	**1.004**	**1.004**	**0.997**	**1.007**	**1.004**	1.012	**0.997**	**0.999**	**1.003**	**0.996**	**1.013**	**1.011**	**1.005**	**1.011**	**1.004**	**1.000**	**1.013**	**1.006**	**1.010**	**1.004**	**1.005**
As	1.889	1.881	1.912	1.884	1.895	1.884	**1.891**	1.893	1.894	1.887	1.894	1.888	1.882	1.892	1.889	1.883	1.881	1.890	1.884	1.883	1.886	1.885	**1.887**
Sb	-	-	0.002	-	-	0.001	**0.000**	0.001	0.001	-	0.000	-	0.000	0.001	-	-	-	-	-	0.001	-	-	**0.000**
S	0.091	0.096	0.069	0.101	0.096	0.097	**0.092**	0.085	0.096	0.098	0.096	0.100	0.091	0.090	0.092	0.095	0.099	0.096	0.092	0.093	0.091	0.097	**0.095**
Se	0.014	0.014	0.013	0.011	0.012	0.012	**0.013**	0.010	0.012	0.016	0.007	0.016	0.014	0.006	0.013	0.011	0.017	0.014	0.010	0.017	0.013	0.014	**0.013**
S(+Se)	**0.105**	**0.111**	**0.082**	**0.112**	**0.108**	**0.109**	**0.104**	0.095	**0.108**	**0.114**	**0.103**	**0.116**	**0.105**	**0.096**	**0.106**	**0.106**	**0.115**	**0.110**	**0.102**	**0.109**	**0.104**	**0.111**	**0.108**

Table A2. Complete electron probe microanalysis data for lollingite (continued)

														800m M2					760m M2
	7RH						8RH							20RH					14RH2
	7rh01	7rh06	7rh07	7rh11	7rh13	mean n=5	8rhl2_1	8rhl2_2	8rhl4_1	8rhl4_2	8rhl4_3	8rhl4_4	mean n=6	0rhpl02_	0rhpl02_	0rhpl02_	0rhpl02_	0rhpl02_	mean n=5	
Cu	0.04	<mdl	<mdl	<mdl	0.02	**0.01**	<mdl	0.06	<mdl	0.01	<mdl	<mdl	**0.01**	<mdl	0.02	0.01	<mdl	0.02	**0.01**	0.01
Mn	<mdl	<mdl	<mdl	<mdl	<mdl	**<mdl**	<mdl	0.01	<mdl	0.01	0.03	<mdl	**0.01**	0.02	<mdl	<mdl	<mdl	<mdl	**0.00**	0.03
Fe	26.36	25.73	25.38	24.53	24.76	**25.35**	26.10	26.06	26.46	26.48	26.22	26.24	**26.26**	26.01	26.21	26.09	26.13	26.17	**26.12**	22.37
Co	0.59	0.76	0.73	0.60	0.87	**0.71**	0.46	0.50	0.53	0.49	0.47	0.54	**0.50**	0.50	0.49	0.48	0.47	0.55	**0.50**	1.81
Ni	1.11	1.55	1.47	1.96	1.23	**1.46**	0.82	0.90	0.96	0.90	0.91	1.02	**0.92**	1.33	1.30	1.25	1.35	1.37	**1.32**	3.44
Sb	0.00	0.08	<mdl	<mdl	0.03	**0.02**	<mdl	<mdl	0.04	<mdl	0.04	0.01	**0.02**	<mdl	<mdl	<mdl	<mdl	<mdl	**<mdl**	<mdl
As	70.48	70.35	70.11	69.65	70.15	**70.15**	70.19	70.40	70.40	69.95	70.27	69.73	**70.16**	69.91	70.06	69.70	69.90	69.99	**69.91**	71.46
S	1.40	1.46	1.40	1.33	1.15	**1.35**	1.08	1.20	1.32	1.38	1.37	1.35	**1.28**	1.49	1.51	1.56	1.39	1.50	**1.49**	0.87
Se	0.40	0.48	0.34	0.40	0.65	**0.46**	0.64	0.59	0.43	0.55	0.58	0.50	**0.55**	0.49	0.36	0.47	0.49	0.61	**0.48**	0.49
Total	**100.39**	**100.41**	**99.42**	**98.47**	**98.87**	**99.51**	**99.29**	**99.73**	**100.14**	**99.77**	**99.90**	**99.40**	**99.70**	**99.74**	**99.95**	**99.55**	**99.74**	**100.20**	**99.84**	100.48
Formulae, calculated to 3 a.p.f.u																				
Cu	0.001	-	-	-	0.001	**0.000**	-	0.002	-	0.000	-	-	**0.000**	-	0.001	0.000	-	0.001	**0.000**	0.000
Mn	-	-	-	-	-	**-**	-	0.000	-	0.000	0.001	-	**0.000**	0.001	-	-	-	-	**0.000**	0.001
Fe	0.949	0.927	0.924	0.903	0.911	**0.923**	0.955	0.948	0.957	0.960	0.951	0.955	**0.954**	0.942	0.947	0.946	0.947	0.943	**0.945**	0.813
Co	0.020	0.026	0.025	0.021	0.030	**0.024**	0.016	0.017	0.018	0.017	0.016	0.019	**0.017**	0.017	0.017	0.017	0.016	0.019	**0.017**	0.062
Ni	0.038	0.053	0.051	0.069	0.043	**0.051**	0.029	0.031	0.033	0.031	0.032	0.035	**0.032**	0.046	0.045	0.043	0.047	0.047	**0.045**	0.119
Total M	**1.009**	**1.006**	**1.000**	**0.993**	**0.985**	**0.999**	**1.000**	**0.999**	**1.008**	**1.008**	**0.999**	**1.009**	**1.004**	**1.006**	**1.009**	**1.006**	**1.010**	**1.010**	**1.008**	0.996
As	1.892	1.889	1.903	1.911	1.924	**1.904**	1.915	1.909	1.897	1.890	1.899	1.892	**1.900**	1.888	1.887	1.884	1.889	1.881	**1.886**	1.936
Sb	0.000	0.001	-	-	0.000	**0.000**	-	-	0.001	-	0.001	0.000	**0.000**	-	-	-	-	-	-	-
S	0.088	0.091	0.089	0.085	0.074	**0.085**	0.069	0.076	0.083	0.087	0.086	0.086	**0.081**	0.094	0.095	0.098	0.088	0.094	**0.094**	0.055
Se	0.010	0.012	0.009	0.010	0.017	**0.012**	0.017	0.015	0.011	0.014	0.015	0.013	**0.014**	0.012	0.009	0.012	0.013	0.016	**0.012**	0.013
S(+Se)	**0.098**	**0.104**	**0.097**	**0.096**	**0.091**	**0.097**	**0.085**	**0.091**	**0.094**	**0.101**	**0.101**	**0.099**	**0.095**	**0.106**	**0.104**	**0.110**	**0.101**	**0.110**	**0.106**	0.068

Table A2. Complete electron probe microanalysis data for lollingite (continued)

	16RH																				
	16RHl2_1	**16RHl2_2**	**16RHl2_3**	**16RHl2_4**	**16RHl4_1**	**16RHl4_2**	**16RHl4_3**	**16RHl4_4**	**16RHl4_5**	**16RHl4_6**	**16RHp6**	**16RHp7**	**16RHp8**	**mean1 n=13**	**16RHl5_1**	**16RHl5_2**	**16RHl5_3**	**16RHl5_4**	**16RHl5_5**	**16RHl6_1**	**16RHl6_2**
Cu	0.03	<mdl	0.04	<mdl	0.03	0.02	0.01	0.02	<mdl	<mdl	<mdl	<mdl	<mdl	**0.01**	<mdl	<mdl	<mdl	0.05	<mdl	0.05	<mdl
Mn	0.01	0.01	<mdl	0.02	0.01	<mdl	0.02	<mdl	<mdl	<mdl	<mdl	<mdl	0.04	**0.01**	<mdl	<mdl	<mdl	<mdl	0.01	<mdl	0.03
Fe	25.04	25.51	25.74	25.67	25.98	26.05	26.16	25.78	26.19	25.76	24.81	25.23	25.08	**25.61**	23.30	23.46	23.23	24.33	23.56	22.59	22.72
Co	0.75	0.68	0.64	0.63	0.72	0.74	0.76	0.67	0.69	0.71	0.68	0.69	0.70	**0.70**	1.01	1.05	1.11	1.18	1.18	1.07	1.09
Ni	2.16	1.77	1.66	1.83	1.56	1.56	1.49	1.43	1.53	1.51	1.16	1.12	1.13	**1.53**	3.37	3.33	3.21	2.63	3.44	3.67	3.60
Sb	<mdl	<mdl	<mdl	0.03	<mdl	<mdl	0.02	0.06	<mdl	<mdl	0.07	0.03	0.01	**0.02**	<mdl	0.07	<mdl	0.03	0.03	0.03	0.01
As	70.91	70.29	70.42	70.23	70.13	70.52	70.05	70.71	70.33	70.48	70.60	70.38	70.71	**70.44**	70.20	70.28	70.64	67.24	70.44	70.28	70.28
S	0.89	1.17	1.24	1.30	1.37	1.32	1.35	1.26	1.32	1.26	0.93	0.91	0.96	**1.18**	1.31	1.31	1.35	3.74	1.33	1.35	1.35
Se	0.45	0.52	0.67	0.50	0.62	0.38	0.58	0.45	0.42	0.56	0.52	0.56	0.49	**0.52**	0.62	0.63	0.42	0.53	0.39	0.55	0.34
Total	**100.26**	**99.96**	**100.40**	**100.22**	**100.43**	**100.60**	**100.43**	**100.37**	**100.47**	**100.29**	**98.78**	**98.92**	**99.11**	**100.02**	**99.82**	**100.13**	**99.97**	**99.74**	**100.39**	**99.58**	**99.42**
Formulae, calculated to 3 a.p.f.u																					
Cu	0.001	-	0.001	0.000	0.001	0.001	0.000	0.001	-	-	-	-	-	**0.000**	-	-	-	0.001	-	0.002	-
Mn	0.001	0.000	0.000	0.001	0.001	-	0.001	-	-	-	-	-	0.001	**0.000**	-	-	-	-	0.000	-	0.001
Fe	0.910	0.926	0.929	0.927	0.936	0.937	0.942	0.931	0.943	0.931	0.917	0.930	0.922	**0.929**	0.847	0.850	0.843	0.859	0.851	0.824	0.829
Co	0.026	0.024	0.022	0.022	0.025	0.025	0.026	0.023	0.024	0.024	0.024	0.024	0.024	**0.024**	0.035	0.036	0.038	0.040	0.040	0.037	0.038
Ni	0.075	0.061	0.057	0.063	0.053	0.053	0.051	0.049	0.052	0.052	0.041	0.039	0.040	**0.053**	0.117	0.115	0.111	0.088	0.118	0.127	0.125
Total M	**1.012**	**1.011**	**1.010**	**1.013**	**1.015**	**1.016**	**1.020**	**1.004**	**1.019**	**1.008**	**0.981**	**0.993**	**0.988**	**1.007**	**0.999**	**1.001**	**0.992**	**0.988**	**1.010**	**0.990**	**0.993**
As	1.920	1.901	1.896	1.892	1.883	1.891	1.880	1.904	1.888	1.899	1.944	1.933	1.938	**1.905**	1.903	1.899	1.911	1.769	1.896	1.910	1.912
Sb	-	-	-	0.000	-	-	0.000	0.001	-	-	0.001	0.001	0.000	**0.000**	-	0.001	-	0.000	0.000	0.000	0.000
S	0.057	0.074	0.078	0.082	0.086	0.083	0.085	0.079	0.083	0.079	0.060	0.058	0.061	**0.074**	0.083	0.082	0.085	0.230	0.084	0.085	0.086
Se	0.012	0.013	0.017	0.013	0.016	0.010	0.015	0.011	0.011	0.014	0.014	0.015	0.013	**0.013**	0.016	0.016	0.011	0.013	0.010	0.014	0.009
S(+Se)	**0.068**	**0.088**	**0.095**	**0.095**	**0.102**	**0.093**	**0.099**	**0.091**	**0.093**	**0.094**	**0.073**	**0.073**	**0.074**	**0.087**	**0.099**	**0.099**	**0.096**	**0.243**	**0.094**	**0.100**	**0.094**

Table A2. Complete electron probe microanalysis data for lollingite (continued)

	560m M2																				
	16RH				13aCH																
2	16RHl6_3	16RHl6_4	16RHl6_5	mean2 n=10	13ach3	13ach7	13achl2_1	13achl2_2	13achl2_3	13achl3_1	13achl3_2	13achl3_3	13achl4_1	13achl4_2	13achl4_3	13achl5_1	13achl5_2	13achl5_3	13achl6_1	13achl6_2	13achl6_3
Cu	0.01	0.01	<mdl	**0.01**	0.02	0.01	<mdl	<mdl	0.01	0.02	<mdl	0.02	<mdl	<mdl	<mdl	<mdl	<mdl	0.02	0.02	0.03	<mdl
Mn	<mdl	0.03	<mdl	**0.01**	0.02	0.04	0.01	<mdl	<mdl	<mdl	0.01	0.01	<mdl	0.03	<mdl	<mdl	<mdl	0.02	<mdl	0.02	<mdl
Fe	22.95	23.10	22.95	**23.22**	27.34	27.18	27.54	27.46	27.51	27.14	26.99	26.82	26.98	27.05	26.95	27.45	27.18	27.47	27.31	27.38	27.03
Co	1.03	1.10	1.24	**1.11**	0.17	0.18	0.12	0.15	0.14	0.18	0.13	0.14	0.18	0.14	0.10	0.17	0.10	0.16	0.13	0.16	0.13
Ni	3.64	3.72	3.78	**3.44**	0.67	0.68	0.69	0.66	0.64	0.60	0.60	0.63	0.63	0.66	0.74	0.65	0.69	0.66	0.67	0.66	0.61
Sb	<mdl	0.05	<mdl	**0.02**	0.03	0.04	<mdl	0.01	0.02	<mdl	0.02	0.07	<mdl	0.08	<mdl	<mdl	<mdl	<mdl	<mdl	0.03	0.00
As	70.22	70.45	70.49	**70.05**	70.55	70.69	70.59	70.13	70.92	70.77	70.69	70.60	70.62	70.97	70.50	70.06	70.85	70.37	70.84	70.78	70.46
S	1.36	1.29	1.26	**1.56**	1.34	1.28	1.35	1.36	1.35	1.22	1.20	1.31	1.21	1.14	1.22	1.35	1.26	1.33	1.40	1.24	1.34
Se	0.53	0.67	0.61	**0.53**	0.53	0.63	0.46	0.46	0.43	0.57	0.45	0.50	0.66	0.58	0.64	0.61	0.47	0.60	0.47	0.59	0.48
Total	**99.75**	**100.42**	**100.34**	**99.96**	**100.66**	**100.74**	**100.76**	**100.22**	**101.03**	**100.50**	**100.10**	**100.10**	**100.28**	**100.65**	**100.15**	**100.29**	**100.55**	**100.64**	**100.84**	**100.89**	**100.05**
Formulae, calculated to 3 a.p.f.u																					
Cu	0.000	0.000	-	**0.000**	0.001	0.000	-	-	0.000	0.001	-	0.001	-	-	-	-	-	0.001	0.001	0.001	-
Mn	-	0.001	-	**0.000**	0.001	0.002	0.000	-	-	-	0.000	0.000	-	0.001	-	-	-	0.001	-	0.001	-
Fe	0.834	0.835	0.830	**0.840**	0.983	0.977	0.988	0.990	0.985	0.979	0.978	0.971	0.976	0.976	0.975	0.989	0.979	0.987	0.979	0.983	0.978
Co	0.035	0.038	0.043	**0.038**	0.006	0.006	0.004	0.005	0.005	0.006	0.005	0.005	0.006	0.005	0.003	0.006	0.003	0.006	0.005	0.005	0.004
Ni	0.126	0.128	0.130	**0.119**	0.023	0.023	0.024	0.022	0.022	0.021	0.021	0.022	0.022	0.023	0.025	0.022	0.024	0.023	0.023	0.022	0.021
Total M	**0.996**	**1.003**	**1.003**	**0.998**	**1.013**	**1.009**	**1.016**	**1.018**	**1.012**	**1.006**	**1.004**	**0.998**	**1.004**	**1.004**	**1.004**	**1.017**	**1.006**	**1.017**	**1.007**	**1.013**	**1.003**
As	1.904	1.899	1.901	**1.890**	1.890	1.894	1.888	1.885	1.893	1.903	1.909	1.905	1.903	1.908	1.902	1.882	1.903	1.885	1.894	1.894	1.900
Sb	-	0.001	-	**0.000**	0.000	0.001	-	0.000	0.000	-	0.000	0.001	-	0.001	-	-	-	-	-	0.000	0.000
S	0.086	0.081	0.080	**0.098**	0.084	0.080	0.084	0.086	0.084	0.077	0.076	0.083	0.076	0.072	0.077	0.085	0.079	0.083	0.087	0.078	0.084
Se	0.014	0.017	0.016	**0.014**	0.013	0.016	0.012	0.012	0.011	0.015	0.011	0.013	0.017	0.015	0.016	0.015	0.012	0.015	0.012	0.015	0.012
S(+Se)	**0.100**	**0.098**	**0.095**	**0.112**	**0.097**	**0.096**	**0.096**	**0.097**	**0.095**	**0.091**	**0.087**	**0.096**	**0.093**	**0.087**	**0.093**	**0.100**	**0.091**	**0.098**	**0.099**	**0.093**	**0.096**

Table A2. Complete electron probe microanalysis data for lollingite (continued)

								420m M1	420m M2												
																Drillcore					
	13aCH							18ach14	3CH	8aCH						1CHAL					
3	13achl7_1	13achl7_2	13achl7_3	13achl9_1	13achl9_2	13achl9_3	mean n=23	18ach14	3ch5	8ach2	8ach4	8ach7	8ach11	8ach14	mean n=5	1chal2	1chalp04	1chalp05	1chalp06	1chalp16	mean n=5
Cu	0.03	<mdl	<mdl	<mdl	<mdl	<mdl	**0.01**	0.02	<mdl	<mdl	<mdl	0.03	<mdl	0.04	**0.01**	0.02	0.04	0.03	<mdl	<mdl	**0.02**
Mn	<mdl	<mdl	<mdl	0.01	0.03	<mdl	**0.01**	<mdl	0.03	<mdl	0.02	<mdl	<mdl	<mdl	**0.00**	<mdl	0.02	0.02	0.02	0.01	**0.02**
Fe	27.40	27.15	27.35	26.88	26.90	26.85	**27.19**	20.64	18.56	25.22	26.28	25.22	25.77	25.53	**25.60**	26.12	25.99	26.38	26.22	25.79	**26.10**
Co	0.20	0.15	0.17	0.18	0.16	0.17	**0.15**	3.30	3.75	0.68	0.45	0.48	0.50	0.50	**0.52**	0.39	0.46	0.46	0.42	0.45	**0.44**
Ni	0.68	0.69	0.70	0.67	0.64	0.68	**0.66**	4.05	5.36	2.10	1.46	1.82	1.16	1.92	**1.69**	1.00	1.27	1.15	1.22	1.10	**1.15**
Sb	<mdl	0.02	<mdl	<mdl	<mdl	<mdl	**0.01**	<mdl	<mdl	<mdl	0.03	<mdl	0.08	0.01	**0.02**	0.01	<mdl	<mdl	<mdl	<mdl	**0.00**
As	70.57	70.31	70.56	70.43	70.51	70.55	**70.58**	70.15	71.13	70.36	70.71	70.58	70.45	70.29	**70.48**	70.28	70.28	70.18	70.58	70.58	**70.38**
S	1.36	1.26	1.26	1.27	1.32	1.31	**1.29**	1.15	0.75	1.33	1.16	1.04	0.94	1.12	**1.12**	1.40	1.42	1.42	1.40	1.40	**1.41**
Se	0.64	0.52	0.42	0.44	0.50	0.48	**0.53**	0.61	0.49	0.52	0.44	0.54	0.47	0.50	**0.49**	0.52	0.50	0.32	0.42	0.52	**0.46**
Total	**100.88**	**100.11**	**100.47**	**99.88**	**100.06**	**100.05**	**100.43**	99.92	100.08	**100.20**	**100.56**	**99.72**	**99.36**	**99.91**	**99.95**	**99.74**	**99.97**	**99.97**	**100.29**	**99.85**	**99.96**
Formulae, calculated to 3 a.p.f.u																					
Cu	0.001	-	-	-	-	-	**0.000**	0.000	-	-	-	0.001	-	0.001	**0.000**	0.001	0.001	0.001	-	-	**0.001**
Mn	-	-	-	0.000	0.001	-	**0.000**	-	0.001	-	0.001	-	-	-	**0.000**	-	0.001	0.001	0.001	0.000	**0.001**
Fe	0.982	0.982	0.985	0.975	0.974	0.972	**0.980**	0.752	0.680	0.912	0.948	0.920	0.944	0.928	**0.930**	0.948	0.940	0.954	0.946	0.936	**0.945**
Co	0.007	0.005	0.006	0.006	0.005	0.006	**0.005**	0.114	0.130	0.023	0.015	0.017	0.017	0.017	**0.018**	0.014	0.016	0.016	0.014	0.015	**0.015**
Ni	0.023	0.024	0.024	0.023	0.022	0.024	**0.023**	0.141	0.187	0.072	0.050	0.063	0.040	0.066	**0.058**	0.035	0.044	0.039	0.042	0.038	**0.039**
Total M	**1.013**	**1.011**	**1.015**	**1.004**	**1.002**	**1.001**	**1.009**	1.007	0.998	**1.007**	**1.014**	**1.001**	**1.002**	**1.012**	**1.007**	**0.997**	**1.002**	**1.011**	**1.003**	**0.989**	**1.000**
As	1.886	1.896	1.895	1.904	1.902	1.904	**1.897**	1.905	1.941	1.896	1.901	1.919	1.925	1.904	**1.909**	1.901	1.896	1.891	1.898	1.909	**1.899**
Sb	-	0.000	-	-	-	-	**0.000**	-	-	-	0.001	-	0.001	0.000	**0.000**	0.000	-	-	-	-	**0.000**
S	0.085	0.079	0.079	0.080	0.083	0.082	**0.081**	0.073	0.048	0.084	0.073	0.066	0.060	0.071	**0.071**	0.088	0.089	0.090	0.088	0.089	**0.089**
Se	0.016	0.013	0.011	0.011	0.013	0.012	**0.013**	0.016	0.013	0.013	0.011	0.014	0.012	0.013	**0.013**	0.013	0.013	0.008	0.011	0.013	**0.012**
S(+Se)	**0.101**	**0.093**	**0.090**	**0.092**	**0.096**	**0.095**	**0.095**	0.089	0.061	**0.097**	**0.084**	**0.080**	**0.072**	**0.084**	**0.083**	**0.102**	**0.102**	**0.098**	**0.099**	**0.102**	**0.101**

Table A2. Complete electron probe microanalysis data for lollingite (continued)

	10CHAL									
	10chall1_	**10chall1_**	**10chall1_**	**10chall1_**	**10chalp0**	**10chalp1**	**10chall5_**	**10chall5_**	**10chall5_**	**mean n=9**
Cu	0.02	<mdl	0.04	0.03	<mdl	<mdl	0.04	<mdl	0.01	**0.02**
Mn	<mdl	0.01	0.00	<mdl	0.02	<mdl	<mdl	<mdl	0.03	**0.01**
Fe	26.67	26.60	26.52	26.32	25.61	25.46	26.59	26.36	26.40	**26.28**
Co	0.40	0.45	0.36	0.42	0.43	0.50	0.46	0.40	0.40	**0.42**
Ni	1.06	1.13	1.11	1.15	1.17	1.61	0.90	0.93	0.88	**1.10**
Sb	0.07	0.02	<mdl	<mdl	<mdl	<mdl	<mdl	<mdl	<mdl	**0.01**
As	70.57	70.79	70.91	70.85	70.67	71.05	70.67	70.62	70.90	**70.78**
S	1.52	1.45	1.49	1.31	1.35	1.21	1.36	1.34	1.34	**1.37**
Se	0.52	0.45	0.48	0.29	0.45	0.52	0.53	0.43	0.48	**0.46**
Total	**100.81**	**100.88**	**100.90**	**100.37**	**99.69**	**100.36**	**100.55**	**100.08**	**100.43**	**100.45**
Formulae, calculated to 3 a.p.f.u										
Cu	0.001	-	0.001	0.001	-	-	0.001	-	0.000	**0.000**
Mn	-	0.000	0.000	-	0.001	-	-	-	0.001	**0.000**
Fe	0.956	0.953	0.950	0.950	0.931	0.921	0.957	0.954	0.952	**0.947**
Co	0.013	0.015	0.012	0.014	0.015	0.017	0.016	0.014	0.014	**0.014**
Ni	0.036	0.038	0.038	0.039	0.040	0.055	0.031	0.032	0.030	**0.038**
Total M	**1.006**	**1.007**	**1.001**	**1.004**	**0.987**	**0.994**	**1.005**	**1.000**	**0.997**	**1.000**
As	1.885	1.891	1.894	1.906	1.916	1.916	1.896	1.905	1.906	**1.902**
Sb	0.001	0.000	-	-	-	-	-	-	-	**0.000**
S	0.095	0.090	0.093	0.082	0.086	0.076	0.085	0.084	0.084	**0.086**
Se	0.013	0.011	0.012	0.008	0.011	0.013	0.013	0.011	0.012	**0.012**
S(+Se)	**0.108**	**0.102**	**0.105**	**0.090**	**0.097**	**0.090**	**0.099**	**0.095**	**0.097**	**0.098**

Table A3. Complete electron probe microanalysis data for pyrrhotite

840m M2

Po(Fe1-xS)

	1rh1	1rh5	**1RH mean n=2**	2rhp01	2rhp02	2rhp03	2rhl03_1	2rhl03_2	2rhl03_3	2rhp11	2rhl05_1	2rhl05_2	2rhl05_3	2rhl05_4	**2RH mean n=11**	7rh08	7rh12	**7RH mean n=2**	8rhl3_1	8rhl3_2	8rhl3_3	8rhl3_4	8rhl6_1
Cu	0.04	0.02	**0.03**	0.00	0.02	0.00	0.03	0.04	0.00	0.00	0.00	0.00	0.00	0.06	**0.01**	0.02	0.06	**0.04**	0.05	0.00	0.05	0.04	0.00
Mn	0.02	0.01	**0.02**	0.01	0.00	0.00	0.00	0.00	0.02	0.00	0.00	0.00	0.00	0.00	**0.00**	0.00	0.00	**0.00**	0.00	0.00	0.02	0.02	0.00
Fe	59.52	59.89	**59.70**	59.52	59.66	59.46	60.60	60.40	60.29	60.74	60.24	60.42	60.33	60.05	**60.16**	60.22	59.39	**59.81**	60.06	60.23	59.96	59.78	59.81
Co	0.00	0.00	**0.00**	0.00	0.00	0.00	0.00	0.02	0.00	0.00	0.00	0.00	0.01	0.01	**0.00**	0.00	0.02	**0.01**	0.03	0.00	0.00	0.00	0.02
Ni	0.04	0.01	**0.02**	0.01	0.01	0.02	0.00	0.00	0.00	0.02	0.01	0.03	0.05	0.04	**0.02**	0.02	0.04	**0.03**	0.02	0.01	0.05	0.04	0.00
Sb	0.04	0.01	**0.03**	0.02	0.00	0.06	0.00	0.02	0.06	0.00	0.00	0.00	0.03	0.06	**0.02**	0.00	0.00	**0.00**	0.00	0.01	0.00	0.00	0.00
As	0.00	0.03	**0.01**	0.02	0.01	0.08	0.09	0.02	0.12	0.12	0.09	0.03	0.05	0.11	**0.07**	0.09	0.10	**0.10**	0.06	0.09	0.11	0.04	0.03
S	39.18	38.83	**39.01**	38.56	38.66	38.98	39.39	38.91	38.96	39.17	39.14	39.01	38.94	38.80	**38.96**	38.65	38.75	**38.70**	38.98	38.78	38.89	38.54	38.68
Se	0.00	0.00	**0.00**	0.00	0.00	0.00	0.00	0.12	0.00	0.03	0.01	0.00	0.00	0.05	**0.02**	0.00	0.00	**0.00**	0.01	0.02	0.03	0.02	0.00
Total	**98.84**	**98.80**	**98.82**	**98.14**	**98.36**	**98.61**	**100.11**	**99.53**	**99.45**	**100.08**	**99.50**	**99.49**	**99.41**	**99.19**	**99.26**	**99.00**	**98.37**	**98.69**	**99.21**	**99.15**	**99.11**	**98.48**	**98.55**
(at 2 apfu)																							
Cu	0.000	0.000	**0.000**	0.000	0.000	0.000	0.000	0.001	0.000	0.000	0.000	0.000	0.000	0.001	**0.000**	0.000	0.001	**0.001**	0.001	0.000	0.001	0.001	0.000
Mn	0.000	0.000	**0.000**	0.000	0.000	0.000	0.000	0.000	0.000	0.000	0.000	0.000	0.000	0.000	**0.000**	0.000	0.000	**0.000**	0.000	0.000	0.000	0.000	0.000
Fe	0.931	0.939	**0.935**	0.939	0.939	0.933	0.937	0.941	0.940	0.941	0.937	0.941	0.941	0.939	**0.939**	0.943	0.935	**0.939**	0.938	0.942	0.937	0.941	0.940
Co	0.000	0.000	**0.000**	0.000	0.000	0.000	0.000	0.000	0.000	0.000	0.000	0.000	0.000	0.000	**0.000**	0.000	0.000	**0.000**	0.000	0.000	0.000	0.000	0.000
Ni	0.001	0.000	**0.000**	0.000	0.000	0.000	0.000	0.000	0.000	0.000	0.000	0.000	0.001	0.001	**0.000**	0.000	0.001	**0.000**	0.000	0.000	0.001	0.001	0.000
As	0.000	0.000	**0.000**	0.000	0.000	0.001	0.001	0.000	0.001	0.001	0.001	0.000	0.001	0.001	**0.001**	0.001	0.001	**0.001**	0.001	0.001	0.001	0.000	0.000
Sb	0.000	0.000	**0.000**	0.000	0.000	0.000	0.000	0.000	0.000	0.000	0.000	0.000	0.000	0.000	**0.000**	0.000	0.000	**0.000**	0.000	0.000	0.000	0.000	0.000
Total M	**0.933**	**0.940**	**0.936**	**0.940**	**0.940**	**0.935**	**0.939**	**0.943**	**0.942**	**0.943**	**0.939**	**0.942**	**0.942**	**0.943**	**0.941**	**0.945**	**0.938**	**0.941**	**0.940**	**0.943**	**0.940**	**0.943**	**0.941**
S	1.067	1.060	**1.064**	1.060	1.060	1.065	1.061	1.056	1.058	1.057	1.061	1.058	1.058	1.057	**1.059**	1.055	1.062	**1.059**	1.060	1.057	1.059	1.057	1.059
Se	0.000	0.000	**0.000**	0.000	0.000	0.000	0.000	0.001	0.000	0.000	0.000	0.000	0.000	0.001	**0.000**	0.000	0.000	**0.000**	0.000	0.000	0.000	0.000	0.000
S(+Se)	**1.067**	**1.060**	**1.064**	**1.060**	**1.060**	**1.065**	**1.061**	**1.057**	**1.058**	**1.057**	**1.061**	**1.058**	**1.058**	**1.057**	**1.059**	**1.055**	**1.062**	**1.059**	**1.060**	**1.057**	**1.060**	**1.057**	**1.059**
M/S	**0.874**	**0.886**	**0.880**	**0.887**	**0.886**	**0.877**	**0.885**	**0.891**	**0.890**	**0.892**	**0.885**	**0.890**	**0.891**	**0.891**	**0.888**	**0.896**	**0.883**	**0.889**	**0.887**	**0.892**	**0.888**	**0.892**	**0.888**

Table A3. Complete electron probe microanalysis data for lollingite (continued)

			800m M2										760m M2							
																				lam Po (F
8rhl6_2	8rhl6_3	**8RH mean n=7**	20rhpl01_	20rhpl01_	20rhpl01_	20rhp1	20rhp4	20rhpl04_	20rhpl04_	20rhpl04_	20rhpl04_	**20RH mean n=9**	**14RHp7**	15RHl1_1	15RHl1_2	15RHl1_3	15RHl1_4	15RHl1_5	**15RH mean n=5**	**15RHp1**
0.00	0.05	**0.03**	0.02	0.04	0.01	0.03	0.00	0.04	0.00	0.02	0.00	**0.02**	**0.00**	0.00	0.00	0.00	0.00	0.00	**0.00**	**0.04**
0.01	0.00	**0.01**	0.01	0.00	0.00	0.01	0.00	0.01	0.03	0.00	0.00	**0.01**	**0.01**	0.00	0.00	0.00	0.00	0.00	**0.00**	**0.00**
59.67	60.03	**59.93**	59.12	58.95	58.85	60.15	60.42	60.35	60.37	60.26	60.13	**59.85**	**60.35**	61.20	60.99	60.81	60.98	60.89	**60.97**	**61.11**
0.00	0.00	**0.01**	0.00	0.00	0.00	0.00	0.00	0.00	0.00	0.00	0.00	**0.00**	**0.00**	0.00	0.00	0.00	0.04	0.00	**0.01**	**0.00**
0.05	0.00	**0.02**	0.00	0.02	0.05	0.04	0.01	0.02	0.04	0.04	0.08	**0.03**	**0.31**	0.19	0.16	0.12	0.13	0.13	**0.15**	**0.15**
0.00	0.00	**0.00**	0.00	0.00	0.00	0.05	0.08	0.02	0.06	0.11	0.03	**0.04**	**0.05**	0.00	0.00	0.00	0.05	0.06	**0.02**	**0.04**
0.06	0.07	**0.07**	0.07	0.10	0.09	0.11	0.07	0.06	0.07	0.09	0.13	**0.09**	**0.08**	0.00	0.12	0.15	0.05	0.07	**0.08**	**0.11**
38.61	38.41	**38.70**	38.14	38.23	38.19	38.68	38.52	38.81	38.68	38.36	38.59	**38.47**	**38.82**	38.78	38.48	38.97	38.71	38.75	**38.74**	**38.90**
0.00	0.00	**0.01**	0.00	0.00	0.00	0.00	0.00	0.01	0.00	0.02	0.02	**0.01**	**0.00**	0.00	0.04	0.00	0.03	0.02	**0.02**	**0.00**
98.41	**98.56**	**98.78**	**97.37**	**97.34**	**97.19**	**99.07**	**99.11**	**99.32**	**99.26**	**98.90**	**98.98**	**98.51**	**99.61**	**100.17**	**99.79**	**100.06**	**100.00**	**99.92**	**99.99**	**100.35**
0.000	0.001	**0.000**	0.000	0.001	0.000	0.000	0.000	0.001	0.000	0.000	0.000	**0.000**	**0.000**	0.000	0.000	0.000	0.000	0.000	**0.000**	**0.001**
0.000	0.000	**0.000**	0.000	0.000	0.000	0.000	0.000	0.000	0.000	0.000	0.000	**0.000**	**0.000**	0.000	0.000	0.000	0.000	0.000	**0.000**	**0.000**
0.939	0.945	**0.940**	0.941	0.938	0.938	0.942	0.947	0.942	0.944	0.947	0.943	**0.942**	**0.940**	0.949	0.951	0.943	0.948	0.947	**0.948**	**0.946**
0.000	0.000	**0.000**	0.000	0.000	0.000	0.000	0.000	0.000	0.000	0.000	0.000	**0.000**	**0.000**	0.000	0.000	0.000	0.001	0.000	**0.000**	**0.000**
0.001	0.000	**0.000**	0.000	0.000	0.001	0.001	0.000	0.000	0.001	0.001	0.001	**0.001**	**0.005**	0.003	0.002	0.002	0.002	0.002	**0.002**	**0.002**
0.001	0.001	**0.001**	0.001	0.001	0.001	0.001	0.001	0.001	0.001	0.001	0.001	**0.001**	**0.001**	0.000	0.001	0.002	0.001	0.001	**0.001**	**0.001**
0.000	0.000	**0.000**	0.000	0.000	0.000	0.000	0.001	0.000	0.000	0.001	0.000	**0.000**	**0.000**	0.000	0.000	0.000	0.000	0.000	**0.000**	**0.000**
0.941	**0.947**	**0.942**	**0.942**	**0.940**	**0.940**	**0.945**	**0.948**	**0.944**	**0.946**	**0.950**	**0.946**	**0.945**	**0.946**	**0.952**	**0.955**	**0.947**	**0.951**	**0.950**	**0.951**	**0.951**
1.059	1.053	**1.058**	1.058	1.060	1.060	1.055	1.052	1.056	1.054	1.050	1.054	**1.055**	**1.054**	1.048	1.045	1.053	1.048	1.050	**1.049**	**1.049**
0.000	0.000	**0.000**	0.000	0.000	0.000	0.000	0.000	0.000	0.000	0.000	0.000	**0.000**	**0.000**	0.000	0.000	0.000	0.000	0.000	**0.000**	**0.000**
1.059	**1.053**	**1.058**	**1.058**	**1.060**	**1.060**	**1.055**	**1.052**	**1.056**	**1.054**	**1.050**	**1.054**	**1.055**	**1.054**	**1.048**	**1.045**	**1.053**	**1.049**	**1.050**	**1.049**	**1.049**
0.889	**0.899**	**0.891**	**0.891**	**0.887**	**0.886**	**0.895**	**0.902**	**0.894**	**0.898**	**0.904**	**0.897**	**0.895**	**0.898**	**0.909**	**0.913**	**0.899**	**0.907**	**0.905**	**0.907**	**0.906**

Table A3. Complete electron probe microanalysis data for lollingite (continued)

eS)														lam Po (FeS)		lam Po (FeS)					
16RHl3_1	16RHl3_2	16RHl3_3	16RHl3_4	16RHl9_1	16RHl9_2	16RHl9_3	16RHl9_4	6RHl11_	6RHl11_	6RHl11_	6RHl11_	6RHl11_5	**mean n=13**	16RHp1	16RHp2	**16RH mean n=2**	17RHl1_1	17RHl1_2	17RHl1_3	17RHl1_4	17RHl1_5
0.04	0.06	0.00	0.00	0.05	0.00	0.04	0.00	0.00	0.01	0.00	0.01	0.00	**0.02**	0.01	0.00	**0.01**	0.00	0.02	0.01	0.00	0.00
0.00	0.00	0.00	0.00	0.00	0.00	0.01	0.00	0.00	0.03	0.01	0.01	0.00	**0.00**	0.00	0.00	**0.00**	0.00	0.00	0.01	0.00	0.01
60.89	61.16	61.19	60.76	60.49	60.32	60.09	59.74	60.59	61.18	60.36	60.93	60.87	**60.66**	60.62	61.64	**61.13**	60.53	60.47	60.37	60.01	60.02
0.00	0.00	0.00	0.00	0.00	0.00	0.00	0.00	0.00	0.00	0.00	0.00	0.00	**0.00**	0.00	0.00	**0.00**	0.00	0.00	0.00	0.00	0.00
0.02	0.03	0.08	0.08	0.10	0.09	0.09	0.10	0.06	0.04	0.08	0.04	0.05	**0.07**	0.00	0.01	**0.00**	0.18	0.22	0.16	0.23	0.19
0.04	0.05	0.00	0.00	0.06	0.03	0.03	0.09	0.00	0.06	0.00	0.07	0.00	**0.03**	0.02	0.09	**0.06**	0.00	0.00	0.09	0.04	0.00
0.03	0.05	0.21	0.05	0.00	0.07	0.12	0.09	0.04	0.03	0.01	0.02	0.11	**0.07**	0.06	0.15	**0.11**	0.11	0.07	0.14	0.05	0.08
38.74	38.81	38.77	38.46	38.73	38.59	38.53	38.70	38.48	38.83	38.44	38.83	38.79	**38.67**	37.85	37.34	**37.59**	38.55	39.08	38.88	39.08	38.86
0.02	0.02	0.02	0.01	0.01	0.01	0.00	0.06	0.00	0.08	0.00	0.05	0.07	**0.03**	0.00	0.00	**0.00**	0.06	0.02	0.00	0.00	0.03
99.78	**100.18**	**100.27**	**99.37**	**99.44**	**99.10**	**98.92**	**98.79**	**99.16**	**100.25**	**98.90**	**99.95**	**99.90**	**99.54**	**98.56**	**99.23**	**98.89**	**99.42**	**99.86**	**99.65**	**99.41**	**99.19**
0.001	0.001	0.000	0.000	0.001	0.000	0.001	0.000	0.000	0.000	0.000	0.000	0.000	**0.000**	0.000	0.000	**0.000**	0.000	0.000	0.000	0.000	0.000
0.000	0.000	0.000	0.000	0.000	0.000	0.000	0.000	0.000	0.000	0.000	0.000	0.000	**0.000**	0.000	0.000	**0.000**	0.000	0.000	0.000	0.000	0.000
0.948	0.949	0.949	0.950	0.944	0.945	0.943	0.938	0.949	0.949	0.947	0.947	0.946	**0.946**	0.958	0.972	**0.965**	0.946	0.939	0.940	0.935	0.938
0.000	0.000	0.000	0.000	0.000	0.000	0.000	0.000	0.000	0.000	0.000	0.000	0.000	**0.000**	0.000	0.000	**0.000**	0.000	0.000	0.000	0.000	0.000
0.000	0.001	0.001	0.001	0.002	0.001	0.001	0.002	0.001	0.001	0.001	0.001	0.001	**0.001**	0.000	0.000	**0.000**	0.003	0.003	0.002	0.003	0.003
0.000	0.001	0.002	0.001	0.000	0.001	0.001	0.001	0.000	0.000	0.000	0.000	0.001	**0.001**	0.001	0.002	**0.001**	0.001	0.001	0.002	0.001	0.001
0.000	0.000	0.000	0.000	0.000	0.000	0.000	0.001	0.000	0.000	0.000	0.000	0.000	**0.000**	0.000	0.001	**0.000**	0.000	0.000	0.001	0.000	0.000
0.949	**0.951**	**0.952**	**0.952**	**0.947**	**0.947**	**0.947**	**0.941**	**0.950**	**0.951**	**0.949**	**0.948**	**0.948**	**0.949**	**0.959**	**0.974**	**0.966**	**0.950**	**0.943**	**0.945**	**0.939**	**0.942**
1.050	1.049	1.047	1.048	1.053	1.053	1.053	1.058	1.050	1.049	1.051	1.051	1.051	**1.051**	1.041	1.026	**1.033**	1.049	1.057	1.055	1.061	1.058
0.000	0.000	0.000	0.000	0.000	0.000	0.000	0.001	0.000	0.001	0.000	0.001	0.001	**0.000**	0.000	0.000	**0.000**	0.001	0.000	0.000	0.000	0.000
1.051	**1.049**	**1.048**	**1.048**	**1.053**	**1.053**	**1.053**	**1.059**	**1.050**	**1.049**	**1.051**	**1.052**	**1.052**	**1.051**	**1.041**	**1.026**	**1.034**	**1.050**	**1.057**	**1.055**	**1.061**	**1.058**
0.903	**0.907**	**0.909**	**0.909**	**0.899**	**0.899**	**0.899**	**0.889**	**0.905**	**0.906**	**0.903**	**0.902**	**0.902**	**0.902**	**0.920**	**0.950**	**0.935**	**0.905**	**0.892**	**0.896**	**0.885**	**0.890**

Table A3. Complete electron probe microanalysis data for lollingite (continued)

						600m M2		580m M2													
					lam Po (FeS)		lam Po (FeS)													lam Po (FeS)	
17RHl3_1	17RHl3_2	17RHl3_3	17RHl3_4	**17RH mean n=9**	**17RHp5**	**1bch2**	**1bch1**	9rhl02_1	9rhl02_2	9rhl02_3	9rhl05_1	9rhl05_2	9rhl05_3	9rhl06_2	9rhl06_3	9rhl08_1	9rhl08_2	9rhl08_3	**9RH mean n=11**	9rhl06_1	9rhp01
0.00	0.02	0.05	0.00	0.01	0.01	0.06	0.04	0.01	0.00	0.00	0.01	0.00	0.04	0.05	0.03	0.01	0.04	0.01	0.02	0.00	0.00
0.00	0.01	0.01	0.01	0.01	0.00	0.01	0.01	0.00	0.01	0.01	0.00	0.00	0.00	0.02	0.01	0.00	0.01	0.00	0.01	0.00	0.01
60.35	60.46	60.61	60.72	60.39	62.10	60.32	62.63	59.74	60.53	60.32	60.04	56.72	60.47	61.08	60.98	59.62	59.04	59.79	59.85	62.06	61.98
0.00	0.00	0.02	0.00	0.00	0.00	0.00	0.00	0.00	0.00	0.00	0.00	0.00	0.01	0.00	0.00	0.00	0.00	0.00	0.00	0.00	0.00
0.15	0.14	0.13	0.13	0.17	0.00	0.24	0.00	0.29	0.31	0.30	0.27	0.25	0.26	0.23	0.27	0.24	0.29	0.22	0.27	0.18	0.00
0.00	0.04	0.00	0.04	0.02	0.06	0.04	0.00	0.06	0.00	0.00	0.00	0.03	0.00	0.00	0.02	0.00	0.00	0.00	0.01	0.08	0.01
0.09	0.06	0.05	0.16	0.09	0.00	0.03	0.02	0.08	0.00	0.01	0.05	0.08	0.00	0.04	0.13	0.00	0.03	0.10	0.05	0.11	0.02
38.86	38.61	38.58	38.67	38.80	36.89	38.74	36.99	38.33	38.66	38.38	38.17	38.21	38.35	38.56	38.69	38.52	38.64	38.54	38.46	37.70	36.36
0.06	0.05	0.05	0.01	0.03	0.00	0.04	0.00	0.00	0.06	0.03	0.03	0.05	0.00	0.00	0.00	0.02	0.00	0.03	0.02	0.01	0.01
99.51	**99.39**	**99.52**	**99.74**	**99.52**	**99.07**	**99.49**	**99.69**	**98.50**	**99.57**	**99.05**	**98.57**	**95.33**	**99.12**	**99.97**	**100.13**	**98.42**	**98.06**	**98.68**	**98.67**	**100.13**	**98.38**
0.000	0.000	0.001	0.000	0.000	0.000	0.001	0.001	0.000	0.000	0.000	0.000	0.000	0.001	0.001	0.000	0.000	0.001	0.000	0.000	0.000	0.000
0.000	0.000	0.000	0.000	0.000	0.000	0.000	0.000	0.000	0.000	0.000	0.000	0.000	0.000	0.000	0.000	0.000	0.000	0.000	0.000	0.000	0.000
0.941	0.945	0.946	0.946	0.942	0.983	0.941	0.985	0.942	0.944	0.946	0.947	0.918	0.948	0.950	0.947	0.939	0.932	0.940	0.941	0.970	0.989
0.000	0.000	0.000	0.000	0.000	0.000	0.000	0.000	0.000	0.000	0.000	0.000	0.000	0.000	0.000	0.000	0.000	0.000	0.000	0.000	0.000	0.000
0.002	0.002	0.002	0.002	0.003	0.000	0.004	0.000	0.004	0.005	0.004	0.004	0.004	0.004	0.003	0.004	0.004	0.004	0.003	0.004	0.003	0.000
0.001	0.001	0.001	0.002	0.001	0.000	0.000	0.000	0.001	0.000	0.000	0.001	0.001	0.000	0.000	0.001	0.000	0.000	0.001	0.001	0.001	0.000
0.000	0.000	0.000	0.000	0.000	0.000	0.000	0.000	0.000	0.000	0.000	0.000	0.000	0.000	0.000	0.000	0.000	0.000	0.000	0.000	0.001	0.000
0.944	**0.948**	**0.950**	**0.950**	**0.946**	**0.983**	**0.946**	**0.986**	**0.948**	**0.949**	**0.951**	**0.951**	**0.923**	**0.953**	**0.955**	**0.953**	**0.943**	**0.937**	**0.944**	**0.946**	**0.974**	**0.989**
1.055	1.051	1.049	1.050	1.054	1.017	1.053	1.014	1.052	1.050	1.049	1.048	1.077	1.047	1.045	1.047	1.057	1.063	1.055	1.054	1.026	1.011
0.001	0.001	0.001	0.000	0.000	0.000	0.000	0.000	0.000	0.001	0.000	0.000	0.001	0.000	0.000	0.000	0.000	0.000	0.000	0.000	0.000	0.000
1.056	**1.052**	**1.050**	**1.050**	**1.054**	**1.017**	**1.054**	**1.014**	**1.052**	**1.051**	**1.049**	**1.049**	**1.077**	**1.047**	**1.045**	**1.047**	**1.057**	**1.063**	**1.056**	**1.054**	**1.026**	**1.011**
0.894	**0.902**	**0.905**	**0.905**	**0.897**	**0.967**	**0.898**	**0.973**	**0.900**	**0.903**	**0.907**	**0.907**	**0.856**	**0.910**	**0.914**	**0.911**	**0.892**	**0.882**	**0.895**	**0.898**	**0.949**	**0.979**

Table A3. Complete electron probe microanalysis data for lollingite (continued)

					560m M2																
				lam Po (FeS)																**lam Po (FeS)**	
9rhp2	9rhl07_1	9rhl07_2	9rhl07_3	**9RH mean n=6**	13ach1	13achl1_1	13achl1_2	13achl1_3	13achl1_4	13achl1_5	13achpt5	13achpt7	13achpt10	13achpt17	13achpt24	13achpt25	13achpt26	**13aCH mean n=13**	13ach2	13achpt1	13achpt2
0.01	0.01	0.03	0.02	**0.01**	0.01	0.05	0.01	0.04	0.10	0.05	0.07	0.06	0.06	0.07	0.07	0.06	0.05	**0.05**	0.06	0.02	0.07
0.03	0.00	0.00	0.00	**0.01**	0.00	0.00	0.00	0.00	0.00	0.01	0.02	0.01	0.00	0.00	0.00	0.00	0.01	**0.00**	0.00	0.01	0.01
62.68	62.69	62.39	62.28	**62.35**	61.15	61.37	61.62	61.22	61.41	61.25	61.32	61.04	60.70	61.02	60.88	60.63	61.24	**61.14**	63.08	61.92	61.00
0.00	0.00	0.03	0.00	**0.01**	0.00	0.00	0.00	0.00	0.00	0.00	0.00	0.00	0.00	0.00	0.00	0.00	0.00	**0.00**	0.00	0.00	0.00
0.06	0.00	0.06	0.05	**0.06**	0.04	0.00	0.00	0.05	0.08	0.00	0.00	0.00	0.01	0.01	0.04	0.02	0.00	**0.02**	0.01	0.04	0.02
0.00	0.00	0.10	0.00	**0.03**	0.06	0.04	0.06	0.00	0.02	0.00	0.01	0.05	0.00	0.04	0.05	0.00	0.00	**0.03**	0.04	0.04	0.00
0.10	0.01	0.07	0.05	**0.06**	0.06	0.11	0.07	0.04	0.00	0.05	0.00	0.00	0.09	0.09	0.01	0.00	0.09	**0.05**	0.02	0.04	0.02
36.46	36.69	36.80	37.03	**36.84**	38.86	38.78	38.98	38.89	38.96	38.79	38.11	38.14	38.62	38.63	38.84	38.77	38.86	**38.71**	36.86	37.89	38.76
0.00	0.00	0.04	0.00	**0.01**	0.01	0.00	0.01	0.00	0.00	0.00	0.00	0.00	0.00	0.03	0.00	0.07	0.02	**0.01**	0.08	0.00	0.00
99.34	**99.39**	**99.52**	**99.44**	**99.37**	**100.19**	**100.37**	**100.75**	**100.25**	**100.57**	**100.15**	**99.54**	**99.30**	**99.47**	**99.90**	**99.88**	**99.56**	**100.27**	**100.02**	**100.14**	**99.96**	**99.88**
0.000	0.000	0.000	0.000	**0.000**	0.000	0.001	0.000	0.001	0.001	0.001	0.001	0.001	0.001	0.001	0.001	0.001	0.001	**0.001**	0.001	0.000	0.001
0.001	0.000	0.000	0.000	**0.000**	0.000	0.000	0.000	0.000	0.000	0.000	0.000	0.000	0.000	0.000	0.000	0.000	0.000	**0.000**	0.000	0.000	0.000
0.992	0.990	0.985	0.982	**0.984**	0.948	0.951	0.951	0.949	0.949	0.950	0.960	0.957	0.948	0.950	0.946	0.945	0.949	**0.950**	0.990	0.967	0.948
0.000	0.000	0.000	0.000	**0.000**	0.000	0.000	0.000	0.000	0.000	0.000	0.000	0.000	0.000	0.000	0.000	0.000	0.000	**0.000**	0.000	0.000	0.000
0.001	0.000	0.001	0.001	**0.001**	0.001	0.000	0.000	0.001	0.001	0.000	0.000	0.000	0.000	0.000	0.001	0.000	0.000	**0.000**	0.000	0.001	0.000
0.001	0.000	0.001	0.001	**0.001**	0.001	0.001	0.001	0.000	0.000	0.001	0.000	0.000	0.001	0.001	0.000	0.000	0.001	**0.001**	0.000	0.000	0.000
0.000	0.000	0.001	0.000	**0.000**	0.000	0.000	0.000	0.000	0.000	0.000	0.000	0.000	0.000	0.000	0.000	0.000	0.000	**0.000**	0.000	0.000	0.000
0.995	**0.990**	**0.988**	**0.983**	**0.987**	**0.950**	**0.953**	**0.952**	**0.950**	**0.951**	**0.952**	**0.961**	**0.958**	**0.950**	**0.952**	**0.948**	**0.946**	**0.951**	**0.952**	**0.991**	**0.969**	**0.950**
1.005	1.010	1.012	1.017	**1.013**	1.050	1.047	1.048	1.049	1.049	1.048	1.039	1.042	1.050	1.047	1.052	1.053	1.049	**1.048**	1.008	1.031	1.050
0.000	0.000	0.000	0.000	**0.000**	0.000	0.000	0.000	0.000	0.000	0.000	0.000	0.000	0.000	0.000	0.000	0.001	0.000	**0.000**	0.001	0.000	0.000
1.005	**1.010**	**1.012**	**1.017**	**1.013**	**1.050**	**1.047**	**1.048**	**1.050**	**1.049**	**1.048**	**1.039**	**1.042**	**1.050**	**1.048**	**1.052**	**1.054**	**1.049**	**1.048**	**1.009**	**1.031**	**1.050**
0.989	**0.981**	**0.976**	**0.967**	**0.974**	**0.905**	**0.911**	**0.909**	**0.906**	**0.907**	**0.908**	**0.925**	**0.920**	**0.904**	**0.909**	**0.902**	**0.898**	**0.906**	**0.908**	**0.983**	**0.940**	**0.905**

Table A3. Complete electron probe microanalysis data for lollingite (continued)

										420m M1						**420m M2**		
								lam Po (FeS)										
13achpt3	13achpt4	13achpt8	13achpt9	13achpt18	13achpt21	13achpt22	13achpt23	**13aCH mean n=11**	**18ach10**	3ch1	3chpt2	3chpt6	3chpt7	3chpt8	**3CH mean n=5**	8ach6	8ach10	**8aCH mean n=2**
0.06	0.04	0.01	0.05	0.07	0.00	0.11	0.04	0.05	0.02	0.03	0.00	0.04	0.03	0.00	0.02	0.02	0.10	0.06
0.00	0.00	0.03	0.00	0.00	0.03	0.00	0.01	0.01	0.00	0.00	0.00	0.00	0.00	0.00	0.00	0.04	0.00	0.02
61.50	61.37	60.47	60.30	60.86	60.93	61.12	60.43	61.18	60.44	59.84	59.06	58.83	60.12	60.43	59.66	59.77	59.86	59.82
0.00	0.00	0.00	0.00	0.00	0.00	0.00	0.00	0.00	0.00	0.00	0.00	0.00	0.05	0.00	0.01	0.00	0.00	0.00
0.05	0.05	0.02	0.05	0.06	0.01	0.00	0.03	0.03	0.13	0.34	0.34	0.31	0.35	0.34	0.34	0.06	0.04	0.05
0.00	0.06	0.02	0.00	0.05	0.00	0.02	0.01	0.02	0.02	0.04	0.00	0.00	0.00	0.03	0.01	0.02	0.04	0.03
0.14	0.07	0.14	0.05	0.08	0.05	0.09	0.11	0.07	0.08	0.12	0.11	0.02	0.11	0.08	0.09	0.08	0.10	0.09
38.82	38.44	38.67	38.92	38.67	38.62	38.98	38.52	38.47	38.82	38.73	38.60	38.68	38.72	38.91	38.73	38.64	38.25	38.45
0.00	0.00	0.00	0.09	0.02	0.00	0.00	0.00	0.02	0.00	0.00	0.02	0.03	0.03	0.08	0.03	0.00	0.00	0.00
100.57	**100.04**	**99.36**	**99.47**	**99.81**	**99.64**	**100.32**	**99.15**	**99.85**	**99.50**	**99.10**	**98.14**	**97.91**	**99.40**	**99.87**	**98.89**	**98.62**	**98.39**	**98.51**
0.001	0.001	0.000	0.001	0.001	0.000	0.002	0.001	0.001	0.000	0.000	0.000	0.001	0.000	0.000	0.000	0.000	0.001	0.001
0.000	0.000	0.000	0.000	0.000	0.001	0.000	0.000	0.000	0.000	0.000	0.000	0.000	0.000	0.000	0.000	0.001	0.000	0.000
0.951	0.955	0.945	0.940	0.948	0.950	0.946	0.946	0.953	0.943	0.937	0.932	0.930	0.939	0.939	0.935	0.939	0.945	0.942
0.000	0.000	0.000	0.000	0.000	0.000	0.000	0.000	0.000	0.000	0.000	0.000	0.000	0.001	0.000	0.000	0.000	0.000	0.000
0.001	0.001	0.000	0.001	0.001	0.000	0.000	0.000	0.000	0.002	0.005	0.005	0.005	0.005	0.005	0.005	0.001	0.001	0.001
0.002	0.001	0.002	0.001	0.001	0.001	0.001	0.001	0.001	0.001	0.001	0.001	0.000	0.001	0.001	0.001	0.001	0.001	0.001
0.000	0.000	0.000	0.000	0.000	0.000	0.000	0.000	0.000	0.000	0.000	0.000	0.000	0.000	0.000	0.000	0.000	0.000	0.000
0.954	**0.958**	**0.948**	**0.942**	**0.951**	**0.951**	**0.949**	**0.949**	**0.956**	**0.946**	**0.944**	**0.939**	**0.935**	**0.946**	**0.945**	**0.942**	**0.942**	**0.948**	**0.945**
1.046	1.042	1.052	1.057	1.049	1.049	1.051	1.051	1.044	1.054	1.056	1.061	1.065	1.053	1.054	1.058	1.058	1.052	1.055
0.000	0.000	0.000	0.001	0.000	0.000	0.000	0.000	0.000	0.000	0.000	0.000	0.000	0.000	0.001	0.000	0.000	0.000	0.000
1.046	**1.042**	**1.052**	**1.058**	**1.049**	**1.049**	**1.051**	**1.051**	**1.044**	**1.054**	**1.056**	**1.061**	**1.065**	**1.054**	**1.055**	**1.058**	**1.058**	**1.052**	**1.055**
0.913	**0.919**	**0.900**	**0.890**	**0.906**	**0.907**	**0.903**	**0.903**	**0.915**	**0.897**	**0.894**	**0.884**	**0.878**	**0.898**	**0.897**	**0.890**	**0.891**	**0.902**	**0.896**

Table A3. Complete electron probe microanalysis data for lollingite (continued)

	Drillcore																
lam Po (FeS)					**lam Po (FeS)**												**lam Po (FeS)**
8ach12	1chalp10	1chalp13	1chalp17	**1CHAL**	**1chalp08**	10chalp04	10chall3_1	10chall3_3	10chall3_4	10chall4_1	10chall4_2	10chall4_3	10chalp08	**10CHAL**	10chalp05	10chall3_2	**10CHAL**
				mean										**mean**			**mean**
				n=3										**n=8**			**n=2**
0.02	0.04	0.00	0.01	**0.02**	**0.00**	0.04	0.02	0.06	0.07	0.07	0.03	0.06	0.11	**0.06**	0.06	0.04	**0.05**
0.01	0.01	0.03	0.01	**0.02**	**0.00**	0.00	0.00	0.00	0.01	0.02	0.00	0.00	0.01	**0.00**	0.01	0.00	**0.00**
62.23	59.61	59.74	59.78	**59.71**	**61.58**	61.11	60.40	60.21	59.92	60.11	60.38	60.42	60.67	**60.40**	62.70	62.27	**62.48**
0.00	0.00	0.00	0.00	**0.00**	**0.01**	0.00	0.01	0.00	0.00	0.00	0.00	0.00	0.00	**0.00**	0.00	0.00	**0.00**
0.06	0.02	0.03	0.00	**0.02**	**0.01**	0.00	0.00	0.03	0.09	0.00	0.05	0.00	0.00	**0.02**	0.03	0.01	**0.02**
0.00	0.00	0.04	0.05	**0.03**	**0.00**	0.00	0.00	0.01	0.00	0.02	0.00	0.04	0.00	**0.01**	0.00	0.01	**0.00**
0.09	0.02	0.07	0.06	**0.05**	**0.12**	0.08	0.07	0.06	0.01	0.00	0.05	0.15	0.00	**0.05**	0.05	0.04	**0.05**
36.44	38.69	38.25	38.93	**38.62**	**37.29**	38.44	38.55	38.81	38.64	38.76	38.60	38.34	38.55	**38.59**	37.35	36.97	**37.16**
0.00	0.01	0.03	0.02	**0.02**	**0.02**	0.00	0.04	0.00	0.06	0.00	0.01	0.00	0.04	**0.02**	0.00	0.00	**0.00**
98.84	**98.38**	**98.19**	**98.87**	**98.48**	**99.04**	**99.67**	**99.08**	**99.19**	**98.80**	**98.98**	**99.13**	**99.00**	**99.38**	**99.15**	**100.20**	**99.33**	**99.77**
0.000	0.001	0.000	0.000	**0.000**	**0.000**	0.000	0.000	0.001	0.001	0.001	0.000	0.001	0.002	**0.001**	0.001	0.001	**0.001**
0.000	0.000	0.000	0.000	**0.000**	**0.000**	0.000	0.000	0.000	0.000	0.000	0.000	0.000	0.000	**0.000**	0.000	0.000	**0.000**
0.989	0.938	0.944	0.936	**0.940**	**0.972**	0.954	0.946	0.941	0.940	0.941	0.945	0.949	0.948	**0.946**	0.981	0.983	**0.982**
0.000	0.000	0.000	0.000	**0.000**	**0.000**	0.000	0.000	0.000	0.000	0.000	0.000	0.000	0.000	**0.000**	0.000	0.000	**0.000**
0.001	0.000	0.000	0.000	**0.000**	**0.000**	0.000	0.000	0.001	0.001	0.000	0.001	0.000	0.000	**0.000**	0.000	0.000	**0.000**
0.001	0.000	0.001	0.001	**0.001**	**0.001**	0.001	0.001	0.001	0.000	0.000	0.001	0.002	0.000	**0.001**	0.001	0.001	**0.001**
0.000	0.000	0.000	0.000	**0.000**	**0.000**	0.000	0.000	0.000	0.000	0.000	0.000	0.000	0.000	**0.000**	0.000	0.000	**0.000**
0.991	**0.939**	**0.946**	**0.938**	**0.941**	**0.974**	**0.955**	**0.948**	**0.943**	**0.943**	**0.943**	**0.947**	**0.951**	**0.950**	**0.948**	**0.983**	**0.984**	**0.983**
1.009	1.061	1.053	1.062	**1.059**	**1.026**	1.045	1.052	1.057	1.056	1.057	1.053	1.049	1.050	**1.052**	1.017	1.016	**1.017**
0.000	0.000	0.000	0.000	**0.000**	**0.000**	0.000	0.000	0.000	0.001	0.000	0.000	0.000	0.000	**0.000**	0.000	0.000	**0.000**
1.009	**1.061**	**1.054**	**1.062**	**1.059**	**1.026**	**1.045**	**1.052**	**1.057**	**1.057**	**1.057**	**1.053**	**1.049**	**1.050**	**1.052**	**1.017**	**1.016**	**1.017**
0.983	**0.885**	**0.898**	**0.883**	**0.889**	**0.950**	**0.914**	**0.900**	**0.893**	**0.892**	**0.891**	**0.900**	**0.907**	**0.905**	**0.900**	**0.966**	**0.968**	**0.967**